STARS

University of Central Florida
STARS

Electronic Theses and Dissertations, 2004-2019

2012

Surface Acoustic Wave (saw) Cryogenic Liquid And Hydrogen Gas Sensors

Brian Fisher
University of Central Florida

Part of the Electrical and Electronics Commons
Find similar works at: https://stars.library.ucf.edu/etd
University of Central Florida Libraries http://library.ucf.edu

This Doctoral Dissertation (Open Access) is brought to you for free and open access by STARS. It has been accepted for inclusion in Electronic Theses and Dissertations, 2004-2019 by an authorized administrator of STARS. For more information, please contact STARS@ucf.edu.

STARS Citation

Fisher, Brian, "Surface Acoustic Wave (saw) Cryogenic Liquid And Hydrogen Gas Sensors" (2012). *Electronic Theses and Dissertations, 2004-2019*. 2438.
https://stars.library.ucf.edu/etd/2438

SURFACE ACOUSTIC WAVE (SAW) CRYOGENIC LIQUID AND HYDROGEN GAS SENSORS

by

BRIAN H. FISHER
B.S. Florida Atlantic University, 2005
M.S. University of Central Florida, 2007

A dissertation submitted in partial fulfillment of the requirements
for the degree of Doctor of Philosophy
in the Department of Electrical Engineering and Computer Science
in the College of Engineering and Computer Science
at the University of Central Florida
Orlando, Florida

Summer Term
2012

Major Professor: Donald C. Malocha

© 2012 Brian Hal Fisher

ABSTRACT

This research was born from NASA Kennedy Space Center's (KSC) need for passive, wireless and individually distinguishable cryogenic liquid and H_2 gas sensors in various facilities. The risks of catastrophic accidents, associated with the storage and use of cryogenic fluids may be minimized by constant monitoring. Accidents involving the release of H_2 gas or LH_2 were responsible for 81% of total accidents in the aerospace industry. These problems may be mitigated by the implementation of a passive (or low-power), wireless, gas detection system, which continuously monitors multiple nodes and reports temperature and H_2 gas presence. Passive, wireless, cryogenic liquid level and hydrogen (H_2) gas sensors were developed on a platform technology called Orthogonal Frequency Coded (OFC) surface acoustic wave (SAW) radio frequency identification (RFID) tag sensors. The OFC-SAW was shown to be mechanically resistant to failure due to thermal shock from repeated cycles between room to liquid nitrogen temperature. This suggests that these tags are ideal for integration into cryogenic Dewar environments for the purposes of cryogenic liquid level detection. Three OFC-SAW H_2 gas sensors were simultaneously wirelessly interrogated while being exposed to various flow rates of H_2 gas. Rapid H_2 detection was achieved for flow rates as low as 1ccm of a 2% H_2, 98% N_2 mixture. A novel method and theory to extract the electrical and mechanical properties of a semiconducting and high conductivity thin-film using SAW amplitude and velocity dispersion measurements were also developed. The SAW device was shown to be a useful tool in analysis and characterization of ultrathin and thin films and physical phenomena such as gas adsorption and desorption mechanisms.

ACKNOWLEDGMENTS

I would first like to thank my grandparents, Vincent and Vinella Hamilton, for all the hardships that they endured to send all eight of their children to school so that my mother, Jannette Hamilton, would value hard work, independence and education above all else. It is her sacrifices and foresight for my educational development that has allowed me to seek the highest attainable degree in Electrical Engineering. My wife, Cecily is most valuable and supportive teammate in reaching the finish line. Her patience and intelligence has assisted me in writing and proofreading and her encouragement was necessary to make it through intense moments of doubt and personal disappointment. I would like to thank everyone who is still apart or has passed through my life and had words of encouragement or admiration at my ambitions. Positive energy is a very powerful medicine when you are fighting the uphill mental battle called the PhD process.

It is no more possible for a single soccer player to win the world cup than it is for me to finish this dissertation. The work that is presented here, is built upon the toils of generations of graduate students in the Consortium of Applied Acoustoelectronic Technology (CAAT), research group at UCF, under the direction of Dr. Donald Malocha. The team members (past and present) include: Mark and Daniel Gallagher, James Humphries III (Trip), Dr. Nikolai Kozlovski, Dr. Derek Puccio, Luis Rodriguez, Mike Roller, Dr. Nancy Saldanha, Bianca Santos and Dr. Yusuke Sato. Dr. Malocha has allowed me the freedom in research to explore my curiosity and outside-the-box ideas, and has built one of the best SAW research groups on the in the world. I plan on following his model when I am a professor in academia.

Thank you to Drs. Xun Gong, Patrick LiKamWa, Samuel Richie, and Robert Youngquist, for respecting my work and accepting the request to be a member of my PhD committee. Dr. Youngquist has been instrumental in the completion of this project, through his strong belief and willingness to fund the technology. I would also like to thank Mr. William 'Cy' Wilson at NASA Langley for his continued support and advice.

The dissertation is a necessary victory for my family, who has experienced so much disappointment and hardship in the last few years. The work that I have completed is dedicated to every poor Jamaican who hopes to accomplish their dreams through higher education but is instead shackled by a lack of resources and opportunity. Finally, I would like to thank my instincts and determination, because you have never lead me wrong.

"...I don't care what's probable, through blood sweat and tears, I am unstoppable."

Anthony Robles

TABLE OF CONTENTS

ABSTRACT iii

ACKNOWLEDGMENTS iv

TABLE OF CONTENTS vi

LIST OF FIGURES xvi

LIST OF TABLES xxxiv

LIST OF ABBREVIATIONS/ACRONYMS xxxvi

CHAPTER 1 INTRODUCTION 1

CHAPTER 2 BACKGROUND 4

2.1 Chapter Overview 4

2.2 SAW Technology 7

2.2.1 SAW Device Fundamentals 10

2.2.1.1 SAW Interdigitated Transducer (IDT) 11

2.2.1.2 SAW Reflector 21

2.2.1.3 Free Space Propagation Loss....23
2.2.1.4 Frequency Response of a 1-port delay line....23
2.2.1.5 Piezoelectric-SAW-Thin Film Interaction....26
2.2.2 OFC-SAW Approach....28
2.2.3 Comparison of OFC-SAW and Semiconductor RFID Platforms....32
2.3 Pressing Problems in Cryogenic Liquid Level Sensing....34
2.4 Pressing Problems in Low-Power Hydrogen Sensing....39
2.4.1 Review of H_2 Detector Technology....42
2.4.2 Hydrogen sensitive thin films....46
2.4.2.1 Metal Films....46
2.4.2.2 Metal Oxide Semiconductor Films....47
2.4.2.3 Nanotube and Nanowire Arrays....48
2.4.3 OFC-SAW sensors vs. previous SAW sensors....49
2.5 CHAPTER 2 Summary....52

CHAPTER 3 PIEZOELECTRIC SAW THIN-FILM INTERACTION 54
3.1 Chapter Overview 54
3.2 Theory 55
3.2.1 One-dimensional Wave Motion in a Solid 55
3.2.2 Amplitude and Velocity Dispersion in Viscoelastic Solids 59
3.2.3 One Dimensional Volume Wave in a Semiconducting Piezoelectric Solid 62
3.2.3.1 Velocity in Short Circuited Piezoelectric Material 62
3.2.3.2 Velocity in Open Circuited Piezoelectric Material 63
3.2.3.3 Electromechanical Coupling Coefficient 64
3.2.3.4 Semiconducting Piezoelectric Material 65
3.2.4 Thin-Film Piezoelectric SAW Interface 67
3.2.4.1 Relaxation Frequency at the Interface 70
3.2.4.2 SAW Attenuation Constant 72
3.2.4.3 SAW Phase Velocity 74

3.2.4.3.1 Acoustoelectric Phase Velocity 74
3.2.4.3.2 Fisher SAW Phase Velocity Approximation 75
3.2.4.3.3 Tiersten's Perturbation Theory 77
3.2.4.3.4 Morgan Empirical Relation for SAW Phase Velocity 78
3.2.5 Separation of the Acoustoelectric and Acoustoelastic Effects 79
3.3 CHAPTER 3 Summary 81
CHAPTER 4 MEASUREMENT OF THE SAW-THIN-FILM ACOUSTOELECTRIC AND ACOUTOELASTIC INTERACTION 85
4.1 Chapter Overview 85
4.2 Experimentation 88
4.2.1 *Ex-Situ* Measurements 88
4.2.2 *In-Situ* Measurements 90
4.2.2.1 Test Fixture 90
4.2.2.2 Software Design 95
4.2.2.3 Experiment Considerations 96

4.3 Results and Discussion 98

4.3.1 *Ex-Situ* Measurements 98

4.3.1.1 Semiconducting Films..98

4.3.1.2 High-Conductivity Metal Films..103

4.3.2 *In-Situ* Observation of Acoustoelectric and Acoustoelastic Mechanisms 108

4.4 CHAPTER 4 Summary..113

CHAPTER 5 PALLADIUM (PD) ULTRA-THIN FILM CHARATERIZATION 115

5.1 Chapter Overview..115

5.2 The Palladium-Hydrogen Interaction..115

5.2.1 Previous Work..115

5.2.2 Pd Thin/Thick Film Background Review 116

5.2.3 Pd Ultra-Thin Film Background Review 117

5.3 Precise Growth of Ultra-Thin Pd Films..119

5.3.1 Analysis of the *In-Situ* Die 120

5.3.2 Die Preparation Procedure 121

5.3.3 Measurement Setup and Procedure 122

5.3.4 *In-Situ* Measurement Results 122

5.3.5 Development of Malocha's Pd Ultrathin Film Approximation 125

5.3.5.1 Prediction of SAW Propagation Loss and Velocity Beneath Pd Films 128

5.4 Ultra-Thin Pd Film Hydrogen Sensitive Resistor 129

5.4.1 Sensitivity to H_2 gas 129

5.4.2 Field-effect dependence 132

5.4.3 Temperature dependence 133

5.5 Film aging, stability and sensor lifetime 133

5.5.1 O_2 Adsorption 134

5.5.2 Film Annealing 136

5.5.3 Film Encapsulation 137

5.5.4 Pd UFT Aging Results and Discussion 138

5.6 SAW Pd UTF Characterization....140

5.6.1 Ultra-Thin-Pd-H_2-SAW Interaction....140

5.6.1.1 Ex-Situ Measurement....140

5.6.1.2 In-Situ Measurement....141

5.7 Chapter Summary....144

CHAPTER 6 TIN DIOXIDE (SNO2) FILM CHARACTERIZATION....146

6.1 Chapter Overview....146

6.2 The H_2-Pd-SnO_2 Interaction....147

6.3 SnO_2 Film Growth and Processing....149

6.3.1 SnO_2 Film Deposition....151

6.3.2 Anneal Cycle....152

6.3.3 Shadow Mask....153

6.3.3.1 Film Thickness Profile....154

6.3.3.2 Propagation Loss Predictions for Non-uniform Films....156

6.4 Hydrogen Gas Sensitivity 161

6.5 Film Aging 166

6.6 CHAPTER 6 Summary 167

CHAPTER 7 OFC-SAW H2 GAS SENSORS 170

7.1 Chapter Overview 170

7.2 Embodiment of OFC RFID Tag Sensor 170

7.3 Tag Insertion Loss and Delay Change Predictions 173

7.4 Fabrication 176

7.5 Measurements 178

7.6 H_2 Sensitivity 182

7.7 Future Work 184

7.8 CHAPTER 7 Summary 185

CHAPTER 8 CRYOGENIC LIQUID LEVEL SENSING 187

8.1 Chapter Overview 187

8.2 Commercial SAW Device Performance 188

8.2.1 Hermetical Sealed Surface Mount Packages 188

8.2.2 Opened Lid Surface Mount Devices 192

8.3 Cryogenic Head Space Temperature Cycling 195

8.3.1 Temperature Head Space Cycling of Devices with Slit lids 196

8.3.2 Package Lid Removal and Inspection 199

8.3.3 Temperature Head Space Cycling of Opened Devices 199

8.3.4 Parallel Oriented Devices 200

8.4 Thermal Shock 201

8.5 OFC Device Performance 202

8.6 CHAPTER 8 Summary 206

CHAPTER 9 DISCUSSION AND CONCLUSIONS 207

LIST OF REFERENCES 210

LIST OF FIGURES

Figure 2-1. A schematic of a passive, wireless, OFC-SAW RFID-tag sensor. If properly designed the SAW propagation parameters are modulated by the presence and the properties of the thin-film. 5

Figure 2-2. Schematic of a passive, wireless sensor network using OFC-SAW RFID tag-sensors. 5

Figure 2-3. Schematic of the SAW transduction process between the interdigitated transducer (IDT) and a piezoelectric crystal. The IDT is bidirectional, thus the SAW propagates in two directions simultaneously. The wave amplitude is in the order of a fewÅ. 8

Figure 2-4. A schematic of the typical photolithographic process metal layer of SAW devices. ..9

Figure 2-5. A schematic of the Fourier transformation of a time-gated sine function................11

Figure 2-6. A schematic of 2fo, 3fo and 4fo IDTs....................12

Figure 2-7. Plot of the relative harmonic efficiency of SAW IDTs: (a) $2f_0$, (b)$3f_0$ and (c) $4f_0$. The number and arrows point to the trace that represents a given harmonic. This figure is taken from [19]....................14

Figure 2-8. A schematic of the electrical representation of an electrode pair in a transducer. 16

Figure 2-9. A schematic of an equivalent electric circuit of a SAW transducer 18

Figure 2-10. Plot of the real and imaginary portions of $Y_{in}(\omega)$ in comparison to the electrical conductance and susceptance for a 50MHz, uniform, $3f_0$, IDT with $N_p=20$, $W_a=20\lambda$ and $R_s=0.2\Omega/\square$ and $h=2000Å$ on YZ-$LiNbO_3$..19

Figure 2-11. Plot of S_{11} of the IDT from Figure 2-10 on smith chart, shows that the impedance at f_0 follows constant Q circle is may be matched using a series inductor...........................20

Figure 2-12. A schematic of a SAW reflector. The wave is reflected at the impedance discontinuity caused by the metal electrodes...21

Figure 2-13. A schematic of wave reflection and transmission between a source, transducer and reflector in 1-port SAW device. 24

Figure 2-14 A: Plot of the magnitude of S_{11} in dB versus frequency; B: Plot of the phase of S_{11} in dB versus frequency. It is a comparison of the modulated-admittance and COM model to measured data for a 50MHz 1-port SAW delay line on YZ-$LiNbO_3$. The IDT is uniform, $3f_0$, $N_p=20$, $W_a=20\lambda$, $R_s=1\Omega/\square$ and $h=2000Å$ *and* the reflector is uniform, $N=81$ and $h=2000Å$. 26

Figure 2-15 Plot of the magnitude of S_{11} in dB versus time. It is a comparison of the modulated-admittance and COM model to measured data for a 50MHz, 1-port, SAW delay line on YZ-$LiNbO_3$. The IDT is uniform, $3f_0$, $N_p=20$, $W_a=20\lambda$, $R_s=1\Omega/\square$ and $h=2000Å$. The reflector is uniform, $N=81$ and $h=2000Å$. The modulated-admittance model does not account for energy storage effect in the response of the reflector bank. 26

Figure 2-16. Schematic of the SAW propagation at the piezoelectric-thin-film interface..........27

Figure 2-17. A schematic of TDM and FDM coding schemes where τ_c is the chip or symbol length and τ_b is the bit length. 29

Figure 2-18. A schematic of OFC technique 29

Figure 2-19. A schematic of a passive wireless OFC-SAW RFID-tag sensor. If properly designed the SAW propagation parameters are modulated by the presence and the properties of the thin-film. 30

Figure 2-20. Plot of the time response and auto-correlation of Figure 2-19 32

Figure 2-21. Picture of the location and schematic of liquid hydrogen (LH_2) and liquid oxygen (LO_2) ECO sensor inside the shuttles external fuel tank. 37

Figure 2-22. Schematic of cryogenic liquid tank with a passive wireless liquid level and gas leak detection system. 39

Figure 2-23. A schematic of a covalently bonded H_2 molecule. 40

Figure 2-24. A schematic of the window of combustibility for H_2 gas mixtures in air at room temperature...41

Figure 2-25. Plot of the minimum ignition energy of H_2 gas as a function of % of H_2 in air at 1atm. 41

Figure 2-26. An example SAW OFC RFID hydrogen sensor embodiment. The device is being tested on an RF probe station and the reflector diffraction pattern is apparent from the OFC reflectors at differing frequencies. 52

Figure 3-1. A schematic of a one dimension volume wave in a solid (a: unperturbed crystal structure, b: longitudinal mode the particle displacement and wave propagation is in the same direction and c: shear mode, the particle motion is perpendicular to the direction of propagation) in a solid when force is applied. 55

Figure 3-2. A schematic of forces exerted on each face of a differential volume of an elastic solid. The force due to the *dxdz* and *dydz* planes have been ignored. 57

Figure 3-3. A schematic representation of a Kelvin-Voigt material which shows material stiffness, *c*, and viscosity mechanism η. The dynamic modulus, $C^*(\omega)$, is the frequency dependent stiffness (or dynamic modulus) of the material when a force, *F*, with angular frequency, ω, is applied in the *z*-direction and causes displacement *dz*. 59

Figure 3-4. Plot of acoustoelectric attenuation constant and phase velocity as a function of ω_r/ω a one-dimensional volume wave in a piezoelectric semiconductor. 67

Figure 3-5. A schematic of SAW propagation in a piezoelectric crystal, beneath a thin film. ε, σ, η, c, and ρ is the electrical permittivity, electrical conductivity, viscosity, stiffness and density, respectively. 67

Figure 3-6. A plot of the decay of the SAW potential in the positive and negative *y*-direction. .70

Figure 3-7. Plot of acoustoelectric attenuation constant and phase velocity as a function of $R_s \cdot v_{sc} \cdot \varepsilon_p$ for a SAW in a piezoelectric. 72

Figure 4-1. A plot of the predicted SAW propagation loss (solid lines) and velocity (dashed lines) as a function of the film's sheet resistance for a SAW on YZ-$LiNbO_3$. The acoustoelectric velocity (dashed lines) all fall on top of each other because it is not dispersive. 88

Figure 4-2. Shows a schematic of SAW device used for film dispersion measurements. 89

Figure 4-3. Shows a schematic of the shadow mask inside the e-beam film deposition system, with dual quartz crystal monitors, and high-vacuum RF feedthroughs. The shadow masking of a SAW device, allows deposition of the film precisely on the SAW propagation path. 93

Figure 4-4 . Picture of the base of the test fixture. The fixture is designed to be mechanically, thermally and electrically stable by using a (2cm x 7.5 cm x 4cm) brass base. SMA connectors were used to make connection between the RF cables and the probes. The RF probes were designed and constructed for stable electrical and mechanical contacts, which eliminates the need for bond wires and packaging. The probes were constructed using small hinges (for vertical motion), PCB, copper prongs (for the probes), and solder (connects PCB and probes). 94

Figure 4-5. A schematic of the SAW die that was design for the *in-situ* fixture. It is a one-port differential delay device with large Al probes pads to facilitate easy contact and low electrical contact-resistance. The thin-film in the SAW propagation path makes contact with a set of Al bus-bars which are used to measure the film's sheet resistance.............94

Figure 4-6. Picture of the shadow mask for the test fixture. The length of the film in the propagation path was controlled using the width of the via hole, which was controlled using a 56 thread-per-inch screw (i.e. 0.454mm lateral movement per revolution). An electrically controlled shutter (constructed using a DC motor) was positioned on the shadow mask to expose or block the evaporating material from the device. 95

Figure 4-7. A picture of the e-beam system, text fixture and data acquisition set-up in class 100 cleanroom...96

Figure 4-8. Plot of the maximum attainable AE propagation loss of a z-propagation SAW on YZ-$LiNbO_3$ as a function of the length of the film in the propagation path....................97

Figure 4-9 A: A plot of the measured SAW propagation loss coefficient for a 10Å Pd film as a function of frequency. The electrical losses (circles and solid red line) are observed once the mechanical losses are subtracted from the total loss and the elastic losses (squares and solid black line) are observed when the electric losses are subtracted. B: is the measured SAW velocity and the velocity prediction for a 10Å Pd film as a function of frequency. 100

Figure 4-10 A: Plot of the measured SAW propagation loss coefficient for a 520Å SnO_2 film as a function of frequency. B: is a plot of the measured SAW velocity and the velocity prediction for a 520Å SnO_2 film as a function of frequency. 101

Figure 4-11 A: Plot of the measured SAW propagation loss coefficient for a 1000Å SiO film as a function of frequency. B: is a plot of the measured SAW velocity and the velocity prediction for a 1000Å SiO film as a function of frequency. 101

Figure 4-12 Plot of the amplitude dispersion of a 350 and 625Å Pd film. The equations are fit the Fisher's and Tiersten's equation by making assumptions for η_{eff} and the complex portion of the shear modulus *SM''*. 105

Figure 4-13 Plot of the amplitude dispersion of a 500, 1000 and 2000Å Al films, All data were gathered from Davis's publication[84]. The equations are fit the Fisher's and Tiersten's equation by making assumptions for η_{eff} and the complex portion of the shear modulus *SM''*. 105

Figure 4-14. SAW velocity beneath metal films on YZ-LiNbO3. Comparison of Fisher's and Tiersten's approximations. 106

Figure 4-15. SAW velocity beneath metal films on ST-Quartz. Comparison of Fisher's and Tiersten's approximations. All data were gathered from Penunuri's publication [81]. ..106

Figure 4-16. The real-time output of data acquisition software; measured S-parameters which are processed to extract propagation loss and delay shift during growth of a Pd film in the SAW propagation path. The plots are updated in real time as film thickness changes..108

Figure 4-17 A plot of the measured and modeled SAW propagation loss (solid lines) and change in group delay (dashed lines) at 54.5 and 109MHz as a function of the Pd film thickness. Pd film's conductivity changes due to the film's thickness, and the SAW propagation loss and velocity are modulated via the acoustoelectric effect. 111

Figure 4-18. The thickness distribution of a 60Å Pd film deposited through a 1mm aperture. The thickness distribution was extracted from light absorption measurements across the film...112

Figure 5-1. A: Orthogonal Frequency Coded (OFC) SAW RFID tag-sensor with Pd film in the delay path for H_2 gas sensing capability. B: Atomic force microscopy (AFM) image of the border between the Pd ultra-thin film and the YZ lithium niobate (YZ-$LiNbO_3$) substrate. The AFM image shows that the film is constructed of a discontinuous network of atomic islands—nanoclusters...119

Figure 5-2. A schematic of the *in-situ* interdigitated resistor (IDR) and the parallel electrode resistor (PER). 121

Figure 5-3. A schematic of UCF's electron being thin film deposition system. CM #1 and 2 are the film thickness monitors which infers a film thickness based on the mass loading on a

quartz crystal oscillator. The use of the secondary shutter is critical to reproducing equivalent films. The *in-situ* thin film resistor is shown parallel to the samples............124

Figure 5-4. Plot of *in-situ* measurement of resistance and thickness via parallel electrode resistor (PER) during deposition of Pd films. The purpose of this plot is to emphasize the difference in data spreading due to the use of the secondary shutter. The traces with which solid diamonds represent depositions performed with the use of the secondary shutter, and the traces with the transparent diamonds represent depositions performed without the use of a secondary shutter. It shows a large scatter for the depositions without the secondary shutter...124

Figure 5-5. Plot of *in-situ* measurement of resistance and thickness via parallel electrode resistor (PER) during deposition of Pd films. These are the same curves shown in Figure 5-4, however they have all been shifted to the same start point ($10^7\Omega$). The exponential rates of change of the resistances between 8 to 50 angstroms are slightly different. This suggests that the films nucleation is slightly different in each deposition.....................125

Figure 5-6. This plot shows the change in film conductivity as a function of film thickness. The trace labeled "UCF Data" are collected *in-situ* using the parallel electrode resistors and 3" quartz wafers onto which Pd films were deposited. Data from the quartz wafers were acquired by depositing Pd films on the substrates, then measuring its thickness via profilometer and its sheet resistance via four point probe...127

Figure 5-7. Close-up of Figure 5-6 shows the conductivity of Pd films in the ultra-thin regime and highlights the difference between the Fuchs-Sondheimer approximation, the derived model and the measured data. UCF Data shown here represent an average of multiple deposition curves. 127

Figure 5-8. Plot of the predicted propagation loss and velocity as a function of Pd thickness for a 62.5MHz SAW on YZ-$LiNbO_3$. The acoustoelectric effect is dominant for Pd film thickness in the 9 to 16 Angstrom range. 128

Figure 5-9. H_2 gas cycling of *in-situ* PER with Pd film. ≈10uA test current was applied to the film. 131

Figure 5-10. IDR gas cycle with ohm meter. ≈100uA test current was applied to the film. 131

Figure 5-11. 2% H_2 gas cycling of 80-finger IDR die with Pd film, with 3V potential applied across the film. The switching times are approximately 1.5 seconds with roughly 50% decrease in resistance. 131

Figure 5-12. A 1V potential applied across the film and current is measured ≈ 2 seconds switching times 167% change in current = 62% decrease in resistance. 132

Figure 5-13. The current voltage characteristic is nonlinear as is expected for a nano-clustered film. 132

Figure 5-14. Comparison of temperature and H_2 gas sensitivity of the Pd UTFs. 133

Figure 5-15. 2% H_2 gas exposure of an ultra-thin film Pd resistor. The abrupt resistance decrease when exposed to H_2 gas is assumed due to a change in the cluster size and consequently the activation energy. After ten months, the fractional change in resistance due H_2 gas exposure has decreased due to aging of the film. 134

Figure 5-16. A_1: Chamber Pressurized with N_2 gas. B_1: Upon initial exposure to ambient air, the resistance increased approximately 18% within 30 seconds. C: When the vacuum chamber was resealed and pumped down to 10-6 Torr, the reaction stopped. A_2: Chamber re-pressurized to 1atm. B_2: The chamber was re-opened and the resistance increased to 60% above its initial value... 136

Figure 5-17. Observation of the resistivity of an ultra-thin Pd film during annealing process. The non-reversible change in resistivity suggests a change in film morphology occurred. 137

Figure 5-18. Schematic demonstrating the benefits of film encapsulation, by coating the ultra-thin Pd film with a dielectric film that traps or repels O_2 molecule but allows H_2 molecules to diffuse through rapidly, and react with palladium. 138

Figure 5-19. The control sample (i.e. un-annealed or encapsulated), annealed and the encapsulated samples were exposed to ambient air while the factional change in film resistivity ($\Delta R/R_o$) as a function of time was observed 139

Figure 5-20. A comparison of the ratios the film's aging rates per unit time (i.e. the ratio of $\Delta R/R_o$ for sample 1 to $\Delta R/R_o$ for sample 2) shows that when a sample is encapsulated with 1500Å of Al_2O_3, $\Delta R/R_o$ is decreased by a factor of approximately 20 when compared to the control sample. 139

Figure 5-21. Plot of measured 62.5MHz SAW propagation loss and velocity when a 11A Pd film is exposed H_2 gas. 140

Figure 5-22. The real-time observation and measurement of the modulation of Pd film's conductivity in the presence of H_2 gas. Consequently, the SAW propagation loss is also modulated via the acoustoelectric effect..143

Figure 5-23. The SAW propagation loss and measured Pd film sheet resistance as a function of H_2 gas exposure (data from Fig. 11). The measured propagation loss vs. measured sheet resistance falls on the predictive acoustoelectric curve, after errors due to film non-uniformity are taken into account..143

Figure 6-1. A schematic of the interaction between hydrogen, palladium and tin oxide...........148

Figure 6-2. A graph of the temperature ramp, anneal and cooling cycles for the OFC-SAW H_2 gas sensors..153

Figure 6-3. Picture of the test fixture and shadow mask for the 915 OFC-SAW device...........154

Figure 6-4. Picture of a 500Å SnO_2 + 20Å Pd film thickness profile after deposition through a 0.5mm aperture shadow mask. This profile measured using a Veeco Dektak Stylus profilometer. 155

Figure 6-5. A plot of the normalized film profile and data fit. The film profile is necessary to calculate the effective sheet resistance of the film. 156

Figure 6-6. A plot of the predicted insertion loss of 915MHz SAW on YZ-$LiNbO_3$ as a function of SnO_2 film thickness and deposition aperture. The predictions are compared to 3 measured data points. 160

Figure 6-7. A plot of the effective sheet resistance of non-uniform SnO_2 films as a function of thickness and deposition aperture.. 160

Figure 6-8. Plot of the 915MHz propagation loss and velocity of a 250Å non-uniform SnO_2 film on YZ-$LiNbO_3$. When the film is exposed to H_2 gas there is an increase in propagation loss and a decrease in velocity. 161

Figure 6-9. The propagation loss and group delay change when a uniform 500Å SnO_2 +20Å Pd film is exposed to H_2 gas. The group delay increase during H_2 exposure because the wave velocity slows due to the decrease in sheet resistance toward the short circuit case. 164

Figure 6-10. The propagation loss and group delay change when a uniform 250Å SnO_2 +20Å Pd film is exposed to H_2 gas. The group delay increase during H_2 exposure because the wave velocity slows due to the decrease in sheet resistance toward the short circuit case. 164

Figure 6-11. The propagation loss and group delay change when a non-uniform 500Å SnO_2 +20Å Pd film is exposed to H_2 gas. The film is annealed for 20 minutes. The group delay increase during H_2 exposure because the wave velocity slows due to the decrease in sheet resistance toward the short circuit case. After each large cycle the gas lines were purged of any remaining H_2 which resulted in the small changes in propagation loss every other cycle. 165

Figure 6-12. The propagation loss and group delay change when a non-uniform 250Å SnO_2 +20Å Pd film is exposed to H_2 gas. The film is annealed for 12 minutes. The group delay increase during H_2 exposure because the wave velocity slows due to the decrease in sheet resistance toward the short circuit case. 165

Figure 6-13. The propagation loss and group delay change when a non-uniform 250Å SnO_2 +20Å Pd film is exposed to H_2 gas. The film is annealed for 5 minutes. The group delay increase during H_2 exposure because the wave velocity slows due to the decrease in sheet resistance toward the short circuit case. 166

Figure 6-14. Plot of the change in propagation loss for a over a 3hr period. There is no observed change for this time period....167

Figure 7-1. A schematic of the 4 OFC-SAW codes that were created 172

Figure 7-2. A plot of the measured S_{11} response of OFC-SAW tags BHF401 to 404....172

Figure 7-3. A plot of the change in insertion as a function of the change in sheet resistance when a 500Å non-uniform SnO_2 film exposed to H_2 gas. 175

Figure 7-4. A plot of the change in insertion as a function of the change in sheet resistance when a 250Å non-uniform SnO_2 film exposed to H_2 gas. 175

Figure 7-5. A predictive plot of the change in group delay as a function of the change in sheet resistance....176

Figure 7-6. A picture of the shadow mask fixture for the film growth on 4 OFC-SAW tags simultaneously....177

Figure 7-7. A picture of the packaged OFC-SAW temperature and H_2 gas sensor with antenna. 177

Figure 7-8. A picture of the wireless test setup for the passive, wireless, OFC-SAW H_2 gas sensors....179

Figure 7-9. A picture of the placement of the Tx/Rx antenna and OFC-SAW tags....180

Figure 7-10. This is a picture of the 3-way splitter and the gas flow to the three sensors. 180

Figure 7-11. A picture of the gas flow tube filling gas precisely onto the SnO_2 film. 181

Figure 7-12. A picture of the VNA and decor data acquisition computer. 181

Figure 7-13. A plot of the MATLAB data acquisition software, which grabs data from the network analyzer, in real time and process 3 devices in ~ 1 second. 182

Figure 7-14 A: Plot of the change in propagation loss as a function of time for 3 passive wireless OFC-SAW devices. B: a plot of the change in propagation loss vs. the flow rate of 2% H_2 gas for device BHF402. 183

Figure 7-15 A: Plot of the change in group delay as a function of time for 3 passive wireless OFC-SAW devices. B: is a plot of the change in group delay vs. the flow rate of 2% H_2 gas for device BHF402. 183

Figure 7-16. Picture of the SAWtenna on black YZ-$LiNbO_3$ substrate. SAW sensor is integrated with the piezoelectric wafer, which eliminates the needs for chip packing, bond wires, solder and PCB. The maximum temperature of operation for this integrated sensor is around 450°C. 184

Figure 8-1. Schematic of cryogenic liquid tank with a passive wireless liquid level and gas leak detection system. 188

Figure 8-2. Dual-sided OFC SAW Device on $LiNbO_3$ 188

Figure 8-3. Hermetically sealed lithium niobate filter passband comparisons, before during and after submersion in liquid nitrogen 190

Figure 8-4. Hermetically sealed quartz filter passband comparisons, before during and after submersion in liquid nitrogen 191

Figure 8-5. A picture of the test fixture that was used to measure the SAW devices when they were submerged in liquid nitrogen. 192

Figure 8-6. $LiNbO_3$ packaged device soldered to PCB with 1mm x 6mm silts in both ends of the package. 193

Figure 8-7. Passband response of repeated cycling of $LiNbO_3$ device with 1mm x 6mm slits in the package lid. 194

Figure 8-8 Passband response of repeated cycling of quartz device with 1mm x 6mm slits in the package lid. 194

Figure 8-9. Photo of $LiNbO_3$ device topology 197

Figure 8-10. Photo of Quartz device topology 197

Figure 8-11. $LiNbO_3$ cryogenic head-space temperature cycling, after lid removal. 198

Figure 8-12. Quartz cryogenic head-space temperature cycling, after lid removal..................198

Figure 8-13. Close-up of second reflector bank of OFC device. This shows the response to repeated temperature cycling from headspace to liquid. The first reflector bank exhibited an equivalent response...204

Figure 8-14. Close-up of the response of the second reflector bank of OFC device after five temperature cycles from room to cryogenic temperature. The first reflector bank exhibited an equivalent response...205

LIST OF TABLES

Table 2-1. Summary of harmonic frequencies from due to sampling frequency 13

Table 2-2. A summary of properties of two commonly used SAW piezoelectric substrates. The values of e_2 and e_3 are the mechanical loading terms and are only applicable for Al electrodes; e_4 and e_5 represent the piezoelectric shorting and mass loading contributions to the reflectivity of a metal strip on the substrate. 16

Table 2-3. Comparison of the semiconductor-RFID and SAW-RFID technologies. 33

Table 2-4. A summary of the critical point and temperature of commonly used cryogenic fluids [30]..34

Table 2-5. A summary of a few major applications of cryogenic fluids....................................35

Table 2-6. Summary of the advantages and disadvantages of continuous liquid level sensors. ..37

Table 2-7. A summary of the LFL and UFL of H_2 gas at various temperatures. This summary shows that the LFL and UFL decreases as temperature is increased 41

Table 2-8. Summary of hydrogen sensor types. 42

Table 2-9. A summary of the performance of current commercially available H_2 gas detection technologies 44

Table 2-10. A summary of accidents involving LH_2 and H_2 gas in industry and aerospace [29]. 46

Table 3-1 is a summary of properties of two commonly used SAW piezoelectric substrates. 84

Table 4-1. Summary of the material parameters that were extracted using the YZ-$LiNbO_3$ SAW device. 100

Table 4-2 Summary of the material parameters that were used to fit the amplitude and velocity dispersion curves for Pd and Al films on YZ-$LiNbO_3$ and ST-Quartz SAW device 104

Table 6-1. An experimental design analysis for SnO_2-Pd films. 151

Table 6-2. Summary of the 915MHz SAW propagation loss across non-uniform films. 156

Table 6-3. A summary of the key process parameters: SnO_2 and Pd thickness, anneal time and film profile and their effect on film parameters: sheet resistance, H_2 gas sensitivity, aging rate and temperature coefficient of resistance (TCR) 163

Table 7-1. A summary of the specifications of OFC-SAW H_2 gas sensors 173

Table 8-1. Performance summary, Off-submersion until the device's signal is lost in noise; On-time after removal from liquid for device to recover to its nominal insertion loss in dry air. 204

LIST OF ABBREVIATIONS/ACRONYMS

AE	Acoustoelectric Effect
BW	Bandwidth
DC	Direct current
ECO	Engine Cutoff
EM	Electromagnetic
FFT	Fast Fourier Transform
FT	Fourier Transform.
IC	Integrated Circuit
IDT	Interdigitated Transducer
KSC	Kennedy Space Center
LFL	Lower Flammability Level
LH_2	Liquid hydrogen
LN_2	Liquid nitrogen
LO_2	Liquid oxygen
MM	Multimeter
NASA	National Aeronautics and Space Administration
NBW	Null bandwidth
NIST	National Institute of Standards and Technology
OFC	Orthogonal Frequency Coding
PCB	Printed Circuit Board

+PR	Positive Photoresist
PS	Power Supply
QCM	Quartz Crystal Monitor
RF	Radio Frequency
RFID	Radio Frequency IDentification
SAW	Surface Acoustic Wave
SMA	Sub-Miniature version A
SSME	Space Shuttle Main Engine
TCD	Temperature Coefficient of Delay
TCF	Temperature Coefficient of Frequency
UCF	University of Central Florida
UEL	Upper Explosive Level
UFL	Upper Flammability Level
UHF	Ultra High Frequency
UTF	Ultra-Thin Film
UV	Ultraviolet
VNA	Vector Network Analyzer
YZ-$LiNbO_3$	Y-cut, Z-propagating Lithium Niobate

CHAPTER 1 INTRODUCTION

This research was born from NASA Kennedy Space Center's (KSC) need for passive, wireless, and individually distinguishable sensors in various facilities. Primarily, the space shuttle's fuel is a mixture of liquid hydrogen and a liquid oxygen oxidizer. The sensors that were used to detect the quantity of these volatile cryogenic liquids in KSC's Dewars suffer from failure due to malfunction of electrical contacts. These wires also conduct heat from the exterior to the tank's interior and contributes to loss of expensive fuel via boiling and evaporation. The pipes that are used to supply the liquid hydrogen occasionally leak, which are difficult to detect and locate, and resulted the scraping of several shuttle launches [1]. Despite the shuttle program's dismantlement, there is still need for these sensors in many other facilities, thus this research in necessary in order to reduce costs and increase safety at NASA or any other facility that uses hazardous chemicals whose location and concentration need to be monitored. The majority of sensors available are semiconductor-based (primarily silicon, Si) devices. They have been found to function poorly in the harsh environments in that NASA operates (i.e. cryogenic liquids, high temperatures and high radiation). Wireless Si-based gas sensors cannot operate at room temperature without high power consumption. Surface Acoustic Wave (SAW) devices have been shown [2-5] to operate in all the aforementioned environments, may implemented as a purely passive and wireless Radio Frequency IDentification (RFID) tag-sensor. This dissertation chronicles the development of passive, wireless, coded, cryogenic liquid level, and hydrogen gas sensors on the SAW device platform.

A wireless sensor network has the ability to report the time and location of a sensing event instantaneously. Kozlovski et al [6, 7], has demonstrated a passive, wireless, RFID-tag and temperature-sensor network with a read range of up to 60m. The RFID tag-sensor—called the Orthogonal Frequency Coded (OFC) SAW tag—is built on a piezoelectric substrate, which serves as its power source, and is activated by a wireless transmission to the device. Adapting the RFID tag to chemical sensing involves the placement of a chemically sensitive film on the SAW substrate [8]. When the film is exposed to the analyte chemical, its electric and mechanical characteristics are changed, consequently altering the propagation characteristics of the SAW, and creating a sensing event. Discontinuous, ultra-thin palladium (Pd) films and tin dioxide (SnO_2) films were used for hydrogen sensing, and the SAW device was shown to be robust enough to repeatedly survive the large temperature change, which makes it an excellent candidate for a cryogenic liquid level sensor.

Chapter 2 provides a review of the fundamental background information necessary to digest this dissertation. This includes a review of basic SAW theory and discussions on pressing problems in low power hydrogen gas and cryogenic liquid sensing. It presents justification for the OFC-SAW RFID approach as opposed to the conventional silicon, integrated circuit (Si-IC) RFID tag sensor platform. Then the focus is shifted to hydrogen sensitive thin films and an explanation for choosing the aforementioned discontinuous, ultra-thin Pd and SnO_2 films for the sensing element.

Chapter 3 features a complete derivation of the acoustoelectric and acoustoelastic effects. This is necessary because these equations provide an approximation for the effect of sufficiently

thin films on SAW velocity and amplitude dispersion in piezoelectric substrates. The derived equations are experimentally verified in Chapter 4.

Chapter 5 details the process of characterizing the ultra-thin Pd films in terms of precise and reproducible growth, the Pd-H_2 gas interaction and the derivation of the ultra-thin film resistivity model, which predicts film resistivity as a function of morphology (i.e. thickness and degree of discontinuity). The experimental results of the Pd thin film H_2 gas sensitive resistor and SAW device is also presented.

Chapter 6 presents the characterization of the SnO_2 films and Chapter 7 discuses the design of the OFC-SAW RFID tag sensor.

Chapter 8 shifts the focus of the dissertation to the cryogenic liquid sensing properties of the OFC-SAW RFID tag. The is accomplished by examining the behavior of commercially available SAW devices, and OFC-SAW tags when repeatedly submerged in cryogenic liquid and various rates, device sizes and orientations.

Finally, chapter 9 provides a summary of the central deductions from this research and provides directions for future research.

CHAPTER 2 BACKGROUND

2.1 Chapter Overview

The cryogenic liquid level and hydrogen (H_2) gas sensors that were developed for this dissertation, were built on a platform technology called Orthogonal Frequency Coded (OFC) surface acoustic wave (SAW) radio frequency identification (RFID) tag sensors (Figure 2-1). Kozlovski and Malocha [6, 7] has used this technology to successfully demonstrate a passive, wireless, temperature-sensing network (Figure 2-2). The OFC-SAW tag is built on the commonly used YZ-lithium niobate (YZ-$LiNbO_3$) piezoelectric substrate—a well-researched SAW device platform—and implements spread spectrum coding in order to achieve multiple-access capability (i.e. read multiple devices simultaneously). These devices have a center frequency, in the 915MHz ISM band and a fraction bandwidth (BW) of approximately 10%. This frequency was chosen because higher frequency translates to smaller antenna, but also higher SAW propagation losses. The propagation losses at the 2.4GHz ISM band are very high and the antenna size at the 433MHz ISM band is too big. For H_2 gas sensing, a tin oxide (SnO_2) film is deposited in the delay path between the SAW transducer and a frequency coded SAW reflector bank; another identical reflector bank on the other side of the SAW transducer is used as a reference for sensing changes. The received SAW signal is correlated against a matched filter producing two compressed pulses; one pulse remains unchanged on exposure to H_2 gas, while the other exhibits changes in insertion loss and delay, due to acoustoelectric interaction of H_2 gas with the SnO_2 film and the SAW.

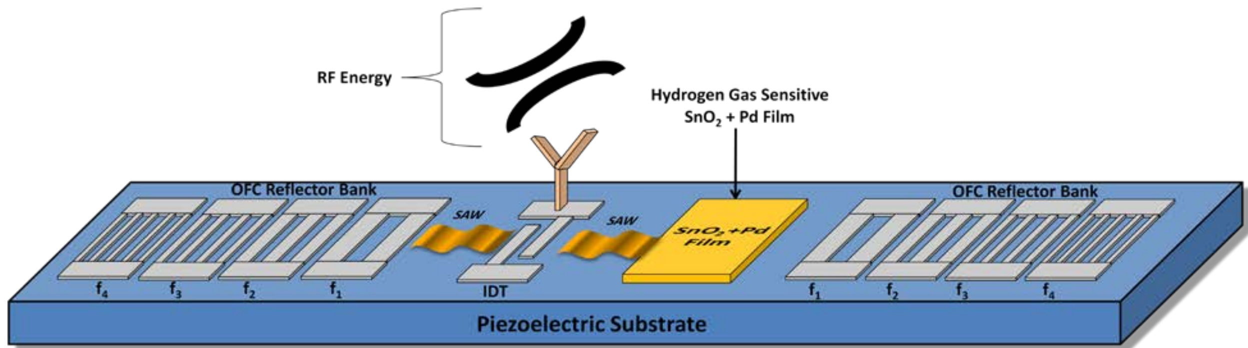

Figure 2-1. A schematic of a passive, wireless, OFC-SAW RFID-tag sensor. If properly designed the SAW propagation parameters are modulated by the presence and the properties of the thin-film.

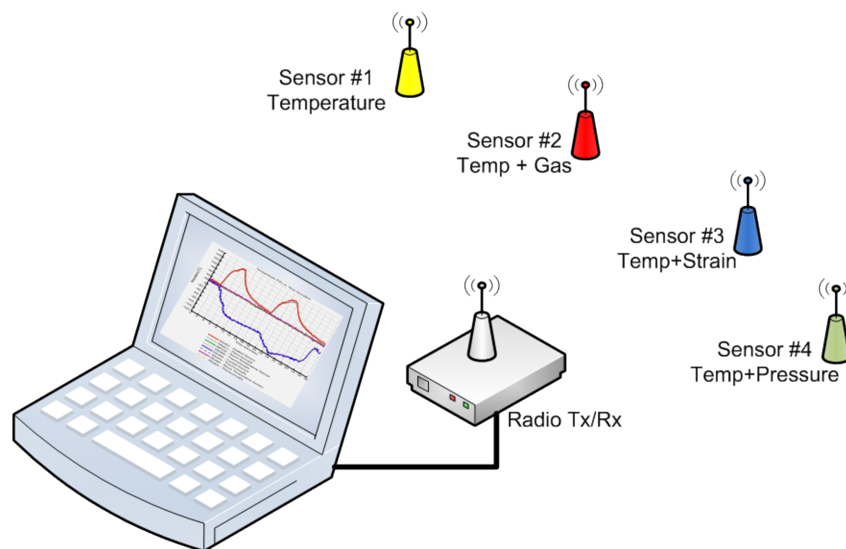

Figure 2-2. Schematic of a passive, wireless sensor network using OFC-SAW RFID tag-sensors.

This technology is suitable for the detection of volatile chemicals in hard-to-reach or hazardous locations where using batteries and running wires is cost and environmentally prohibitive. SAW devices are suitable for operation in harsh environments because they have

been shown to operate over a wide temperature range (-270°C to 1000°C) [3, 4] and in high radiation environments (up to 400MRads) [2]. SAW-RFID tags have been shown to successfully operate in enclosures that are completely surrounded by conducting walls—a Faraday cage [9]. Operation in Faraday cages are not possible with traditional passive, wireless, semiconductor-based RFID technologies [10]. These capabilities have placed SAW-RFID tags near the top of a short list of solutions for passive wireless sensors for industrial environments and outer-space, which is the primary source of NASA's interest.

This chapter provides a review of the fundamental background information necessary to digest this dissertation, while attempting being as self contained as possible. It is composed of four sections: (1) SAW technology, (2) cryogenic liquid sensing (3) hydrogen gas sensing and (4) a summary of the major conclusions from each section. The SAW technology section reviews the basics of the SAW device's interdigitated transducer (IDT) and reflector and provides the constitutive equations for first-order design of a one-port device. Section 2.2 also discusses the OFC-SAW approach and compares it to other viable passive wireless RFID tag-sensor solutions. Section 2.3 reviews the origins of cryogenic liquids, its many uses, the dangers associated with said use, and proposes viable solutions—using the OFC-SAW platform—to improve safety and cut costs by measuring the level of cryogenic liquids in containment vessels. Section 2.4 discusses the conditions in which H_2 use is hazardous, the risks associated with the conventional H_2 gas detection and proposes solutions—using the OFC-SAW platform—to improve safety and cut costs. This is followed by a brief introduction to the H_2 gas sensitive thin films that are used in this dissertation and a comparison of the OFC-SAW sensors to previous

SAW H_2 gas senor research. Section 2.5 summaries the major points of the chapter in order to prepare the reader for the remainder of the dissertation.

2.2 SAW Technology

SAW devices are primarily used as bandpass filter elements in the UHF band (10MHz to 3GHz) in cell phones, televisions and radar systems and most recently radio frequency identification (RFID) tags [11]. They operate by using an interdigitated transducer (IDT) to transform RF electrical signals into an ultrasonic electromechanical wave and vice versa via a piezoelectric transduction process in a piezoelectric crystal. The wave amplitude is in the order of a few Angstroms. A SAW in a piezoelectric substrate is an electromechanical wave because SAW is accompanied by a traveling electric field. This occurs because the molecules in the solid are aligned in electric dipole pairs. When an RF electric field is applied to the solid these dipole pairs are forced to rotate, consequently creating a mechanical wave and an electric field. Piezoelectric substrates are commonly characterized by the ratio of electrical to mechanical energy in the SAW, this is called the electromechanical coupling coefficient, and is mathematically referred to as K^2. The term piezoelectricity literally means “squeeze electricity”, because whenever a mechanical force is applied to a piezoelectric crystal (i.e. squeezing), electrical energy is generated and vice versa. This phenomenon occurs naturally in some materials such as quartz crystals and others such as lithium niobate ($LiNbO_3$) need to be poled by a high electric field in order to gain piezoelectric properties. The velocity of a typical SAW is 10^5 times slower than an electromagnetic (EM) wave, the SAW’s wave length is 10^5 times

smaller than an EM wave's, and it is possible to perform very complex signal processing functions in a very small volume.

Single-port delay-line devices are typically composed of an IDT and a reflector, which reflects some or the entire mechanical wave energy (Figure 2-3). When the SAW device is used in a wireless configuration, an antenna is attached to the IDT (Figure 2-1). The antenna captures the RF energy, that the transducer converts to an ultrasonic mechanical wave that travels down the crystal, bounces off the reflector, then travels back to the transducer, converted back to electrical energy, and is finally re-radiated by the antenna.

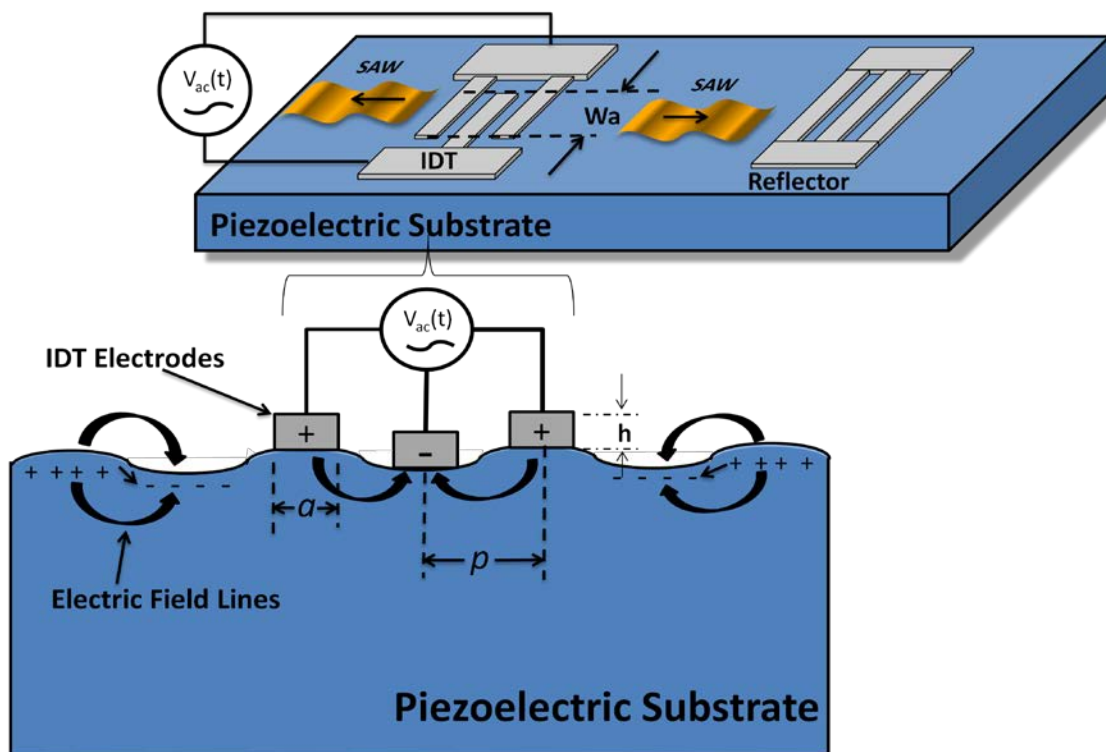

Figure 2-3. Schematic of the SAW transduction process between the interdigitated transducer (IDT) and a piezoelectric crystal. The IDT is bidirectional, thus the SAW propagates in two directions simultaneously. The wave amplitude is in the order of a fewÅ.

The IDT and reflectors structures are usually constructed from thin metal films by single layer photolithography. A schematic of the process steps for the SAW devices constructed in this dissertation are shown in Figure 2-4. All SAW devices in this dissertation propagate in the z-direction on a Y-cut $LiNbO_3$ substrate (YZ-$LiNbO_3$). This cut of the $LiNbO_3$ crystal is commonly used for SAW devices because of its high electromechanical coupling factor and self collimating (i.e. minimizes wave diffraction) properties, which help to decrease losses in the device. YZ-$LiNbO_3$ is also has a very high temperature coefficient of delay (TCD = -94ppm/^{0}C), which is desirable for temperature sensing applications but undesirable for gas sensors or filters. ST-cut X-propagating quartz is another popular substrate that has a TCD = 0ppm/^{0}C but unfortunately has very low coupling and is not self collimating.

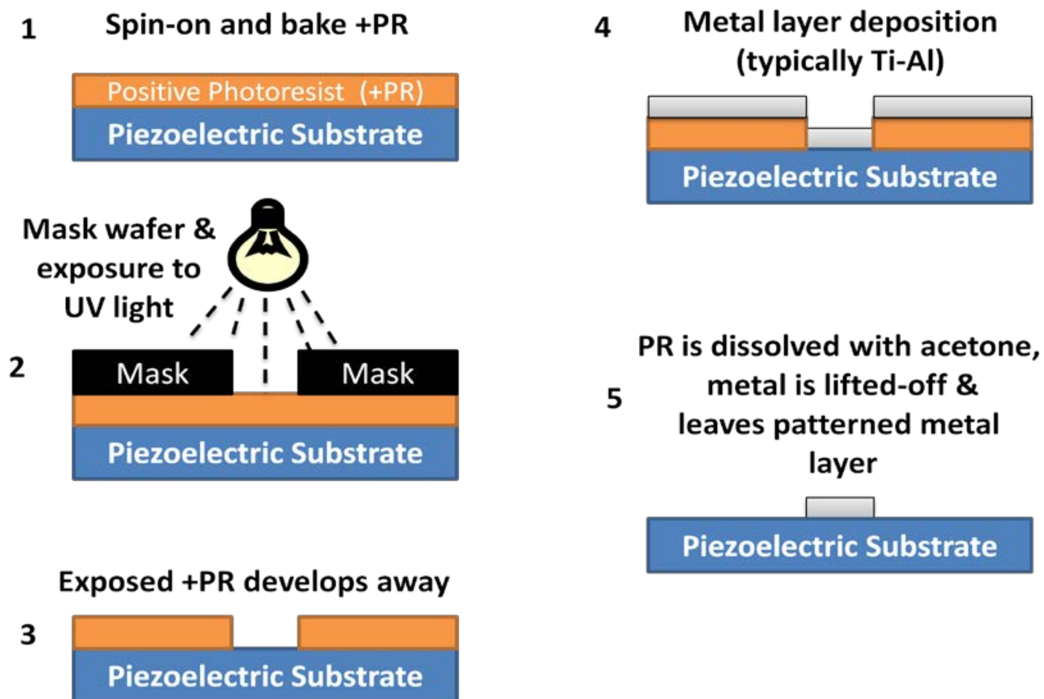

Figure 2-4. A schematic of the typical photolithographic process metal layer of SAW devices.

2.2.1 SAW Device Fundamentals

This section presents an abridged review of SAW IDT and reflector, the IDT's equivalent circuit model, the temperature sensitivity of the piezoelectric crystal and the interaction between a SAW and a thin film in the wave's propagation path. There is a wealth of references available on SAW devices but only a few are cited here [11-14].

When an electrical impulse is applied to the IDT, a truncated sinusoidal wave is created; the first order frequency response of the SAW device may be approximated using the impulse response and Fourier Transform (FT) pairs in Figure 2-5. The FT of a sine wave, $(\sin(\omega_0 t))$, that is time truncated to the length τ, produces a *sinc* function in the frequency domain with center frequency ω_0 and null bandwidth (NBW) of $2/\tau$. This is concept was used to develop the impulse response (IR) model and provides a quick method for SAW filter design using simple IDT structures [15]. The IR model is valid for non-reflective, uniform and apodized transducers. Apodization refers to the shape of the window function, and may be manipulated to generate almost any bandpass filter shape characteristic [16]. The IR model is also used to calculate the electrical parameters of uniform non-reflective IDTs.

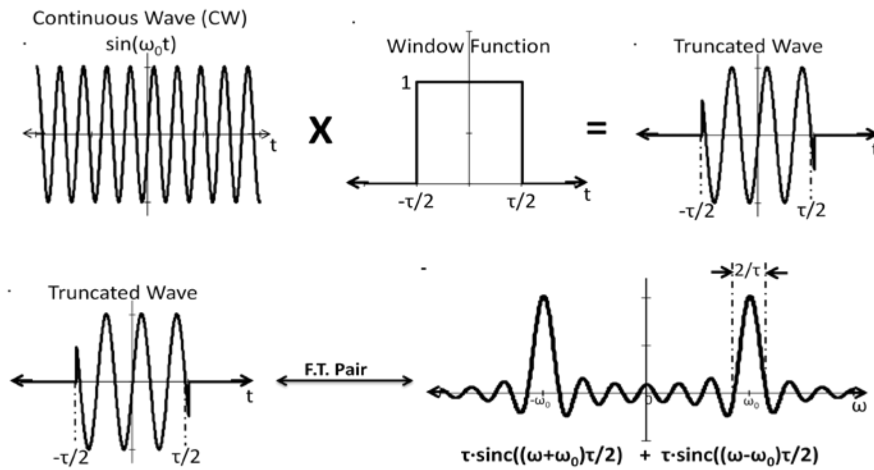

Figure 2-5. A schematic of the Fourier transformation of a time-gated sine function.

2.2.1.1 SAW Interdigitated Transducer (IDT)

The IDT in Figure 2-3 has two electrodes and two spaces per wavelength, and is called a $2f_0$ transducer (i.e. $f_s=2f_0$ is the sampling frequency). If the width of the electrodes and space are equal (i.e. $a/p=50\%$) the electrode width is one fourth the wavelength ($\lambda/4$); similarly, for $f_s=3f_0$ and $f_s=4f_0$ transducers the electrode width is $\lambda/6$ and $\lambda/8$, respectively. $3f_0$ and $4f_0$ transducers are used to minimize internal reflections, and bulk mode conversions in the IDT [17, 18]. Internal reflections are problematic in delay-line devices because energy is trapped in the transducer instead of being launched; this increases losses in the device. Bulk mode conversions refers to the creation of a wave that propagates into the bulk of the crystal and may constructively and/or deconstructively interfere with the SAW, this also causes losses [18].

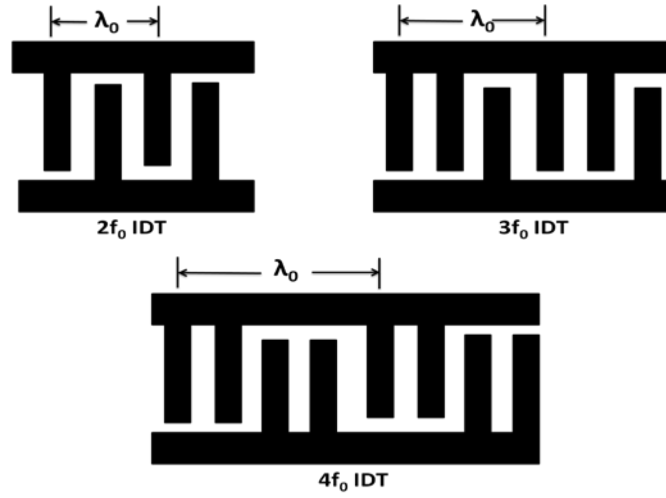

Figure 2-6. A schematic of 2fo, 3fo and 4fo IDTs

IDTs operate at integer multiples of their fundamental frequencies (i.e. harmonics). Harmonic operation is necessary when fabrication limitations prohibit the construction of high frequency devices or if the dispersion behavior of a film or device is being studied—as will be demonstrated in this dissertation (CHAPTER 4). The frequency response of a of a time sampled function is given by the sampling theorem as

$$X_s(\omega) = \sum_{k=-\infty}^{\infty} X(\omega - k\omega_s) \tag{2-1}$$

where ω is the radian frequency, given by

$$\omega = 2\pi f \tag{2-2}$$

where f is the frequency in Hertz. From Figure 2-5 the frequency response of a time gated sine wave is given by

$$X(\omega) = \frac{\pi\tau}{j} \cdot \left[\text{sinc}\left((\omega + \omega_0) \cdot \frac{\tau}{2} \right) + \text{sinc}\left((\omega - \omega_0) \cdot \frac{\tau}{2} \right) \right] \tag{2-3}$$

Combining equations (2-1) and (2-3) yields the equation for the frequency response of a sampled, time truncated and gated sine wave and is given by

$$X_s(\omega) = \sum_{k=-\infty}^{\infty}\left[\frac{\pi\tau}{j}\cdot\left(\text{sinc}\left((\omega - k\omega_s + \omega_0)\cdot\frac{\tau}{2}\right) + \text{sinc}\left((\omega + k\omega_s - \omega_0)\cdot\frac{\tau}{2}\right)\right)\right] \tag{2-4}$$

The resulting harmonics from equation (2-4) are given by ω_0-$k\omega_s$ and $k\omega_s$-ω_0; the harmonics for values of k between -2 to 2 is presented in Table 2-1.

Table 2-1. Summary of harmonic frequencies from due to sampling frequency

k	ω_s	ω_0-$k\omega_s$	$k\omega_s$- ω_0		ω_s	ω_0-$k\omega_s$	$k\omega_s$- ω_0		ω_s	ω_0-$k\omega_s$	$k\omega_s$- ω_0
-2	2 ω_0	5 ω_0	-5 ω_0		3 ω_0	7 ω_0	**-7** ω_0		4 ω_0	9 ω_0	-9 ω_0
-1	2 ω_0	3 ω_0	-3 ω_0		3 ω_0	4 ω_0	-4 ω_0		4 ω_0	5 ω_0	-5 ω_0
0	2 ω_0	1 ω_0	-1 ω_0		3 ω_0	1 ω_0	-1 ω_0		4 ω_0	1 ω_0	-1 ω_0
1	2 ω_0	-1 ω_0	1 ω_0		3 ω_0	-2 ω_0	2 ω_0		4 ω_0	-3 ω_0	3 ω_0
2	2 ω_0	-3 ω_0	3 ω_0		3 ω_0	-5 ω_0	5 ω_0		4 ω_0	-7 ω_0	7 ω_0

Not all harmonics shown by equation (2-4) are generated by an IDT, because the IDT's overall fundamental and harmonic frequency response is a function of the product of the element factor (which varies with *a/p* ratio) and array factor [11, 14, 19]. The array factor gives the harmonic independent response of the IDT and the element factor describes the elemental field distributions beneath an individual finger of an excited IDT. A summary of the harmonic efficiency as a function of *a/p* ratio for $2f_o$, $3f_o$ and $4f_o$ IDTs is shown in Figure 2-7 [19]. The figure shows that a $3f_0$ IDT with *a/p = 60%* with generate operate at several harmonics; this device will be used to study the dispersion characteristic of thin films in chapter 4.

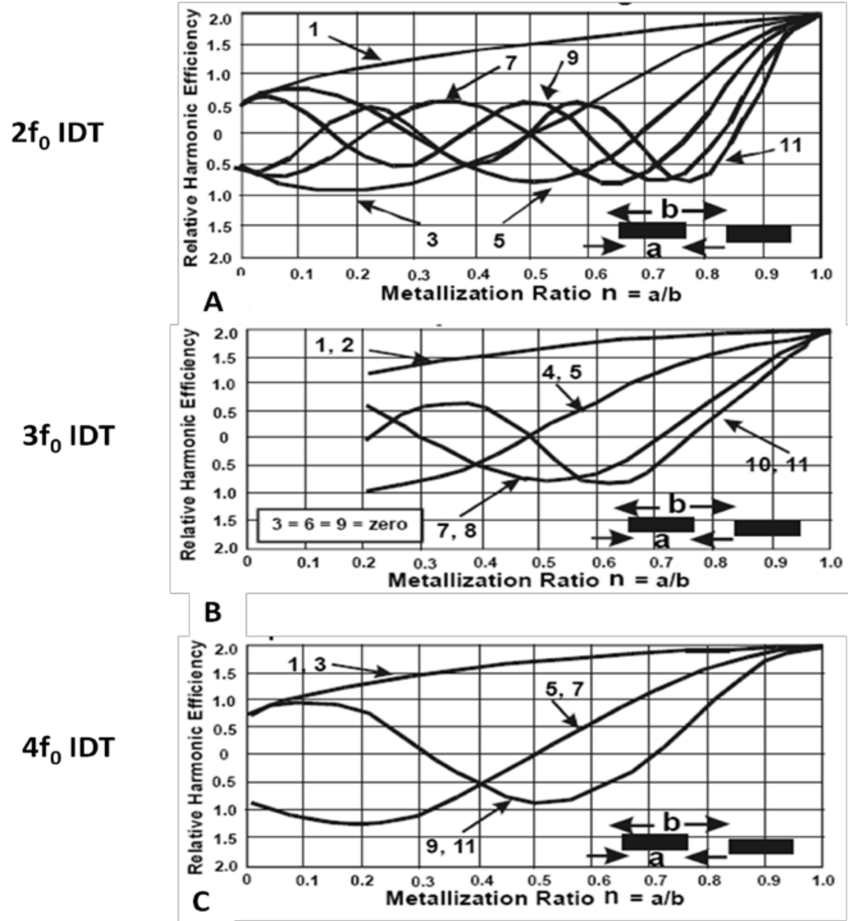

Figure 2-7. Plot of the relative harmonic efficiency of SAW IDTs: (a) $2f_0$, (b)$3f_0$ and (c) $4f_0$. The number and arrows point to the trace that represents a given harmonic. This figure is taken from [19].

The null bandwidth (NBW) of the IDT is given by

$$NBW = \frac{2}{\tau} = \frac{2f_0}{N_p} \tag{2-5}$$

where N_p is the number of wavelengths at center frequency. The fundamental frequency (i.e. 1st harmonic) of the IDT is given by

$$f_0 = \frac{v_{IDT}}{\frac{f_s}{f_0} p} \tag{2-6}$$

where v_{IDT}, is the SAW velocity beneath the IDT. The mass and electrical loading of the metal electrodes affect this velocity. If the energy storage is ignored, the velocity beneath the IDT may be approximated by

$$v_{IDT} = v_f \left(1 - \frac{K^2}{4} - e_2 \left(\frac{hf}{v_f} \right) - e_3 \left(\frac{hf}{v_f} \right)^2 \right) \tag{2-7}$$

where, h is the height of the electrode, and e_2 and e_3 are the mechanical loading terms and v_f is the free surface SAW velocity in the piezoelectric substrate given by

$$v_f = \sqrt{\frac{c_{eff}}{\rho}\left(1 + K^2\right)} = v_{sc}\sqrt{\left(1 + K^2\right)} \tag{2-8}$$

$$K^2 = \frac{e_{eff}^{\ 2}}{c_{eff}\varepsilon_p} \tag{2-9}$$

where ρ, K^2, c_{eff}, e_{eff}, ε_p is the mass density, electromechanical coupling coefficient, effective stiffness, piezoelectric constant and permittivity of the substrate, respectively. v_{sc} is called the short circuit velocity of the SAW and occurs when a high conductivity film shorts out the piezoelectric effect. A summary of the properties of two commonly used SAW piezoelectric substrates is presented in Table 2-2.

Table 2-2. A summary of properties of two commonly used SAW piezoelectric substrates. The values of e_2 and e_3 are the mechanical loading terms and are only applicable for Al electrodes; e_4 and e_5 represent the piezoelectric shorting and mass loading contributions to the reflectivity of a metal strip on the substrate.

	$LiNbO_3$	ST-X- Quartz
Crystalline Cut	Y	42.75^0 rotated Y
Prop direction	Z	X
K^2 (%)	4.6	0.16
ε_P (pF/cm)	4.6	0.5
v_f (m/s)	3488	3157
Mass Density (g/cm^3)	4.65	2.65
e_1	0.7	0.7
e_2	0.3	0.02
e_3	0	7.9
e_4	-0.5136	-0.75
e_5	-0.167	-0.550156
TCD (ppm/^{0}C)	-94	0

The IDT is a primarily capacitive because it is composed of electrodes of opposing polarity separated by a dielectric but it also possesses a series resistance due to the finite resistance of the electrodes. The electrical representation of an electrode pair is shown in Figure 2-8, where R_F^+ and R_F^- is the series resistance of the positive and negative electrodes, respectively.

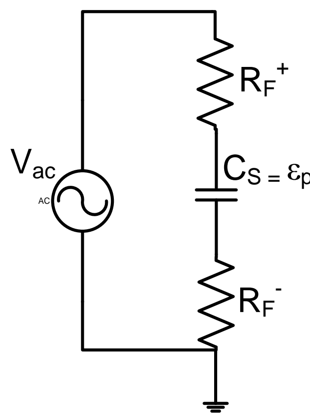

Figure 2-8. A schematic of the electrical representation of an electrode pair in a transducer.

The total electrode resistance for the IDT is given by [20]

$$R_F = R_F^{+}{}_{eq} + R_F^{-}{}_{eq} = \left(\sum_{\#+elctrodes} \frac{1}{R_F^{+}} \right) + \left(\sum_{\#-elctrodes} \frac{1}{R_F^{-}} \right) \tag{2-10}$$

$$R_F = R_s \frac{W_a}{W_e} \tag{2-11}$$

where R_s is the sheet resistance (in *Ω/☐*) of the electrode film, W_a is the beam width of the transducer, W_e is the electrode width, "*#+electrodes*" is the number of positive electrodes and "*#-electrodes*" is the number of negative electrodes. The static capacitance of the entire IDT, C_t is, given by [11]

$$C_t = N_p W_a \varepsilon_p \tag{2-12}$$

The total input admittance of the IDT includes a frequency dependent conductance, $G_a(\omega)$, and a Hilbert Transform susceptance, $B_a(\omega)$, that are caused by the electro-acoustic transduction process and is given by [11]

$$G_a(f) = \alpha f_0 \varepsilon_P W_a N_P{}^2 K^2 \left(\operatorname{sinc}\left(\pi \frac{(f - f_0)}{f_0} N_P \right) \right)^2 \tag{2-13}$$

$$B_a(f) = G_a(f_0) \left(\frac{ \sin\left(\frac{2\pi(f - f_0)}{f_0} N_P \right) - \frac{2\pi(f - f_0)}{f_0} N_P }{ 2\left(\frac{\pi(f - f_0)}{f_0} N_P \right)^2 } \right) \tag{2-14}$$

From literature [11], the value of α in equation (2-13) is ~9 and 9.77 for $2f_0$ and $4f_0$ IDTs respectively; for $3f_0$ IDTs α was experimentally determined to be ~5.9. The electric representation of the SAW transducer is presented in Figure 2-9

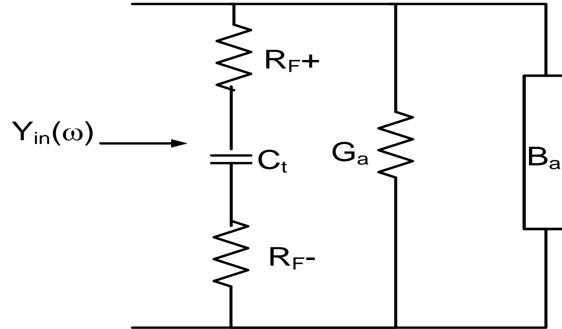

Figure 2-9. A schematic of an equivalent electric circuit of a SAW transducer

$$Y_{in}(\omega) = \left(\frac{1}{R_F + \frac{1}{j\omega C_t}} \right) + G_a(\omega) + jB_a(\omega) \tag{2-15}$$

A plot of the real and imaginary portions of the input admittance, $Y_{in}(\omega)$, in comparison to the electrical conductance and susceptance for a 50MHz, uniform, $3f_0$, IDT with $N_p=20$, $W_a=20\lambda$ and $R_s=0.2\Omega/\square$ and $h=2000Å$ on YZ-$LiNbO_3$ is shown in Figure 2-10. It is apparent that the static electrical conductance and susceptance of the IDT is modulated by the acoustic conductance and susceptance.

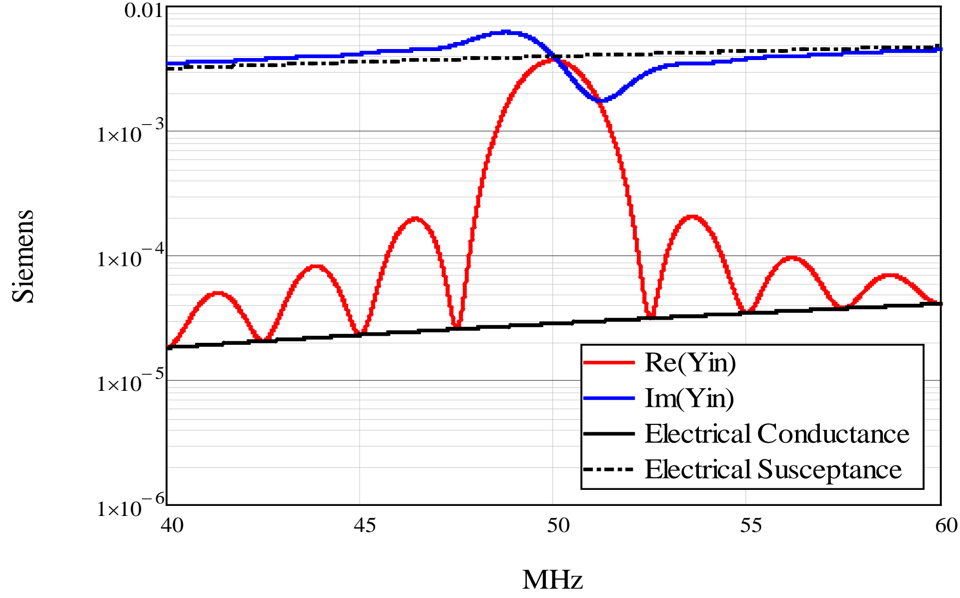

Figure 2-10. Plot of the real and imaginary portions of $Y_{in}(\omega)$ in comparison to the electrical conductance and susceptance for a 50MHz, uniform, $3f_0$, IDT with $N_p=20$, $W_a=20\lambda$ and $R_s=0.2\Omega/\square$ and $h=2000Å$ on YZ-$LiNbO_3$.

The quality factor, Q, of the transducer is the ratio of stored to dissipated energy. If the finger resistance, R_F, is negligible, the Q, at center frequency is given by

$$Q_{\omega_0} = \frac{\mathrm{Im}(Y_{in}(\omega_0))}{\mathrm{Re}(Y_{in}(\omega_0))} \approx \frac{1}{\alpha \cdot N_p K^2} \tag{2-16}$$

From equation (2-16), the Q of the transducer is a function of N_p and K^2, so the Q unaffected by changes in the beam width, W_a, or if multiple identical IDTs are connected in series, parallel or combinations of the two. During IDT design, modulating W_a and/or connecting multiple transducers in series or parallel may be necessary to minimize electrical impedance mismatch-loss by matching the IDT's input admittance with the admittance of the antenna or RF input source [21]. A constant Q circle on the smith chart is used to plot the transducers, amplitude input reflection coefficient as the IDT transitions from high impedance (multiple IDTs in series

and/or small W_a) to low impedance (multiple IDTs is parallel or large Wa). The amplitude input reflection coefficient is equal to the S_{11} scattering parameter, and is given by

$$S11_{in}(\omega) = \frac{Y_0 - Y_{in}(\omega)}{Y_0 + Y_{in}(\omega)} \tag{2-17}$$

where Y_0 is the characteristic impedance of the transmission line that is connected to the IDT. Figure 2-11 is a plot of the S_{11} on smith chart, for the IDT from Figure 2-10. It shows that $S_{11in}(\omega_0)$ follows a constant Q circle when transducers are placed in series or parallel; once the impedance is on the 50Ω circle it may be matched using a series inductor.

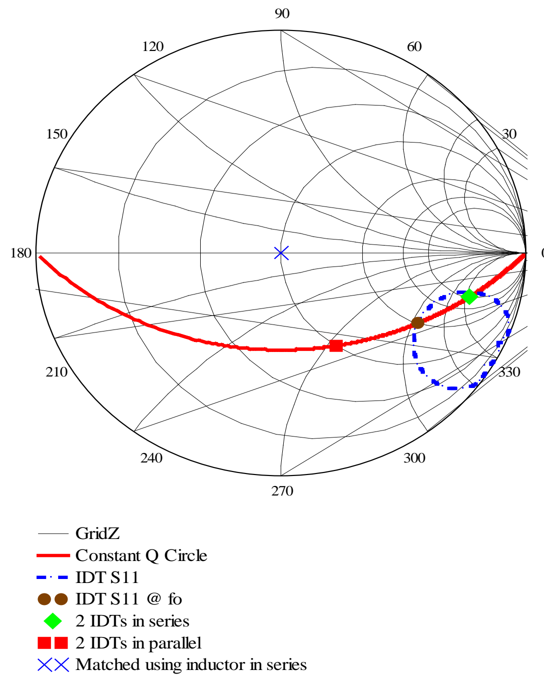

Figure 2-11. Plot of S_{11} of the IDT from Figure 2-10 on smith chart, shows that the impedance at f_0 follows constant Q circle is may be matched using a series inductor.

2.2.1.2 SAW Reflector

A SAW wave is reflected whenever there is an impedance discontinuity in the wave's propagation path. The typical SAW reflector is composed of periodic metal electrodes of width *λ/4* either connected via a bus bar (shorted) or disconnected (opened) (Figure 2-12). The use of open electrodes is generally avoided due to undesired regeneration and spurious effects [12]. The impedance beneath the electrode, *Zo+ΔZ*, is different than the free space impedance, *Zo*, and results a reflection of a portion of SAW at electrode-free space boundary.

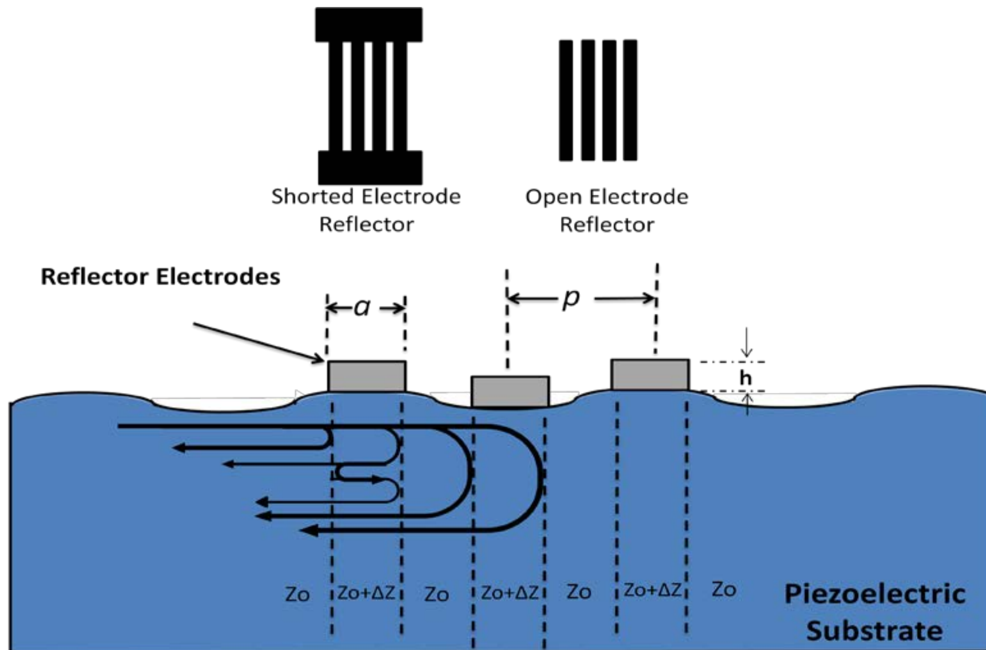

Figure 2-12. A schematic of a SAW reflector. The wave is reflected at the impedance discontinuity caused by the metal electrodes.

At each interface there is a small reflection, *r*, given by [12]

$$r = j\frac{\Delta Z}{Z_0}\sin\left(\frac{a}{p}\pi\frac{f}{f_0}\right) = j\left(e_4\frac{K^2}{2} + e_5\frac{hf}{v_{REF}}\right)\sin\left(\frac{a}{p}\pi\frac{f}{f_0}\right) \qquad (2\text{-}18)$$

where e_4 and e_5 represent the piezoelectric shorting and mass loading contributions to the reflectivity [22]. The magnitude of the net reflection from the entire array is given by [12]

$$|R| = \tanh(N|r|) \tag{2-19}$$

where N is the total number of electrodes in the reflector array. The null bandwidth (NBW), of the reflector bank is given by [12]

$$NBW = f_0 \frac{2|r|}{\pi} \sqrt{1 + \left(\frac{\pi}{N|r|^2} \right)} \tag{2-20}$$

For $N|r| << \pi$, equation (2-20) becomes

$$NBW = f_0 \frac{2}{N} \tag{2-21}$$

and the transfer function of the reflector may be approximated by a sinc function given by

$$H_{REF}(\omega) \approx |R| \mathrm{sinc}\left(\frac{2\pi(f - f_0)}{NBW} \right) \approx |R| \mathrm{sinc}\left(\frac{\pi(f - f_0)}{f_0} N \right) \tag{2-22}$$

Synchronous reflections occur when the fundamental frequency of the reflector is given by

$$f_0 = \frac{v_{REF}}{2p} \tag{2-23}$$

Unlike IDTs reflectors operate at every harmonic, however the reflectivity per strip, r, is different at each harmonic [23]. The SAW velocity beneath the reflector may approximated by [20, 22]

$$v_{REF} = v_f\left(1 - e_1\frac{K^2}{2} - e_2\frac{hf_0}{v_f} - e_3\left(\frac{hf_0}{v_f}\right)^2\right) \tag{2-24}$$

where e_1 is the electrical loading term, e_2 and e_3 is the mechanical loading terms. A summary of properties of two commonly used SAW piezoelectric substrates is presented in Table 2-2.

2.2.1.3 Free Space Propagation Loss

SAWs suffer from propagation loss due a thermoelastic viscosity in the substrate and the coupling the wave with air molecules [11]. The thermoelastic viscosity of the piezoelectric substrate is derived in CHAPTER 3. These losses dominate at high frequencies and may be abated by vacuuming and hermetically sealing the SAW device under vacuum. The room-temperature propagation loss for YZ-$LiNbO_3$ was empirically found to be [11]

$$\alpha_{LN}(f) = \left[0.19\frac{f}{GHz} + 0.88\left(\frac{f}{GHz}\right)^2\right]\frac{dB}{\mu s} \tag{2-25}$$

and the room-temperature propagation loss for ST-X-Quartz was empirically found to be [11]

$$\alpha_{QTZ}(f) = \left[0.47\frac{f}{GHz} + 2.62\left(\frac{f}{GHz}\right)^2\right]\frac{dB}{\mu s} \tag{2-26}$$

2.2.1.4 Frequency Response of a 1-port delay line

The basics of transducer and reflector design were covered in the preceding sections it is now feasible to develop a first order model for the response of a 1-prt SAW tag. In practice SAW devices are modeled using the coupling of modes (COM) model, which was originally

developed for optics [20]. The COM model is based on the principle that the SAW motion is a combination of uncoupled forward *f(x,t)* and reverse *r(x,t)* propagating modes (i.e. standing waves). When the IDT is excited with an electrical signal, there is an initial reflection due to the difference in impedance between the voltage source and the IDT. The energy that is absorbed by the IDT is converted to an electromechanical wave and is transmitted in two directions simultaneously. The wave travels down the crystal bounces off the reflector back toward the transducer where it is once a partially reflected or regenerated by the IDT (Figure 2-13). The wave continually travels between the reflector and transducer until there is no energy remaining and the reflections die off; these multiple transits create a standing wave pattern (Figure 2-13). A thorough explanation of the COM model is beyond the scope of this dissertation; however a simplified, first-order, modulated-admittance approximation, that gives comparable results to the COM model is presented.

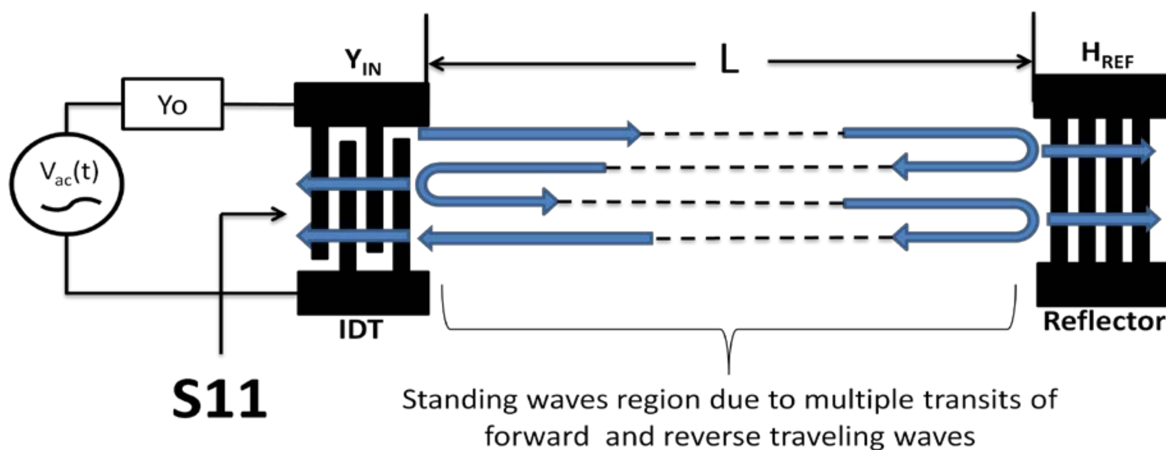

Figure 2-13. A schematic of wave reflection and transmission between a source, transducer and reflector in 1-port SAW device.

The IDT is a 3-port device, it consists of 1 electrical port and 2 acoustic ports and the reflector only has consists of 2 acoustic ports. The acoustic admittance of the IDT is periodically modulated by the reflected waves from the reflector bank—with amplitude $H_{REF}(\omega)$ at times $\tau_D = 2kL/\omega,\ 4kL/\omega,\ 6kL/\omega,$ etc —as the SAW propagates back and forth between the IDT and reflector. The input admittance of the IDT is modulated by to multiple reflections and given by

$$Y_{in_Total}(\omega) = Y_{in}(\omega) + H_{REF}(\omega) G_a(\omega) \exp(-j2kL) \tag{2-27}$$

where k is the free space propagation constant given by

$$k = \frac{\omega_0}{v_f} \tag{2-28}$$

The input amplitude reflection coefficient of the transducer is simply given by

$$S11 = \frac{Yo - Y_{in_Total}(\omega)}{Yo - Y_{in_Total}(\omega)} \tag{2-29}$$

$G_a(\omega)$, $Y_{in}(\omega)$ and $H_{REF}(\omega)$ is given by equations, (2-13), (2-15), and (2-22) respectively. Figure 2-14 and Figure 2-15 shows a comparison of S_{11} of the modulated-admittance and COM model to measured data for a 50MHz, 1-port, SAW delay line on YZ-$LiNbO_3$. The IDT is a uniform, $3f_0$, N_p=20, W_a=20λ, R_s=1Ω/□ and h=2000Å and the reflector is uniform, N=81 and h=2000Å. These figures show good agreement between the modulated-admittance and COM models and the measured data. Figure 2-15 is the plot of S_{11} in the time domain, which was achieved using a Fast Fourier Transform (FFT). It shows that the simplified transmission line model does not account for energy storage effect in the response of the reflector bank.

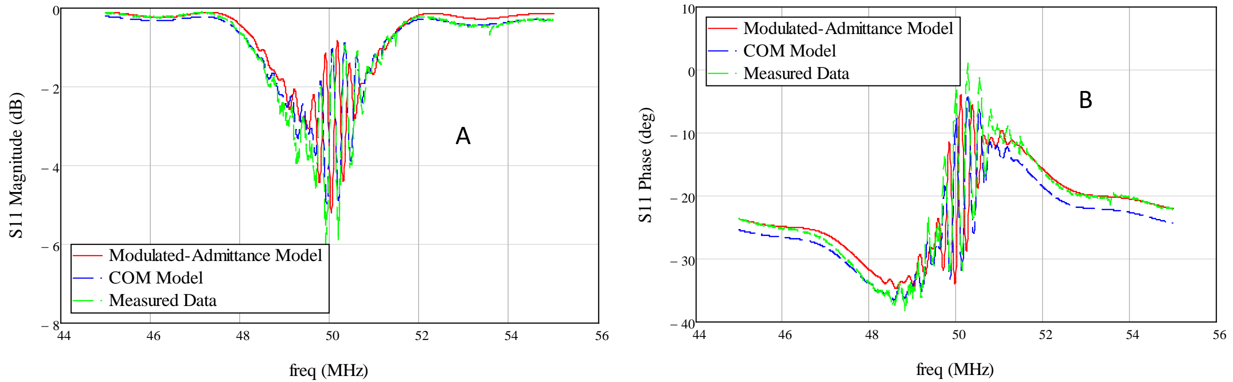

Figure 2-14 A: Plot of the magnitude of S_{11} in dB versus frequency; B: Plot of the phase of S_{11} in dB versus frequency. It is a comparison of the modulated-admittance and COM model to measured data for a 50MHz 1-port SAW delay line on YZ-$LiNbO_3$. The IDT is uniform, $3f_0$, N_p=20, W_a=20λ, R_s=1Ω/☐ and *h=2000Å and* the reflector is uniform, *N=81* and *h=2000Å*.

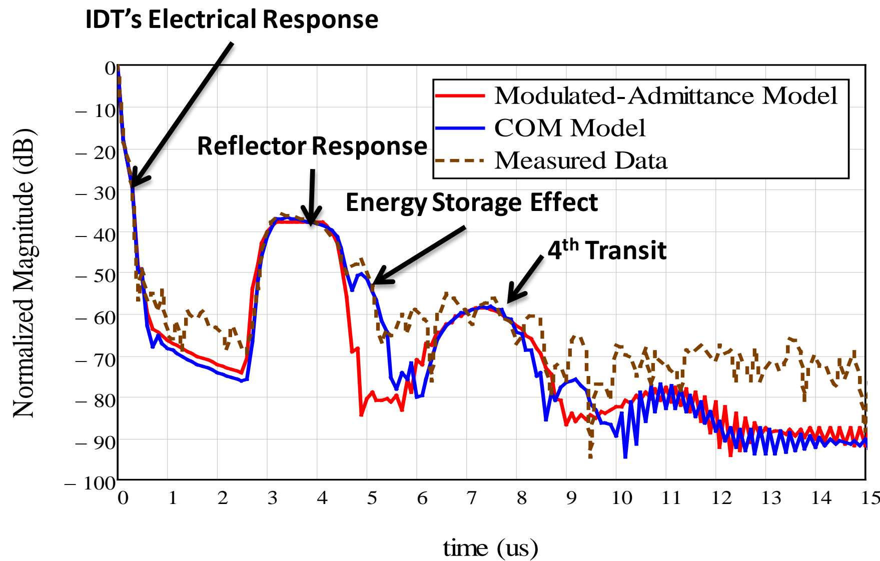

Figure 2-15 Plot of the magnitude of S_{11} in dB versus time. It is a comparison of the modulated-admittance and COM model to measured data for a 50MHz, 1-port, SAW delay line on YZ-$LiNbO_3$. The IDT is uniform, $3f_0$, N_p=20, W_a=20λ, R_s=1Ω/☐ and *h=2000Å*. The reflector is uniform, *N=81* and *h=2000Å*. The modulated-admittance model does not account for energy storage effect in the response of the reflector bank.

2.2.1.5 Piezoelectric-SAW-Thin Film Interaction

The SAW is trapped at the surface of the crystal, consequently the propagation characteristics of the SAW is influenced by the properties of any media in contact or very close

proximity to the surface of the piezoelectric crystal. It is well documented that surface acoustic wave (SAW) devices operate well as chemical sensors when a chemically sensitive film is placed on the piezoelectric substrate [8, 13]. When the 1-port SAW device is used as a gas sensor the amplitude and delay of the main reflector response (Figure 2-15) is modulated by the presence and concentration of the gas. This is governed by two major effects: (1) the thin-film acoustoelectric effect in SAW devices because it describes the interaction of electrical energy between a SAW in a piezoelectric medium and a thin-film placed in the wave's propagation path and (2) the acoustoelastic interaction because it describes the effects of elastic properties of the film on the propagation characteristics of the SAW.

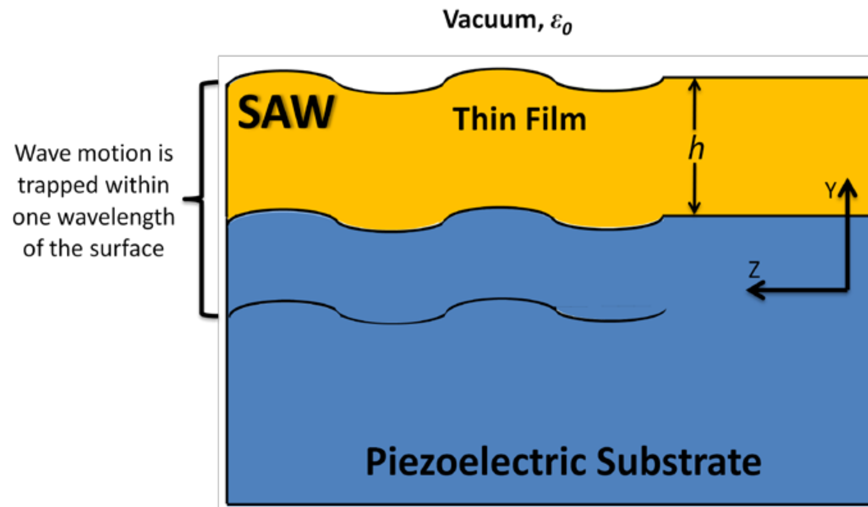

Figure 2-16. Schematic of the SAW propagation at the piezoelectric-thin-film interface.

The thin-film acoustoelectric and acoustoelastic equations are used to predict the change in SAW propagation loss and velocity as a function of the electrical and mechanical characteristics of the film. These equations are used in the design and characterization of SAW-based thin-film chemical and physical sensors (i.e. temperature, humidity, viscosity, voltage,

current, hall effects, etc.). A derivation of SAW acoustoelectric and acoustoelastic equations is presented in CHAPTER 3 and the equation and experimentally verified in CHAPTER 4.

A high-quality, chemically-sensitive film should exhibit a change in electrical and/or mechanical properties in the presence of the analyte chemical, such that the propagation of a SAW in the crystal is affected (i.e. amplitude, frequency and/or delay). Palladium (Pd), platinum (Pt), and tin-dioxide (SnO_2) thin films (or a combination of the three) have been frequently used for H_2 gas detection [24]. Experimentation with Pd and SnO_2 thin films are detailed in chapters 5 and 6, respectively.

2.2.2 OFC-SAW Approach

Multiplexing is necessary whenever more than one message signal is simultaneously transmitted over a channel. The most common multiplexing techniques are time division multiplexing (TDM) and frequency division multiplexing (FDM). The orthogonal frequency coding (OFC) scheme is a hybridization of orthogonal frequency division multiplexing (OFDM) and binary phase shift keying (BPSK) coding techniques (Figure 2-17). OFC achieves coding diversity in frequency, time and phase by incorporating the frequency diversity of OFDM and the time and phase diversity of BPSK (Figure 2-18). In comparison, previous authors have used single frequency schemes such as code division multiple access (CDMA) that are narrower band than OFC but has very high insertion loss when implemented in a SAW device, and low processing gain [25].

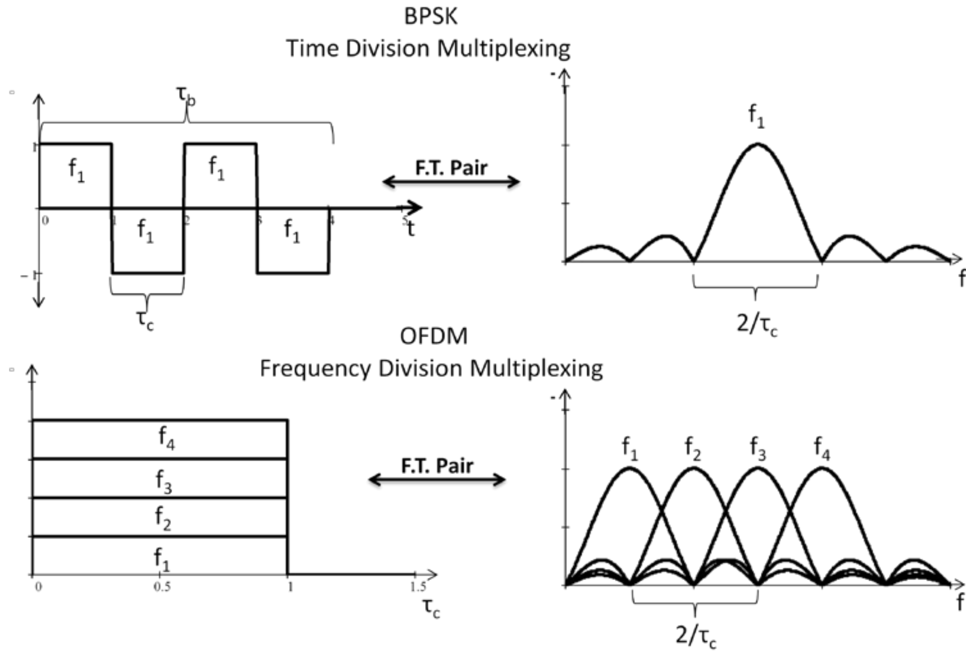

Figure 2-17. A schematic of TDM and FDM coding schemes where τ_c is the chip or symbol length and τ_b is the bit length.

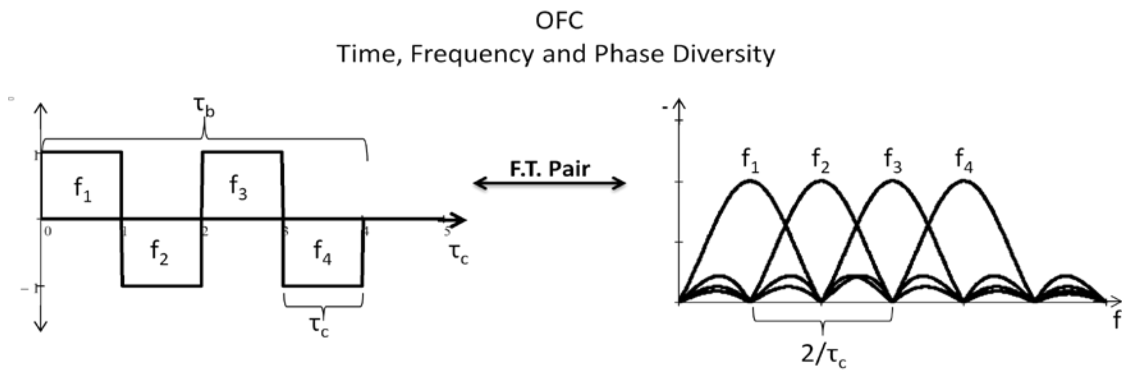

Figure 2-18. A schematic of OFC technique

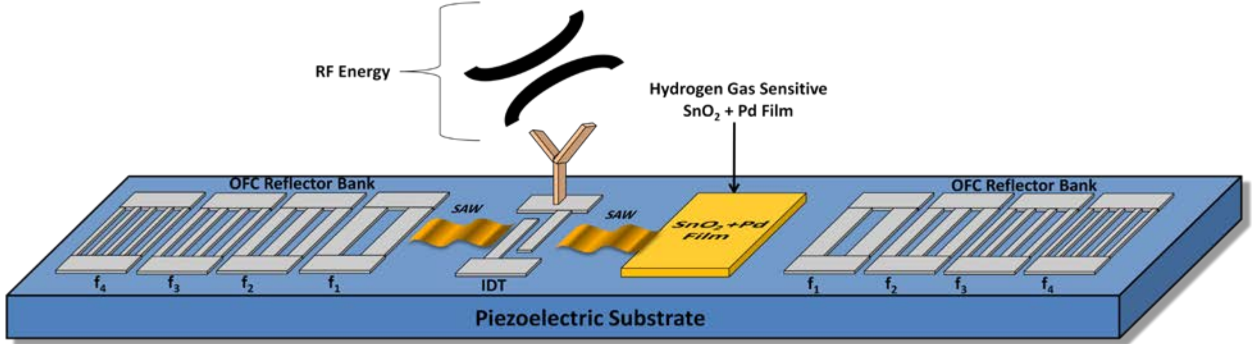

Figure 2-19. A schematic of a passive wireless OFC-SAW RFID-tag sensor. If properly designed the SAW propagation parameters are modulated by the presence and the properties of the thin-film.

The layout of a 1-port dual delay OFC-SAW RFID tag-sensor is shown in Figure 2-19. The OFC reflector bank is composed of sequential reflectors (called chips) with center frequencies from f_1 to f_4. The frequencies $(f_1\text{-}f_4)$ are orthogonal in time and frequency to each other to minimize interference between chips as the SAW travels beneath the reflector bank. There are two functional descriptions for the orthogonal frequencies given by

$$h_1(t) = \sum_{n=0}^{N_c} a_n \cdot \cos\left(\frac{2n\pi \cdot t}{\tau_c}\right) \cdot rect\left(\frac{t}{\tau_c}\right) \tag{2-30}$$

$$h_2(t) = \sum_{m=0}^{N_c} a_m \cdot \cos\left(\frac{(2m+1)\pi \cdot t}{\tau_c}\right) \cdot rect\left(\frac{t}{\tau_c}\right) \tag{2-31}$$

where

$$rect(x) = \begin{cases} 1, & |\mathrm{x}| \le 0.5 \\ 0, & \text{otherwise} \end{cases} \tag{2-32}$$

where N_c is the number of chips, τ_c is the time duration of each chip, a_n is the chip's amplitude, and each cosine term in equations (2-30) and (2-31) represents a time gated sinusoid whose local center frequencies are given by

$$f_n(t) = \left(\frac{n}{\tau_c} \right) \tag{2-33}$$

and

$$f_m(t) = \left(\frac{2m+1}{\tau_c} \right) \tag{2-34}$$

Coding diversity is attained by shuffling the frequencies (i.e. $f_1 \ldots f_4$ to f_3, f_1, f_4, f_2) in time and shifting the phase of each frequency between +1 and -1. The phase coding sequence typically follows a pseudo noise (PN) sequence such as Barker codes, which reduces the sidelobes of auto-correlated compressed pulse. PN-OFC coding, produces $2^{Nc}N_c!$ codes, whereas *PN* coding only offers 2^{Nc} codes. The increased coding diversity gives the OFC technique greater processing gain than BPSK or OFDM techniques and translates to a greater number of coding possibilities, lower loss and longer range [22].

Signal detection is achieved by correlating against a matched filter (i.e. ideal code sequence) to produce a compressed pulse. The input reflection coefficient (S_{11}) time domain response of the OFC-SAW sensor in Figure 2-19, and its auto-correlation is shown in Figure 2-20. If the film is properly designed, the SAW propagation parameters are modulated by the presence and the properties of the chemically-sensitive thin-film and the amplitude and delay of the second correlation peak is modulated in the event of gas detection.

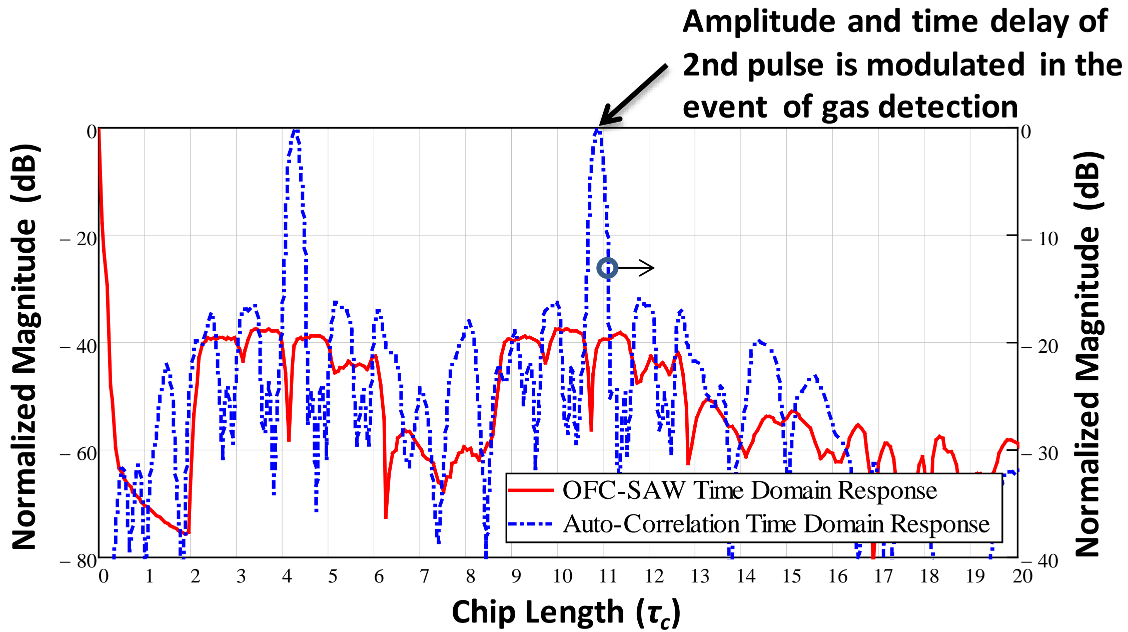

Figure 2-20. Plot of the time response and auto-correlation of Figure 2-19

2.2.3 Comparison of OFC-SAW and Semiconductor RFID Platforms

Semiconductor-based RFID devices are primarily built on silicon (Si) these devices must use DC power to be activated; consequently a strong continuous RF power transmission is required to rectify for DC power [10]. The maximum read range is determined by Si-RFID tag's threshold voltage and causes it to have a shorter read range than SAW-based RFID tags. Si-RFID devices primarily rely on amplitude and pulse width modulation techniques to code sensor information and are more vulnerable to interference than OFC coding techniques. SAW-based RFID requires no minimum power requirement for tag activation, and needs only a single RF pulse of trigger a reading. The maximum read range of the tag is determined by signal to noise (S/N) ratio requirement of the tag reader and is implemented using interference resistant spread

spectrum modulation. SAW devices have been shown operate over a wider temperature range (-270°C to 1000°C) [3, 4] and in higher radiation environments (up to 400MRads) [2], than their Si counterparts. Enclosures that are completely surrounded by conducting walls are called a Faraday cages because emitted radio waves are trapped within the structure by the conductive walls. The conducting walls causes multiple reflections that creates a problem called multipath fading due to the constructive and destructive interference of the received multiple signals [26]. The multipath fading problem is exacerbated in continuous wave (CW) systems such as traditional semiconductor based RFID-tag-sensors [10] whereas SAW-RFID technology have been shown to successfully operate [9]in RF cages. A comparison of the semiconductor and SAW-RFID technologies is presented in Table 2-3. These properties suggest that SAW-RFID tags are the clear choice for operation in harsh operation environments.

Table 2-3. Comparison of the semiconductor-RFID and SAW-RFID technologies.

Category	**Si-RFID**	**OFC-SAW-RFID**
Minimum Power	Requires strong continuous power transmission to rectify for DC power.	No minimum power requirement for tag operation. SAW device needs only a single RF pulse for reading.
Coding	Amplitude and pulse width modulation highly vulnerable to interference.	Interference resistant spread spectrum modulation
Read Range	Maximum read range determined by tag threshold voltage.	Maximum read range determined by signal to noise (S/N) ratio requirement of the tag reader
Temperature Range of Operation	-40°C to 140°C [27]	-270°C to 1000°C
Radiation Hardness	300kRad [28]	400MRad
Operation in Faraday Cage	No	Yes

2.3 Pressing Problems in Cryogenic Liquid Level Sensing

The word cryogenic is derived from two Greek terms that when combined, literally translates into " to produce frost;" it was formally defined as "the science and art of producing cold" by Kamerlingh Onnes in 1894 [29]. Cryogenic fluids are considered "those fluids whose normal boiling temperatures at atmospheric pressures are below 273K [30]" and the National Institute of Standards and Technology (NIST) classifies cryogenic temperatures as those below 93.15K (-180^{0}C). A cryogenic liquid is created when a gas is compressed and cooled below its critical point. A summary of the critical point and temperature of commonly used cryogenic fluids is presented in Table 2-4.

Table 2-4. A summary of the critical point and temperature of commonly used cryogenic fluids [30].

Element	Critical Temperature	Critical Pressure	Normal boiling point (@ 1 atm)
Helium (He)	5.19K	227.46kPa	4.22K
Hydrogen (H)	32.94K	1283.8kPa	20.28K
Oxygen (O)	154.58K	5043kPa	90.19K
Nitrogen (N)	126.26K	3399kPa	77.36K

To prevent boiling and evaporation, the liquid must be stored in a temperature insulated vessel. From this necessity, in 1882, Jules Violle invented a double walled glass vessel with vacuum between the walls, and a reflective silver coating on the exterior of the vessel. The vacuum prevents the thermal conduction of heat and the reflective coating limits the radiative transmission of heat energy [29]. James Dewar improved upon Voille's design in 1890 by silvering both the interior and exterior of the vessel and revolutionized the use of cryogenic fluids for practical use in a variety of applications.

The study of cryogenics has led to the discovery of superconductivity (by Onnes), and precipitated large advances in the study of magnetism. NASA uses cryogenic liquid fluid tanks, for both ground and space vessels in routine operations. The electronics in infrared telescopes and X-ray spectrometers and other various instruments are cooled to decrease thermal noise and detect weak signals from outer space. Cryogenic liquids are used in many other industries such as medical, metal, chemical and power generation and transmission; a summary of the major applications is presented in Table 2-5.

Table 2-5. A summary of a few major applications of cryogenic fluids

Industry	Applications
Energy	1. Cooling to lower power transmission losses 2. Liquid natural gas (LNG) 3. Nuclear power: supply, purification, separation, or other special gas treatments [31] 4. Superconductors: generators, faults detection
Medical	5. MRI, cryosurgery, cryopreservation, cryo-desiccation
Metal	6. Cryogenic hardening and processing to improve mechanical properties
Military	7. Superconducting QUantum Interference Device (SQUID) for high accuracy mine and submarine detection.
Transportation	8. Magnetic levitation with superconductor

Dr. Robert H Goddard produced the first successful demonstration of a liquid-oxygen-gasoline propellant in a rocket in 1926 [29]. He realized that H_2 and oxygen (O_2) (and other elements) burn explosively and occupy has less space in their liquid form—H_2 in its liquid form occupies 840^{-1} the space as in its gaseous form. Thanks to the principles of the Dewar flask, theses volatile fuels could be safely stored indefinitely, transported with small losses, and

contained in a launch vehicle. It was these concepts that Werner von Braun used to design and fuel tanks for NASA's Saturn V rocket and transported Armstrong and company from Cape Canaveral to the moon.

Cryogenic liquid-level determinations are essential to propellant loading, management, and utilization and to other diagnostic or control functions such as engine cutoff [29]. Engine cutoff (ECO) sensor system is used to protect the Space Shuttle's Main Engines (SSME) from disastrous failure due to propellant depletion [32]. The location and schematic of liquid hydrogen (LH_2) and liquid oxygen (LO_2) ECO sensor inside the shuttles external fuel tank is shown in Figure 2-21. The ECO sensor sends continuous wet indications when submerged in fuel and dry indications once the level is beneath the sensors. The malfunction or miscommunication with ECO sensors is responsible for the scrubbing of at least three NASA Space Transport System (STS) missions: STS-114, STS-115 and STS-122 [1, 32, 33]. A review of 124 NASA STS missions between 1981 and 2011 revealed that 25 launches were scrubbed or delayed primarily due to gas leaks from cryogenic fluid lines or cryogenic sensor malfunction [1]. The hazards of storing cryogenic fluids are also extended to inert elements such as liquid nitrogen (LN_2). In the event of a spill or leak, LN_2 boils, becomes gaseous N_2 and quickly expands to over 700x its liquid volume, thereby displacing oxygen and causing injury or death by asphyxiation in poorly ventilated areas [34].

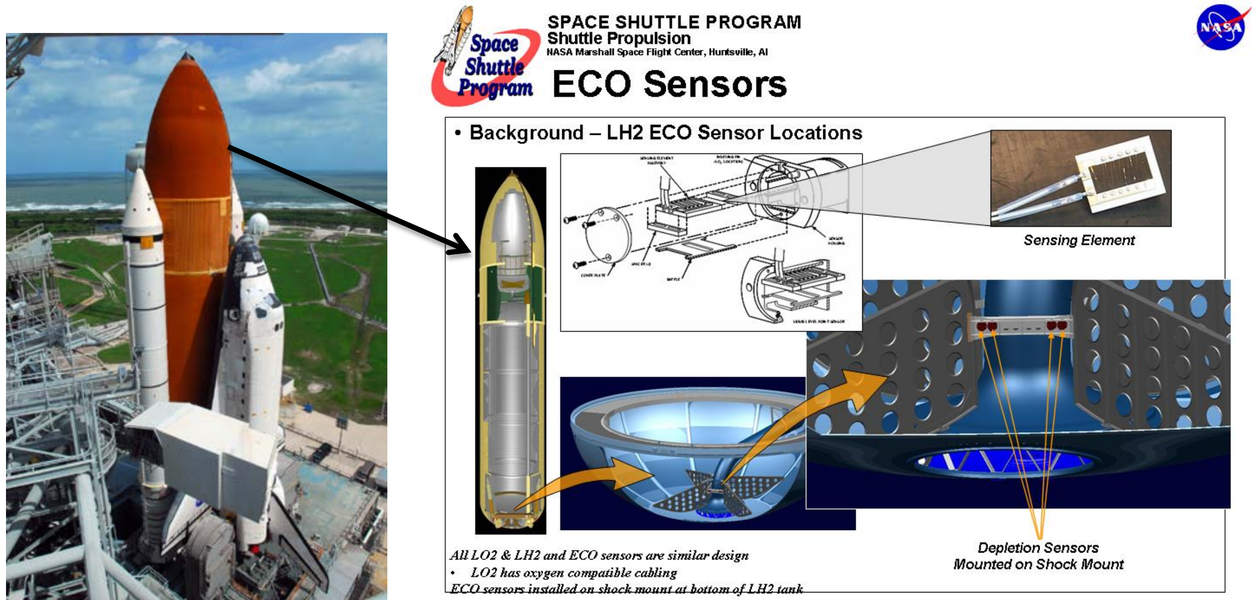

Figure 2-21. Picture of the location and schematic of liquid hydrogen (LH_2) and liquid oxygen (LO_2) ECO sensor inside the shuttles external fuel tank.

The risks of catastrophic accidents, associated with the storage and use of cryogenic fluids may be minimized by constant monitoring of the cryogenic liquid level inside the tank and a network of gas detectors outside the Dewars; unfortunately, continuous and reliable monitoring has proven to be problematic. There are many cryogenic liquid level sensors, all of which have various advantages and disadvantages depending on the application; a summary of the cryogenic liquid sensors and their disadvantages are presented in Table 2-6 [29].

Table 2-6. Summary of the advantages and disadvantages of continuous liquid level sensors.

Method	Disadvantages
Direct Weighing Scheme	Weighing very large tanks may not be practical
Differential Pressure	Low signal to noise ratio low density elements such as H_2 and He
Capacitance	Requires long electrodes, that extends the length of the Dewar and adds undesired heat conduction
Acoustic	False measurements results for extraneous interfaces, caused by vapor bubbles in the liquid
Nuclear radiation	Need radioactive shielding

There are a wealth of problems for cryogenic sensor devices, primarily mechanical stress and strain—which impacts reliability—, undesirable device heat generation in the vessel, and a host of others. Failure of the electrical connections is cited as the primary cause of ECO sensor miscommunication [32], thus an ideal solution should involve the interrogation of passive, wireless, sensor-nodes inside of cryogenic Dewars or fuel tanks. The tanks interior is a Faraday cage because it is composed of a dielectric region completely surrounded by conducting walls. This eliminates Si-RFID tag solutions because it cannot operate in Faraday cages in addition to the extreme cold, which makes many semiconductor-based sensors inoperable due to freeze-out of conduction carriers. SAW delay-line devices have been shown to successfully operate as RFID-tag-sensor networks [6, 7], at extremely low temperatures without any serious performance degradation [4, 5], and in a Faraday cage [9]. An un-encapsulated wireless SAW RFID tag will simply cease to operate when submerged in liquid and report temperature at a given location in the tanks as the liquid level decreases beneath the sensor (Figure 2-21). Experimentation with OFC-SAW RFID cryogenic liquid level detection is presented in CHAPTER 8.

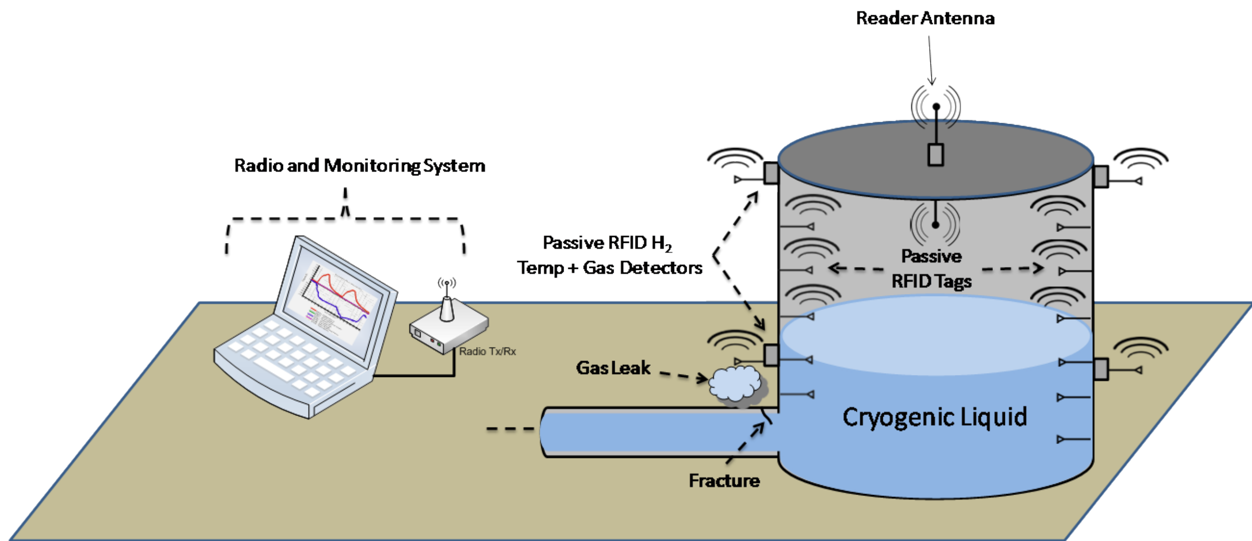

Figure 2-22. Schematic of cryogenic liquid tank with a passive wireless liquid level and gas leak detection system.

2.4 Pressing Problems in Low-Power Hydrogen Sensing

Hydrogen (H) is the most widely used element because of its abundance, weight and catalytic properties. These catalytic properties may create dangerous conditions in the event of a gas leak. Hydrogen atoms consists of one proton and one electron, and typically form covalent bonds with each other to produce a diatomic molecule, H_2, that is composed of the sharing of two electrons between two protons, which fills to 1s2 electron orbital, and produces a stable molecule (Figure 2-23). H_2 gas molecules are small and can diffuse through many materials considered airtight. Constant exposure to H_2 causes a phenomenon known as “hydrogen embrittlement” in many materials [35, 36]. Embrittlement reduces the ductility and tensile strength of containment vessels to the point of fracture, which makes H_2 more difficult to contain than other gasses.

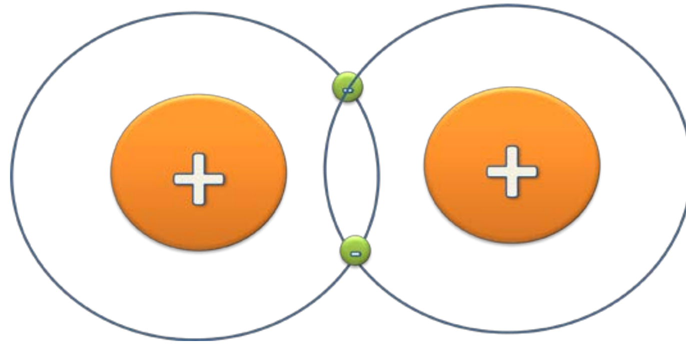

Figure 2-23. A schematic of a covalently bonded H_2 molecule.

At 1 atm, fire hazards exist for H_2-O_2 mixtures between the lower flammability limit (LFL) of 4% and upper flammability limit (UFL) of 94% H_2 by volume [29]. In air the LFL and UFL of H_2 is 4.1% and 75% H_2 by volume, respectively, because the O_2 composition of air is only 21%. The LFL and UFL and is also temperature dependent; a summary of these values is presented in Table 2-7 [37]. The minimum ignition energy required to ignite of H_2 gas is between only 17μJ to 1mJ at 1atm depending on H_2 gas concentration in air, and decreases as temperature is increased (Figure 2-25) [38]. In comparison, the typical static electric discharge caused by humans in normal activity lie the range of 1-100mJ [39], thus, all personnel in an enclosed area must be evacuated before the H_2 concentration in atmosphere reaches the LFL.

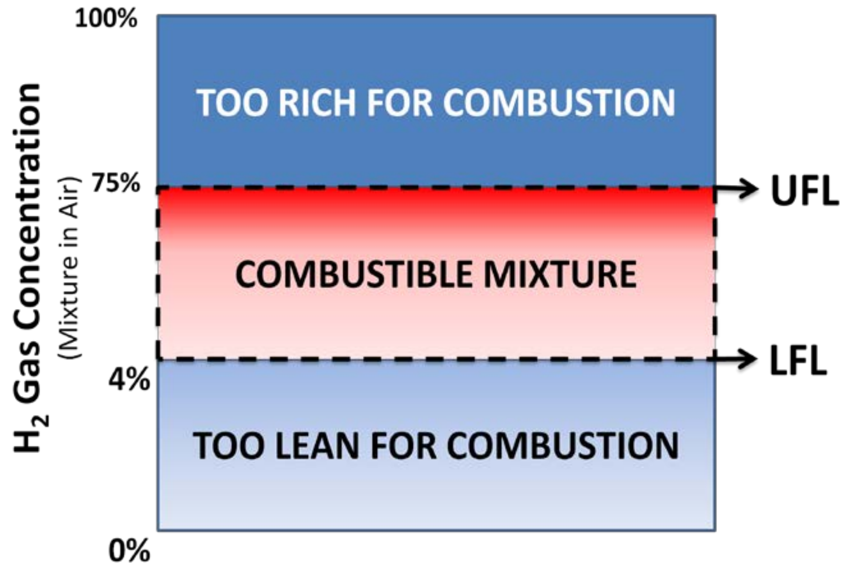

Figure 2-24. A schematic of the window of combustibility for H_2 gas mixtures in air at room temperature.

Table 2-7. A summary of the LFL and UFL of H_2 gas at various temperatures. This summary shows that the LFL and UFL decreases as temperature is increased

Temperature (^{0}C)	LFL (% Volume)	UFL (% Volume)
20	4.1	75.6
100	3.4	77.6
200	2.9	81.3
300	2.0	83.9
400	1.4	87.6

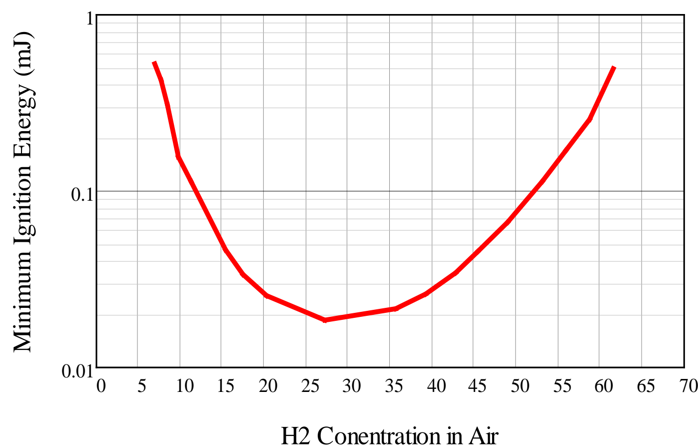

Figure 2-25. Plot of the minimum ignition energy of H_2 gas as a function of % of H_2 in air at 1atm.

Liquid hydrogen (LH_2) leaks in atmosphere boils vigorously and creates a cloud of water vapor and H_2 gas. Due to the buoyancy of H_2 gas in air, it diffuses rapidly and will not likely form a persistent flammable mixture in open unconfined areas, so the flammability zone will be confined to an area very close to the leak's location. For turbulent leaks from high pressure lines or tanks, the H_2 gas is diluted to nearly the composition of air within 500 diameters of the hole [40]. For example a 1mm diameter leak will support a flame that is around 0.5m or less in length. Ignited H_2 gas burns with an almost nearly invisible pale-blue flame at around 2200^0C, thus, H_2 gas detection prior to concentrations near the LFL is critical, to minimize the occurrences of accidents.

2.4.1 Review of H_2 Detector Technology

There are eight primary types of hydrogen gas detectors, a summary of which is presented in Table 2-8 and Table 2-9; these tables are taken from [24].

Table 2-8. Summary of hydrogen sensor types.

Technology	Operating Principle/Device	Physical change/measurand	Advantages	Disadvantages
Catalytic	Pellistor	Temperature and Resistance	Robust, stable, long lifetime, wide operating temperature range	Not hydrogen selective, high power consumption, requires at least 5 to 10% O_2 to operate, susceptible to poisoning by phosphorus sulfur and silicon compounds
	Thermoelectric	Thermoelectric voltage	Room temperature operation and low power consumption	Long response times, sensitive to temperature fluctuations, requires 5 to 10% oxygen to operate
Thermal Conductivity	Calorimetric	Temperature, Resistance and Voltage	Very wide measuring range, go bust, does not require oxygen to operate, long-term stability, resistant to poisoning, simple construction, low-cost, fast measurement response times	High lower detection limits, cross sensitivity helium, reaction with heating wire can occur

Technology	Operating Principle/Device	Physical change/measurand	Advantages	Disadvantages
Electrochemical	Amperometric	Electrical current	Sensitive down to 100 ppm, low power consumption, resistant to poisoning, heating of sensor element not required, operation at high ambient temperature possible	Narrow temperature range using some electrolytes, restricted lifetime, regular calibration needed, sensitivity to carbon monoxide, aging, and cost
	Potentiometric	Electromotive force		
Resistance Based	Semiconducting Metal-Oxide	Resistance	High sensitivity, fast response, acceptable lifetime, wide operating temperature, range, low-cost, and modest power consumption	Poor selectivity, interference from humidity and temperature, high operating temperature, contamination, susceptible to aging and memory effects, and requires oxygen to operate
	Metallic Resistor	Resistance	Very wide detection range, rapid response, selective, long-term stability, and can operate in the absence of oxygen	Dependence on temperature, affected by total gas pressure, poisoned by tin dioxide hydrogen sulfide, susceptible to aging effects and cost.
Work Function Based	Schottky diode	Current and Voltage	Micromachineble, low-cost, small size, mass production possible.	Susceptible to drift
	MOS field effect transistor	Current and Voltage	Fast response, accurate measurement, influence from ambient parameters, high selectivity and sensitivity, small size, and mass production possible.	Baseline and hydrogen induced drift, hysteresis, and saturates at modest concentrations.
	MIS Capacitor	Capacitance	High sensitivity and selectivity, fast response, low power consumption, low cost, small size, and mass production possible.	Drift and hysteresis
Mechanical	Cantilever	Length, Bending, and Curvature	Micromachineble, small size, no source of ignition in explosive atmospheres, does not require oxygen to operate.	Slow response time, susceptible to poisoning, susceptible to hydrogen induced aging effects.
Optical	Optrode	Transmission, Reflectance, Wavelength, Polarization and Phase shift	No source of ignition in explosive atmospheres, unaffected by electromagnetic interference, wide area monitoring, and can operate in absence of oxygen.	Interference from ambient light, drift due to aging effects, and poisoning by sulfur and dioxide and hydrogen sulfide.
Acoustic	Quartz crystal microbalance	Frequency, Time, wave velocity	Very high sensitivity, room temperature 100° C. operation, and can operate in absence of oxygen.	Interference from humidity and temperature, and drift
	Surface acoustic wave	Frequency, Time, wave velocity	High sensitivity, room temperature operation, and can operate in absence of oxygen	Unstable at high temperature, interference from humidity and temperature
	Ultrasonic	Frequency, Time, wave velocity	Very wide detection range, in nine measurement, rapid response, usually a fraction of a second, low power consumption, long-term stability, and can't operate in the absence of oxygen.	Knowledge of the acoustic properties of material through which sound travels is necessary, substantial amount of electronics needed for high accuracy.

Table 2-9. A summary of the performance of current commercially available H_2 gas detection technologies

Technology	Principle/ Device	H_2 Detection Range	Accuracy	Response Time	Power consumption	Gas Environment	Lifetime (years)
Catalytic	Pellistor	ppm - 4%	<+/-5%	<30s	1000mW	-20 to 70^0C 5-95% RH 70-130kPa	5
Thermal Conductivity	Calorimetric	1 -100%	+/-2%	<10s	<500mW	0 to 50^0C 0-95% RH 80-120kPa	5
Electrochemical	Amperometric	5ppm-4%	<+/-4%	<90s	2-700mW	-20 to 55^0C 5-95% RH 80-110kPa	2
Resistance Based	Semiconducti ng Metal-Oxide	10ppm-2%	+/-10-30%	<20s	<800mW	-20 to 70^0C 10-95% RH 80-120kPa	<10
	Metallic Resistor	0.1 -100%	<+/-5%	<15s	>25mW	-0 to 45^0C 0-95% RH Up to 700kPa	
Work Function Based	Capacitor	10ppm-5%	<+/-7%	<60s	4000mW	-20 to 40^0C 0-95% RH 80-120kPa	10
	MOS field effect transistor	10ppb-4.4%	<+/-7%	<2s	700mW	-40 to 110^0C 5-95% RH 70-130kPa	10
Optical	Optrode	0.1 -100%	<+/-0.1%	<60s	1000mW	-15 to 50^0C 0-95% RH 75-175kPa	>2

Of the commercially available sensor technologies summarized in Table 2-8 and Table 2-9, only resistance and work-function based technologies may integrated with a compact low-power wireless platform [41]. Acoustic technologies may also be implemented in a passive wireless embodiment, however none are commercially available [42].

Reversible detection of H_2 gas at room temperature is difficult because the activation energy required to desorb H_2 gas from sensitive film is typically higher than kT at 300K (where k = $1.38 \times 10^{-23} JK^{-1}$ is Boltzmann's constant, and T is absolute temperature in Kelvin). Most commercially available H_2 gas sensors use localized heaters that control the operating temperature, which is typically greater than 300^0C for catalytic bead gas sensors and 50 to 150^oC for solid-state gas sensors [43]. The localized heaters require relatively high constant current,

which translates to limited battery life of sensor of wireless sensor nodes. The temperature requirement of catalytic bead sensors makes their use hazardous in the event of a H_2 gas leak because the gas' auto-ignition temperature is around 579°C at 1atm [29]. The operating temperature of solid-state gas sensors (50 to 150°C) and is not as hazardous as the as a catalytic bead sensor. However, the probability of spark discharges increases as humidity decreases and for a given moisture content, humidity is approximately halved for a 10 degree rise in temperature [44]. This suggests that a sensor that operates at elevated temperatures increases the probability of H_2 combustion via decreasing the minimum ignition energy [38], the LFL [37] and increasing the probability of spark discharge. One of the world most notable disasters, the Hindenburg, may have been caused by a spark discharge, which ignited incendiary paint, and ignited the hydrogen gas contained in or leaking from the airship [45]. Accidents involving the release of H_2 gas or LH_2 were responsible for 81% of total accidents in the aerospace industry in 1974 [29]. A summary of type of accident and the percentage of accidents which involve LH_2 and H_2 gas is presented in Table 2-10.

These problems may be mitigated by the implementation of a passive (or low-power), wireless, room-temperature gas detection system, which continuously monitors multiple nodes and reports temperature and H_2 gas presence.

Table 2-10. A summary of accidents involving LH_2 and H_2 gas in industry and aerospace [29].

Sector	Type of Accident	Percentage of Total Accidents (per industry)
Industrial	Undetected leaks	22
	H_2-O_2 off gassing explosions	17
	Piping and pressure vessel ruptures	14
Aerospace	Release of H_2 gas or LH_2	81
	Ignition of H_2 to atmosphere	41
	Ignition of H_2 to enclosures	22

2.4.2 Hydrogen sensitive thin films

Due to their high surface to volume ratio, nanocrystalline thin-films are generally preferred over their bulk counterparts for the purposes of gas detection. For example a 300Å iron particle has about 5% atoms on the surface and a 100Å particle has 20% of atoms on the surface. In contrast a 30Å particle has 50% of atoms on the surface [46]. High surface to volume rates leads to large adsorption rates for gases and vapors. Films that are used for gas detection are pure metals, alloys or compound semiconductors. Recently, thin-films have been combined with arrays of nanotubes or nanowires to create structures with very high surface to volume ratios and high gas sensitivity [46, 47]. A review of metals alloys, semiconducting thin films and nanowire/ nanotube arrays is presented.

2.4.2.1 Metal Films

Nickel (Ni), palladium (Pd), and platinum (Pt) are Group 8 transition elements of the periodic table and are commonly referred to as "platinum metals" [48]. All three of these elements are most commonly employed as catalysts for hydrogenation reaction. When exposed to gaseous hydrogen or hydrocarbons these elements may undergo a measureable change in

mechanical and electrical parameters and are consequently used as sensors of these volatile gasses. Pd is commonly used for hydrogen gas detection because it has a higher solubility to hydrogen gas—i.e. greater sensitivity— than either than either Pt or Ni over a very wide range of temperatures and pressures [48]. For room temperature sensors, alloys are generally preferred because pure metals suffer from a phase transition due to hydride formation, which requires high temperatures to reverse. Annealing of the pure Pd at high temperature in order to desorb the hydrogen causes an irreversible deformation of the sensor and leads to eventual electrical and/or mechanical failure [48]. Discontinuous ultra-thin (1-50Å) Pd films have been used for room temperature hydrogen gas detection because they exhibit a sharp decrease in electrical resistance when exposed to hydrogen gas [49, 50]. These films have a high sheet resistance, which makes them suitable for integration with a SAW device via the acoustoelectric effect. Films of this nature were characterized using resistor structures and integrated with SAW devices. The findings of the Pd film's characterization are presented in CHAPTER 5.

2.4.2.2 Metal Oxide Semiconductor Films

Metal oxide semiconductors are also frequently used for gas detection of hydrocarbons. At elevated temperatures hydrocarbons interact with surface adsorbed O_2 molecules on the film to create excess electrons which results in a decrease in the film's surface electrical resistivity. Common H_2 sensitive oxide semiconductors include: tin oxide (SnO_2), zinc oxide (ZnO), titanium oxide (TiO_2), iron oxide (Fe_2O_3), nickel oxide (NiO), gallium oxide (Ga_2O_3), indium oxide (In_2O_3), selenium oxide (Sb_2O_5), molybdenum oxide (MoO_3), and tungsten oxide (WO_3) [24]. SnO_2 is the most widely used and has been studied 1968. The selectivity of the oxides may

be increased by doping with catalytic metals such as Pd, Pt, Au, Ag and Cu. Recently, authors doped SnO_2 with indium oxide (In_2O_3) and an ultra-thin Pt film and successfully reduced the temperature of operation to room temperature [51, 52]. This breakthrough eliminates the need for a substrate heater, thereby decreasing the sensor power consumption and making this film a candidate for passive, wireless, room temperature hydrogen gas sensing. Thin-film semiconductors are ideal for integration with SAW devices because the sheet resistance is sufficiently high to couple with the SAW via the acoustoelectric effect. Catalytically-doped SnO_2 films were characterized and integrated with SAW devices; the results of this work is presented in CHAPTER 6.

2.4.2.3 Nanotube and Nanowire Arrays

Nanotube and nanowires are tubes or wires of a given material with at least one dimension 10Å to 1000Å. In gas detection purposes wires are constructed from the previously listed semiconducting metal oxides, or in few cases a pure metals (Pd for H_2 gas detection [53]) and Si [46]. Films are grown in a variety of techniques but can be divided into two broad categories: liquid or solution-based techniques and vapor-phase techniques. The growth of nanowires is difficult compared to the growth of metal or semiconductor films. Transfer of nanowires to different substrates is a low-yield process, which makes integration with a SAW device difficult. One author has demonstrated a passive wireless H_2 gas sensor by electrically loading an IDT with a Pd coated ZnO nanowire array on a thin film resistor structure[42]. This device will be discussed in the next section.

2.4.3 OFC-SAW sensors vs. previous SAW sensors

The use of SAW devices as sensors was introduced in the 1970's and continues to be explored to date. The use of SAW with Pd thin films for as H_2 sensors has also had a wealth of publications to date and only a few examples are referenced here [54-64]. It has been recognized that Pd absorbs hydrogen and this absorption may change the mechanical or acoustoelectric parameters of the SAW-film interaction. The first SAW based hydrogen sensor was demonstrated by D'Amico et al. in 1982 [54-56]. In his report, D'Amico utilized SAW single and dual delay line oscillators in order to observe the frequency shift, due to mass loading caused by a thick Pd film (1900-7600Å) in the delay path. These devices were exposed to 0.001%, 0.1% and 1% concetrations of H_2 gas (balance N_2). The fractional change in frequency was found to be proportional to film thickness; a 1900Å film caused 15ppm shift while the 7600Å film caused a 100ppm frequency shift. The reaction rates ranged from 0.8 to 21Hz/s depending on gas concentration and flow rate. The total rise time ranged from 5 to 70 minutes depending on gas concentration and flow rate. In general, the rise time increased with flow rate but decreased with gas concentration.

Jakubik et al. [57, 59, 60] also implemented a SAW dual delay line oscillator for H_2 gas sensing, with the distiction of using a bilayer structure in the delay path. A 1200Å dielectric film—copper phthalocycanine, (CuPc), nickel phthalocycanine, (NiPc), or metal-free phthalocycanine, (H_2Pc)—was placed between the SAW substrate and a 200Å Pd film. The dielectric prevented the Pd film from shorting out the AE response of the SAW. The mass loading effect of hydrogenated CuPc, NiPc, and H_2Pc and 200Å Pd films are small when compared to the electrical response, thus, the acoustoelectric response is the dominant sensing

mechanism. These devices were exposed to H_2 gas concentrations from 1.5-4%, and a 40ppm shift in center frequency resulted. The reaction rates varied linearly with H_2 gas concentration where a 1.5% H_2 gas concentration caused a 2.1Hz/s reaction rate and 6.7 min total rise time and a 4% H_2 gas produced 21Hz/s with a total rise time of 1 minute. The fall times were all typically 5minutes and these devices were reversible at room temperature and pressure.

Yamanaka et al. [58] introduced the ball SAW device hydrogen sensor. This consisted of a piezoelectric quartz crystal sphere with a single interdigitated transducer at its equator and a 200Å Pd film in the SAW propagation path. When exposed to 3% H_2 gas, a reversible 10ppm change in velocity with a response time of around 60 seconds was observed. There was also a small decrease in amplitude due to H_2 gas exposure, the magnitude of which was appeared to be frequency dependent. The authors did not know the precise cause of the attenuation but theorized that it will be used as a supplementary H_2 sensing mechanism.

The devices designed by D'Amico and Jakubik are active and wired and comprise the majority of the SAW-based hydrogen sensing designs found in literature. Yamanaka's ball SAW sensor designed by may be implented passively and wirelessly, but unfortunately, it is relatively difficult and expensive to fabricate. Thus, a different approach was need in order to implent a passive, wireless, SAW based hydrogen gas sensor.

A SAW-based hydrogen sensor that may be implemented passively, and wirelessly has been successfully demonstrated by Huang et al. He uses a H_2 sensitive resistor to modulate the electrical load on a SAW interdigitated transducer (IDT), consequently modulating the fraction of energy that is reflected by the IDT when the resistor is exposed to H_2 gas [42]. Huang's

device has a response time of approximately 15 minutes, which may be hazardous in situations where H_2 gas leaks above the LEL are not detected in time to avoid an accident. Furthermore these devices are not coded and are not individually distinguishable in a sensor network.

The devices that were developed in this dissertation are based on integrating the hydrogen-sensitive thin-film with the piezoelectric SAW substrate and modulated the amplitude and phase of the wave via the acoustoelectric effect. Hydrogen-sensitive ultra-thin films (UTF) of Pd and SnO_2 films, which is coated with a Pd-UTF, were utilized. The sensors showed an instantaneous response, that consists of a large fractional change in SAW propagation characteristics when exposed to 2% H_2 gas. One early device is shown in Figure 2-26 where a Pd thin-film, which can affect the amplitude or delay of the reflected signal, is placed in the propagation path between a transducer and an orthogonal frequency coded (OFC) reflector. A second OFC reflector, which has no Pd film in the propagation path, acts as a reference. To build an operational device, first the SAW film interaction needs to be investigated (CHAPTER 3 and CHAPTER 4) and the Pd (CHAPTER 5) and SnO_2 films (CHAPTER 6) needs to be characterized.

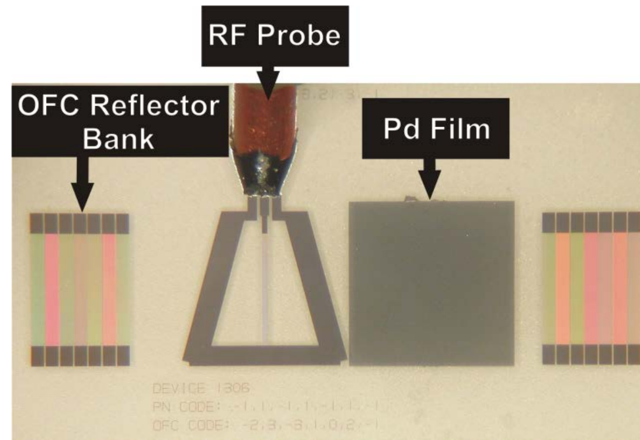

Figure 2-26. An example SAW OFC RFID hydrogen sensor embodiment. The device is being tested on an RF probe station and the reflector diffraction pattern is apparent from the OFC reflectors at differing frequencies.

2.5 CHAPTER 2 Summary

The main points of Chapter 2 are as follows:

1. Failure of the electrical connections is cited as the primary cause of cryogenic liquid sensor miscommunication, thus an ideal solution should involve the interrogation of passive, wireless, sensor-nodes inside to cryogenic Dewars or fuel tanks.
2. The SAW is greatly attenuated by the cryogenic liquid, a wireless SAW RFID tag will simply cease to operate when submerged in liquid and report temperature at a given location in the tanks as the liquid level decreases beneath the sensor (see Figure 2-22).
3. Accidents involving the release of H_2 gas or LH_2 were responsible for 81% of total accidents in the aerospace industry.
4. These problems may be mitigated by the implementation of a passive (or low-power), wireless, room-temperature gas detection system, which continuously monitors multiple nodes and reports temperature and H_2 gas presence.

5. The goal of this research is to make these sensors passive (i.e. without batteries), wireless and individually identifiable. A wireless sensor network will have the ability to report the time as well as the location of a sensing event instantaneously.
6. The passive, wireless, OFC-SAW tag-sensor is built on the commonly used YZ-lithium niobate (YZ-$LiNbO_3$) piezoelectric substrate—a well-researched SAW device platform—and implements spread spectrum coding in order to achieve multiple-access capability (i.e. read multiple devices simultaneously).
7. It is well documented that surface acoustic wave (SAW) devices operate well as chemical sensors when a chemically sensitive film is placed on the piezoelectric substrate. The film and substrate interaction is governed by two major effects: (1) the thin-film acoustoelectric effect in SAW devices because it describes the interaction of electrical energy between a SAW in a piezoelectric medium and a thin-film placed in the wave's propagation path and (2) the acoustoelastic interaction because it describes the effects of elastic properties of the film on the propagation characteristics of the SAW (see CHAPTER 3).
8. Pd UTF and SnO_2 films have a high sheet resistance which makes them suitable for integration with a SAW device via the acoustoelectric effect.
9. The devices that were developed in this dissertation are based on integrating the hydrogen-sensitive thin-film with the piezoelectric SAW substrate and modulated the amplitude and phase of the wave via the acoustoelectric effect.

CHAPTER 3 PIEZOELECTRIC SAW THIN-FILM INTERACTION

3.1 Chapter Overview

This chapter presents the theoretical analysis of the SAW-thin film interaction. This is necessary because the H_2 gas sensors, which were constructed for this dissertation, involves the growth of a thin-film in the SAW propagation path. A surface acoustic wave (SAW) traveling in a piezoelectric substrate, with a thin-film layer in the acoustic path, may undergo a measureable change in the SAW's amplitude and velocity. The perturbation in the SAW's parameters is a combination of the acoustoelectric and acoustoelastic SAW-thin film interactions. If film's electrical conductivity is very high or very low (i.e. good conductor or insulator), the SAW's perturbation is primarily due to the film's mechanical properties. If the film is semiconducting, the perturbation of the SAW is dependent on both the electric and mechanical properties of the film. The acoustoelastic perturbation is due to the mechanical stiffness and viscosity of the film. In the acoustoelectric regime, the majority of the change is dependent upon the electrical properties (i.e. sheet resistance and electron mobility) of the film. The film's electrical properties may be dependent on a variety of physical parameters such as thickness, temperature, pressure, gas/chemical presence, etc. If properly implemented, the SAW-thin-film acoustoelectric interaction is useful in the analysis of the properties of thin films, as well as thin-film physical sensors.

The derivation of the acoustoelectric and acoustoelastic mechanisms is composed of two parts: (1) derive the acoustoelectric and acoustoelastic equations for a one-dimensional volume wave (bulk mode) in an isotropic piezoelectric semiconductor and (2) extend the bulk mode

solution to SAW propagation in an anisotropic piezoelectric substrate, beneath a thin film. For simplicity, the one-dimensional solution assumes that the wave's propagation direction and particle displacement are in the same direction and the particle displacement and stresses that are perpendicular to the wave's direction of propagation are ignored. This methodology is meant to show the reader how the form of the piezoelectric SAW dispersion equations is generated without the use of complex multi-degree tensor notation. These derivations include the combined effect of electrical parameters, mass loading and film viscosity, which has traditionally been excluded from the piezoelectric SAW theory.

3.2 Theory

3.2.1 One-dimensional Wave Motion in a Solid

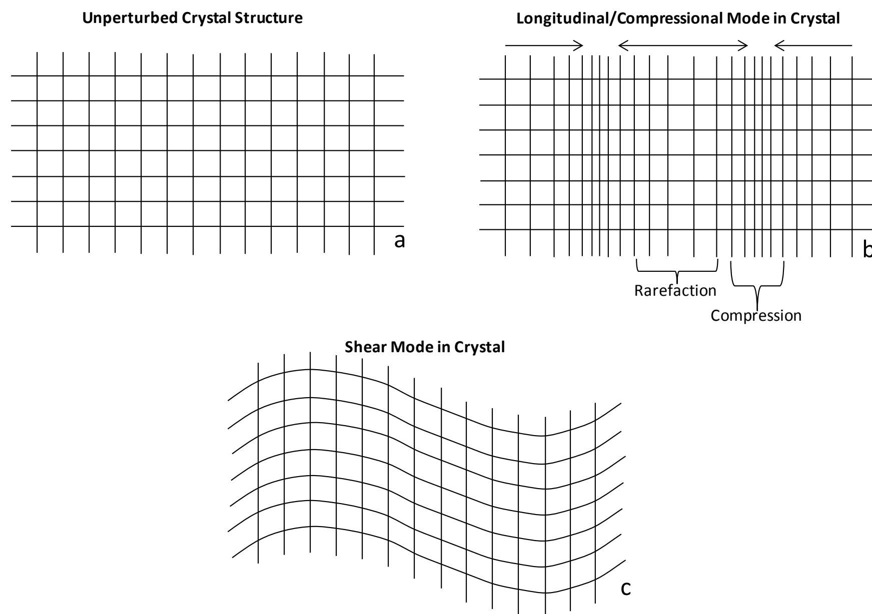

Figure 3-1. A schematic of a one dimension volume wave in a solid (a: unperturbed crystal structure, b: longitudinal mode the particle displacement and wave propagation is in the same direction and c: shear mode, the particle motion is perpendicular to the direction of propagation) in a solid when force is applied.

From classical physics the stress, T, (3-1) in a material is defined as the force per unit area on said material and is given by the material stiffness, c, multiplied by the strain, S (3-2). The strain is defined as the ratio of the elongation of the material (ΔL) to its initial length, L.

$$T = Stress = \frac{Force}{Area} = cS \tag{3-1}$$

$$S = \frac{\Delta L}{L} = \frac{\partial \mu}{\partial z} \tag{3-2}$$

where $\partial \mu$ is the change in particle displacement in the ∂z direction. According to Newton's Law, *force = mass x acceleration*; the mass, m, of a unit volume, $dx \cdot dy \cdot dz$, with mass density, ρ, is

$$m = \rho \cdot dx \cdot dy \cdot dz \tag{3-3}$$

and the acceleration, a, is the partial derivative of the particle velocity with respect to time, given by

$$a = \frac{\partial^2 \mu}{\partial t^2} \tag{3-4}$$

The force on the unit volume is

$$F = \rho \cdot dx \cdot dy \cdot dz \cdot \frac{\partial^2 \mu}{\partial t^2} \tag{3-5}$$

From Figure 3-2, the forces due to the *dxdz* and *dydz* planes have been ignored and the net force in the positive z-direction is given by [13]

$$F_z = (T_{zz} + dT_{zz}) \cdot dxdy - T_{zz}dxdy = dT_{zz}dxdy = \rho \cdot dx \cdot dy \cdot dz \frac{\partial^2 \mu}{\partial t^2}$$

$$\therefore dT_{zz} = \rho \cdot dz \frac{\partial^2 \mu}{\partial t^2} \tag{3-6}$$

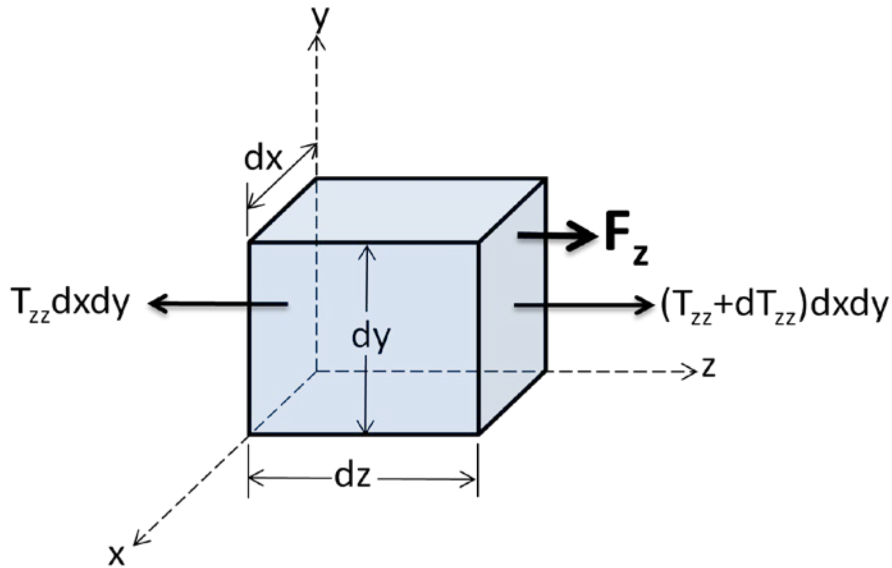

Figure 3-2. A schematic of forces exerted on each face of a differential volume of an elastic solid. The force due to the *dxdz* and *dydz* planes have been ignored.

From (3-6) the change in stress in the direction of the force, *dz,* is

$$\frac{dT_{zz}}{dz} = \rho \frac{\partial^2 \mu}{\partial t^2} \tag{3-7}$$

Combining (3-1) and (3-7) yields

$$\frac{\partial T}{\partial z} = c \frac{\partial S}{\partial z} = c \frac{\partial^2 \mu}{\partial z^2} = \rho \frac{\partial^2 \mu}{\partial t^2} \tag{3-8}$$

Equation (3-8) is the one-dimensional wave equation for force in a solid may be rearranged by cancelling $\partial^2\mu$ on both sides of the equation, to yield the particle velocity in the *z*-direction, $(\partial z/\partial t)$, given by

$$\sqrt{\frac{\partial z^2}{\partial t^2}} = \sqrt{\frac{c}{\rho}} \tag{3-9}$$

The phase velocity is determined by first assuming a solution for the particle displacement in the wave equation. For plane wave propagation in the *z*-direction, the particle displacement, μ, is given by

$$\mu = \mu_o \exp(j(\omega \cdot t - k \cdot z)) \tag{3-10}$$

where ω is the radian frequency, t is time, and k is the wave number. Substitute (3-10) into (3-8) and solve for the dispersion relation *(ω/k)* yields

$$c \cdot k^2 \cdot \mu = \rho \cdot \omega^2 \mu$$

$$\frac{\omega}{k} = \sqrt{\frac{c}{\rho}} \tag{3-11}$$

From (3-9) and (3-11) it is apparent the phase and particle velocity are equal for a one-dimensional volume wave motion. If c is complex *(c^*)*, which occurs in viscoelastic and semiconducting piezoelectric solids, the dispersion relation produces wave attenuation or amplification, and because ω is purely real then the propagation constant k must be complex, and is given by

$$k = \beta + j \cdot \alpha \tag{3-12}$$

Substitute (3-12) into (3-10) yields

$$\mu = \mu_o \exp\left(j\left(\omega t - (\beta + j\alpha)z\right)\right) = \mu_o \exp\left(j\omega t - j\beta \cdot x + \alpha \cdot z\right) = \mu_o \exp(\alpha \cdot z) \exp\left(j\omega t - j\beta \cdot z\right) \tag{3-13}$$

where α is the attenuation constant if it is < 0 or the amplification constant if it is > 0. The attenuation or amplification coefficient in *dB* per unit length is given by

$$PL_{dB/L} = 20\log_{10}\left(\exp(\alpha \cdot L)\right) = \frac{20}{\ln(10)} \cdot \alpha \cdot L = 8.686 \cdot \alpha \cdot L \tag{3-14}$$

where L is the length of the propagation path. Substitute (3-12) into (3-11) and solve for the wave attenuation constant, α, yields

$$\alpha = \omega \, \mathrm{Im}\left\{ \frac{1}{\sqrt{\frac{c^*}{\rho}}} \right\} \tag{3-15}$$

The phase velocity is the real portion of the dispersion relation and is given by

$$v_p = \mathrm{Re}\left\{ \frac{\omega}{k} \right\} = \mathrm{Re}\left\{ \sqrt{\frac{c^*}{\rho}} \right\} \tag{3-16}$$

3.2.2 Amplitude and Velocity Dispersion in Viscoelastic Solids

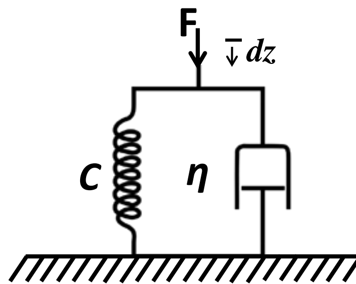

Figure 3-3. A schematic representation of a Kelvin-Voigt material which shows material stiffness, *c*, and viscosity mechanism *η*. The dynamic modulus, *C*(ω)*, is the frequency dependent stiffness (or dynamic modulus) of the material when a force, *F*, with angular frequency, *ω*, is applied in the *z*-direction and causes displacement *dz*.

If a material is acoustically lossy, a damping term, η, commonly known as viscosity, must be added to the stress equations. A simple model for materials of this type is the Kelvin-Voigt solid (Figure 3-3), the transfer function of which is similar to the input impedance of a series

inductor-resistor circuit. The viscosity is reactive and effectively changes the stiffness of the solid whenever a time varying force is applied; the resulting stress is given by

$$T = cS + \eta \frac{\partial S}{\partial t} \xleftrightarrow{\textit{Fourier}\text{ Transform Pair}} (c + j\omega\eta)S(\omega)$$

Thus the effective frequency dependent stiffness is given by

$$c^* = (c + j\omega\eta) \tag{3-17}$$

The phase velocity in the z-direction, $\partial z/\partial t$ and is given by (3-16) the solution of which is

$$v_p = \mathrm{Re}\left\{\sqrt{\frac{(c + j\omega\eta)}{\rho}}\right\} = \sqrt{\frac{c}{\rho}} \tag{3-18}$$

From (3-15) the attenuation constant is given by

$$\alpha = \mathrm{Im}\left\{\frac{\omega}{\sqrt{\frac{c^*}{\rho}}}\right\} = \frac{\omega}{v_p}\mathrm{Im}\left\{\left(1 + \frac{j\omega\eta}{c}\right)^{-\frac{1}{2}}\right\} \tag{3-19}$$

A function, $(x+y)^r$, may be simplified using the generalized binomial theorem if $|x|>|y|$ and r is any complex number. In equation (3-19) the stiffness, c, for solids is in the order of *GPa* and $\omega\eta$ in the UHF range is in the order of *MPa* for thin solid films; the ratio of $\omega\eta/c \ll 1$. Applying Newton's Generalized Binomial Theorem to (3-19) yields

$$\alpha = \frac{\omega}{v_p}\mathrm{Im}\left\{1 - \frac{1}{2}\frac{j\omega\eta}{c}\right\} = -\frac{\omega^2\eta\rho^{\frac{1}{2}}}{2c^{\frac{3}{2}}} = -\frac{\omega^2\eta}{2\rho v_p{}^3} \tag{3-20}$$

Because α is negative, it is an attenuation constant due to the viscosity of the solid.

Ultrasonic attenuation in a metals was first report by Bömmel [65] in 1954. From that work, the concept of a phonon viscosity damped ultrasonic wave was introduced by Mason [66]. Mason suggested that the attenuation was due to two primary mechanisms: (1) The viscosity caused by "a simple phenomological" interaction between the vibrating lattice and the electron gas; and (2) a viscosity caused by a thermoelastic process that occurs when a compressed solid becomes heated and energy is lost from the acoustic wave by thermal conduction between the warm and cold parts, which is dependent on the thermal conductivity of the material [67]. Accordingly, the effect is highly temperature dependent, though at room temperature, the temperature effect is small, as reported by Spencer et al [68]. For metal films, Mason [66] found that the phonon viscosity may be approximated by

$$\eta_e = \frac{\sigma \cdot \left(\frac{h}{2\pi}\right)^2 \left(\frac{3\pi^2 N_e N_A \rho}{M}\right)^{\frac{2}{3}}}{5q^2} \tag{3-21}$$

where σ, the electrical conductivity of the film, h is Plank's constant, N_A is Avogadro's number, N_e is the number of conduction electrons per atom, ρ is the mass density, q is the electron charge and M is the molar mass of the film. Rice [69] approximated the viscosity due to thermoelastic attenuation as

$$\eta_L = \frac{13}{12}\frac{K_T T}{20v^2} \tag{3-22}$$

where K_T is the thermal conductivity, T is the absolute temperature and v is the phonon group velocity. Rice [69] found that the total phonon viscosity in a given material is the sum of (3-21) and (3-22), i.e.

$$\eta = \eta_e + \eta_L \tag{3-23}$$

3.2.3 One Dimensional Volume Wave in a Semiconducting Piezoelectric Solid

From classical physics, the constitutive piezoelectric relations are given by

$$T = c^E S - eE \tag{3-24}$$

$$D = eS + \varepsilon_p E \tag{3-25}$$

where c^E is the stiffness of the piezoelectric material due to a constant electric field, E, and e is the piezoelectric coefficient, ε_p is the electrical permittivity and D is the electric flux density of the piezoelectric medium. The acoustic wave velocity is very slow as compared to an electromagnetic (EM) wave's velocity, so the behavior of the currents, are governed by the Maxwell's electrostatic approximations [70, 71]

$$E = -\nabla\phi, \quad \mathrm{D} = \varepsilon\mathrm{E}, \; \nabla \bullet D = Q_v \tag{3-26}$$

where Q_v is the volume charge density and the charge continuity equation is given by

$$\begin{gathered} \nabla \bullet J = -\frac{\partial Q_v}{\partial t} = -\frac{\partial \nabla \bullet D}{\partial t} \\ \therefore \text{in one dimension } \frac{\partial J_z}{\partial z} = -\frac{\partial}{\partial t}\left[\frac{\partial D_z}{\partial z}\right] \end{gathered} \tag{3-27}$$

J is the current density of the medium given by

$$J = \sigma E \tag{3-28}$$

The DC conductivity, σ, of the piezoelectric semiconductor can be modulated between zero and infinity by light excitation. Diffusion effects are ignored for these calculations.

3.2.3.1 Velocity in Short Circuited Piezoelectric Material

If the DC electrical conductivity of the piezoelectric is sufficiently high (i.e. $\sigma \rightarrow \infty$), the electric field is short circuited (i.e. $E=0$), and the gradient of (3-24) is given by (3-8). The phase

velocity and attenuation is the same as the viscoelastic case given by (3-16) and (3-20), respectively. In this case $v_p = v_{sc}$ which is known as the short circuit velocity.

3.2.3.2 Velocity in Open Circuited Piezoelectric Material

The open circuit condition occurs when the DC electrical conductivity of the piezoelectric substrate is small (i.e. $\sigma \rightarrow 0$). Equation (3-25) is inserted into the continuity equation (3-27) which is equal to *0* due to the absence of free charges. Assuming plane wave solution in the form of (3-10) for *S* and *E* and solving for the electric field, *E*, as a function of the strain, *S*, yields:

$$
\begin{gathered}
0 = -\frac{\partial J}{\partial z} = \frac{\partial}{\partial t}\left[\frac{\partial D}{\partial z}\right] \\
-\frac{\partial \sigma E}{\partial z} = ik\sigma E = \frac{\partial(-jk(eS + \varepsilon_P E))}{\partial t} = \omega k(eS + \varepsilon_P E) \\
\therefore -eS = \varepsilon_P E \\
\therefore E = -\frac{e}{\varepsilon_p} S
\end{gathered}
\tag{3-29}
$$

Substituting (3-29) and (3-17) into (3-24) yields

$$
T = \left[c^E \left(1 + \frac{e^2}{c^E \varepsilon_P} \right) + j\omega\eta \right] S \tag{3-30}
$$

The complex modulus of the medium is given by

$$
c^* = c^E \left(1 + \frac{e^2}{c^E \varepsilon_P} \right) + j\omega\eta \tag{3-31}
$$

and the open-circuit velocity of the piezoelectric substrate, v_{oc}, is

$$v_{oc} = \mathrm{Re}\left\{\sqrt{\frac{c^*}{\rho}}\right\} = \sqrt{\frac{c^E}{\rho}\left(1+\frac{e^2}{c^E\varepsilon_P}\right)} = v_{sc}\sqrt{\left(1+\frac{e^2}{c^E\varepsilon_P}\right)} \tag{3-32}$$

Applying Newton's Generalized Binomial Theorem to (3-32) yields

$$v_{oc} = v_{sc}\left(1+\frac{e^2}{2c^E\varepsilon_P}\right) \tag{3-33}$$

The attenuation constant is the same as that given for the viscoelastic medium (3-20).

3.2.3.3 Electromechanical Coupling Coefficient

The electromechanical coupling coefficient, K, of a piezoelectric is the electrical portion of the wave energy and is given by [11]

$$K^2 = 2\frac{v_{oc}-v_{sc}}{v_{oc}} \tag{3-34}$$

Substituting (3-33) into (3-34) yields

$$K^2 = 2\frac{v_{sc}\left(1+\frac{e^2}{2c^E\varepsilon_P}\right)-v_{sc}}{v_{sc}\left(1+\frac{e^2}{2c^E\varepsilon_P}\right)} \rightarrow \frac{\left(\frac{e^2}{c^E\varepsilon_P}\right)}{\left(1+\frac{e^2}{2c^E\varepsilon_P}\right)} \approx \frac{e^2}{c^E\varepsilon_P} \tag{3-35}$$

Equation (3-35) is only valid for $(e^2/c^E\varepsilon_P)<20\%$. For commonly used piezoelectric substrates the maximum value for K^2 for pure SAW modes is <5% (Table 3-1).

3.2.3.4 Semiconducting Piezoelectric Material

When the DC conductivity, σ, of the piezoelectric medium is finite, equation (3-25), is inserted into the continuity equation (3-27) and assuming plane wave solution in the form of (3-10) for S and E and solving for the electric field, E, as a function of the strain, S, yields:

$$-\frac{\partial J}{\partial z} = \frac{\partial}{\partial t}\left[\frac{\partial D}{\partial z}\right]$$

$$-\frac{\partial \sigma E}{\partial z} = jk\sigma E = \frac{\partial(-jk(eS + \varepsilon_P E))}{\partial t} = \omega k(eS + \varepsilon_P E)$$

$$\therefore (\omega\varepsilon_P - j\sigma)E = \omega e S \tag{3-36}$$

$$\therefore \therefore E = \frac{\omega e S}{(\omega\varepsilon_P - j\sigma)} = -\frac{e}{\varepsilon}\frac{1 + j\dfrac{\sigma}{\omega\varepsilon_p}}{1+\left(\dfrac{\sigma}{\omega\varepsilon_p}\right)^2}S$$

Substitute (3-17) and (3-36) into (3-24) to solve for stress, T as a function of strain, S yields

$$T = \left[c^E\left(1 + \frac{e^2}{c^E\varepsilon_p}\frac{1 + j\frac{\omega_r}{\omega}}{1+\left(\frac{\omega_r}{\omega}\right)^2}\right) + j\omega\eta\right]S \tag{3-37}$$

where ω_r is the dielectric relaxation frequency given by

$$\omega_r = \frac{\sigma}{\varepsilon_p} \tag{3-38}$$

The dielectric relaxation frequency of a material specifies the frequency above which a material begins to store charge i.e. behave like a insulator [72]. Substitute (3-35) into (3-37) yields

$$T = c^* \cdot S \tag{3-39}$$

$$c^* = c^E \left(1 + K^2 \frac{1 + j\frac{\omega_r}{\omega}}{1 + \left(\frac{\omega_r}{\omega}\right)^2} \right) + j\omega\eta \tag{3-40}$$

From (3-16) the phase velocity is given by

$$v_p = \mathrm{Re}\left\{ \sqrt{\frac{c^*}{\rho}} \right\} = v_{sc} \left(1 + \frac{K^2}{2} \frac{1}{\left(1 + \left(\frac{\omega_r}{\omega}\right)^2 \right)} \right) \tag{3-41}$$

and from (3-19) the attenuation constant α, is given by

$$\alpha = \mathrm{Im}\left\{ \frac{\omega}{\sqrt{\frac{c^*}{\rho}}} \right\} = -\left(\frac{\omega \cdot K^2}{2v_{sc}} \frac{\frac{\omega_r}{\omega}}{\left(1 + \left(\frac{\omega_r}{\omega}\right)^2 \right)} + \frac{\omega^2 \eta}{2{v_p}^3 \rho} \right) \tag{3-42}$$

From (3-42) the wave attenuation constant is a combination of the acoustoelectric (i.e. K^2 and ω_r) and acoustoelastic mechanisms (i.e. η, c and ρ). The acoustoelectric portion of equation (3-42) was first presented by Hudson and White in 1961 [71], and the acoustoelastic portion of equation (3-42) was first presented by Bömmel in 1954 [65]. The acoustoelectric attenuation is symmetric about ω_r/ω because the substrate behaves like a conductor (i.e short circuit) when $\omega_r >> \omega$ and like an insulator (i.e. open circuit) when $\omega_r << \omega$ (Figure 3-4). The acoustoelectric loss is constant because it is to be independent of ω_r.

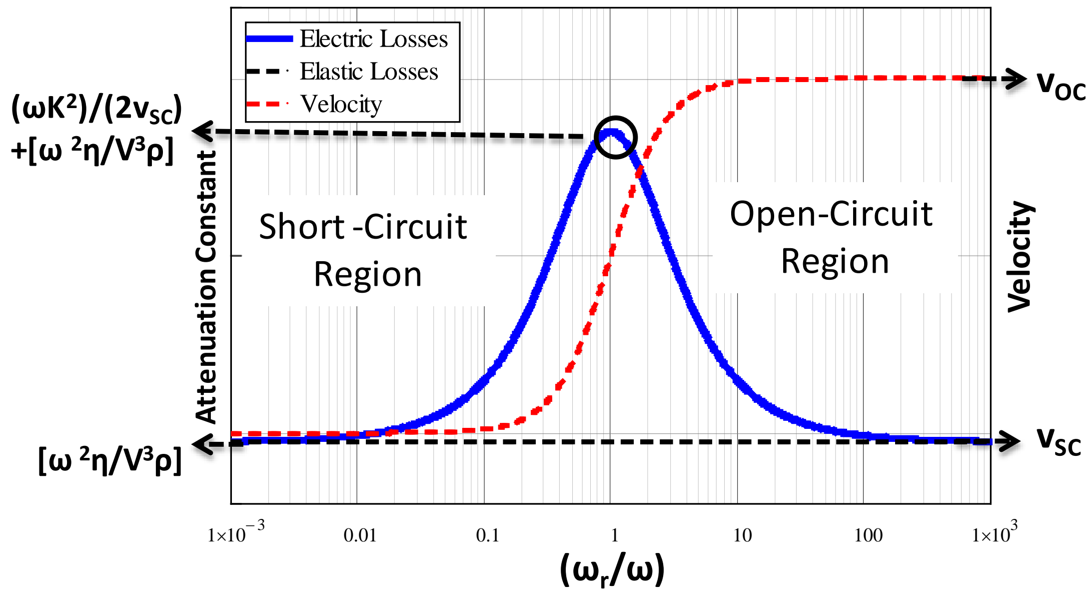

Figure 3-4. Plot of acoustoelectric attenuation constant and phase velocity as a function of ω_r/ω a one-dimensional volume wave in a piezoelectric semiconductor.

3.2.4 Thin-Film Piezoelectric SAW Interface

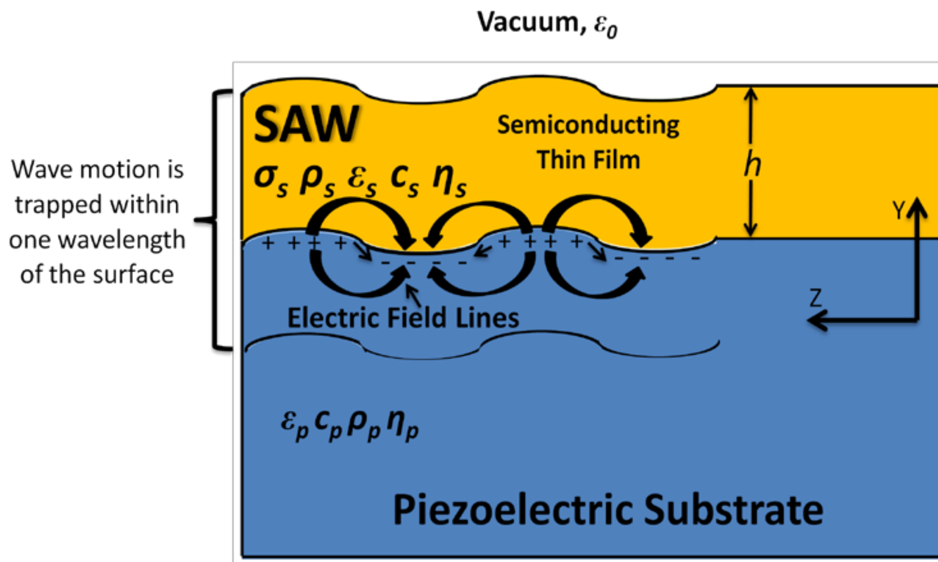

Figure 3-5. A schematic of SAW propagation in a piezoelectric crystal, beneath a thin film. ε, σ, η, c, and ρ is the electrical permittivity, electrical conductivity, viscosity, stiffness and density, respectively.

The acoustoelectric interaction in SAWs occurs because a propagating SAW in a piezoelectric substrate is accompanied by an electric field. The moving electric field causes the displacement of bound charges in the piezoelectric, which creates displacement currents in the substrate and conduction currents in the film (assuming that it is a conductor or semiconductor). The magnitude of the ratio of the conduction to displacement currents is called the loss tangent of the interface.

A strong interaction between the film and SAW occurs when the magnitude of the conduction to displacement currents at the film-substrate interface are equal (i.e., loss tangent = 1) (Figure 3-7). This results in a large propagation loss in the SAW and a velocity shift halfway between the open- and short-circuit velocities of the substrate. The open-circuit case occurs when the film's conductance is very small in comparison to the substrate's conductance. The short-circuit case occurs when the film's conductance is very high in comparison to the substrate's conductance. This short circuits the electric field, E, and eliminates the piezoelectric effect at the surface of the piezoelectric

A SAW by definition is trapped within one wavelength of the surface of the film (Figure 3-5). It is a combination of decaying transverse and longitudinal modes in an anisotropic piezoelectric medium. The acoustoelectric and acoustoelastic solution for the dispersion relation of a SAW, propagating in a piezoelectric substrate, beneath a semiconducting thin film [70, 73] is similar to the solution for one-dimensional volume wave propagation in a piezoelectric semiconductor [71] (i.e. equations (3-41) and (3-42)). The solutions for the bulk wave assume that the piezoelectric is a semiconductor (i.e. σ_p is finite) whereas the piezoelectric in Figure 3-5

is an electrical insulator (i.e. $\sigma_p = 0 \cdot S/m$) with a semiconducting thin film in the propagation path. The primary difference between the solutions for the dispersion relation of volume and surface waves in a piezoelectric medium is the dielectric relaxation frequency. For SAWs, the finite film thickness, h, and exponential decay of the wave motion into the substrate must be taken into account.

Bound charges are generated due to the movement of electric dipoles by the ultrasonic wave. The decay of wave motion into the substrate causes a decay in the concentration of bound charges in the y-direction. These bound charges create a decaying surface potential and electric field. From Figure 3-5 the surface potential propagates in the z-direction and decays exponentially in the y-direction; $y=0$ occurs at the film substrate interface and $y=-h$ is the film's surface. The surface potential, φ, is given by (3-43) [73] and the decay component in the y-direction is plotted in Figure 3-6.

$$\phi = \phi_0[\exp(-ky) + \exp(ky)]\exp(j(\omega t - kz)) \tag{3-43}$$

where ϕ_0 is the electric field intensity at the film-substrate interface. From Figure 3-6 the magnitude of the potentials above and into the substrate are approximately equal for the distances less than *1%* of the SAW wavelength, λ. For films with $kh << 1$ (such as the films that are used for H_2 gas detection) the surface potential is simplified to the non-decaying plane wave solution.

$$\phi = \phi_0 \exp(j(\omega t - kz)) \tag{3-44}$$

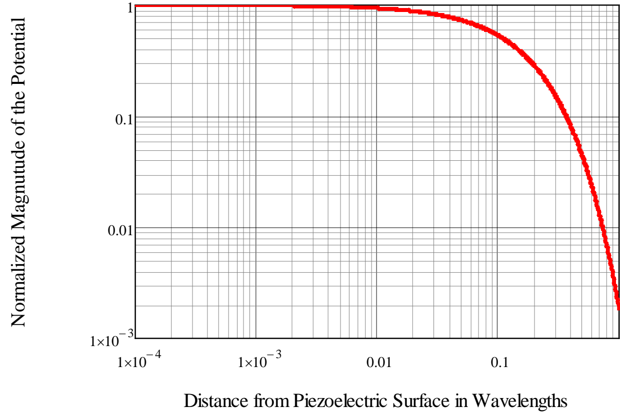

Figure 3-6. A plot of the decay of the SAW potential in the positive and negative *y*-direction.

3.2.4.1 Relaxation Frequency at the Interface

The dielectric relaxation frequency, ω_r, at the film-substrate interface is the inverse of the relaxation time [74] is given by

$$\omega_r = \frac{1}{\tau_r} = \frac{G}{C} \tag{3-45}$$

where G is the shunt conductivity per unit area and C is the shunt capacitance per area in the film. G is given by [13].

$$G = k^2 \sigma_s h = \frac{k^2}{R_s} \tag{3-46}$$

where R_s is the film's sheet resistance in $\Omega/\square$. The shunt conductance per unit area in the film is integral of the current per unit volume over the film thickness, *h,* divided by the surface potential ϕ (3-44); and the current per unit volume is the divergence of the conduction current density. The derivation is as follows

$$G = \frac{1}{\phi}\int_0^h (\nabla \cdot J)dy$$

$$J = \sigma_s E, \quad E = -\nabla\phi = jk\phi$$

$$\therefore J = j\sigma_s k\phi \quad \text{and } \nabla \cdot J = \sigma_s k^2 \phi$$

$$G = \frac{1}{\phi}\int_0^h (\nabla \cdot J)dy = k^2 \sigma_s h$$

The shunt capacitance per area, C, [13] is given by

$$C = (\varepsilon_0 + \varepsilon_p)k \tag{3-47}$$

C is the magnitude of the electric flux density divided by the surface potential, ϕ, and may be derived as follows

$$\mathrm{C} = \left|\frac{\mathrm{D}}{\phi}\right|, \quad \mathrm{D} = \varepsilon \mathrm{E}, \quad E = jk\phi \quad \therefore D = j\varepsilon k\phi$$

$$\therefore C = \left|\frac{\mathrm{D}}{\phi}\right| = \varepsilon \cdot k$$

The piezoelectric and vacuum surfaces are parallel, so the total capacitance is the sum of the charge storage both mediums; there are no displacement charges in the film due to the conduction process. The relaxation frequency is calculated by plugging (3-46) and (3-47) into (3-45) to yield

$$\omega_r = \frac{k}{R_s \cdot (\varepsilon_P + \varepsilon_0)} \tag{3-48}$$

$$\therefore \frac{\omega_r}{\omega} = \frac{k}{\omega \cdot R_s \cdot (\varepsilon_P + \varepsilon_0)} = \frac{1}{R_s \cdot v \cdot (\varepsilon_P + \varepsilon_0)} \tag{3-49}$$

Equation (3-49) is substituted into (3-41) and (3-42) to find the SAW acoustoelectric velocity and propagation constant, respectively.

3.2.4.2 SAW Attenuation Constant

The SAW attenuation constant is found by substituting (3-49) into (3-42) to yield

$$\alpha = -\left(\frac{2\pi \cdot f \cdot K^2}{2v_{sc}} \frac{R_s \cdot v_{sc} \cdot (\varepsilon_P + \varepsilon_0)}{\left(1 + \left(R_s \cdot v_{sc} \cdot (\varepsilon_P + \varepsilon_0)\right)^2\right)} + \frac{(2\pi \cdot f)^2 \eta_{eff}}{2v_{saw}{}^3 \rho_{eff}} \right) \tag{3-50}$$

where f is the frequency. The acoustoelectric portion (K^2, R_s, ε_p) of (3-50) is similar to the solutions of Adler [74], Datta [12] and Ballantine et al [13] and the rigorously-derived solution of Ingebrigtsen [73]. A plot of α is shown in Figure 3-7; it is evident that when $R_s{\cdot}v_{sc}{\cdot}\boldsymbol{\varepsilon}_p = 1$ there is a large transfer of energy from the substrate to the film due to the acoustoelectric interaction. The acoustoelectric loss is constant because it is to be independent of R_S.

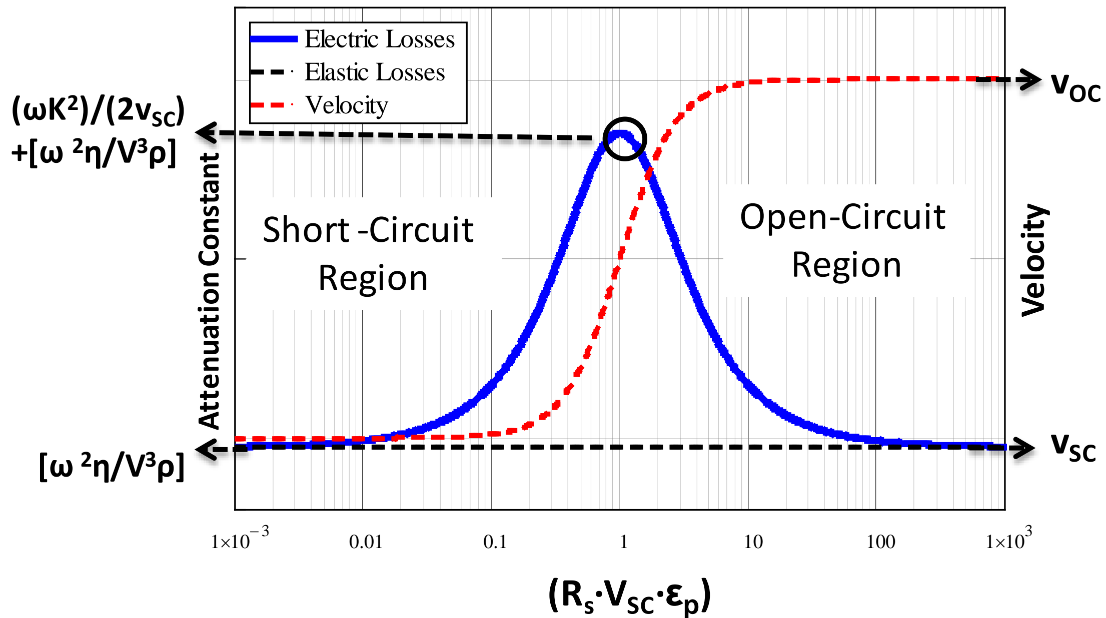

Figure 3-7. Plot of acoustoelectric attenuation constant and phase velocity as a function of $R_s{\cdot}v_{sc}{\cdot}\boldsymbol{\varepsilon}_p$ for a SAW in a piezoelectric.

The acoustoelastic term (η and ρ) in (3-50) are accompanied by the subscript '*eff* ' to signify that they are effective quantities. A SAW is a combination of decaying shear/transverse and compressional/longitudinal modes in an anisotropic piezoelectric medium, so η and ρ should be represented by tensors; for simplicity, the subscript '*eff* ' represent the effective values of the tensors. The acoustoelastic portion of (3-50) and the measured free-space propagation loss of a z-propagating SAW in YZ-$LiNbO_3$ and a x-propagating SAW in ST-quartz was used by Bajak et al [75] and King et al [76] to find the effective viscosity in each material to be roughly $3.78x10^{-4} Pa\cdot s$ for YZ-$LiNbO_3$ and $4.76x10^{-4} Pa\cdot s$ for ST-quartz at room temperature. This thermoelastic viscosity is responsible for the f^2 dependent term in the empirical, room-temperature, free-space propagation loss for YZ-$LiNbO_3$ and ST-Quartz that was published by Morgan [11]. The room-temperature propagation loss for YZ-$LiNbO_3$ was empirically found to be

$$\alpha_{LN}(f)=\left[0.545\frac{f}{GHz}+2.523\left(\frac{f}{GHz}\right)^2\right]\frac{dB}{cm} \tag{3-51}$$

and the room-temperature propagation loss for ST-X-Quartz was empirically found to be

$$\alpha_{QTZ}(f)=\left[1.488\frac{f}{GHz}+8.295\left(\frac{f}{GHz}\right)^2\right]\frac{dB}{cm} \tag{3-52}$$

The portion of the free-space propagation loss which follows an f^1 power dependency was experimentally and analytically determined by Slobodnik [77] to be the result of the SAW coupling to gas molecules and is given by

$$\alpha_{gas}(f)=\left[\frac{f\cdot P}{\rho_p {v_{saw}}^2}\left(\frac{\gamma\cdot M}{R\cdot T}\right)^{\frac{1}{2}}\right] \tag{3-53}$$

where P is the gas pressure, M is the molecular weight, R is the universal gas constant, T is the temperature, γ is gas ratio of specific heat at a constant pressure to the specific heat at a constant volume (i.e. the heat capacity ratio), and ρ_p and v_{saw} the substrate's mass density and SAW velocity, respectively. OFC-SAW RFID tags operate at 915MHz and from (3-51) and (3-52) gas loading accounts for around 20% of the total free-space losses at this frequency. The sensors are design to detect H_2 gas concentrations beneath the 4% LEL. The addition of 4% H_2 gas in ambient atmosphere at 1atm will not produce a measureable change in SAW propagation loss due to gas loading.

3.2.4.3 SAW Phase Velocity

3.2.4.3.1 Acoustoelectric Phase Velocity

The acoustoelectric portion of the SAW phase velocity is found by substituting (3-49) into (3-41) to yield

$$v_{AE} = v_{sc} \cdot \left(1 + \frac{K^2}{2} \frac{1}{\left(1 + \frac{1}{\left(R_s \cdot v_{sc} \cdot (\varepsilon_P + \varepsilon_0) \right)^2} \right)} \right) \tag{3-54}$$

This equation is similar to the solution presented by Datta [12] and Ballantine [13] given by

$$v_{AE} = v_{oc} \cdot \left(1 - \frac{K^2}{2} \frac{1}{\left(1 + \left(R_s \cdot v_{oc} \cdot (\varepsilon_P + \varepsilon_0) \right)^2 \right)} \right) \tag{3-55}$$

If the film's sheet resistance is high (i.e. $R_s \rightarrow \infty$), then (3-54) and (3-55) becomes the open circuit case velocity given by

$$v_{AE} = v_{OC} = v_{sc} \cdot \left(1 + \frac{K^2}{2}\right) \tag{3-56}$$

and if the film's sheet resistance is low (i.e. $R_s \rightarrow 0$), then (3-54) and (3-55) becomes the short circuit velocity, v_{sc}.

3.2.4.3.2 Fisher SAW Phase Velocity Approximation

The total SAW phase velocity is given by

$$v_{saw} = \sqrt{\frac{c_{eff}}{\rho_{eff}}} \tag{3-57}$$

The effective mass density, ρ_{eff} and effective stiffness, c_{eff} seen by the SAW is proportional to the ratio of thickness-wavelength product and may be represented by

$$\rho_{eff}(h, f) = \rho_F \left(D \frac{h \cdot f}{v_{AE}}\right) + \rho_P \left(1 - D \frac{h \cdot f}{v_{AE}}\right) \tag{3-58}$$

and

$$c_{eff}(h, f) = v_{RF}{}^2 \rho_F \left(D \frac{h \cdot f}{v_{AE}}\right) + v_{AE}{}^2 \rho_P \left(1 - D \frac{h \cdot f}{v_{AE}}\right) \tag{3-59}$$

where the subscripts '*F*' and *'P'* represents properties of the film and substrate, respectively; v_{RF} is the Raleigh SAW velocity of a bulk film, SAW acoustoelectric velocity v_{AE} is given by (3-54) and D is a piezoelectric material constant.

Equations (3-58) and (3-59) were derived based on the work of Hadjoub's [78], who showed that as the film get thicker than a wavelength the SAW becomes trapped in the film because by definition the SAW is confined within one wavelength of the surface. In a first order approximation, the effective density and stiffness, which is seen by the SAW, is a combination

the film and substrate properties within one wavelength of the film's surface; so as $h/\lambda \rightarrow 0$, $v_{saw} \rightarrow v_{AE}$ and as $h/\lambda \rightarrow 1$, $v_{saw} \rightarrow v_{RF}$. The fraction of the wave that is contained in the film is given by the left half of (3-58) i.e.

$$\text{Fraction of SAW in the Film} = \rho_F\left(D\frac{h\cdot f}{v_{AE}}\right) = \rho_F\left(D\frac{h}{\lambda}\right) \tag{3-60}$$

and the fraction of the wave that is contained in the piezoelectric substrate is given by the right half of (3-58) i.e.

$$\text{Fraction of SAW in the Piezoelectric Substrate} = \rho_P\left(1-D\frac{h\cdot f}{v_{AE}}\right) = \rho_P\left(1-D\frac{h}{\lambda}\right) \tag{3-61}$$

The effective stiffness, (3-59) comes from

$$c = v^2\rho \tag{3-62}$$

and the fraction of film stiffness is given by the left half of (3-59) i.e.

$$\text{Fraction of SAW stiffness in the film} = v_F{}^2\rho_F\left(D\frac{h\cdot f}{v_{AE}}\right) \tag{3-63}$$

and the stiffness in the piezoelectric substrate is given by the right half of (3-59) i.e.

$$\text{Fraction of SAW stiffness in the piezoelectric substrate} = v_{AE}{}^2\rho_P\left(1-D\frac{h\cdot f}{v_{AE}}\right) \tag{3-64}$$

The Rayleigh SAW velocity, V_{RF}, of an isotropic bulk material is calculated by find the roots of (3-65) [79]

$$\left(\frac{v_{RF}}{v_{shear}}\right)^6 - 8\left(\frac{v_{RF}}{v_{shear}}\right)^4 + 8\left(3-2\left(\frac{v_{shear}}{v_{long}}\right)^2\right)\left(\frac{v_{RF}}{v_{shear}}\right)^2 - 16\left(1-\left(\frac{v_{shear}}{v_{long}}\right)^2\right) = 0 \tag{3-65}$$

where v_{shear} and v_{long} is the shear and longitudinal velocities of the bulk material, respectively, and are given by [79]

$$v_{shear} = \sqrt{\frac{SM}{\rho_F}} \qquad \text{and} \qquad v_{long} = \sqrt{\frac{BM + \frac{SM}{3}}{\rho_F}} \tag{3-66}$$

where *SM* and *BM* is the bulk and shear moduli of the film material. This equation has a real root that is approximated by [79]

$$\frac{v_{RF}}{v_{shear}} = \frac{0.87 + 1.12 \cdot \nu}{1 + \nu} \tag{3-67}$$

where v is the Poisson's ratio given by

$$\nu = \frac{3BM - 2SM}{2(3BM - 2SM)} \tag{3-68}$$

The piezoelectric material constant *D* in (3-57) may be analytically calculated by equating (3-57) to Tiersten's perturbation approximation [13, 80] (3-70) and solving for *D*. For YZ-$LiNbO_3$ and ST-Quartz, *D* was experimentally found to be equal to π and 1.5, respectively, using measured data from CHAPTER 4 of this dissertation and the published experimental results of Penunuri [81].

3.2.4.3.3 Tiersten's Perturbation Theory

Tiersten's used perturbation theory [13, 80] to derive a dispersion relation for acoustically thin films given by

$$\frac{\Delta\alpha}{k_0} - i\frac{\Delta v}{v_0} = -i\omega h\left(c_{PE1}\left(\rho_F - \frac{SM}{v_0^{\ 2}} \right) + c_{PE2}\rho_F + c_{PE3}\left(\rho_F - \frac{4SM(3BM + SM)}{v_0^{\ 2}(3BM + 4SM)} \right) \right) \tag{3-69}$$

where $c_{PE1,2,3}$ is the SAW-film coupling parameter in the x, y, and z direction, respectively; v_0 is the unperturbed SAW velocity v_{AE} is given by (3-54). The SAW phase velocity is given by

$$v_{saw} = v_{AE}\left(1 + \mathrm{Im}\left\{\frac{\Delta\alpha}{k_0} - i\frac{\Delta v}{v_0}\right\}\right) = v_{AE}\left(1 + \frac{\Delta v}{v_{AE}}\right) \tag{3-70}$$

The acoustoelastic attenuation constant, α_{EL}, is non-zero if the bulk and/or shear moduli of the film is complex and is given by

$$\alpha_{EL} = \frac{\omega}{v_{AE}}\mathrm{Re}\left\{\frac{\Delta\alpha}{k_0} - i\frac{\Delta v}{v_0}\right\} \tag{3-71}$$

3.2.4.3.4 Morgan Empirical Relation for SAW Phase Velocity

Morgan [82] developed an empirical relation for SAW velocity beneath a high conductivity metal film. The empirical relation was amended to predict the velocity beneath a practically conducting film, and is given by

$$v_{saw} = v_{AE}\cdot\left(1 - C\frac{h\cdot f}{v_{OC}}\right) \tag{3-72}$$

where C is a constant determined by a combination of the film substrate parameters, and may be determined using a curve fit. The constant C may be analytically calculated by equating (3-72) to Tiersten's perturbation approximation [13, 80] (3-70) and solving for C which yields

$$C = \frac{v_{oc}}{f\cdot h}v_{AE}\left(1 + \frac{\Delta v}{v_{AE}}\right) \tag{3-73}$$

3.2.5 Separation of the Acoustoelectric and Acoustoelastic Effects

The attenuation constant (3-50) $\alpha(f)$ may be measured as a function of frequencies f_1 and f_2 (i.e. the amplitude dispersion), from which a system of equations are created and the acoustoelectric and acoustoelastic terms are solved using matrices.

$$\alpha(f) = -\left(\frac{2\pi \cdot f \cdot K^2}{2v_{sc}} \frac{R_s \cdot v_{sc} \cdot (\varepsilon_P + \varepsilon_0)}{\left(1 + \left(R_s \cdot v_{sc} \cdot (\varepsilon_P + \varepsilon_0)\right)^2\right)} + \frac{(2\pi \cdot f)^2 \eta_{eff}}{2v_{saw}{}^3 \rho_{eff}} \right) = -\left(A \cdot f + B \cdot f^2\right) \tag{3-74}$$

where the acoustoelectric coefficient is given by

$$A = \frac{2\pi \cdot K^2}{2v_{oc}} \frac{R_s \cdot v_{oc} \cdot (\varepsilon_P + \varepsilon_0)}{1 + \left[R_s \cdot v_{oc} \cdot (\varepsilon_P + \varepsilon_0)\right]^2} \tag{3-75}$$

and the acoustoelastic coefficient is given by

$$B = \frac{(2\pi)^2 \cdot \eta_{eff}}{2v_{saw}{}^3 \rho_{eff}} \tag{3-76}$$

$$\begin{bmatrix} \alpha(f_1) \\ \alpha(f_2) \end{bmatrix} = \begin{bmatrix} f_1 & f_1{}^2 \\ f_2 & f_2{}^2 \end{bmatrix} \cdot \begin{bmatrix} A \\ B \end{bmatrix} \quad \therefore \quad \begin{bmatrix} A \\ B \end{bmatrix} = \begin{bmatrix} f_1 & f_1{}^2 \\ f_2 & f_2{}^2 \end{bmatrix}^{-1} \cdot \begin{bmatrix} \alpha(f_1) \\ \alpha(f_2) \end{bmatrix} \tag{3-77}$$

Combine equations (3-77) with (3-75) and (3-76) yields

$$A = \frac{2\pi \cdot K^2}{2v_{oc}} \frac{R_s \cdot v_{oc} \cdot (\varepsilon_P + \varepsilon_0)}{1 + [R_s \cdot v_{oc} \cdot (\varepsilon_P + \varepsilon_0)]^2} = -\frac{\alpha(f_1) \cdot f_2}{f_1^{\ 2} - f_1 f_2} - \frac{\alpha(f_2) \cdot f_1}{f_2^{\ 2} - f_1 f_2} \tag{3-78}$$

$$B = \frac{(2\pi)^2 \cdot \eta_{eff}}{2 v_{saw}^{\ 3} \rho_{eff}} = \frac{\alpha(f_1)}{f_1^{\ 2} - f_1 f_2} - \frac{\alpha(f_2) \cdot f_1}{f_2 \cdot (f_2^{\ 2} - f_1 f_2)} \tag{3-79}$$

From (3-78) the film's sheet resistance, R_s, may be calculated using the quadratic equation, and is given by

$$R_S = \frac{1}{2}\left[-\frac{\pi \cdot K^2}{\mathrm{A} \cdot v_{oc}^{\ 2}(\varepsilon_P + \varepsilon_0)} \pm \left(\left(\frac{\pi \cdot K^2}{\mathrm{A} \cdot v_{oc}^{\ 2}(\varepsilon_P + \varepsilon_0)} \right)^2 - 4 \cdot \left(\frac{1}{(v_{oc}(\varepsilon_P + \varepsilon_0))^2} \right) \right)^{\frac{1}{2}} \right] = R_{S1} \ \& \ R_{S2} \tag{3-80}$$

There are two solutions for R_S; the correct value is determined by comparing the measured to predicted SAW velocities. The predicted velocity is obtained by plugging R_{S1} and R_{S2} and film thickness, h into Fisher's (3-57), Tiersten's (3-70) or Morgan's (3-72) SAW phase velocity approximation. The use of the Fisher's and Tiersten's equations require knowledge of the bulk and shear moduli of the bulk film, which is not always known. It those cases, it is easier to use Morgan's approximation because the material constant, C, can be determined using a simple curve fit. The correct R_s value is chosen by

$$R_S = \begin{cases} R_{S1} & \text{if } \mathrm{v}_{\text{saw_measured}} = v_{saw}(R_{S1}, f, h) \\ R_{S2} & \text{if } \mathrm{v}_{\text{saw_measured}} = v_{saw}(R_{S2}, f, h) \end{cases} \tag{3-81}$$

The solution to the acoustoelastic term (3-79), B, in combination the measured velocity and the effective mass density, ρ_{eff} ,(3-58), are used to calculate the effective phonon viscosity, η_{eff}, at the film substrate interface. The effective phonon viscosity, η_{eff}, may be compared to

Mason's [66] (3-21) and Rice's [69] (3-22) formulas for phonon viscosity in a solid media. This method may be used to study acoustic loss mechanisms for a variety of film substrate combinations.

This technique may be used for the separation of the air-loading and elastic losses in. equations (3-51) and (3-52). The air loading losses may be compared to (3-53) to solve for gas pressure and/or molecular weight.

3.3 CHAPTER 3 Summary

This chapter presented the theoretical analysis of the SAW-thin film interaction. This is necessary because the H_2 gas sensors that were constructed for this dissertation involves the growth of a thin-film in the SAW propagation path. Experimental verification of the previously derived equations are presented in CHAPTER 4. The most important equations from CHAPTER 3 are as follows:

1. The SAW acoustoelectric phase velocity is given by

$$v_{AE} = v_{sc} \cdot \left(1 + \frac{K^2}{2} \frac{1}{\left(1 + \frac{1}{\left(R_s \cdot v_{sc} \cdot (\varepsilon_P + \varepsilon_0) \right)^2} \right)} \right) \qquad (3\text{-}54)$$

R_s is the film's sheet resistance in $\Omega/\square$.

K^2, ε_p, v_{sc} is the electromechanical coupling coefficient, effective electrical permittivity and short-circuit velocity of the piezoelectric substrate, respectively (Table 3-1).

ε_0, is the electrical permittivity of free space.

2. The SAW attenuation constant is found given by

$$\alpha = -\left(\frac{2\pi \cdot f \cdot K^2}{2v_{sc}} \frac{R_s \cdot v_{sc} \cdot (\varepsilon_P + \varepsilon_0)}{\left(1 + \left(R_s \cdot v_{sc} \cdot (\varepsilon_P + \varepsilon_0)\right)^2\right)} + \frac{(2\pi \cdot f)^2 \eta_{eff}}{2v_{saw}{}^3 \rho_{eff}} \right) \quad (3\text{-}50)$$

If a material is acoustically lossy, a damping term, η, commonly known as viscosity, must be added to the stress equations.

3. Fisher Phase Velocity Approximation

$$v_{saw} = \sqrt{\frac{c_{eff}}{\rho_{eff}}} \quad (3\text{-}57)$$

$$\rho_{eff}(h,f) = \rho_F \left(D \frac{h \cdot f}{v_{AE}} \right) + \rho_P \left(1 - D \frac{h \cdot f}{v_{AE}} \right) \quad (3\text{-}58)$$

$$c_{eff}(h,f) = v_{RF}{}^2 \rho_F \left(D \frac{h \cdot f}{v_{AE}} \right) + v_{AE}{}^2 \rho_P \left(1 - D \frac{h \cdot f}{v_{AE}} \right) \quad (3\text{-}59)$$

where h is the film thickness, the subscripts 'F' and 'P' represents properties of the film and substrate, respectively; v_F is the SAW velocity of a bulk film, SAW acoustoelectric velocity v_{AE} is given by (3-54) and D is a piezoelectric material constant.

For YZ-$LiNbO_3$ and ST-Quartz, D was experimentally determined to be equal to π and 1.5, respectively.

4. Tiersten's used perturbation theory [13, 80] to derive a dispersion relation for acoustically thin films given by

$$\frac{\Delta\alpha}{k_0} - i\frac{\Delta v}{v_0} = -i\omega h \left(c_{PE1} \left(\rho_F - \frac{SM}{v_0{}^2} \right) + c_{PE2} \rho_F + c_{PE3} \left(\rho_F - \frac{4SM(3BM + SM)}{v_0{}^2 (3BM + 4SM)} \right) \right) \quad (3\text{-}69)$$

where $c_{PE1,2,3}$ is the SAW-film coupling parameter in the x, y, and z direction, respectively; v_0 is the unperturbed SAW velocity v_{AE} is given by (3-54). The acoustoelastic attenuation constant, α_{EL}, is non-zero if the bulk and/or shear moduli of the film is complex and is given by

$$\alpha_{EL} = \frac{\omega}{v_{AE}} \mathrm{Re}\left\{ \frac{\Delta\alpha}{k_0} - i\frac{\Delta v}{v_0} \right\} \tag{3-71}$$

and the SAW phase velocity is given by

$$v_{saw} = v_{AE}\left(1 + \mathrm{Im}\left\{ \frac{\Delta\alpha}{k_0} - i\frac{\Delta v}{v_0} \right\} \right) = v_{AE}\left(1 + \frac{\Delta v}{v_{AE}} \right) \tag{3-70}$$

5. Morgan [82] developed an empirical relation for SAW velocity beneath a thin film

$$v_{saw} = v_{AE} \cdot \left(1 - C\frac{h \cdot f}{v_{OC}} \right) \tag{3-72}$$

   where C is a constant determined by a combination of the film substrate parameters.

6. The acoustoelectric and acoustoelastic mechanisms may be separated by measuring the amplitude and velocity dispersion at frequencies f_1 and f_2 (i.e. the amplitude dispersion). The acoustoelectric term is given by

$$A = \frac{2\pi \cdot K^2}{2v_{oc}} \frac{R_s \cdot v_{oc} \cdot (\varepsilon_P + \varepsilon_0)}{1 + \left[R_s \cdot v_{oc} \cdot (\varepsilon_P + \varepsilon_0) \right]^2} = -\frac{\alpha(f_1) \cdot f_2}{f_1^{\,2} - f_1 f_2} - \frac{\alpha(f_2) \cdot f_1}{f_2^{\,2} - f_1 f_2} \tag{3-78}$$

   The acoustoelastic term is given by

$$B = \frac{(2\pi)^2 \cdot \eta_{eff}}{2v_{saw}^{\;3}\rho_{eff}} = \frac{\alpha(f_1)}{f_1^{\,2} - f_1 f_2} - \frac{\alpha(f_2) \cdot f_1}{f_2 \cdot \left(f_2^{\,2} - f_1 f_2 \right)} \tag{3-79}$$

   and the sheet resistance is given by

$$R_S = \frac{1}{2}\left[-\frac{\pi \cdot K^2}{A \cdot v_{oc}{}^2 (\varepsilon_P + \varepsilon_0)} \pm \left(\left(\frac{\pi \cdot K^2}{A \cdot v_{oc}{}^2 (\varepsilon_P + \varepsilon_0)} \right)^2 - 4 \cdot \left(\frac{1}{\left(v_{oc} (\varepsilon_P + \varepsilon_0)\right)^2} \right) \right)^{\frac{1}{2}} \right] = R_{S1} \ \& \ R_{S2} \quad (3\text{-}80)$$

There are two solutions for R_S; the correct value is determined by comparing the measured to predicted SAW velocities.

$$R_S = \begin{cases} R_{S1} & \text{if } v_{\text{saw_measured}} = v_{saw}(R_{S1}, f, h) \\ R_{S2} & \text{if } v_{\text{saw_measured}} = v_{saw}(R_{S2}, f, h) \end{cases} \quad (3\text{-}81)$$

The solution to the acoustoelastic term (3-79), B, in combination the measured velocity and the effective mass density, ρ_{eff} ,(3-58), are used to calculate the effective phonon viscosity, η_{eff}, at the film substrate interface.

Table 3-1 is a summary of properties of two commonly used SAW piezoelectric substrates.

	$LiNbO_3$	**ST-X- Quartz**
Crystalline Cut	Y	42.75^0 rotated Y
SAW Prop direction	Z	X
K^2 (%)	4.6	0.16
ε_P (pF/cm)	4.6	0.5
v_{oc} (m/s)	3488	3159
v_{sc} (m/s)	3408	3157
Mass Density (g/cm^3)	4.65	2.65
TCD ($ppm/^0C$)	-94	0
D	π	1.5
η_p (Pa-s)	$3.78\text{x}10^{-4}$	$4.76\text{x}10^{-4}$
c_{PE1} (10^{-7}·cm^2·s/g)	0	0.013
c_{PE2} (10^{-7}·cm^2·s/g)	1.195	1.421
c_{PE3} (10^{-7}·cm^2·s/g)	0.46	0.615

CHAPTER 4 MEASUREMENT OF THE SAW-THIN-FILM ACOUSTOELECTRIC AND ACOUTOELASTIC INTERACTION

4.1 Chapter Overview

This chapter presents experimental results that validate the SAW-thin film acoustoelectric and acoustoelastic equations, which were presented in CHAPTER 3. The equations of interest are the attenuation constant (3-50), and SAW phase velocity approximations of Fisher (3-57), Tiersten (3-70) and Morgan (3-72). The validation of these equations is necessary because they will be used for the design of integrated SAW H_2 gas sensors. The SAW propagation loss and velocity were measured over a wide frequency range in order to observe the amplitude and velocity dispersion characteristic. The acoustoelectric and acoustoelastic mechanisms were separated using the measured dispersion characteristics and the procedure in section 3.2.5. *Ex-situ* experiments were performed on semiconducting and high-conductivity films. *In-situ* experiments were performed during the growth of a Pd film to observe the thin-film acoustoelectric and acoustoelastic interactions real-time. Semiconducting films have sheet resistance values in the range where both the acoustoelectric and acoustoelastic effect may be observed; a plot of the acoustoelectric propagation loss and velocity on YZ-$LiNbO_3$ is shown in Figure 4-1. High-conductivity metal films were also evaluated using data gathered for this study and from similar experiments in the literature. The high-conductivity metal films short-circuits the acoustoelectric effect and allows the observation of acoustoelastic SAW dispersion.

In a series of *ex-situ* observations, three vapor-deposited semiconducting thin-films were analyzed: palladium (Pd) ultrathin-film (UTF), tin dioxide (SnO_2), and silicon monoxide (SiO).

Pd UTF and SnO_2 are typically utilized for H_2 gas detection and SiO is an easily evaporated insulator that is used as an encapsulation layer and may be electrically conductive due to poor stoichiometry after vapor deposition. High-conductivity films of Pd and aluminum (Al), chromium (Cr), and molybdenum (Mo) were used to measure the acoustoelastic dispersion. The measured data were compared to the attenuation constant and SAW phase velocity approximations by inserting known film properties (when available) into the equations, and mathematically extracting the unknown film properties by performing a fit to the measured data. The results of this research demonstrate a novel method to extract the electrical and mechanical properties of a semiconducting and high conductivity thin-film by measuring the amplitude and velocity dispersion of a surface acoustic wave (SAW) when said thin-film is placed in the SAW's propagation path.

In the series of *in-situ* experiments, a robust test fixture and measurement system were designed to perform the real-time observation of the thin-film acoustoelectric and acoustoelastic interactions. This system is useful for the design and characterization of SAW-based thin-film chemical and physical sensors (i.e., temperature, humidity, viscosity, voltage, current, hall effects, etc.). An *in-situ* test fixture was designed to be mechanically, thermally and electrically stable. Data have been taken for many SAW devices and the results show that the use of the *in-situ* procedure yielded: agreement between theoretical predictions and the measured data. The experimental results also include the observation and measurement of the SAW-thin-film interaction in real-time during the deposition (*in-situ*) of thin palladium (Pd) films. Section 4.2.2 presents the approach taken in configuring an electron beam evaporation system for ultra-thin-film characterization and the design of test fixtures, data acquisition configuration, and

experimental procedures to extract and analyze SAW parameters in real time, and to extract the thin-film properties under test.

Real-time, *in-situ* observation of the acoustoelectric effect has been reported by previous authors [13]. Because the time required for the sweep in their system would be in the order of one to several minutes, the authors recommend that measurement of the entire frequency response of the SAW device should be avoided. Consequently, they [13] used SAW delay line sensors in an oscillator configuration. This approach prevents the simultaneous measurement of multiple harmonics of the SAW device, which is useful when attempting to characterize the dispersion characteristics of thin films. Understanding the dispersion of thin films on SAWs is not only necessary to properly design SAW-based sensors, but it is a useful tool in evaluating the parameters of delicate ultra-thin films without the need for probe contact.

For this study, the acoustoelectric interaction was observed by measuring the film's thickness and sheet resistance, and the SAW's propagation loss and velocity simultaneously. The open to short-circuit transition of the acoustoelectric effect may be observed by depositing a thin-film in the SAW's propagation path and measuring the aforementioned parameters during the film's growth. In metal films, the conductivity transitions from zero to high conductivity (i.e., open to short-circuit) as the film is deposited and the thickness, *t*, increases. In this experiment, Pd films were deposited in the propagation path on a z-propagating SAW in YZ-$LiNbO_3$ while the propagation loss and velocity were measured at the SAW's 1st and 2nd harmonics (54.5 and 109MHz) simultaneously. A plot of the acoustoelectric losses at 54.4 and 109MHz is shown in Figure 4-1.

The experimental procedure is presented in Section 4.2. The results are presented and discussed in section 4.3. A summary of the major findings in this chapter is presented in section 4.4.

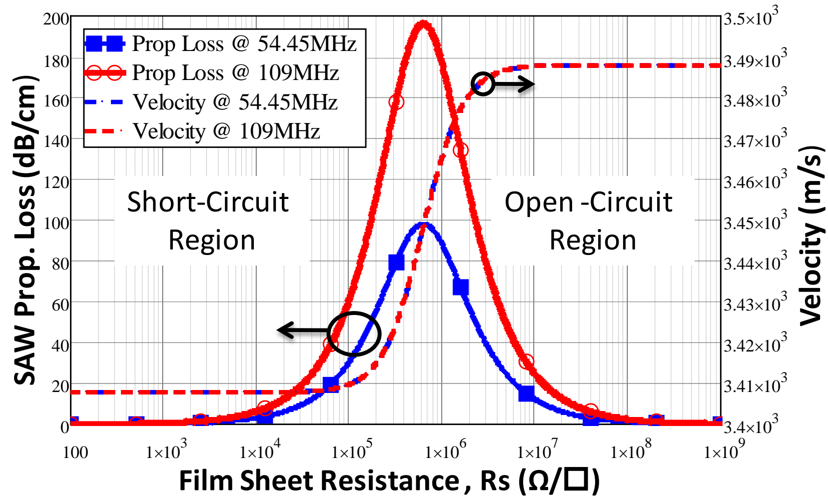

Figure 4-1. A plot of the predicted SAW propagation loss (solid lines) and velocity (dashed lines) as a function of the film's sheet resistance for a SAW on YZ-$LiNbO_3$. The acoustoelectric velocity (dashed lines) all fall on top of each other because it is not dispersive.

4.2 <u>Experimentation</u>

4.2.1 *Ex-Situ* Measurements

The thin-films were patterned using standard photolithographic techniques (Figure 2-4) and deposited using an electron beam evaporation system. A base pressure of around 10^{-6} Torr was achieved before evaporation and the substrate temperature was approximately 40^0C. A quartz crystal thickness monitor was used to record the inferred metal thickness and was located in close proximity to the samples. The thickness monitor was calibrated as carefully as possible

to attempt reproducibility and accuracy. The sheet resistance was measured on a film that was grown in parallel using a four point probe and/or a thin-film resistor structure for the Pd UFT films. The experimental details of the thin-film deposition and measurement are presented.

A vector network analyzer (VNA) was used to measure the amplitude and velocity dispersion characteristic of the films over a wide frequency span (62MHz to 1GHz). These measurements were performed using standard 2-port SAW delay lines (Figure 4-2) on a single wafer, from 14 different devices operating at fundamental and harmonic frequencies.

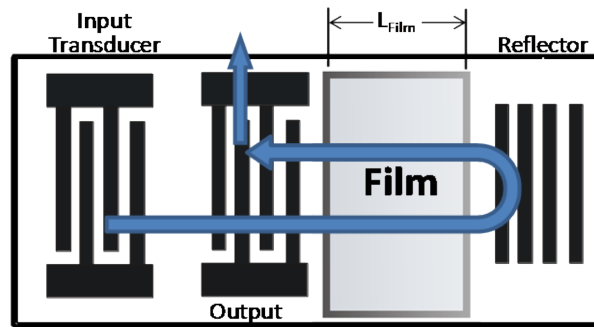

Figure 4-2. Shows a schematic of SAW device used for film dispersion measurements.

The SAW propagation loss was extracted by measuring the ratio of reflected wave amplitude with the film to the reflected wave amplitude without the film. The S_{21} scattering parameter of each device was measured and stored as a control prior to film growth. The films were patterned into the propagation path, and S_{21} was measured once more. The attenuation coefficient in decibels (*dB*) per unit length is given by

$$PL_{dB/L} = 20\log_{10}\left(\exp(\alpha \cdot L_{film})\right)$$
$$= \frac{20}{\ln(10)} \cdot \alpha \cdot L_{film} = 8.686 \cdot \alpha \cdot L_{film} \quad (4\text{-}1)$$

where PL_{dB} is the measured propagation loss in dB, L_{film} is the length of film in the propagation path, and the attenuation constant is given by

$$\alpha = \frac{PL_{dB}}{8.686 \cdot L_{film}} \quad (4\text{-}2)$$

The group delay, τ_g, was extracted by gating the time domain response S_{21} response and performing a fast Fourier transform (FFT) to obtain the frequency response. τ_g is the derivative of the phase with respect to frequency $(-d\theta/d\omega)$ from which, the velocity is extracted, because L_{film} is known. The velocity is a function of the measured group delay change, $\Delta\tau_g$, and is given by

$$v_{SAW_measured} = \left(\frac{1}{v_{oc}} - \frac{\Delta\tau_g}{L_{film}}\right)^{-1} \quad (4\text{-}3)$$

4.2.2 *In-Situ* Measurements

4.2.2.1 Test Fixture

An *in-situ* fixture was designed to mask the SAW device so that the film is only deposited in the desired area (Figure 4-3). The fixture was placed inside an electron-beam thin film deposition chamber, where RF cables were connected to the fixture to interrogate the SAW and measure film resistance (Figure 4-3). The RF cables were connected to the measurement

equipment via a high-vacuum feedthrough, which was constructed from an aluminum (Al) nut and bolt, semi-rigid coaxial transmission lines, and high-vacuum epoxy.

The test fixture was designed to be mechanically, thermally and electrically stable by using a (2cm x 7.5 cm x 4cm) brass base (Figure 4-4). Sub-miniature version A (SMA) connectors were used to connect the RF cables and the probes. The RF probes were designed for stable electrical and mechanical contacts, which eliminate the need for bond wires and packaging. The probes were constructed using small hinges (for vertical motion), PCB, copper prongs (for the probes), and solder (connects PCB and probes) (Figure 4-4). Threaded screws were used to apply a vertical force on the probes and hold the SAW device die in place to create stable electrical and mechanical contact to the SAW device.

A picture of the YZ-$LiNbO_3$ SAW die, which was used in these experiments, is shown attached to the base in Figure 4-4, a detailed schematic of the die is provided in Figure 4-5. The schematic of the die shows a one-port differential delay device with large Al probe pads to facilitate easy contact and low electrical contact-resistance. The thin-film in the SAW propagation path makes contact with a set of Al bus-bars, which are used to measure the film's sheet resistance. Similarly, two-port delay lines were also constructed. There are two RF probes on the fixture which allow simultaneous measurement of a one-port device and film resistivity, or a two-port device. A secondary fixture was created that allows simultaneous two-port and film resistivity measurement.

The shadow mask for the fixture is shown in Figure 4-6, and was also constructed from brass. For stability, the shadow mask was attached to the base with threaded screws. The length

of the film in the propagation path was controlled using the width of the via-hole that was controlled using a 56 thread-per-inch screw (i.e., 0.454mm lateral movement per revolution). An electrically-controlled shutter (constructed using a DC motor and Al sheet metal) was positioned on the shadow mask to expose or block the evaporating material from the device. This function is important as it allows precise stop and start times for the film deposition on the substrate, and the possibility of deposition automation through computer controls. The distance between the aperture and the substrate is approximately 5mm.

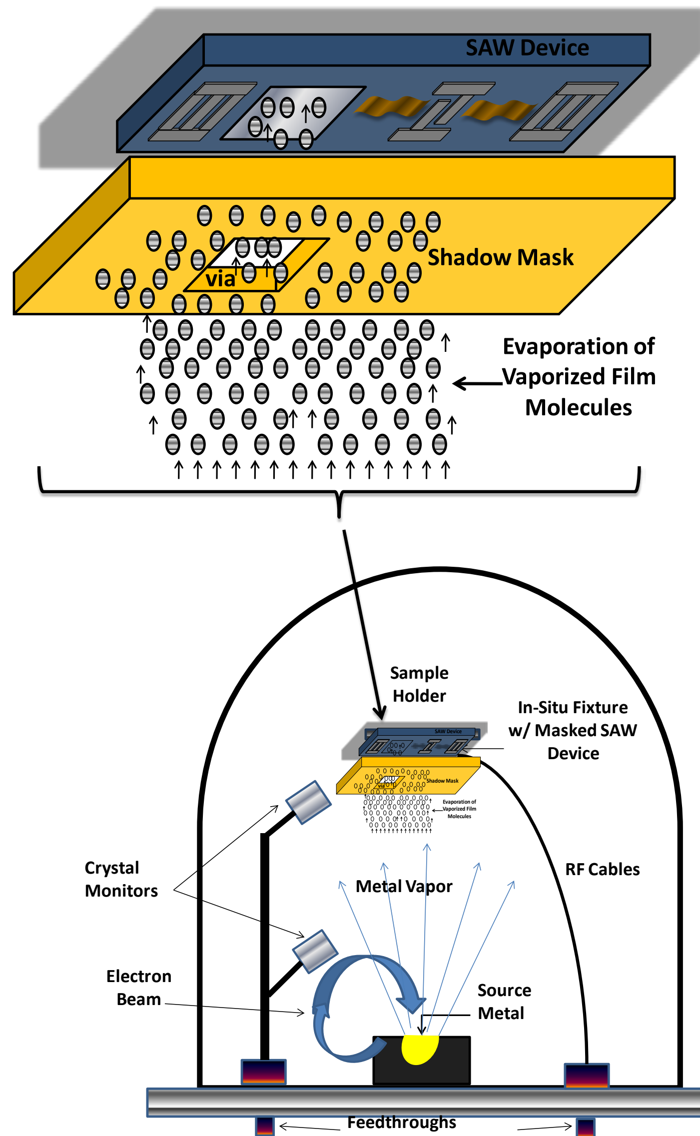

Figure 4-3. Shows a schematic of the shadow mask inside the e-beam film deposition system, with dual quartz crystal monitors, and high-vacuum RF feedthroughs. The shadow masking of a SAW device, allows deposition of the film precisely on the SAW propagation path.

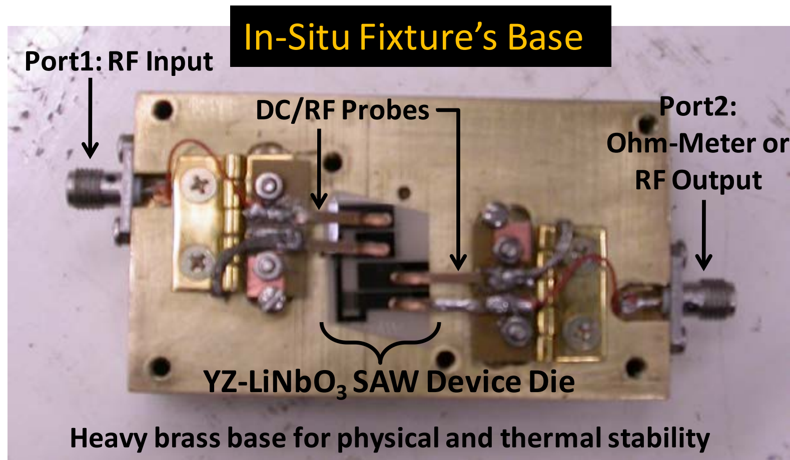

Figure 4-4 . Picture of the base of the test fixture. The fixture is designed to be mechanically, thermally and electrically stable by using a (2cm x 7.5 cm x 4cm) brass base. SMA connectors were used to make connection between the RF cables and the probes. The RF probes were designed and constructed for stable electrical and mechanical contacts, which eliminates the need for bond wires and packaging. The probes were constructed using small hinges (for vertical motion), PCB, copper prongs (for the probes), and solder (connects PCB and probes).

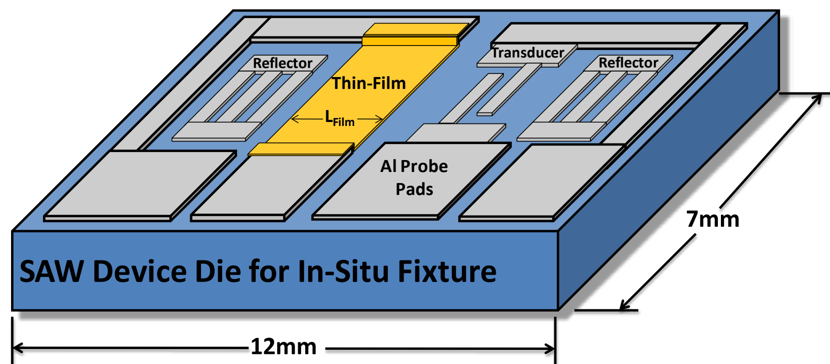

Figure 4-5. A schematic of the SAW die that was design for the *in-situ* fixture. It is a one-port differential delay device with large Al probes pads to facilitate easy contact and low electrical contact-resistance. The thin-film in the SAW propagation path makes contact with a set of Al bus-bars which are used to measure the film's sheet resistance.

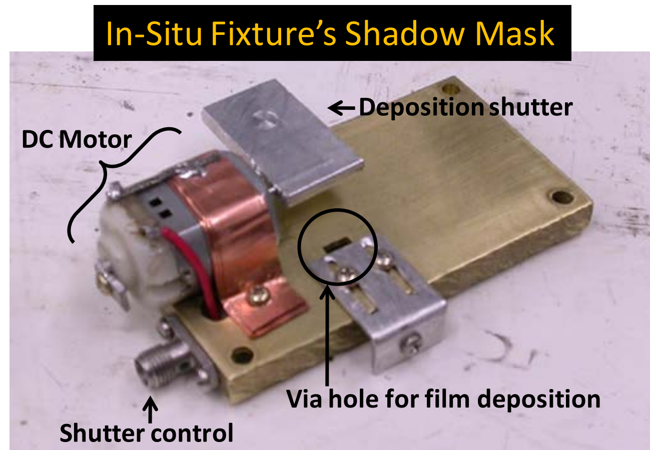

Figure 4-6. Picture of the shadow mask for the test fixture. The length of the film in the propagation path was controlled using the width of the via hole, which was controlled using a 56 thread-per-inch screw (i.e. 0.454mm lateral movement per revolution). An electrically controlled shutter (constructed using a DC motor) was positioned on the shadow mask to expose or block the evaporating material from the device.

4.2.2.2 Software Design

The equipment used to acquire data are as follows: a vector network analyzer (VNA) to measure S-parameters, a multi-meter (MM) to measure film resistance, a power supply (PS) that outputs constant voltages for I-V sweeps, and a quartz crystal monitor (QCM) to measure film thickness. The measurement equipment was controlled with a program created in Visual Basic and MATLAB. Microsoft's Visual Basic was used to control equipment and grab data because, Agilent, the manufacturer of the VNA, MM and PS supplied free sample code for each machine, which was combined and modified to make one central control program. Visual Basic is limited in its data analysis capability, so it was necessary to export the data to MATLAB, where they were analyzed in real-time. In the MATLAB toolbox, there is a program called "exlink", which allows MATLAB to be controlled via Visual Basic. This functionality was essential to achieve

the real-time analysis capability. The VNA, MM, PS and control computer are all positioned beside the e-beam chamber as shown in Figure 4-7.

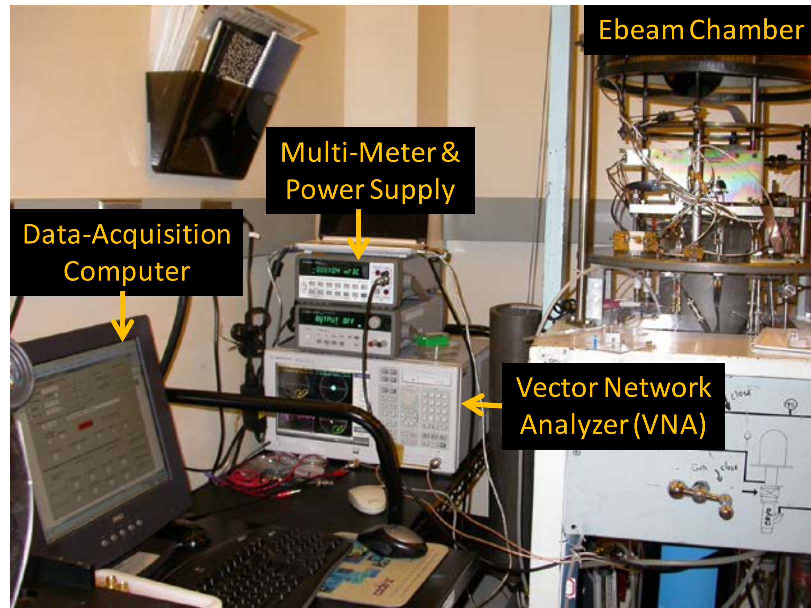

Figure 4-7. A picture of the e-beam system, text fixture and data acquisition set-up in class 100 cleanroom.

4.2.2.3 Experiment Considerations

The goal of this experiment is to measure SAW propagation loss and velocity; so it is important to maintain a signal-to-noise ratio (S/N) that is greater than *0dB*. The length of the film in the propagation path controls the maximum propagation loss of the SAW, so it is necessary to design for a film length that will not bury the SAW response in noise. From (3-50), the maximum acoustoelectric attenuation occurs when the film's sheet resistance is equal to the inverse of the product of the effective permittivity and open circuit velocity of the substrate, reducing (3-50) to

$$\alpha_{\max} = -\frac{\pi \cdot f \cdot k^2}{2v_{oc}} \quad (4\text{-}4)$$

The maximum attainable propagation loss in dB is given by

$$PL_{\max_dB} = 8.686 \cdot \alpha_{\max} \cdot L_{film} \quad (4\text{-}5)$$

where L_{film} is the length of the film in the propagation path. Figure 4-8 shows a plot of the maximum attainable propagation loss as a function of the length the film in the SAW propagation path at 50, 100, and 1000MHz. For the experiments performed in this section, L_{film} = 1mm.

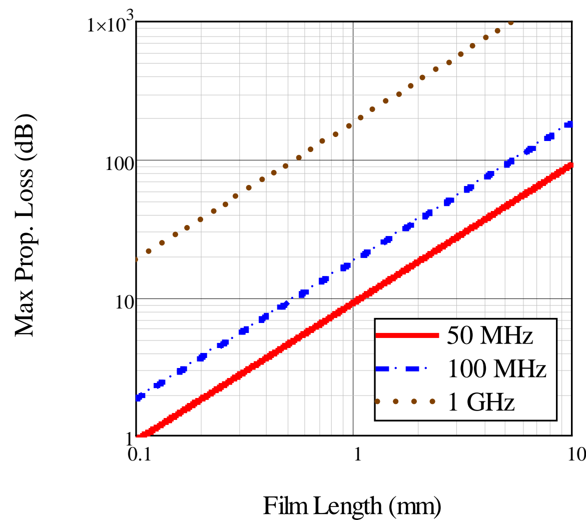

Figure 4-8. Plot of the maximum attainable AE propagation loss of a z-propagation SAW on YZ-$LiNbO_3$ as a function of the length of the film in the propagation path.

4.3 Results and Discussion

4.3.1 *Ex-Situ* Measurements

4.3.1.1 Semiconducting Films

The plot of the measured propagation loss and velocity versus frequency of a nominally 0.9 to 1.1Å thick discontinuous Pd film, a 520Å SnO_2 film and a 1000Å SiO film are shown in Figure 4-9, Figure 4-10 and Figure 4-11, respectively. For each film, the acoustoelectric and acoustoelastic coefficients, *A* & *B* respectively, and the sheet resistances R_{S1} and R_{S2}, were extracted using the raw data (signified by 'X's) and the procedure outlined in section 3.2.5. The acoustoelastic loss constant is $B{\cdot}f^{\,2}$ and the acoustoelectric loss constant is $A{\cdot}f$; the total propagation loss in dB per unit length is given by

$$PL_{dB/cm} = 8.686(A \cdot f + B \cdot f^2) \tag{4-6}$$

To yield the acoustoelectric losses, $8.686{\cdot}B{\cdot}f^{\,2}$ is subtracted from the total measured loss and $8.686{\cdot}A{\cdot}f$ is subtracted from the total measured losses to yield the acoustoelectric losses. Fisher's and Tiersten's (3-71) attenuation constant equations were fit to $8.686{\cdot}B{\cdot}f^{\,2}$ using iteratively determined values for η_{eff} in Fisher's equation and the complex portion of the shear modulus *SM''* in Tiersten's equation. Fisher's equation is a combination of the right (acoustoelastic) portion of (3-50) and the velocity approximation (3-57). All the traces for the acoustoelastic losses and fit fall directly on top of each other and are indistinguishable.

The extracted sheet resistances R_{S1} and R_{S2} were plugged into Fisher's (3-57), Tiersten's (3-70) and Morgan's (3-72) SAW phase approximations and compared to the measured SAW

velocity versus frequency data. Only the *R*s value that produced the correct velocity predictions are plotted the figures. The film bulk and shear moduli (*BM* and *SM,* respectively) for Pd and SnO_2 films that were used in Fisher and Tiersten's equations were found in literature. At the time of this dissertation, the *BM* and *SM* of SiO were not published in the available literature and were extracted using the following procedure:

1. Fit Morgan's approximation (3-72) to the measured data by calculating the film-substrate constant *C*.
2. Equate Fisher's (3-57) and Morgan's approximations and solve for the Raleigh velocity, V_{RF}.
3. Iteratively increment the *BM* and *SM* in equation (3-73) until it equals the empirically determined constant, *C* in step 1.
4. Convert the iteratively determined *BM* and *SM* to the longitudinal and shear velocities using (3-66).
5. Plug V_{shear} and V_{long} into (3-65) and solve for the Raleigh velocity, V_{RF}. If it is equal to velocity found in step *2* then the *BM* and *SM* values are correct; if not, repeats steps 3 to 5.

This procedure was tested with the Pd and SnO_2 data and the published *BM* and *SM* for the film were successfully extracted. A summary of all the films' values that were used is presented in Table 4-1.

Table 4-1. Summary of the material parameters that were extracted using the YZ-$LiNbO_3$ SAW device.

	Pd	SnO_2	SiO
Thickness (Å)	10	520	1000
A (s/m)	3.209 x 10^{-6}	1.322 x 10^{-6}	1.491 x 10^{-7}
B (s^2/m)	1.352 x 10^{-15}	*2.322* x 10^{-16}	*4.247* x 10^{-17}
C	3.12	1.47	0.04
R_{s1} (Ω/☐)	**7.998 x 10^6**	1.952 x 10^7	**1.732 x 10^8**
R_{s2}(Ω/☐)	4. 578 x 10^4	**1.99 x 10^4**	2.243 x 10^3
Measured Rs (Ω/☐) **(method)**	8.333x 10^6 *(Thin Film Resistor)*	3.2 x 10^4 *(4 point probe)*	Off scale *(4 point probe)*
η_{eff} (Pa-s)	1.2x10^{-2}	2x10^{-3}	3.6x10^{-4}
Bulk Modulus (GPa)	180	218	100
Shear Modulus (GPa)	44	35	27.7
Complex Shear Modulus (GPa)	180	0.3	0.035
V_R	1799	2127	3392

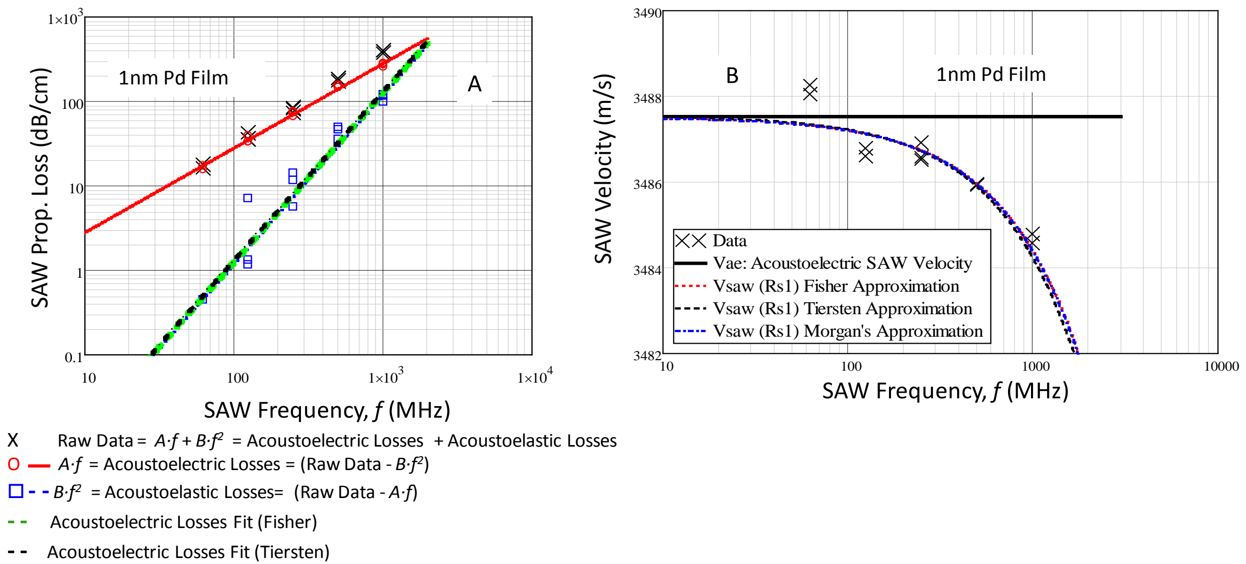

Figure 4-9 A: A plot of the measured SAW propagation loss coefficient for a 10Å Pd film as a function of frequency. The electrical losses (circles and solid red line) are observed once the mechanical losses are subtracted from the total loss and the elastic losses (squares and solid black line) are observed when the electric losses are subtracted. B: is the measured SAW velocity and the velocity prediction for a 10Å Pd film as a function of frequency.

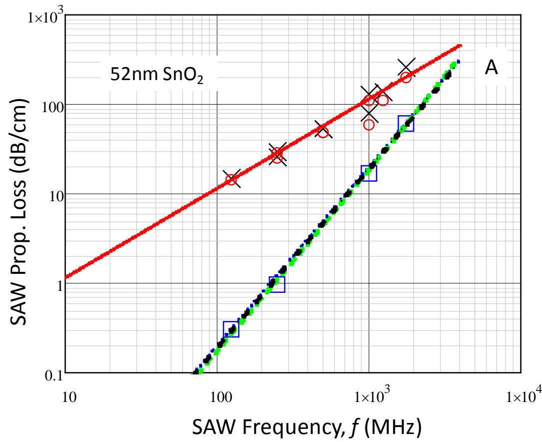

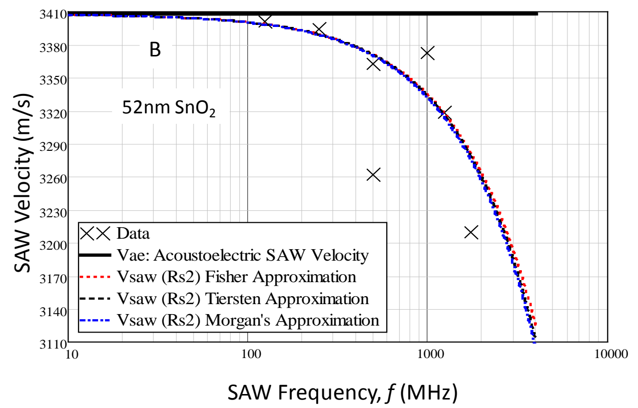

X Raw Data = $A{\cdot}f + B{\cdot}f^2$ = Acoustoelectric Losses + Acoustoelastic Losses

O —— $A{\cdot}f$ = Acoustoelectric Losses = (Raw Data - $B{\cdot}f^2$)

□ - - $B{\cdot}f^2$ = Acoustoelastic Losses= (Raw Data - $A{\cdot}f$)

- - Acoustoelectric Losses Fit (Fisher)

- - Acoustoelectric Losses Fit (Tiersten)

Figure 4-10 A: Plot of the measured SAW propagation loss coefficient for a 520Å SnO_2 film as a function of frequency. B: is a plot of the measured SAW velocity and the velocity prediction for a 520Å SnO_2 film as a function of frequency.

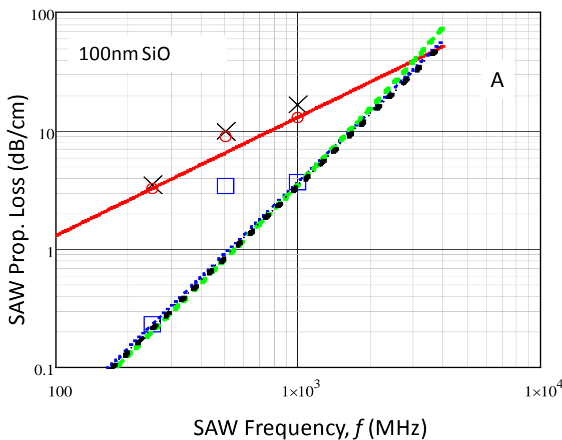

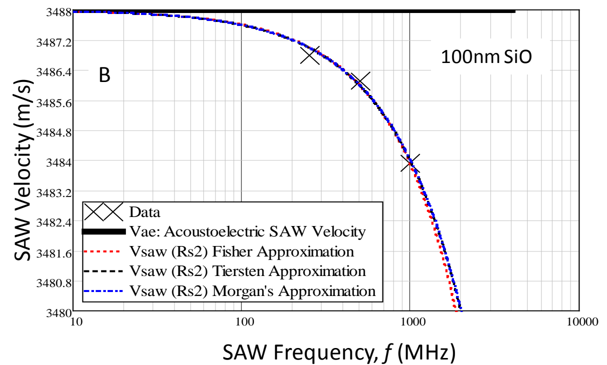

X Raw Data = $A{\cdot}f + B{\cdot}f^2$ = Acoustoelectric Losses + Acoustoelastic Losses

O —— $A{\cdot}f$ = Acoustoelectric Losses = (Raw Data - $B{\cdot}f^2$)

□ - - $B{\cdot}f^2$ = Acoustoelastic Losses= (Raw Data - $A{\cdot}f$)

- - Acoustoelectric Losses Fit (Fisher)

- - Acoustoelectric Losses Fit (Tiersten)

Figure 4-11 A: Plot of the measured SAW propagation loss coefficient for a 1000Å SiO film as a function of frequency. B: is a plot of the measured SAW velocity and the velocity prediction for a 1000Å SiO film as a function of frequency.

From Table 4-1, the R_S values which for the SAW showed good agreement with the values that were measured using the 4-point probe or thin-film resistor. The measured R_S for the Pd UTF using the thin-film resistor is about 4% greater than the R_S measurement using the SAW device. The difference is most likely due to contact resistance issues at the film electrode interface in the thin-film resistor structure that causes artificially high resistance measurements. A 4-point probe may be used to eliminate the contact resistance problem, but could not be used to measure this film due to its discontinuous nature. The R_S for the SnO_2 film were measured with a 4-point probe and were ~ 33% greater than the value extracted using the SAW device; this difference may be due film non-uniformity. The R_S of the SiO film were too high to be measured using the available 4-point probe; however, Anastasio's work [83] showed that the conductivity of vapor-deposited SiO films are dependent upon the growth procedure.

The acoustoelectric coefficient, B, quantifies the mechanical losses of the film and is highest for the Pd UTF, followed by SnO_2 and SiO. The extracted effective viscosities, η_{eff}, and complex shear modulus, SM'', follows the same trend. These numbers may indicate the nature of the material at the film-substrate interface. The Pd UTF is amorphous, discontinuous and has mobile islands because it is a noble metal and does not bond well to the substrate; it is expected to have higher mechanical losses due to these factors. The SiO and SnO_2 films are polycrystalline and are less lossy than the Pd. The difference in the losses between SnO_2 and SiO may be due a variety of factors that are beyond the scope of this dissertation, but are appealing areas of inquiry. The acoustoelastic losses are relatively insignificant at low frequencies (125MHz), but can become significant at high frequencies. Figure 4-10A shows a 520Å SnO_2 film has 15dB/cm of elastic losses at 1GHz, which accounts for 15% of the total

losses, and must be considered in the design of 915MHz H_2 gas sensors with a SnO_2 film as the active layer.

The extracted sheet resistances combined with the approximations of Fisher, Tiersten and Morgan provided acceptable fits for the measured SAW velocities. The velocity fit to the Pd UTF data were surprising because thin-films typically do not possess the same mechanical stiffness as the bulk material. The equations were also used to extract the bulk and shear moduli (*BM* and *SM*) of the 1000Å SiO film. The extraction procedure was used to verify the published *BM* and *SM* for Pd and SnO_2.

These findings suggest that the acoustoelectric and acoustoelastic equations that were developed in CHAPTER 3 are sufficient for the prediction of SAW propagation loss and velocity. SAW attenuation constant (3-50), and SAW phase velocity approximations of Fisher (3-57), Tiersten (3-70) or Morgan (3-72) will be utilized throughout the remainder of this dissertation; in the characterization of SAW-Pd UTF H_2 interaction and SnO_2 in CHAPTER 5 and CHAPTER 6 respectively, and the design of the OFC SAW H_2 gas sensors in CHAPTER 7.

4.3.1.2 High-Conductivity Metal Films

The acoustoelastic dispersion is observed when the acoustoelectric fields are eliminated by the shorting effect of a high-conductivity film. Films of 350Å and 625Å Pd and 500Å and 1000Å Al were patterned onto YZ-$LiNbO_3$ and the amplitude and velocity dispersion were measured. The amplitude dispersion data for various thickness of Al on YZ-$LiNbO_3$ were taken from publication of Davis' [84] experiments. Velocity dispersion data for Al, Cr, and Mo films

on ST-Quartz were taken from Penunuri's [81] publication. The amplitude dispersion of Pd and Al films on YZ-$LiNbO_3$ is shown in Figure 4-12 and Figure 4-13. Fisher and Tiersten's (3-71) attenuation constant equations were fit to the data using iteratively determined values for η_{eff} in Fisher's equation and the complex portion of the shear modulus, *SM''*, in Tiersten's equation. The velocity dispersion curves for the films on YZ-$LiNbO_3$ (Figure 4-14) and ST-quartz (Figure 4-15) are plotted as a function of the thickness-wave number product ($h \cdot k$). The *BM* and *SM* for all films were found in literature. A summary of the values is presented in Table 4-2; the summary of the properties of the piezoelectric substrate is presented in Table 3-1.

Table 4-2 Summary of the material parameters that were used to fit the amplitude and velocity dispersion curves for Pd and Al films on YZ-$LiNbO_3$ and ST-Quartz SAW device

Substrate	**YZ-$LiNbO_3$**	**YZ-$LiNbO_3$**	**YZ-$LiNbO_3$**	**YZ-$LiNbO_3$**	**YZ-$LiNbO_3$**	**YZ-$LiNbO_3$**	**ST-Quartz**	**ST-Quartz**
Film	Pd	Pd	Pd	Al	Al	Al	Cr	Mo
Thickness (Å)	10	350	625	500	1000	2000	----	----
η_{eff} (Pa-s)	1.2×10^{-2}	5×10^{-3}	2.2×10^{-3}	7.6×10^{-4}	9.3×10^{-4}	1.16×10^{-3}	-----	---
Bulk Modulus (GPa)	180	180	180	76	76	76	160	230
Shear Modulus (GPa)	44	44	44	26	26	26	115	126
Complex Shear Modulus (GPa)	180	1.2	0.28	0.18	0.18	0.18	----	----
V_R	1799	1799	1799	2907	2907	2907	3661	3239

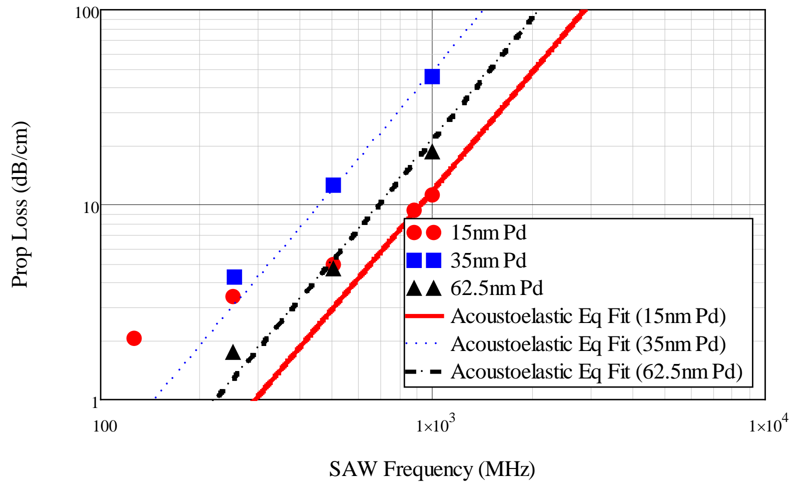

Figure 4-12 Plot of the amplitude dispersion of a 350 and 625Å Pd film. The equations are fit the Fisher's and Tiersten's equation by making assumptions for η_{eff} and the complex portion of the shear modulus SM''.

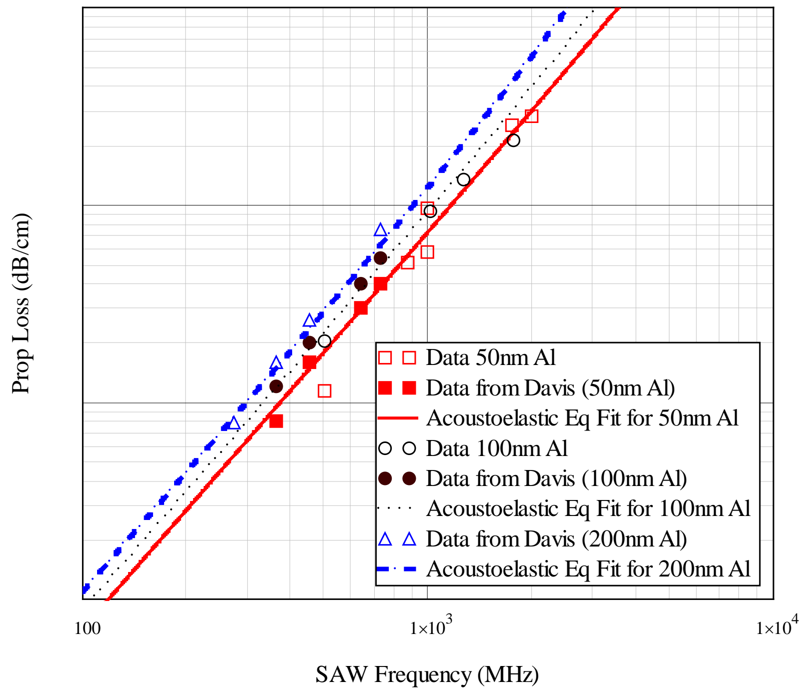

Figure 4-13 Plot of the amplitude dispersion of a 500, 1000 and 2000Å Al films, All data were gathered from Davis's publication[84]. The equations are fit the Fisher's and Tiersten's equation by making assumptions for η_{eff} and the complex portion of the shear modulus SM''.

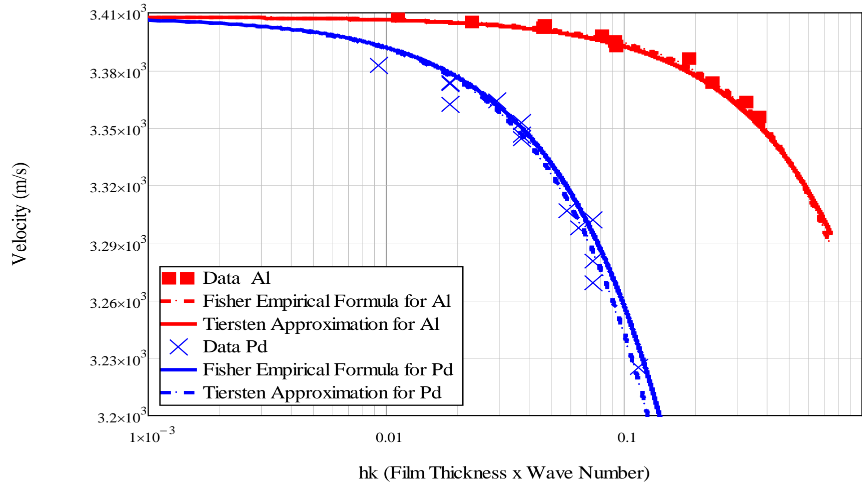

Figure 4-14. SAW velocity beneath metal films on YZ-LiNbO3. Comparison of Fisher's and Tiersten's approximations.

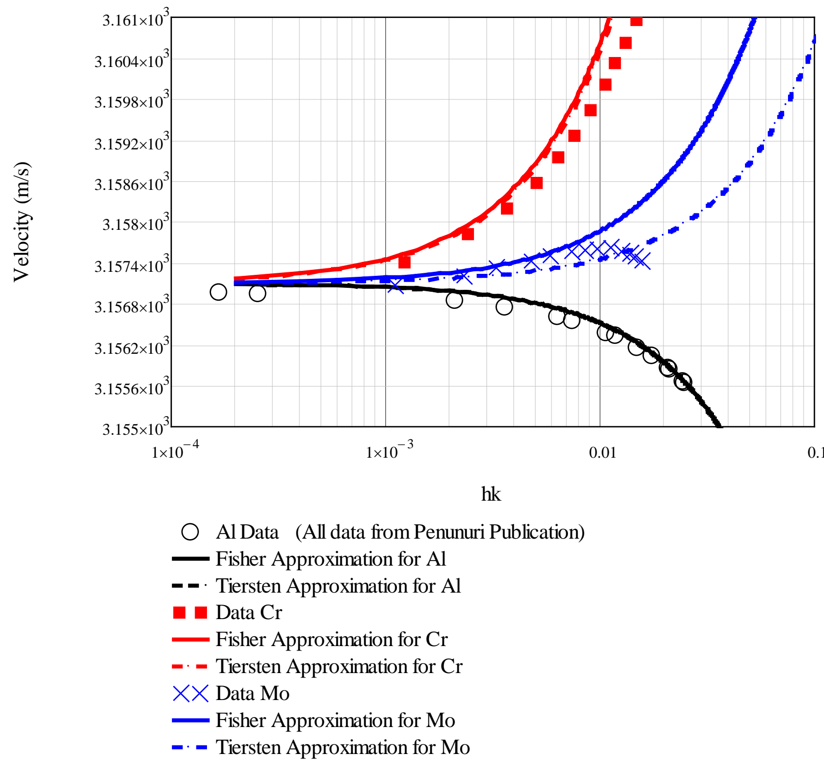

Figure 4-15. SAW velocity beneath metal films on ST-Quartz. Comparison of Fisher's and Tiersten's approximations. All data were gathered from Penunuri's publication [81].

The acoustoelastic predictions for high-conductivity films are the right half of equation (3-50) because the left portion of the equation goes to zero when the film's conductivity is high. Figure 4-12 and Figure 4-13 suggest that the acoustoelastic losses beneath high-conductivity metal films increase in direct proportion to the film's thickness and are reflected in the extracted effective viscosity and complex shear modulus. This behavior is a clear effect in the Al data (Figure 4-13) and but unclear in the Pd data (Figure 4-12) where the losses are higher for the 350Å film than the 625Å. The 150Å film shows higher losses than both the 35 and 625Å films at low frequencies and lower losses at high frequencies. This is most like due to two issues: (1) experimental error is high at low frequencies because the propagation loss is small, and (2) Pd films have poor adhesion to the substrate as compared to Al. Poor adhesion is known to cause artificially high SAW propagation loss beneath thin-films. The thickness dependence of the effective viscosity and complex shear modulus may reveal information about the structure of the films; but a study of this nature is outside the scope of this dissertation.

Fisher and Tiersten's SAW phase velocity approximations provided good fits for the measured velocity dispersion for Al and Pd films on YZ-$LiNbO_3$ (Figure 4-14) and Al, Cr and Mo films on ST-Quartz (Figure 4-15). Fisher's approximation provides a better fit for the measured data for Mo on quartz than Tiersten's approximation. Both approximations differ from the measured data for Cr. Fisher's and Tiersten's approximations were derived based on the assumption that the films were isotropic in nature, they do not account for second order effects, which may be occurring in the Mo films.

4.3.2 *In-Situ* Observation of Acoustoelectric and Acoustoelastic Mechanisms

The VNA was used to sweep a wide frequency range and capture data at multiple SAW harmonic operation points (54.4 and 109MHz). A screen shot of the data output from the MATLAB software is shown in Figure 4-16. The upper left plot is the time domain response of the SAW, which is transformed to the frequency domain in the upper right plot. This plot is then truncated to the 1dB bandwidth of the SAW response (middle left) from which the SAW propagation loss (middle right), center frequency (lower left) and group delay change (lower right) are extracted. The data were sampled at a rate of 3sec/sample, and at a growth rate of 0.1Å/sec, resulting in a sample every 0.3Å. A post processed plot of the SAW propagation loss and velocity as a function of Pd film thickness at 54.5 and 109MHz is given in Figure 4-17.

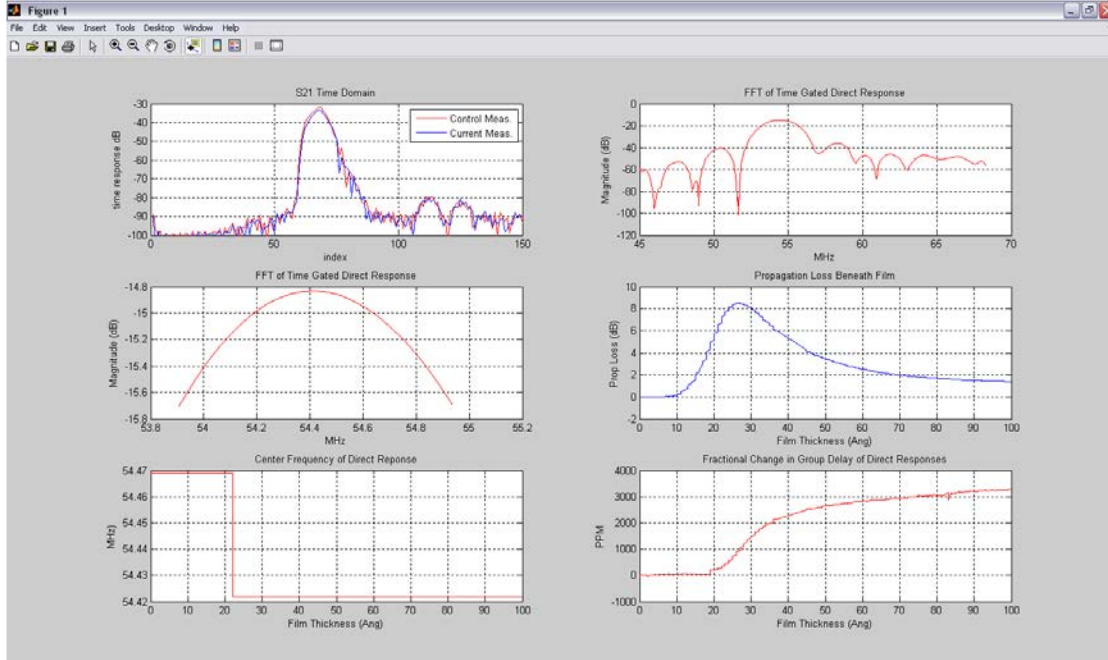

Figure 4-16. The real-time output of data acquisition software; measured S-parameters which are processed to extract propagation loss and delay shift during growth of a Pd film in the SAW propagation path. The plots are updated in real time as film thickness changes.

The velocity is a function of the measured group delay change, $\Delta\tau_g$, and is given by (4-3). The propagation loss in dB/cm is the measured absolute propagation loss (in dB) divided by L_{film} (in cm), which is ideally equal to the width of the film-deposition aperture referred in Figure 4-6. Ideally, the film's thickness profile should be uniform; otherwise experimental error is introduced in the inferred propagation loss and velocity. The non-uniform distribution of the film is difficult to correct because the thickness-dependent sheet resistance, $R_S(t)$, varies as a function of film thickness (section 5.3), and the film's thickness varies across the film. Accordingly, the acoustoelectric interaction causes the SAW propagation loss and velocity to vary across the film.

The minimization of the error requires the measurement of the film's thickness distribution. A light meter was used to infer the film's thickness distribution by measuring the fraction of light absorbed by the film as a function of its position on the film. Ultra-thin metal films are optically semi-transparent and as the film's thickness increases, a greater percentage of light is reflected or absorbed. For the film deposited in Figure 4-17, the thickness-profile was found to follow a Gaussian distribution (Figure 4-18) and is given by

$$h(t,x) = t\left(1.128\exp\left(-4\left(\frac{x}{mm}\right)^2\right) - 0.128\right) \tag{4-7}$$

where x is the position (in mm) along the film, t is the thickness at the center of the film and is assumed to be equal to the thickness measured with the crystal monitors. Though unintended, films with a non-uniform profiles are better gas detectors than uniform films because of increase surface area and bonding sites for the analyte.

Because the film's profile is Gaussian, the fraction of light transmitted at the film's center is less than at its edges. An analytic form of $R_S(t)$ for Pd films was developed by dividing Malocha's empirical resistivity equation (5-5) by the film thickness, t

$$R_S(t) = \frac{\rho_\infty}{t}\left(\left(1 + \frac{3\lambda_\infty}{8t}\right) + \left(1 + e^{-m(t-t_c)}\right)\right) \tag{4-8}$$

where t is the film thickness, ρ_∞ is the resistivity, λ_∞ is the electron mean free path of the bulk metal, m is the slope and exponential change in $R_S(t)$ when the film is discontinuous, and t_c is the critical thickness when the film becomes continuous; m and t_c are determined by a curve fit. As films are deposited, they are initially discontinuous and electrical conduction is achieved via quantum mechanical tunneling. As more material is deposited, the islands get larger and closer together, which decreases the activation energy and causes an exponential change in the sheet resistance; this is modeled by the Arrhenius term in (4-8). Once enough material is deposited, the islands connect and the change in resistance as a function of thickness becomes small; this is modeled using the Fuchs-Sondheimer approximation. An ultrathin-film with a Gaussian thickness profile may have a greater degree of discontinuity (i.e., smaller islands and further apart) at the film's edges than at the center, or transition from discontinuous at the edges to continuity at the center.

In the following analysis, the film's Gaussian profile was assumed constant throughout the film's growth. The measured propagation loss in dB and $\Delta\tau_g$ are given by

$$PL(f,t) = -8.686 \int_{L_{film}} \left[\alpha\left(f, \left[R_S\left(h(t,x)\right)\right]^{-1}\right)\right] \cdot dx \tag{4-9}$$

$$\Delta\tau_g(f,t) = \int_{L_{film}} \left[\left(\frac{1}{v_p\left(f,\left[R_S(h(t,x))\right]^{-1}\right)} - \frac{1}{v_{oc}} \right) \right] \cdot dx \tag{4-10}$$

where α and v_p are given by acoustoelectric portion of equations (3-50) and (3-72), respectively. A plot of the measured and modeled SAW propagation loss and $\Delta\tau_g$, as a function of Pd film thickness at 54.5 and 109MHz is provided in Figure 4-17. The values that were used to fit (4-9) and (4-10) to the measured data are: $\rho_\infty = 10^{-5}\Omega$-cm, $\lambda_\infty = 400$Å, $m = (7\text{ Ang})^{-1}$ and $t_c = 100$Å.

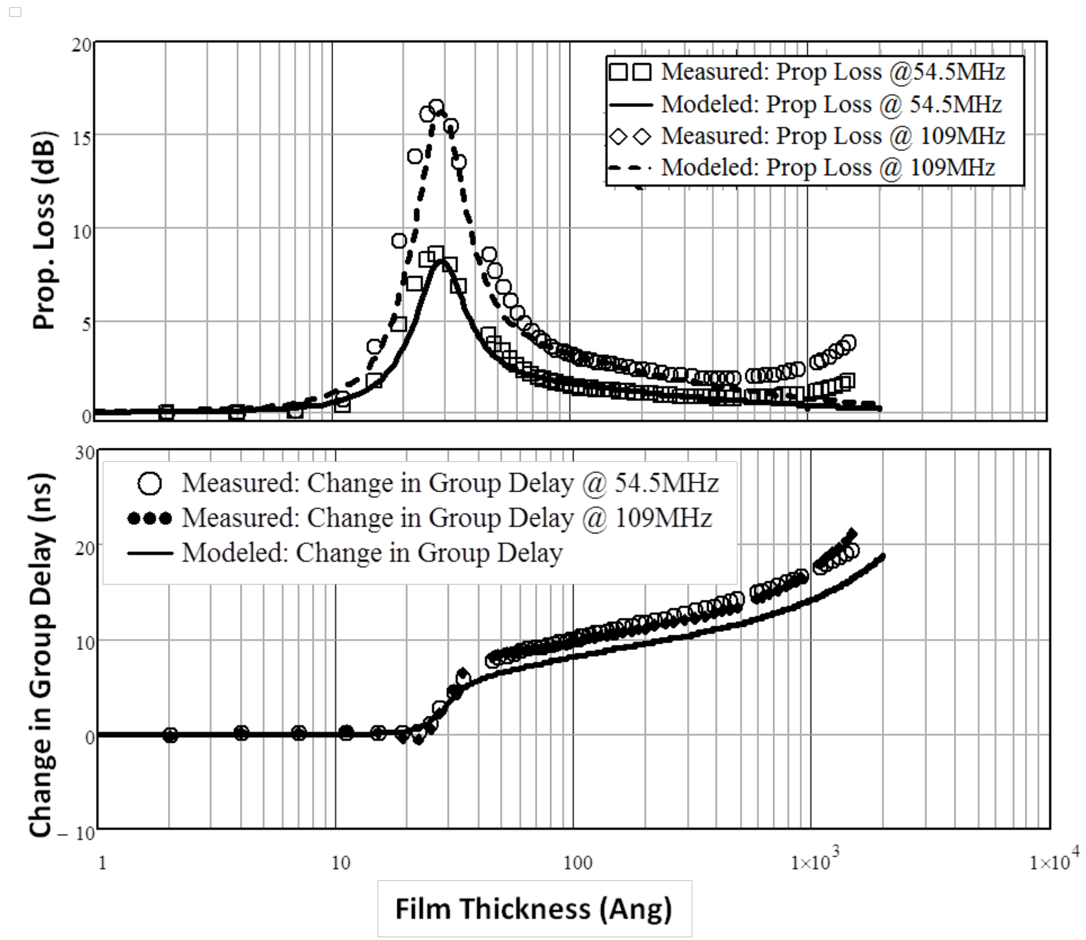

Figure 4-17 A plot of the measured and modeled SAW propagation loss (solid lines) and change in group delay (dashed lines) at 54.5 and 109MHz as a function of the Pd film thickness. Pd film's conductivity changes due to the film's thickness, and the SAW propagation loss and velocity are modulated via the acoustoelectric effect.

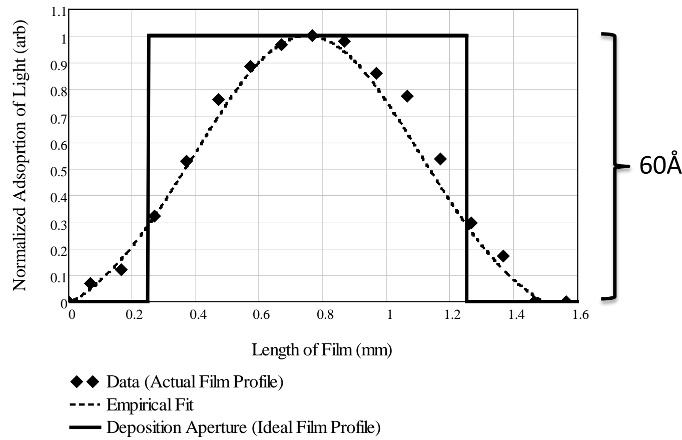

Figure 4-18. The thickness distribution of a 60Å Pd film deposited through a 1mm aperture. The thickness distribution was extracted from light absorption measurements across the film.

The comparison between the measured data with the data fit (Figure 4-17) suggests that the SAW attenuation constant (3-50) and SAW phase velocity approximations of Fisher (3-57), Tiersten (3-70) or Morgan (3-72) are suitable methods to model SAW dispersion across films with non-uniform profiles. This capability is important because issues associated with discontinuous non-uniform films and *in-situ* measurement of the SAW acoustoelectric effect has not been previously addressed in literature. Films with these morphologies are preferred for gas sensing applications because they have a greater surface area, which makes them more sensitive to analytes [49, 50].

There is a small difference between the measured data and data fit when the film thickness is greater than 500Å. This difference is due to the dominant acoustoelastic losses, which are not accounted for by this simple model. The incorporation of the viscous effects requires the development of the thickness dependent viscosity model for the thin films and is

outside the scope of this research; however, it will be expanded in future research. There may also be other unaccounted second order effects such as spurious generated modes, which interfere constructively and de-constructively with the SAW amplitude and velocity at the 1st and 2nd harmonics.

4.4 CHAPTER 4 Summary

1. This chapter presented experimental results that validated the SAW-thin-film acoustoelectric and acoustoelastic equations that were presented in CHAPTER 3.
2. The equations of interest are the attenuation constant (3-50), and SAW phase velocity approximations of Fisher (3-57), Tiersten (3-70) and Morgan (3-72).
3. The validation of these equations are necessary because they will be used to design integrated SAW H_2 gas sensors.
4. The SAW propagation loss and velocity were measured over a wide frequency range to observe the amplitude and velocity dispersion characteristic.
5. The acoustoelectric and acoustoelastic mechanisms were separated using the measured dispersion characteristics and the procedure in section 3.2.5. Both semiconducting and high-conductivity films were analyzed in this study.
6. Three vapor-deposited semiconducting thin-films were analyzed: palladium (Pd) ultrathin-film (UTF), tin dioxide (SnO_2), and silicon monoxide (SiO).
7. The measured data were compared to the attenuation constant and SAW phase velocity approximations by inserting known film properties (when available) into the equations,

and mathematically extracting the unknown film properties by performing a fit to the measured data.

8. From Table 4-1 the R_S values for the SAW showed good agreement with the values that were measured using the 4-point probe or a thin film resistor extracted.
9. The extracted sheet resistances and the approximations of Fisher, Tiersten and Morgan provided very good fits for the measured SAW velocities.
10. Fisher and Tiersten's SAW phase velocity approximations provided good fits for the measured velocity dispersion for Al and Pd films on YZ-$LiNbO_3$ and Al, Cr and Mo films on ST-Quartz.
11. The design of a test fixture and data acquisition software for the real-time measurement and analysis of the SAW-thin-film acoustoelectric interaction was demonstrated. The fixture allows for simultaneous measurement of SAW propagation loss, velocity, and film sheet resistance. The results presented suggest that the software, fixturing and *in-situ* measurements are a suitable tool for SAW sensor thin film research.
12. The results of this portion of the research demonstrates a novel method to extract the electrical and mechanical properties of a semiconducting and high conductivity thin film by measuring the amplitude and velocity dispersion of a SAW when said thin-film is placed in the SAW's propagation path.
13. The equations are suitable for the design and characterization of the integrated OFC-SAW H_2 gas sensors.

CHAPTER 5 PALLADIUM (PD) ULTRA-THIN FILM CHARATERIZATION

5.1 Chapter Overview

This chapter discusses the efforts to characterize Pd UTFs for the purpose of SAW H_2 gas sensing. The Pd-H_2 reaction is discussed in section 5.2. It is difficult to reproducibly create ultra-thin films of Pd, so a procedure was developed to increase precision (section 5.3). An empirical model for the SAW resistivity as a function of thickness was developed for the SAW predictions. Resistors were used to evaluate the sheet resistance and sensitivity (section 5.4) of the films prior to depositing them on a SAW device to observe the SAW-film-H_2 gas interaction (section 5.6). The film was exposed to 2% H_2 gas (98%N_2) and the response was observed in real-time. The film sensitivity to high electric fields and temperature were also evaluated. The film's aging behavior in atmosphere is discussed in section 5.5.

5.2 The Palladium-Hydrogen Interaction

5.2.1 Previous Work

Thin films fall into three categories: ultra-thin, thin and thick films. These regimes are primarily distinguished by the film's electrical conduction mechanisms. Some ultra-thin films are composed of a discontinuous network of atomic clusters, in which the primary method of electrical conduction is thermally activated quantum tunneling across the discontinuities. Thin and thick films however, depend on electron scattering as the primary means of electrical conduction. The two regimes are classified by the ratio of film thickness to the mean free

electron path; for thin films this ratio is less than 10%; conversely for thick film this ratio is greater than 10% [85]. Pd films 500Å and greater have been reported to behave like bulk materials [86]. In terms of the palladium-hydrogen (Pd-H) interaction thin and thick films behave equivalently, ultra-thin films however, behave differently.

5.2.2 Pd Thin/Thick Film Background Review

A wealth of studies has been performed on the Pd-H interaction as a function of temperature, H_2 gas concentration and pressure [86, 87]. This strong temperature and pressure dependence prompted scientist to analyze the interaction as function of the interaction enthalpies which is a weak function of temperature [88]. For this discussion the analysis of the Pd-H interaction is most intuitively understood in terms of H concentration and pressure. It is necessary to bound the discussion to room temperature and low hydrogen concentrations (below the lower explosive limit of approximately 4%) because after all, this is the intended area of operation.

The absorption of hydrogen by Pd was first observed in 1868 by Thomas Grahab [89]. Since then, Pd has been widely used for hydrogen purification and sensing because it has the highest hydrogen solubility of any element at atmospheric pressure. H_2 dissociates on Pd surfaces; additional H atoms diffuse into Pd to form palladium hydride (PdH_x) [88]. This causes an increase in the mass and electrical resistivity of the Pd. The increase in mass and resistivity continues until chemical equilibrium between the gas phase, adsorbed and absorbed hydrogen is reached. The magnitude of the change varies with H concentration. The process may or may not be reversible at room temperature depending on the type of chemical bond that is formed [49].

For Pd films (200Å to 50μm), a 10% increase in Pd resistivity is reported for exposure to 4% hydrogen gas concentrations[90, 91]. The reaction times of these sensors are dependent on H_2 gas concentration and flow rate and film thickness [55]. Typical reported times at range from five minutes to hours in some cases.

5.2.3 Pd Ultra-Thin Film Background Review

The focus of this Pd thin film research was to characterize films in the ultra-thin to thin-film range, from approximately 1-100Å in thickness. Almost all previous publications on Pd hydrogen sensors have had films in the 200-10,000Å thickness range [54-60, 89, 91-95]. Films in the ultra-thin regime behave much differently than thicker films due to film morphology, different physical conduction mechanisms, and different gas interactions.

Under appropriate growth conditions ultra-thin films may have a nano-clustered morphology [96, 97] (Figure 5-1). Electrical conduction is achieved via thermally activated quantum tunneling between the nano-clusters [98]. When exposed to hydrogen gas the Pd clusters "swell" due to hydrogen induced lattice expansion (HILE), consequently creating a greater number of conductive pathways and decreasing the tunneling gap, and causing a dramatic decrease in electrical resistivity [50, 99, 100]. This behavior typically occurs in the high resistivity range where the acoustoelectric effect is most dominant.

Electrical conduction between islands is the primary achieved by quantum mechanical tunneling through the substrate [101] because the film is discontinuous. The electrical conductivity is given by the Arrhenius equation (5-1) as

$$\sigma(\delta E) = \sigma_0 e^{\frac{-\delta E}{k_b T}} \tag{5-1}$$

where σ_o the intrinsic conductivity determined by the material and film geometry, T is the absolute temperature in Kelvin, k_b is Boltzmann's constant and δE is the activation energy required to transport an electron from one island to another and is given by the Neugebuer et al [98] equation (5-2)

$$\delta E = \frac{q^2}{4\pi\varepsilon_r\varepsilon_0}\left(\frac{1}{r} - \frac{1}{r+s}\right) \tag{5-2}$$

where q is the electron charge, ε_r is the relative permittivity of the substrate, ε_o the permittivity of free space, r is the radius of the nano-clusters and s the space between the nanoclusters. When exposed to H_2 gas Pd clusters expand causing an increase in the Pd nanocluster's radius, r, and a decrease in the separation, s, between the clusters. This results in a very fast and exponential decrease in the film's resistivity consequently making the film an excellent sensor for H_2 gas.

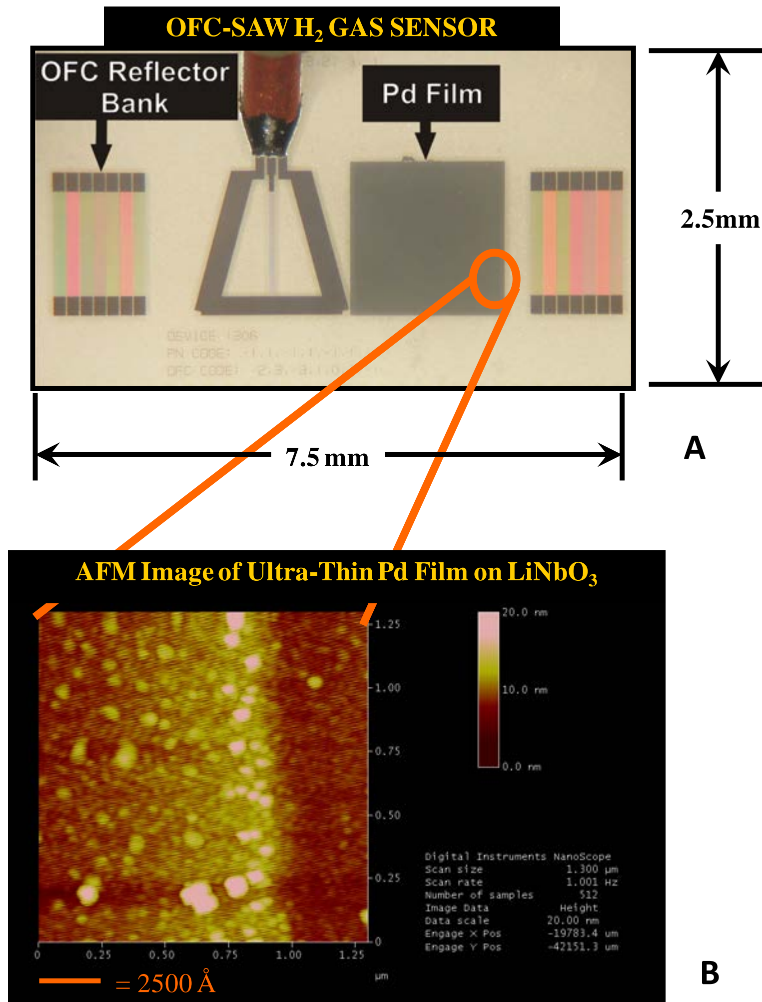

Figure 5-1. A: Orthogonal Frequency Coded (OFC) SAW RFID tag-sensor with Pd film in the delay path for H_2 gas sensing capability. B: Atomic force microscopy (AFM) image of the border between the Pd ultra-thin film and the YZ lithium niobate (YZ-$LiNbO_3$) substrate. The AFM image shows that the film is constructed of a discontinuous network of atomic islands—nanoclusters.

5.3 Precise Growth of Ultra-Thin Pd Films

It is necessary to understand the conductivity of Pd films as a function of thickness in order to design SAW-based hydrogen gas sensor. A Pd thin film conductivity model was developed based on the Fuchs-Sondheimer approximation. The necessary Pd-thickness curves were generated by depositing Pd films of various thicknesses on 3 inch quartz wafers in addition

to implementing an *in-situ* resistance measurement scheme. The *in-situ* process monitors the films resistance at various thicknesses via a resistor structure during film growth. From the *in-situ* resistor data, the film's conductivity is extracted. The films were grown on 3 inch quartz wafers and measured via four point probe and profilometer. The data was combined to calculate the film's conductivity.

5.3.1 Analysis of the *In-Situ* Die

There are four *in-situ* resistor designs that were used in experimentation, three of them were inter-digitated resistor (IDR) designs and the fourth was two large electrodes separated by a distance (parallel electrode resistor, PER). The IDR designs are as follows:

- Number of Fingers per bus bar: 10, 20 or 40
- Finger width: 8µm
- Aperture: 1.44mm
- a/p ratio: 50%
- Bus bar dimensions: 5mm x 5mm x 0.18µm
- Substrate: 3" ST Quartz wafers
- Electrode Material: Gold

The fourth *in-situ* resistor design (parallel electrode resistor, PER) specifications are as follows:

- Bus bar dimensions: 5mm x 5mm x 0.18µm
- Electrode Material: Gold
- Separation between electrodes: 0.3mm
- Substrate: 3" ST Quartz wafers

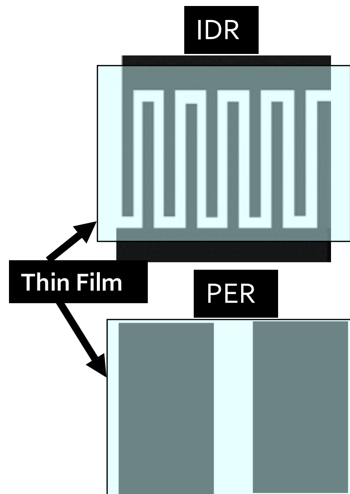

Figure 5-2. A schematic of the *in-situ* interdigitated resistor (IDR) and the parallel electrode resistor (PER).

Gold was chosen as the electrode material due to its inability to oxidize at room temperature. When a thin film is applied to the *in-situ* structures a resistor is created. The electrical resistance of the structure (with the thin film) is proportional to the total number of unit squares in the area between the electrodes. For the *in-situ* resistor designs used here the unit squares are parallel to each other, thus, the equivalent number of squares is the inverse of the total number of squares. In the case of the 0.3mm separated pads the equivalent number is squares is simply 0.3mm/5mm = 0.06.

5.3.2 Die Preparation Procedure

Through repeated experimentation, it was found that the die's substrate preparation prior to film deposition was critical to reproducing films. After dicing, the die is cleaned repeatedly with acetone and methanol soaked clean-room grade swabs and plasma cleaned with O_2 at 150Watts for 1min in an AutoGlow® Plasma system.

5.3.3 Measurement Setup and Procedure

During deposition the film thickness is monitored by water cooled dual quartz microbalances. The monitoring unit is the SQM180 from Sigma Instruments, which has the capability of measuring growth rates as low as one hundredth of an angstrom per second. The resistance was monitored by the computer controlled Agilent 34401 Multimeter, through which resistance data were acquired. At the end, a data file of time versus thickness versus resistance was attained, from which, the conductivity versus thickness plot was extracted.

5.3.4 *In-Situ* Measurement Results

The *in-situ* resistor that was used is the parallel electrode resistor (PER) design. The plots indicate that between 7 to 25Å thick films, there is a steep exponential change in the film conductivity. A five angstrom change might result in a two order of magnitude change in conductivity. If the measurement from the quartz microbalances varies by 3 angstroms over the ultra-thin region the plotted conductivities may vary by as much as 3 orders of magnitude (Figure 5-4 and Figure 5-5). The two most important variables in creating the conductivity versus thickness curves are DC resistance via multimeter and film thickness via quartz crystal monitors. The quartz microbalances are known to vary with an age dependency, so the high vacuum resistance measurements are considered absolute. The DC resistance associated with the resistance curve are used as an indicator of the rate of change of the film's conductivity. The point of the maximum rate of change suggests the area close to the percolation boundary.

A considerable amount of effort was spent in calibration and preparation of the system to achieve consistent results and convergence of data over various depositions. The convergence

suggests that the same film is being reproduced in each deposition by an electron beam thin film evaporation system. This is an important development as it implies that comparatively behaving hydrogen gas sensors may be repeatedly created.

For the purposes in this work, the film needs to be as porous as possible, thus the slowest stable growth attainable was used (0.1Å/s). Substrate temperature is also important to film development; generally, temperature is directly proportional to the film's porosity [97]. A standard pre-deposition time period (10 minutes) was instituted where the Pd source was allowed to warm to evaporation temperature and establish a stable deposition rate—consequently, bringing the chamber and substrate to a steady state temperature prior to beginning the film growth. Equally important, was the use of a secondary shutter (Figure 5-3) that shielded the samples until the chamber was brought up to steady state temperature. Using Figure 5-3 as a reference, the source shutter is initially open and the secondary shutter closed to allow the crystal monitors and the chamber to reach a steady state temperature. This secondary shutter was absolutely critical to reproducibly growing ultra-thin films with little scatter in the measured resistance; a comparison of resistance curves versus thickness with and without the secondary shutter is presented in Figure 5-4. The resistance curves show a scatter due to variations in the measured thickness. For the traces where the secondary shutter was not used, the standard deviation of the measured thicknesses was 3.62Å. For the cases where the secondary shutter was used the measured thickness show a standard deviation of 1.25Å. Then, the curves were all shifted so that they all shared the same starting point at 10^7kΩ (Figure 5-5). Ideally, if the film's nucleation is identical is each case, the resistance curves (which is an indication of nanocluster density) should overlap perfectly, this however, is not the case shown by the plot. From Figure

5-5, it is evident that the exponential rates of change of the resistances between 8 to 40Å are slightly different; this suggests that the films' nucleation is slightly different in each deposition. Even with the small spreading in the ultra-thin region, the curves provide a good approximation of the density of the nanoclusters on the substrate.

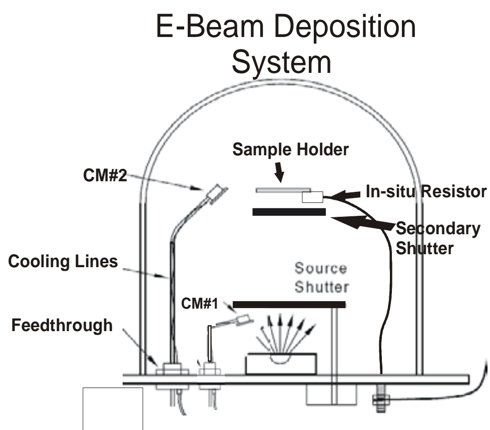

Figure 5-3. A schematic of UCF's electron being thin film deposition system. CM #1 and 2 are the film thickness monitors which infers a film thickness based on the mass loading on a quartz crystal oscillator. The use of the secondary shutter is critical to reproducing equivalent films. The *in-situ* thin film resistor is shown parallel to the samples

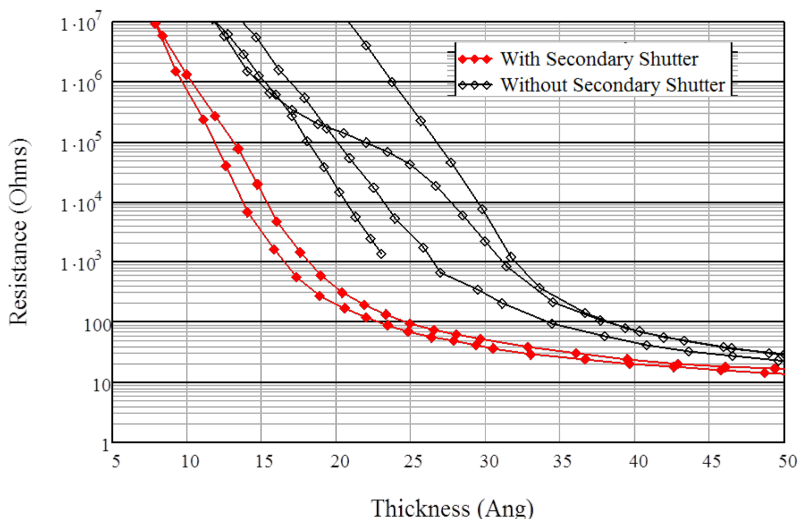

Figure 5-4. Plot of *in-situ* measurement of resistance and thickness via parallel electrode resistor (PER) during deposition of Pd films. The purpose of this plot is to emphasize the difference in data spreading due to the use of the secondary shutter. The traces with which solid diamonds represent depositions performed with the use of the secondary shutter, and the traces with the transparent diamonds represent depositions

performed without the use of a secondary shutter. It shows a large scatter for the depositions without the secondary shutter.

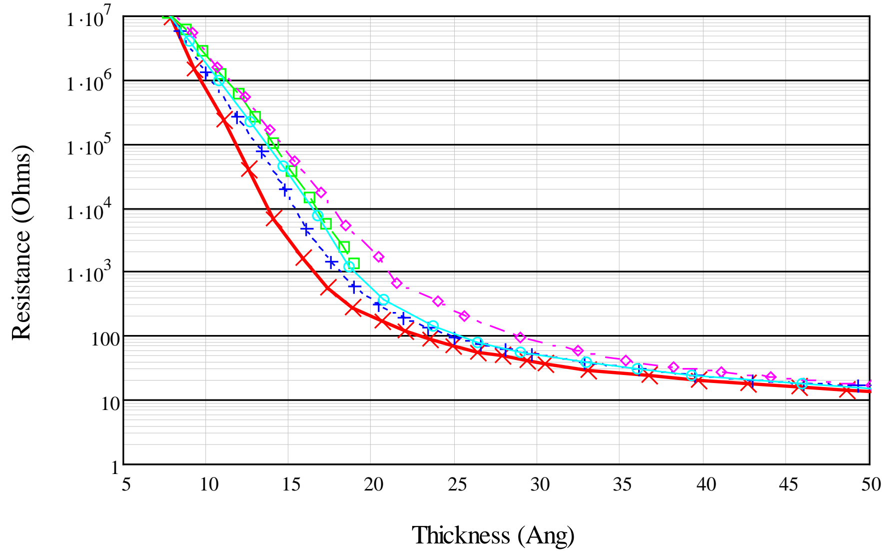

Figure 5-5. Plot of *in-situ* measurement of resistance and thickness via parallel electrode resistor (PER) during deposition of Pd films. These are the same curves shown in Figure 5-4, however they have all been shifted to the same start point ($10^7\Omega$). The exponential rates of change of the resistances between 8 to 50 angstroms are slightly different. This suggests that the films nucleation is slightly different in each deposition.

5.3.5 Development of Malocha's Pd Ultrathin Film Approximation

K. Fuchs and E.H. Sondheimer derived a model for the electrical resistivity of metals as a function of film thickness, based on the mean free path of electrons in an infinitely thick medium (Eq. (5-3) and (5-4)). The mean free path is defined as the average distance an electron travels before it collides with the lattice of the medium.

$$\rho_{thin} = \frac{4\rho_\infty \lambda_\infty}{3t \cdot \left(\ln\left(\frac{\lambda_\infty}{t} \right) 0.4228 \right)} \tag{5-3}$$

$$\rho_{thick} = \rho_\infty \left(1 + \frac{3}{8} \frac{\lambda_\infty}{t} \right) \tag{5-4}$$

Equation (5-3) shows Sondheimer's approximation for thin films, where t is the film thickness, ρ_∞ is the resistivity of an infinitely thick metal and λ_∞ is the mean free electron path in an infinitely thick film. Equation (5-4) shows Sondheimer's approximation for thick films. When compared to the raw data, Sondheimer's approximations showed poor agreement for films that were below 30 angstroms thick (Figure 5-6). Malocha developed a model that included an exponential component to Sondheimer's thick film approximation that matches the data more closely.

$$\rho_{thick} = \rho_\infty \left[\left(1 + \frac{3}{8} \frac{\lambda_\infty}{t} \right) + \left(\frac{1}{b} + e^{-m(t-t_c)} \right) \right] \tag{5-5}$$

Equation (5-5) displays the amended Fuchs-Sondheimer Relation resistivity equation. Where m and b are constants determined by curve fitting, m controls the rate of exponential decay in the ultra-thin region; the critical thickness, t_c, is the approximate thickness that the measured data and the Sondheimer's approximations disagree. There are a few data points that deviate between 17 to 30 angstroms. This deviation is due to the curve fit and suggests that equation (5-5) needs to be amended to account for that transition region. Even with these deviations, the model shows fairly good agreement with the measured data over the ranges of thickness. The values that were used for the data fit in Figure 5-6 and Figure 5-7 are $\rho_\infty = 1.053 \times 10^{-7}$ Ω-m,$\sigma_\infty = 9.5 \times 10^{6}$ S/m, λ_∞ = 1000Å, t_c = 22.5Å, m = (1.09Ang)$^{-1}$,b = 10. A comparison of equation (5-5) to the Arrhenius Eq (5-1) shows the exponent $m(t\text{-}t_c)$ in (5-5) is equal to the ratio of the activation energy (δE) and k_bT. δE is a function of the cluster radius and the space between them, both of which change as a function of film thickness. Thus, an approximation that models the film's resistivity as a function of morphology may be developed.

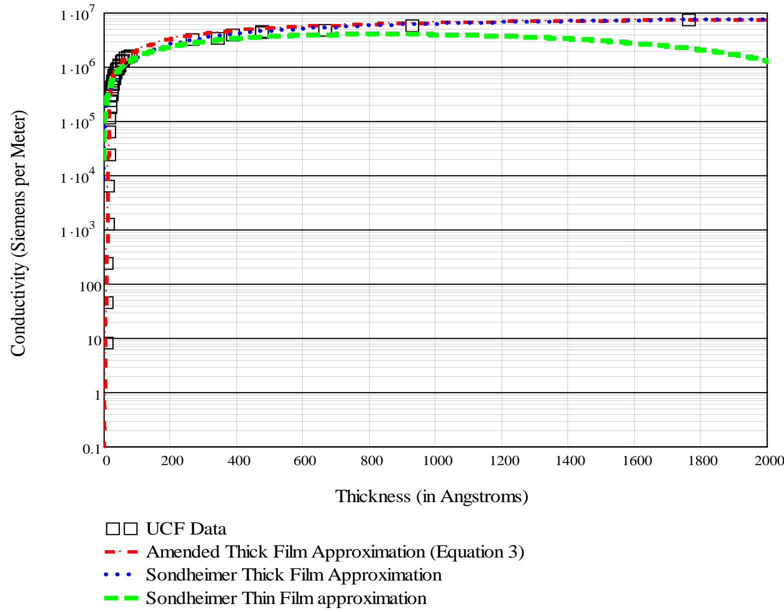

Figure 5-6. This plot shows the change in film conductivity as a function of film thickness. The trace labeled "UCF Data" are collected *in-situ* using the parallel electrode resistors and 3" quartz wafers onto which Pd films were deposited. Data from the quartz wafers were acquired by depositing Pd films on the substrates, then measuring its thickness via profilometer and its sheet resistance via four point probe.

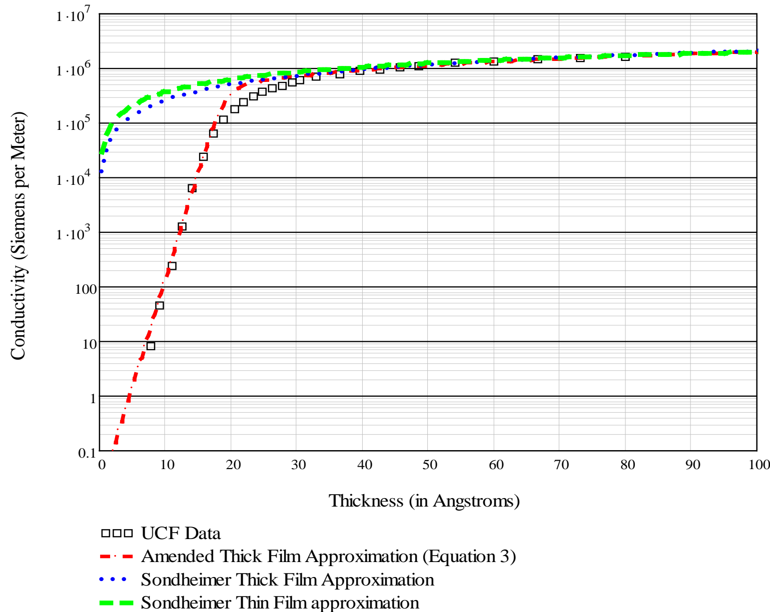

Figure 5-7. Close-up of Figure 5-6 shows the conductivity of Pd films in the ultra-thin regime and highlights the difference between the Fuchs-Sondheimer approximation, the derived model and the measured data. UCF Data shown here represent an average of multiple deposition curves.

5.3.5.1 Prediction of SAW Propagation Loss and Velocity Beneath Pd Films

The sheet resistance, R_S was calculated by dividing equation (5-5) by the thickness, t and plugging R_S into the acoustoelectric equation, (3-50), to predict the film thicknesses where the acoustoelectric effect is dominant. A plot of the predicted propagation loss and velocity beneath Pd in the propagation path of a 62.5MHz SAW in YZ-$LiNbO_3$ is shown in Figure 5-8. From Figure 4-9, the acoustoelastic losses beneath a 10Å Pd film on YZ-$LiNbO_3$ account for about 3% of the total losses at 62.5MHz and are consequently neglected in the predictive plot. Error bars are used show the spread of expected amplitude and velocity due to the +/-1.25Å precision (section 5.3.4) in the measured thickness. The measured propagation loss beneath a 10Å and 13Å Pd film falls within the predicted data spread. The H_2 gas response of this film is presented in section 5.6.1.1.

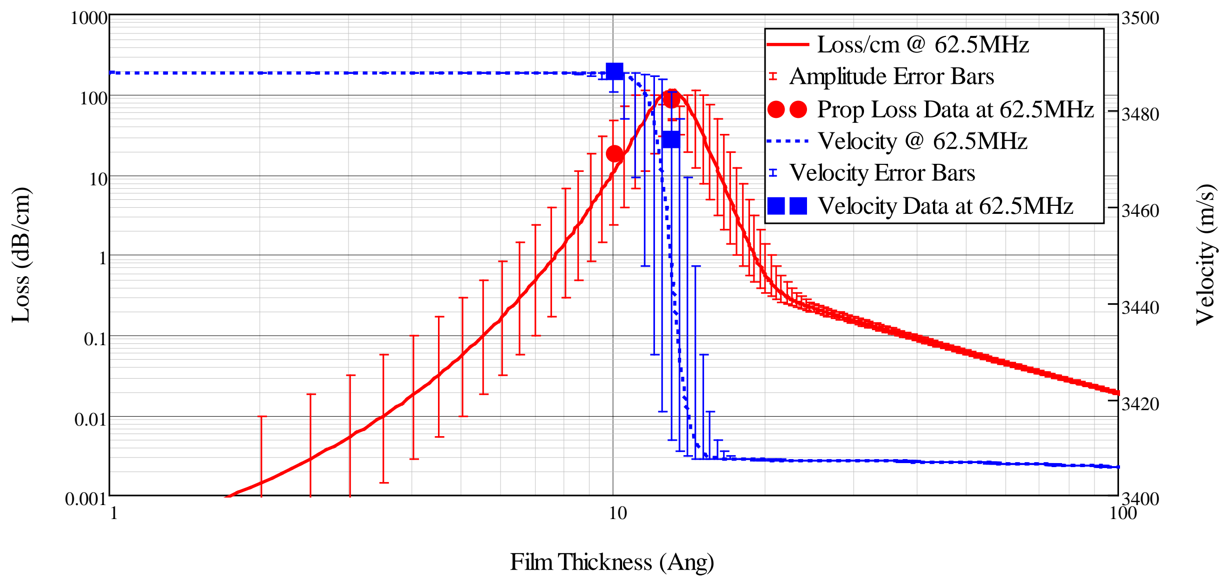

Figure 5-8. Plot of the predicted propagation loss and velocity as a function of Pd thickness for a 62.5MHz SAW on YZ-$LiNbO_3$. The acoustoelectric effect is dominant for Pd film thickness in the 9 to 16 Angstrom range.

5.4 Ultra-Thin Pd Film Hydrogen Sensitive Resistor

5.4.1 Sensitivity to H_2 gas

Several iterative Pd film depositions were performed on the *in-situ* PER. The goal was to grow films with resistances close to the knee of the resistance curve Figure 5-5. Each film was cycled with 2% H_2 gas while the resistance was observed. The depositions proceeded up the curve until successful reversible H_2 gas sensor was found. Films that were not successful only exhibited a single change in response to 2% H_2 gas then ceased changing. The film with the best sensitivity and performance was at ≈50kΩ on the PER at an approximate thickness of 15Å. Parallel to the deposition of the *in-situ* PER was an 80-finger IDR die and a lithium niobate wafer on which were SAW devices and other resistor structures. The SAW response will be treated in section 5.6. The benefit of growing Pd films on a PER and IDR simultaneously, is that a potential placed across an IDR will produce a much larger electrical field than an equivalent potential across a PER. Thus, any electric field or potential effect on the Pd ultrathin film may be observed. Secondly, the function of the IDR is to lower the overall DC resistance on the film because it has a larger number of parallel squares than the PER.

The H_2 gas cycling of the PER and IDR are shown in Figure 5-9, Figure 5-10 and Figure 5-11. In Figure 5-9, the PER was connected to the Agilent 34401A multimeter and the resistance was observed as it was exposed to 2% H_2 (98% N_2) gas. The film on the PER showed an initial sharp increase in resistance, due to H_2 exposure. After a few cycles the resistance began to

decrease in response to 2% H_2 gas exposure. There was still an overall increase in resistance with each successive cycle, possibly due to the formation of palladium hydride (PdHx). There is also a slow exponential decay in resistance with each cycle, the reason for this is not clear. The film on the 80 finger IDR behaved identically (Figure 5-10) to the one deposited on the PER, however the overall resistance was scaled due to the resistor design.

The multimeter applies a test current and measures a voltage in order to calculate the resistance via ohms law ($V=I \cdot R$). In the case where the resistance is between $1M\Omega$ to $10M\Omega$ a test current of 5μA is applied. For the case where the resistance is 0 to 10kΩ a 1mA test current is applied, and 100μA for 10kΩ to 100kΩ. For a thin-film resistor 1mA is a fairly large amount of current to place across a film, this high amount of energy might aid the formation of PdH_x. Thus, a voltage potential of 1 to 3V was applied to the 80 finger IDR. When a 3V potential was placed across the film only 0.1mA current resulted (Figure 5-11). A decrease in film resistance in the presence of 2% H_2 resulted in rapid changes in current flow through the film with an equally rapid return to the current flow prior to 2% H_2 gas cycling (Figure 5-11). The switching times are approximately 1.5 seconds with around 50% decrease in resistance. The most stable Pd UFT resistor is shown in figure 5-12, it was grown on a 40 finger IDR. A 1V potential applied across the film and current is measured ≈ 2 seconds switching times 167% change in current = 62% decrease in resistance. These results suggest that the behavior of Pd UTFs, in the presence of 2% H_2 gas maybe partially due to a field effect.

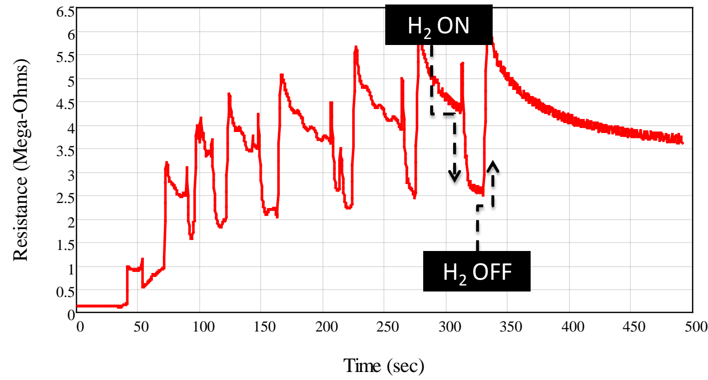

Figure 5-9. H_2 gas cycling of *in-situ* PER with Pd film. ≈10uA test current was applied to the film

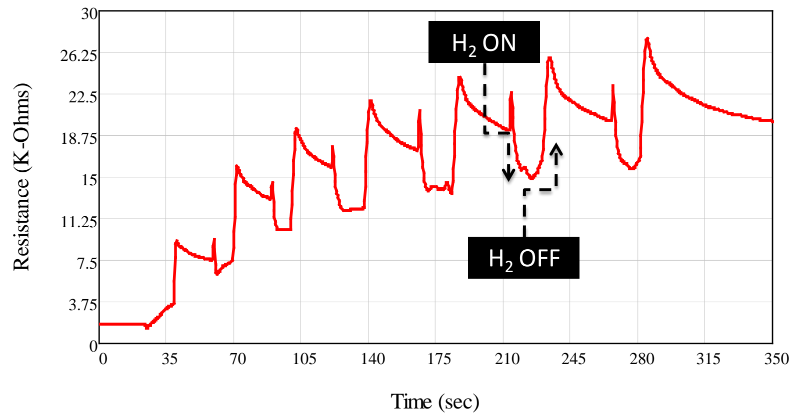

Figure 5-10. IDR gas cycle with ohm meter. ≈100uA test current was applied to the film

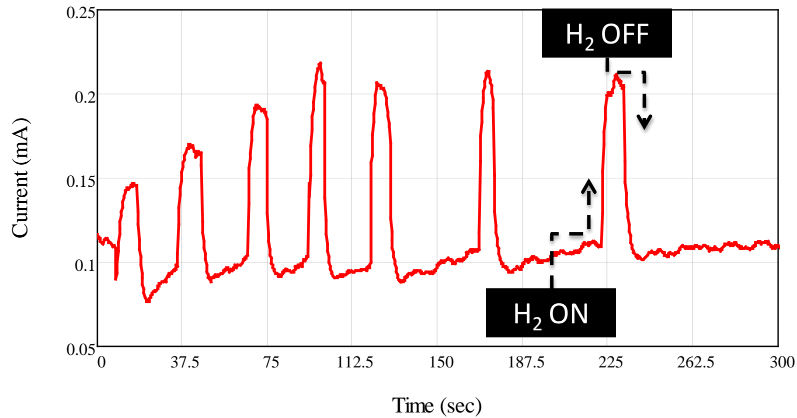

Figure 5-11. 2% H_2 gas cycling of 80-finger IDR die with Pd film, with 3V potential applied across the film. The switching times are approximately 1.5 seconds with roughly 50% decrease in resistance.

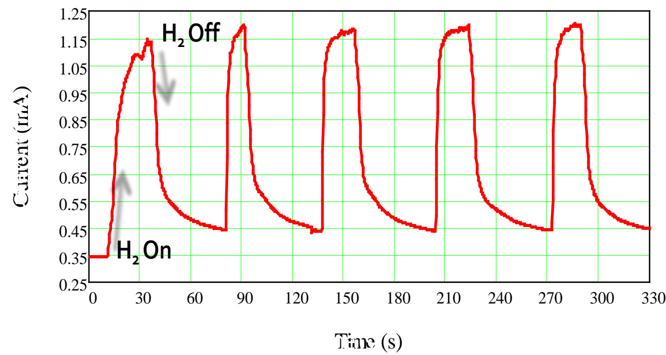

Figure 5-12. A 1V potential applied across the film and current is measured ≈ 2 seconds switching times 167% change in current = 62% decrease in resistance.

5.4.2 Field-effect dependence

Field-effect behavior in discontinuous metal films was first reported by Weinberg Neugebuer et al [98] in 1962. His work showed that as the conduction is due to quantum mechanical tunneling between the cluster and as the electric potential is increased the activation energy required to move electrons between clusters decreases, which decreases measured resistance. For the film shown in Figure 5-12 the I-V characteristics is presented in Figure 5-13.

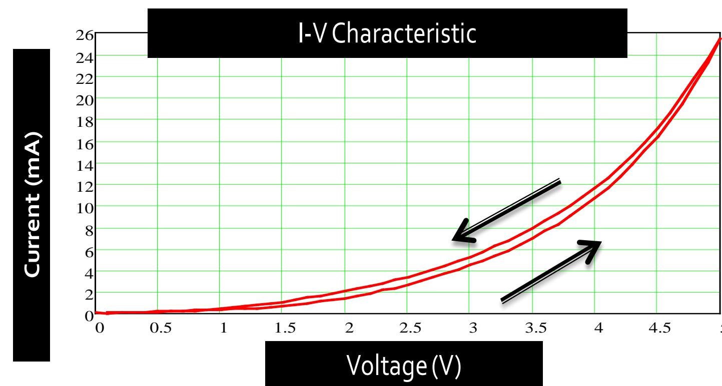

Figure 5-13. The current voltage characteristic is nonlinear as is expected for a nano-clustered film Suggests that main conduction mechanism is quantum tunneling

5.4.3 Temperature dependence

To quantify the film's sensitivity to H_2 gas versus temperature, a heat gun($\approx 70^oC$) was applied directly to the film. This caused a decrease in resistance due to a $\approx 47^oC$ degree increase in temperature due a negative temperature coefficient of resistance (-TCR) (Figure 5-14). The % change in due to $\Delta T=47^oC \approx 2.6\%$, $\approx 500ppm/^oC$ and the % change due to 2% H_2 gas $\approx 24\%$. This suggests that the primary conduction mechanism is quantum tunneling.

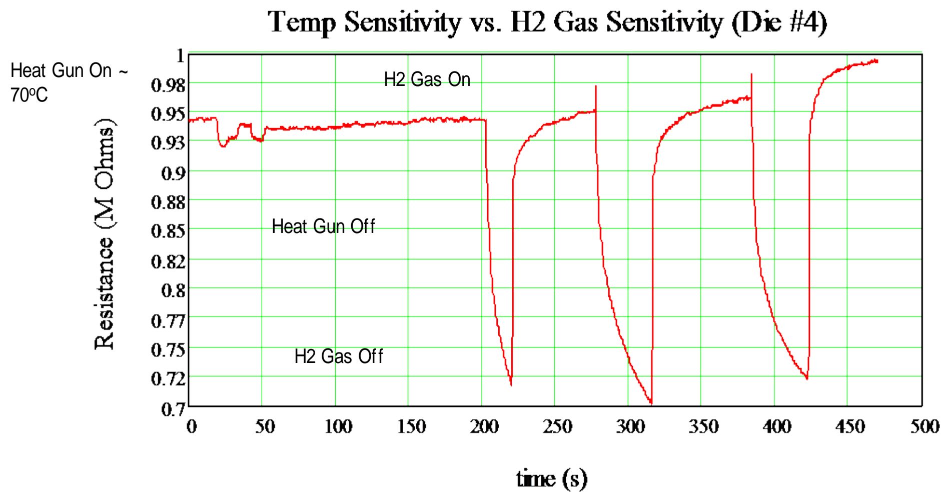

Figure 5-14. Comparison of temperature and H_2 gas sensitivity of the Pd UTFs.

5.5 Film aging, stability and sensor lifetime

Palladium (Pd) UTFs were first exhibited a very fast (<1second) and high fractional change in sheet resistance due to exposure to H_2 gas (Figure 5-15). Unfortunately, the ultra-thin Pd films suffer from oxygen adsorption when exposed to ambient atmosphere. Oxygen adsorption was observed in this study to cause a gradual increase in the film's resistivity when exposed to O_2 gas. A consequence of the O_2 adsorption is the gradual de-sensitivity of the Pd film to H_2 gas, ultimately shortening the sensor's lifetime (Figure 5-15). The purpose of this

section is to observe the aging behavior of ultra-thin Pd films in ambient atmosphere (1atm, 79% N_2, 21% O_2, 44% humidity, 21°C), and investigate methods to slow or stop this process, thereby extending the usable life of the SAW-H_2 gas sensor.

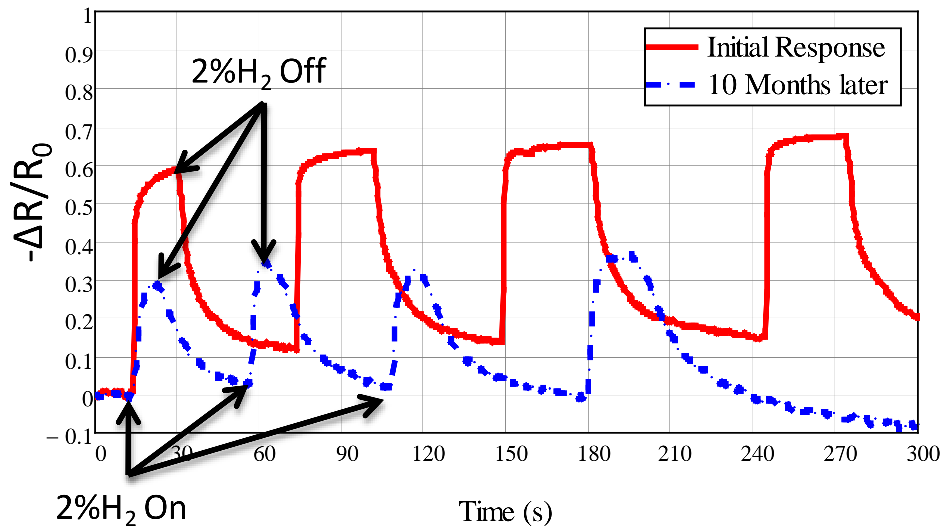

Figure 5-15. 2% H_2 gas exposure of an ultra-thin film Pd resistor. The abrupt resistance decrease when exposed to H_2 gas is assumed due to a change in the cluster size and consequently the activation energy. After ten months, the fractional change in resistance due H_2 gas exposure has decreased due to aging of the film.

5.5.1 O_2 Adsorption

The Pd films, which are grown under the conditions previously discussed, (5.3) are likely to have an amorphous or highly defective crystalline structure (Figure 5-1) [102]. In physical adsorption, O_2 molecules stick to crystalline defect sites on the Pd film's surface. The O_2 molecules steal conduction carriers from the film, which causes a dramatic increase in the electrical resistivity. An *in-situ* resistor structure was used to measure the film's resistivity during growth and the subsequent exposure of said film to various gasses. A significant increase

in electrical resistivity was observed when the Pd film was exposed to ambient air (Figure 5-16). N_2 was observed to have little effect on the film's resistivity. The humidity effect was investigated by annealing the film in open atmosphere, which should evaporate any condensed water molecules thus causing a reversible change in resistivity. The result of annealing the film in open air only served to increase the resistance more rapidly and changed the appearance of the film to a light white shade. The reaction appears to be accelerated by added energy (annealing), forms a whitish coat when annealed in atmosphere and causes increased film resistivity in O_2 atmosphere. The result of this experiment suggests that oxygen adsorption may be the primary mechanism in the observed resistivity increase. Similar observations were reported by Yen [103] in 1974 for oxygen adsorption on zinc oxide thin films.

There are three main techniques that may be employed to slow the adsorption process: (1) use of a Pd alloys, (2) annealing and (3) film encapsulation. Pd-Fe and Pd-Ni alloys were reported by Pitt et al [104] to be ineffective in slowing film aging, thus it was not considered in this study.

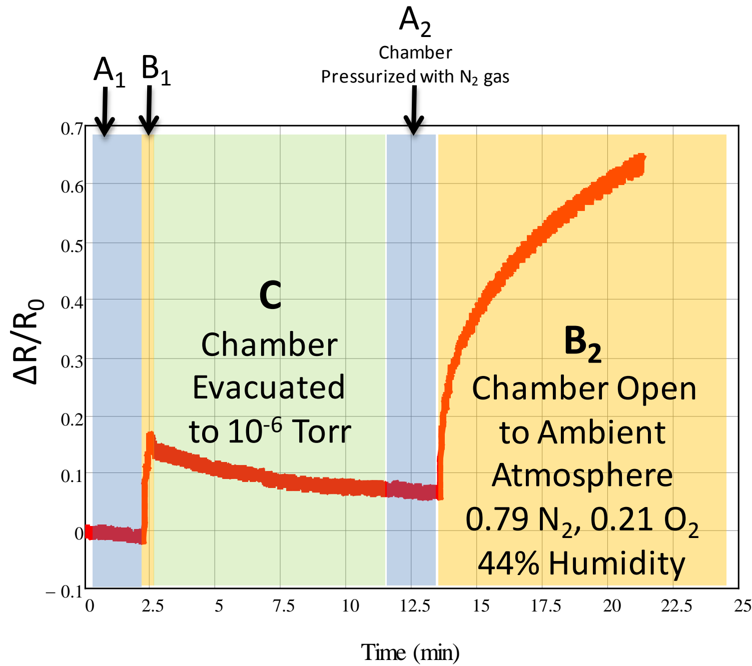

Figure 5-16. A_1: Chamber Pressurized with N_2 gas. B_1: Upon initial exposure to ambient air, the resistance increased approximately 18% within 30 seconds. C: When the vacuum chamber was resealed and pumped down to 10-6 Torr, the reaction stopped. A_2: Chamber re-pressurized to 1atm. B_2: The chamber was re-opened and the resistance increased to 60% above its initial value.

5.5.2 Film Annealing

Annealing (when done at the appropriate temperatures), heals the surface defects in the film thus providing less nucleation sites for adsorption [102]. The Pd UTFs were annealed at temperatures up to 290°C for two hours in a 10^{-4} Torr environment, while the resistance and temperature were monitored (Figure 5-17). Annealing caused the film's resistivity to decrease by an order of magnitude (Figure 5-17); this suggests that a change in film morphology occurred. If the nanoclusters are merging due to added energy from the annealing process, then the activation energy changes because it is dependent on cluster size and separation distance is shown in equation (5-2). This change in activation energy causes an exponential change in resistance as observed in Figure 5-17.

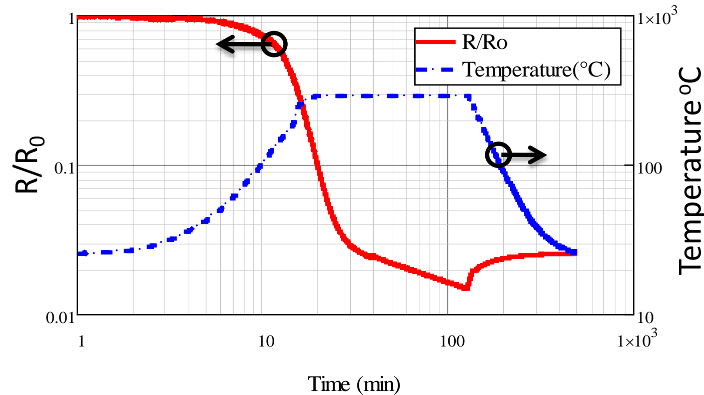

Figure 5-17. Observation of the resistivity of an ultra-thin Pd film during annealing process. The non-reversible change in resistivity suggests a change in film morphology occurred.

5.5.3 Film Encapsulation

Film encapsulation is accomplished by coating the Pd film with a dielectric film that traps or repels O_2 molecules but allows H_2 molecules to diffuse through rapidly. Oxides are commonly used for thin film encapsulation coatings due to their ability to dramatically slow the diffusion of O_2. Pitts et al [104, 105] reported that use the tungsten trioxide (WO_3) as an encapsulation layer for Pd films extended the life of their fiber-optic H_2 gas sensors by over a year. Aside from oxides, Lith et al. [100] reported using a photoresist layer to encapsulate and stabilize Pd-UTFs with only a negligible effect of sensitivity of the film to H_2 gas. Photoresist and other soft polymer-type films cannot be used on a pure SAW mode as it severely damps the wave.

It is necessary to grow a dielectric encapsulation film atop the Pd film without breaking vacuum. The Pd films were grown using an electron beam evaporator, it was crucial to find an oxide film that may be evaporated with an electron beam. WO_3 is not easily evaporated with an ebeam without dissociation into W and O_2 gas and furthermore, was not available at the time of

this experimentation. Aluminum oxide (Al_2O_3) and silicon monoxide (SiO) may be evaporated in an ebeam with minimal risk of the molecules dissociating [106]. Ultra-thin Pd films were coated with 500Å and 1500Å of Al_2O_3 because SiO was not available at the time of this experimentation.

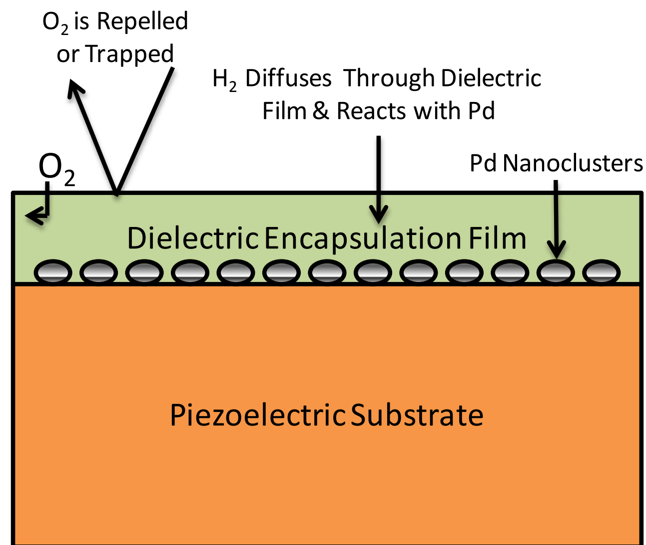

Figure 5-18. Schematic demonstrating the benefits of film encapsulation, by coating the ultra-thin Pd film with a dielectric film that traps or repels O_2 molecule but allows H_2 molecules to diffuse through rapidly, and react with palladium.

5.5.4 Pd UFT Aging Results and Discussion

The annealed and the encapsulated samples were exposed to ambient air while the factional change in film resistivity ($\Delta R/R_o$) as a function of time was observed. A comparison of $\Delta R/R_o$ for the control sample (i.e. un-annealed or encapsulated), the annealed, and the encapsulated samples, is presented in Figure 5-19. The results show that the $\Delta R/R_o$ per unit time for encapsulated films is dramatically lower than the un-annealed and annealed samples. A comparison of the ratios the film's aging rates per unit time (i.e. the ratio of $\Delta R/R_o$ for sample 1

to $\Delta R/R_o$ for sample 2) shows that when a sample is encapsulated with 1500Å of Al_2O_3, $\Delta R/R_o$ is decreased by a factor of approximately 20 when compared to the control sample (Figure 5-20). This data suggests that a combination of film annealing at 290°C and then encapsulating the film with 1500Å of Al_2O_3 may be the most effective method of maximizing lifetime of the SAW Pd UTF H_2 gas sensor.

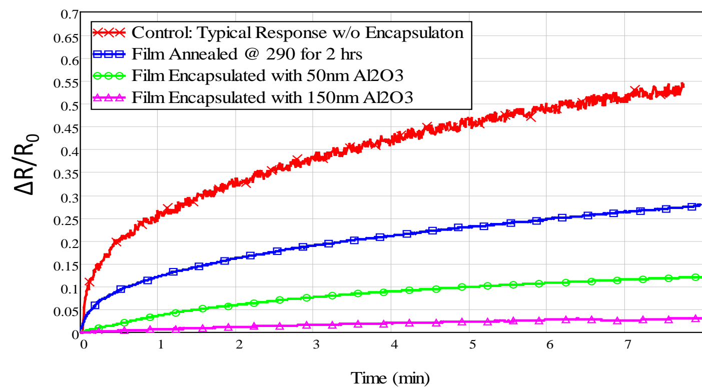

Figure 5-19. The control sample (i.e. un-annealed or encapsulated), annealed and the encapsulated samples were exposed to ambient air while the factional change in film resistivity ($\Delta R/R_o$) as a function of time was observed

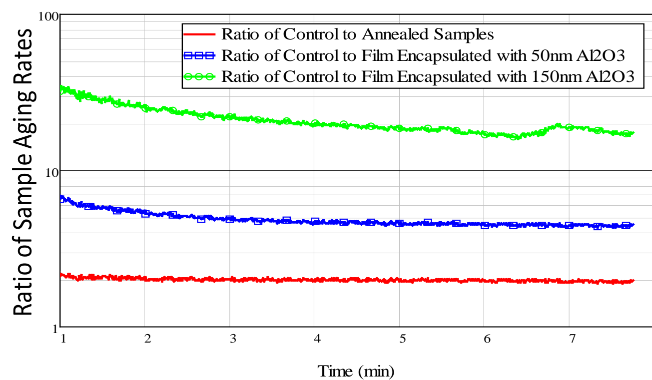

Figure 5-20. A comparison of the ratios the film's aging rates per unit time (i.e. the ratio of $\Delta R/R_o$ for sample 1 to $\Delta R/R_o$ for sample 2) shows that when a sample is encapsulated with 1500Å of Al_2O_3, $\Delta R/R_o$ is decreased by a factor of approximately 20 when compared to the control sample.

5.6 SAW Pd UTF Characterization

5.6.1 Ultra-Thin-Pd-H_2-SAW Interaction

5.6.1.1 Ex-Situ Measurement

An 13Å Pd-UTF was pattern onto the delay path of a 62.5MHz SAW device and the propagation loss and velocity was measured using the procedure presented in section 4.2.1. The film was exposed to a 2%H_2 98% N_2 gas mixture for 10 second durations and the S-parameters were measured before and after each cycle; a plot of the measured propagation loss and velocity as a function of the extracted sheet resistance is shown in .Figure 5-21. There is an increase in velocity and decrease in propagation loss with each successive H_2 gas cycle, which indicates the film's sheet resistance is increasing after each H_2 gas exposure. An *in-situ* fixture was needed to observe the SAW-Pd-H_2 interaction on real-time.

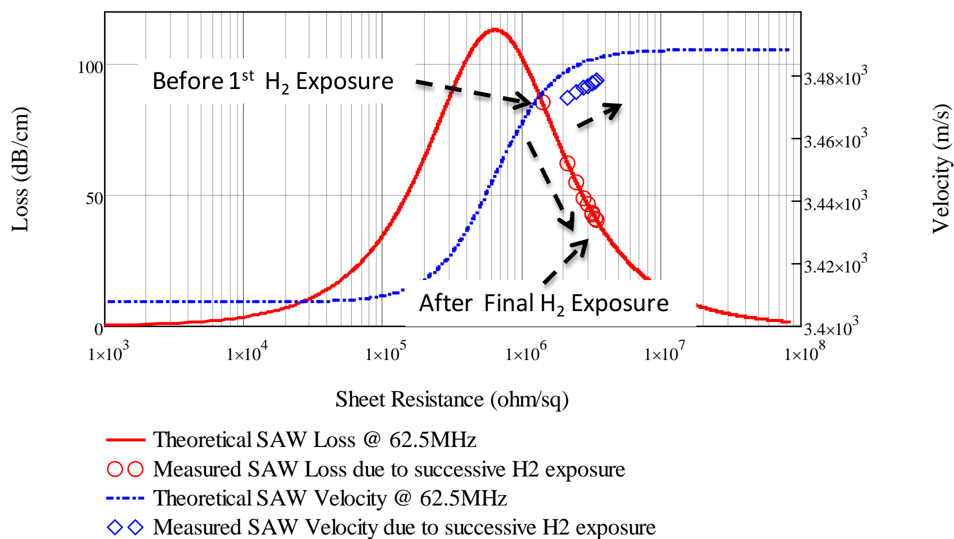

Figure 5-21. Plot of measured 62.5MHz SAW propagation loss and velocity when a 11A Pd film is exposed H_2 gas.

5.6.1.2 In-Situ Measurement

The SAW *in-situ* measurement system (section 4.2) was used to characterize the response of the SAW-Pd-H_2 gas interaction as a function of time. In this experiment, the Pd-film deposition was stopped at high SAW attenuation, removed from the high vacuum environment, and exposed to 2% H_2 gas (balance N_2) in multiple on/off cycles. The result of the SAW-Pd-H_2 gas interaction is presented in Figure 5-22 and Figure 5-23. Figure 5-22 shows the real-time observation and measurement of the modulation of Pd film's conductivity in the presence of H_2 gas. The SAW propagation loss is also modulated via the acoustoelectric effect. The abrupt increase in propagation loss—area A— shows the response of the SAW when the Pd film is exposed to 2% H_2 gas. The abrupt decrease in propagation loss—area B—shows the response when the film is not exposed to 2% H_2 gas. The resistivity increased is with each exposure to H_2 gas (as observed in Figure 5-21) and was accompanied by a gradual increase in resistivity over time. If the increase in resistivity associated with H_2 gas exposure is excluded, there remains a gradual increase in resistance (as observed with the H_2 PER in Figure 5-9 and Figure 5-10), caused by the aging of the ultra-thin Pd film in ambient atmosphere (section 5.5)[107]. The rate of the gradual increase was found to decrease with annealing or encapsulation, however, the sensitivity to H_2 gas was poor and/or films were not stable for a long enough time period to be considered for long-term H_2 gas detection. A hybridization between the well-studied SnO_2 semiconducting films and Pd UTF produced great results for sensitivity and long-term stability and will be presented in CHAPTER 6.

The SAW-H_2 gas sensor measurements were compared to the acoustoelectric effect theory in Figure 5-23 by plotting the previously-measured propagation loss versus measured

sheet resistance. The raw data are offset from the theory due to a calculation error of the sheet resistance that is attributed to the film's non-uniform profile and variable contact resistance of the film with the electrodes. The variable contact resistance occurs because the discontinuous films may irreversibly change morphology when exposed to H_2 gas. The change in morphology complicates the removal of contact resistance issues from the measured data. If the film is uniform the sheet resistance is simply the measured resistance divided by the number of squares of material between the electrodes. The sheet resistance of the Gaussian distributed film is given by

$$R_{S_Gaussian}(t) = \int_{L_{film}} R_S(h(t,x))dx \approx \frac{R_M}{N_{Seq}} \tag{5-6}$$

where R_M is the measured resistance and N_{Seq} is the equivalent number of squares between the electrodes. Using (5-6) the N_{Seq} may be calculated because all other parameters are known; for the data presented the in Figure 5-23, $N_{Seq} \approx 4$. A secondary method of performing this correction is to plug the measured propagation loss values into the acoustoelectric loss equation (3-50), to solve for the sheet resistance, R_S, and then divide the measured resistance, R_M, by the calculated R_S to solve for N_{Seq}; using the secondary method $N_{Seq} \approx 4.5$. These techniques demonstrates how a SAW device may be used to evaluate the DC electrical parameters of delicate films without contact from probes that may damage samples and/or add experimental error.

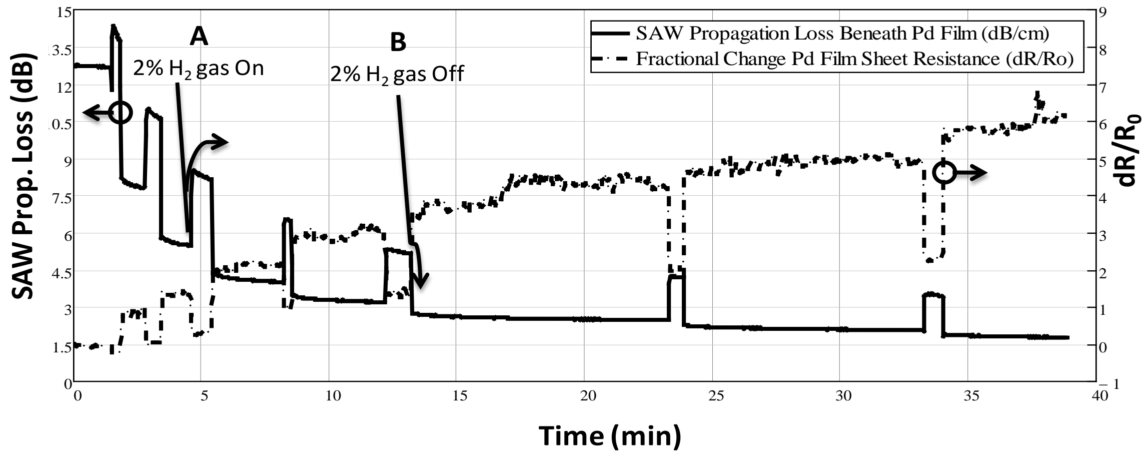

Figure 5-22. The real-time observation and measurement of the modulation of Pd film's conductivity in the presence of H_2 gas. Consequently, the SAW propagation loss is also modulated via the acoustoelectric effect.

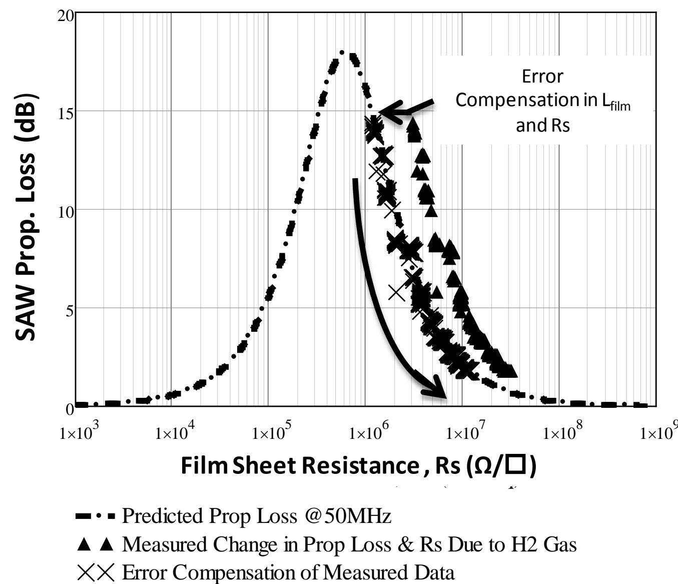

Figure 5-23. The SAW propagation loss and measured Pd film sheet resistance as a function of H_2 gas exposure (data from Fig. 11). The measured propagation loss vs. measured sheet resistance falls on the predictive acoustoelectric curve, after errors due to film non-uniformity are taken into account.

5.7 Chapter Summary

1. Under appropriate growth conditions UTFs may have a nano-clustered morphology (Figure 5-1). Electrical conduction is achieved via thermally activated quantum tunneling between the nano-clusters [98]. When exposed to hydrogen gas the Pd clusters "swell" due to hydrogen induced lattice expansion (HILE), consequently creating a greater number of conductive pathways and decreasing the tunneling gap, thus causing a dramatic decrease in electrical resistivity [50, 99, 100]. This behavior typically occurs in the high resistivity range where the acoustoelectric effect is most dominant.
2. In order to design SAW device hydrogen gas sensors, it is necessary to understand the conductivity of Pd films as a function of thickness.
3. A Pd thin film conductivity model was developed based on the Fuchs-Sondheimer approximation.
4. The *in-situ* process monitors the films resistance at various thicknesses via a resistor structure during film growth.
5. Palladium (Pd) UTFs were first exhibited a very fast (<1second) and high fractional change in sheet resistance due to exposure to H_2 gas. The film with the best sensitivity and performance was at ≈50kΩ on the PER at an approximate thickness of ≈15Å.
6. The ultra-thin Pd films suffer from oxygen adsorption when exposed to ambient atmosphere.
7. The rate of the gradual increase was found to decrease with annealing or encapsulation, however, the sensitivity to H_2 gas was poor and/or films were not stable for a long enough time period to be considered for long-term H_2 gas detection. A hybridization

between the well-studied SnO_2 semiconducting films and Pd UTF produced great results for sensitivity and long-term stability as will be presented in CHAPTER 6.

8. Demonstrated the real-time observation and measurement of the modulation of Pd film's conductivity in the presence of H_2 gas. Consequently, the SAW propagation loss is also modulated via the acoustoelectric effect.

CHAPTER 6 TIN DIOXIDE (SNO2) FILM CHARACTERIZATION

6.1 Chapter Overview

Tin dioxide (SnO_2) films have been used for the detection of hydrocarbon gases since the 1970s [108]. These films are known to be stable of a few years but have typical operating temperatures of 150 to 300^oC [24], which made them prohibitive for gas detection at room temperature. The addition of a thin-film activation layer of palladium (Pd) or platinum (Pt) makes the film more sensitive and selective to H_2 gas and lowers the activation energy (and thereby the operating temperature)[51, 52]. Shukla et al [51, 52] and has reported room temperature operation and a 99.99% decrease in resistance when the film is doped with In_2O_3, layered with a Pt UTF, stacked in multiple layers (of SnO_2-Pt- SnO_2-Pt) and annealed at 400^oC for 1 hour. The response kinetics of the H_2-Pt-SnO_2 interaction are discussed in section 6.2. The sheet resistance of these films can be controlled by thickness, doping and annealing, which makes them ideal for integration with the piezoelectric SAW substrate. The sheet resistance of the SnO_2 film needs to be close to the intrinsic impedance of the piezoelectric substrate in order to use the acoustoelectric effect to modulate the propagation loss and velocity of the SAW via H_2 gas exposure.

The integration of the SnO_2 films with the OFC-SAW device requires significant process development and characterization of the SnO_2 films on YZ-$LiNbO_3$ (section 6.3). There are a wealth of references on the characterization of vapor deposited SnO_2 films on a variety of substrates—none of which are YZ-$LiNbO_3$. For this work, the film is deposited using an electron beam evaporator and then annealed in an air atmosphere to stimulate grain growth. The

annealing temperature of YZ-$LiNbO_3$ is limited to 350^0 to 400^0C to prevent the de-poling of the substrate (i.e. temperature where the crystal loses its piezoelectric properties)[109]. The film's crystalline orientation, grain-size and morphology has a strong effect on its sensitivity to H_2 gas[51, 52]. The length of annealing time affects the film's gas sensitivity and aging (i.e., gradual increase in resistance over time, which limits the film's usable lifetime) [106] (section 6.4 and 6.5).

6.2 The H_2-Pd-SnO_2 Interaction

The H_2-Pt-SnO_2 interaction is discussed in detail in [51, 52] a brief review is presented. The charge carriers, which are responsible for the semiconductivity in SnO_2 films, are the remaining Sn ions and non-stoichiometric Sn_xO_y molecules after film growth and processing[110]. SnO_2 films adsorb O_2 or O molecules when first exposed to air. The oxygen steals conduction electrons from the tin oxide, which creates O_2^- and O^- ions, and leaves positively charged metal cat ions beneath the particle surface. This creates a space charge layer that inhibits electrical conduction at the particle surface. The H_2 molecules act as a reducing agent by dissociating on the surface of the Pt or Pd catalyst and reacting with the O^- ions (Figure 6-1). This reduction eliminates the space charge layer by and releasing the electron back to the conduction band of SnO_2, lowering the potential barrier for electron conduction and creates an exponential change in electrical resistance.

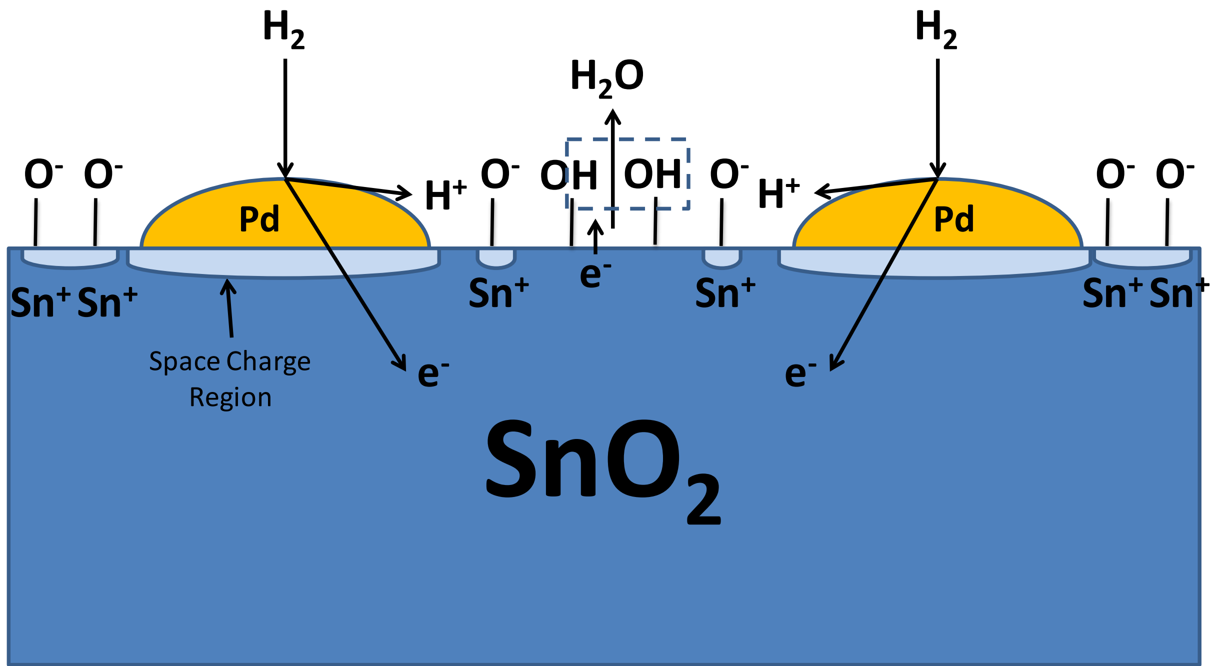

Figure 6-1. A schematic of the interaction between hydrogen, palladium and tin oxide.

The chemical reaction is summarized as follows [51]:

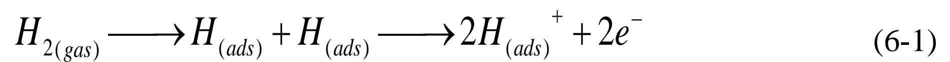

$$H_{2(gas)} \longrightarrow H_{(ads)} + H_{(ads)} \longrightarrow 2H_{(ads)}^{+} + 2e^{-} \tag{6-1}$$

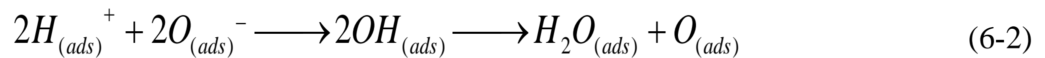

$$2H_{(ads)}^{+} + 2O_{(ads)}^{-} \longrightarrow 2OH_{(ads)} \longrightarrow H_2O_{(ads)} + O_{(ads)} \tag{6-2}$$

$$O_{(ads)} + e^{-} \longrightarrow O_{(ads)}^{-} \tag{6-3}$$

The net reaction is

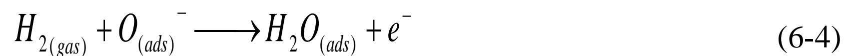

$$H_{2(gas)} + O_{(ads)}^{-} \longrightarrow H_2O_{(ads)} + e^{-} \tag{6-4}$$

The change in resistance is modeled by the Arrhenius equation [51]

$$R_{gas} = R_{air} e^{\frac{qV_{gb}}{k_b T}} \tag{6-5}$$

where R_{gas} is the sensor resistance when exposed to hydrogen gas, R_{air} is the film resistance in air, q is the electron charge , T is the absolute temperature in Kelvin, k_b is Boltzmann's constant and V_{gb} is the surface potential barrier, which is a function of surface-adsorbed oxygen ions. Equation (6-5) is similar in form to the Arrhenius equation for the Pd-UTF H_2 interaction (5-1). The film's sensitivity is given by

$$\frac{R_{air} - R_{gas}}{R_{air}} = 1 - e^{\frac{qV_{gb}}{k_b T}} \tag{6-6}$$

6.3 SnO_2 Film Growth and Processing

The room temperature hydrogen sensitive films, which were developed by Shukla [51, 52], were grown using the sol-gel method where tin and indium were suspended in an isopropoxide and toluene solution and the substrate was dip coated and slowly pulled to form a thin layer. A thin Pt film was sputtered or flash evaporated onto the SnO_2, the process was repeated until the desired film thickness was achieved and then the structure was fired in air at 450°C for 1 hour to enhance crystallinity, grain size and sensitivity. They found that the gas sensitivity was the greatest when the polycrystalline grain size was less than 100Å and film thickness of at least 1100Å, and these were the key factors for selection the anneal time and temperature.

Sol-gel deposition was not available at the time of this dissertation so films were vapor deposited using an electron beam film deposition system. Kahn [110] found that electron beam evaporated SnO_2 films that were grown on BK7 glass possessed polycrystalline morphology with a dominant <110> orientation with a particle size of around 55Å when annealed at 350°C for 2 hours.

The reproducible growth of thin semiconducting films requires the identification and precise control of critical process parameters using an experimental decision analysis. This is an analytical process in which the effect of the independent variables (IV) are weighted based on their impact on the desired dependent variables (DV). The independent variables are the process parameters that may be controlled, these include: substrate temperature during film growth, film deposition rate, SnO_2 film thickness, Pd film thickness, annealing temperature, annealing time and the film's thickness profile. The dependent variables are the film properties that result from the processing steps, these include: sheet resistance, gas sensitivity, and aging rate. For each DV, the IVs are ranked from lowest (1) to highest (# of IVs) based on their impact on each DV; an experimental decision analysis is presented in Table 6-1. The values that were assigned to each IV is based on previous experimental experience and a literature review. The sum of each column is the summation of the number of IVs and serves and a error check and the value or experimental importance of the IV is the sum of each row. From Table 6-1 the most important parameter is the film thickness profile, followed by tie between the annealing time and Pd film thickness then SnO_2 film thickness . The effect of each of the these parameters will be evaluated in section 6.4.

Table 6-1. An experimental design analysis for SnO_2-Pd films.

	IV↓ DV→	Sheet Resistance	H_2 Gas Sensitivity	Aging Rate	Value of IV
1	**Substrate temperature during film growth**	1	1	1	**3**
2	**Film growth rate**	2	2	2	**6**
3	**SnO_2 film thickness**	5	5	3	**13**
4	**Pd film thickness**	4	4	4	**12**
5	**Annealing time**	3	3	5	**11**
6	**Film Thickness Profile**	6	6	6	**18**
	Check Sum	**21**	**21**	**21**	**63**

6.3.1 SnO_2 Film Deposition

SnO_2 film depositions were performed using an electronic beam evaporator with 99.9% pure pellets, which were purchased from Kurt J Lesker Company. It was evaporated from an Al_2O_3 crucible liner using 10kV and 28 to 32mA of current. The evaporation current is relatively low because SnO_2 sublimes and creates very high deposition rates at relatively low currents. High deposition rates are known to create porous films−which are desired for gas sensing−but very poor control over the desired thickness. The SnO_2 depositions were kept at 3 to 5Å/s to ensure reproducibility. A substrate temperature controller and O_2 gas injection were also installed on the ebeam system to control deposition environment as precisely as possible. Elevating the substrate temperature has the added benefit of desorbing surface adsorbed molecules, which survive the substrate cleaning process. The substrate temperature was controlled at 60°C and an O_2 pressure of $3x10^{-5}$Torr was introduced after the chamber was evacuated to less than $3x10^{-6}$Torr. The O_2 gas was evacuated before the Pd UTF was evaporated; the Pd UTF was grown using the procedure reported in section 5.3.

SnO_2 films need to be grown precisely in the propagation path of the SAW and was accomplished in two methods: (1) the films were patterned using standard photolithographic techniques (which created a uniform thickness profile) or (2) it is evaporated through a shadow mask onto a packaged and bonded device (which created a non-uniform thickness profile, see section 4.3.2). Films were patterned onto a diced wafer with 4 to 8 devices. After deposition the wafer needed coated in PR, diced once more into individual devices, adhered to a package and gold-wired bonded. These additional steps increase risks for loss. The devices that were packaged and bonded prior to film deposition require no additional processing.

6.3.2 Anneal Cycle

Successful integration of SnO_2 with a the YZ-$LiNbO_3$ substrate requires that the annealing temperature be kept below 400°C to protect the piezoelectric properties of the substrate[109] and the Al electrodes from oxidizing [111]. To err on the side of caution, 350° was chosen as the anneal temperature for all devices. The devices were placed in a glass Petri dish and annealed in a programmable furnace in an air environment. The furnace was set to its maximum ramp rate of 21°C/min and required 15min to reach 350°C. The soak time was varied from 5 to 60 minutes. When the soak time was completed the devices were removed for the furnace and allowed to cool in air for 5 minutes. A picture of a 5min anneal cycle is shown in Figure 6-2.

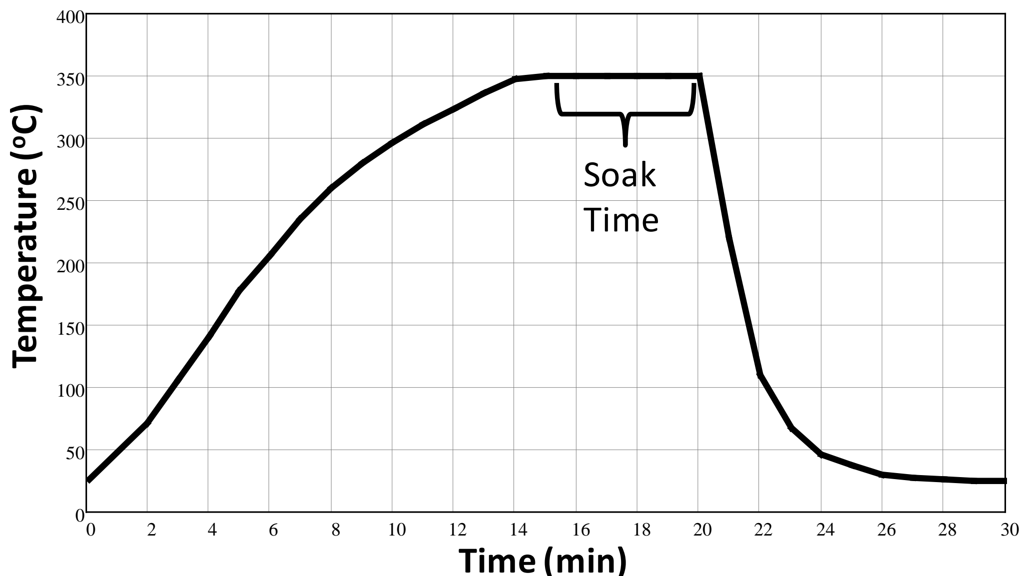

Figure 6-2. A graph of the temperature ramp, anneal and cooling cycles for the OFC-SAW H_2 gas sensors.

6.3.3 Shadow Mask

A secondary *in-situ* fixture was designed to allow the deposition and measurement of packaged devices. It was constructed on 64mil thick FR4 PCB with SMA connectors for RF connection and was designed to measure both a one and two port devices (Figure 6-3). The distance between the aperture and the substrate is approximately 2mm. The shadow mask was made from 150µm copper foil. Referencing the experimental considerations in section 4.2.2.3, 250µm and 500µm aperture widths were used to ensure that the signal was not buried in noise at maximum attenuation at 915MHz.

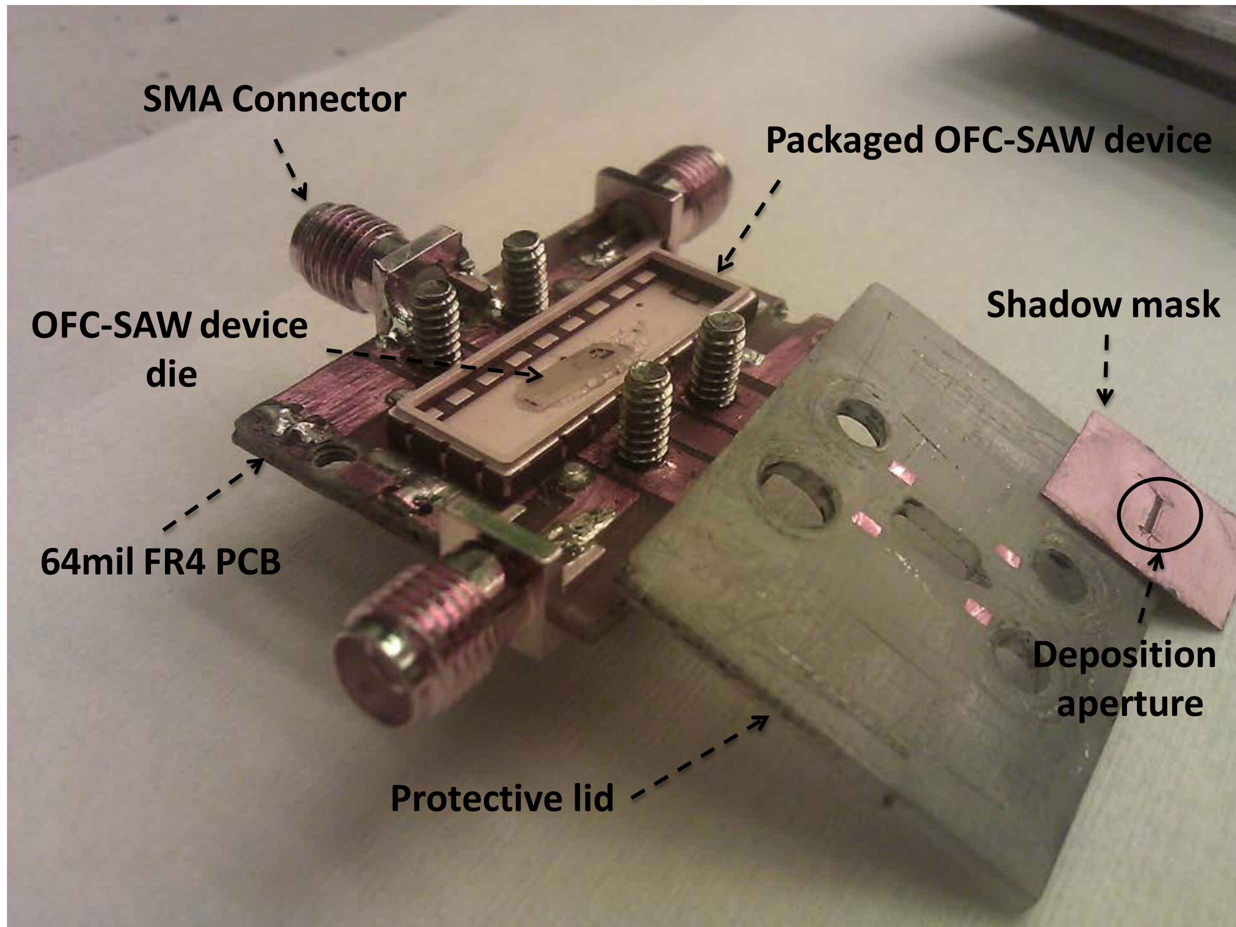

Figure 6-3. Picture of the test fixture and shadow mask for the 915 OFC-SAW device.

6.3.3.1 Film Thickness Profile

After deposition and annealing the film's thickness profile was measured using Veeco Dektak Stylus profilometer. The film thickness profile was non-uniform (Figure 6-4) but not entirely Gaussian as previously observed (Figure 4-18). The difference in profile is most likely due to the difference in distance between the aperture and substrate. On the previous fixture the distance is around 5mm and in this instance it is less than 2mm. The film profile was normalized

such that it is centered about *0-mm* and the maximum amplitude is = *1*. The slope in the side walls were found to follow a Gaussian distribution given by eq (6-7) and the film profile, *h(t,x),* as a function of the deposition aperture is given by (6-8) and is plotted in Figure 6-5. The film profile is necessary to calculate the effective sheet resistance, SAW propagation loss and delay change across the across the non-uniform film as demonstrated in section 4.3.2.

$$h_{Gass}(t,x) = t \cdot \left(3.761 \exp\left(-44.4 \left(\frac{x}{mm} \right)^2 \right) - 2.761 \right) \tag{6-7}$$

$$\begin{aligned}
h_1(t,x) &= \begin{cases} x < \dfrac{aperture}{2} \cdot 0.7 & 0.5 \\ otherwise & 0.5 \cdot h_{Gass}\left(t, x - \dfrac{\text{aperture}}{2} \cdot 0.7 \right) \end{cases} \\
h_2(t,x) &= \begin{cases} x > -\dfrac{\text{aperture}}{2} \cdot 0.7 & 0.5 \\ otherwise & 0.5 \cdot h_{Gass}\left(t, x + \dfrac{\text{aperture}}{2} \cdot 0.7 \right) \end{cases} \\
h(t,x) &= h_1(t,x) + h_2(t,x)
\end{aligned} \tag{6-8}$$

where '*aperture*' refers to the width of the film deposition aperture.

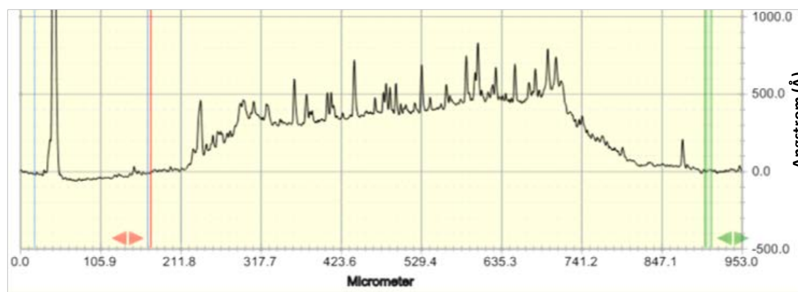

Figure 6-4. Picture of a 500Å SnO_2 + 20Å Pd film thickness profile after deposition through a 0.5mm aperture shadow mask. This profile measured using a Veeco Dektak Stylus profilometer.

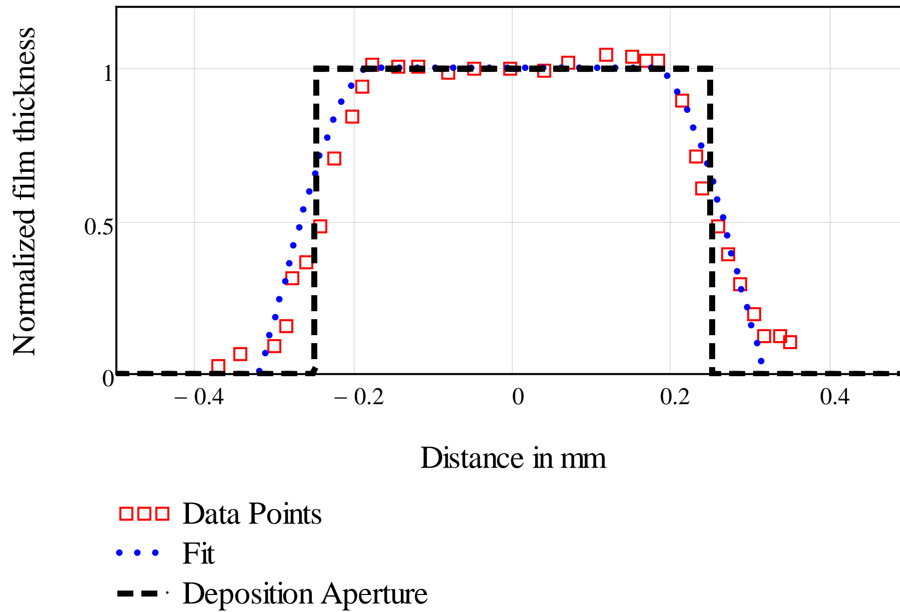

Figure 6-5. A plot of the normalized film profile and data fit. The film profile is necessary to calculate the effective sheet resistance of the film.

6.3.3.2 Propagation Loss Predictions for Non-uniform Films

The propagation loss across three films on a 915MHz SAW is presented in Table 6-2; these films were deposited through two different aperture widths and had two different thicknesses.

Table 6-2. Summary of the 915MHz SAW propagation loss across non-uniform films.

Sample#	**SnO_2 Film Thickness (Å)**	**Pd Film Thickness (Å)**	**Aperture (mm)**	**Insertion Loss (dB)**
072111	500	20	0.5	30
041912	250	20	0.5	14.862
052312	250	20	0.25	8.1

The SAW propagation loss across a non-uniform film was given in section 4.3.2 and is by equation (4-9)

$$PL(f,t) = -8.686 \int_{L_{film}} \left[\alpha\left(f, \left[R_S\left(h(t,x)\right)\right]^{-1}\right)\right] \cdot dx \tag{4-9}$$

where α is given by acoustoelectric portion of equation (3-50). The Malocha film resistivity approximation (section 5.3.5), for UTFs was used for the predictive models in section 4.3.2 because it accounts for the transition from discontinuity to continuity in the films. The Pd UTF is amorphous and discontinuous whereas the SnO_2 film is continuous and polycrystalline when annealed. Mayadas-Shatzkes [112] have calculated the resistivity of a polycrystalline film in which three types of scattering mechanisms are simultaneously operative: an isotropic back-ground scattering (due to phonons and point defects), scattering due to grain boundaries, and scattering due to external surfaces. The sheet resistance as a function of thickness, t, is given by

$$R_S(t) = \frac{\rho}{t} \tag{6-9}$$

where the electrical resistivity ρ is given the Mayadas-Shatzkes approximation

$$
\begin{aligned}
&\rho = \rho_\infty \frac{\phi(t,\lambda_\infty,p,R,D)}{f(\lambda_\infty,R,D)} \\
&\phi(t,\lambda_\infty,p,R,D) = \left[1 - \frac{3(1-p)}{2\cdot k(t,\lambda_\infty,R,D)} \times \sum_{i=0}^{N-1} \left[\left[\left[\left(1+\frac{N-1}{N}i\right)^{-3} - \left(1+\frac{N-1}{N}i\right)^{-5} \right] \times \frac{1-\exp\left(-k(t,\lambda_\infty,R,D)\left(1+\frac{N-1}{N}i\right)\right)}{1-p\cdot\exp\left(-k(t,\lambda_\infty,R,D)\left(1+\frac{N-1}{N}i\right)\right)} \left(\frac{N-1}{N}\right) \right] \right] \right]^{-1} \\
&k(t,\lambda_\infty,R,D) = \frac{t}{\lambda_\infty f(\lambda_\infty,R,D)} \\
&f(\lambda_\infty,R,D) = 3\left[\frac{1}{3} - \frac{\alpha(\lambda_\infty,R,D)}{2} + \alpha(\lambda_\infty,R,D)^2 - \alpha(\lambda_\infty,R,D)^3 \cdot \ln\left[1+\frac{1}{\alpha(\lambda_\infty,R,D)}\right]\right] \\
&\alpha(\lambda_\infty,R,D) = \frac{\lambda_\infty R}{D(1-R)}
\end{aligned}
\tag{6-10}
$$

where p is the specularity parameter for the surface, λ_∞ is the mean free path of the electrons for a bulk material, R is the grain boundary reflection coefficient and D is the mean grain size, assuming the grain size distribution is Gaussian. The specularity parameter, p, is the fractional of electrons that are reflected at the surface and bottom of the film; it is set to *0*, because the reflections are assured to be diffuse, additionally, its value does not appear to have a significant impact on the calculations. The SnO_2 grain size, D, may be approximated to *50Å* based on the work of Khan [110], the bulk resistivity, ρ_∞ was experimentally determined to be around *0.3Ω·cm* on average. The mean free path λ_∞ is assumed to be equal to the grain size, D, because the grain sizes are relatively small. The last remaining and most critical parameter is R, the fraction of electrons that are reflected at the grain boundaries. This number has the most significant impact on the film's resistivity calculation and was set to 98.3% to fit equation (4-9) to the measured acoustoelectric propagation loss from sample # *072111* (Table 6-2). From

section 4.2.1 the acoustoelastic losses account for around 10% to the total loss beneath SnO_2 films at 915MHz. The reported insertion loss includes the acoustoelastic losses and must be removed. A plot of the predicted acoustoelectric propagation loss as a function of deposition aperture and film thickness is shown in Figure 6-6. The measured data for the other two samples in Table 6-2 are also have good agreement with the predictions. Calculating the effective sheet resistance across the film simply requires the integration of the sheet resistance across the film (6-11); a plot of the effective sheet resistance as a function of deposition aperture and film thickness is shown in Figure 6-7.

$$R_{S_Eff}(t) = \int_{L_{film}} R_S(h(t,x))dx \qquad (6\text{-}11)$$

The predictive plots of Figure 6-6 and Figure 6-7 will be used for the design of the OFC-SAW H_2 gas sensor network in section 7.3. Figure 6-8 shows the propagation loss and velocity of a non-uniform 250Å film (sample 052312); when the film is exposed to H2 gas the sheet resistance decrease causes a

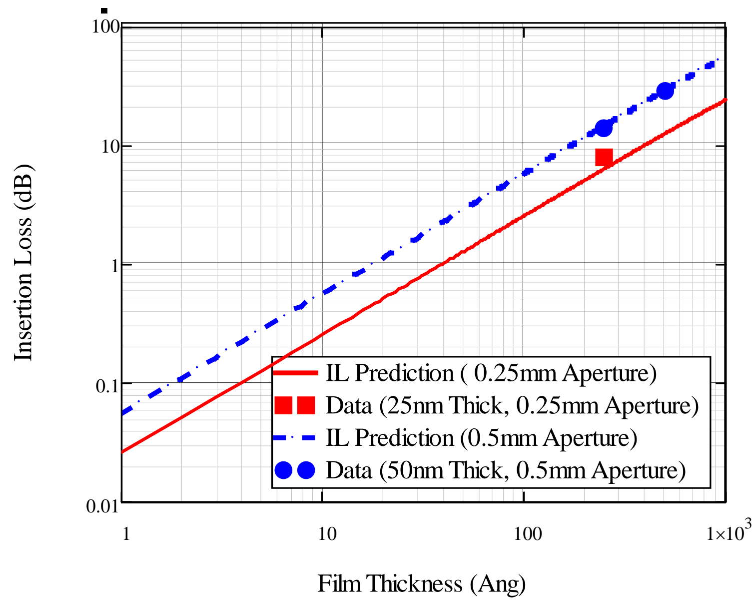

Figure 6-6. A plot of the predicted insertion loss of 915MHz SAW on YZ-$LiNbO_3$ as a function of SnO_2 film thickness and deposition aperture. The predictions are compared to 3 measured data points.

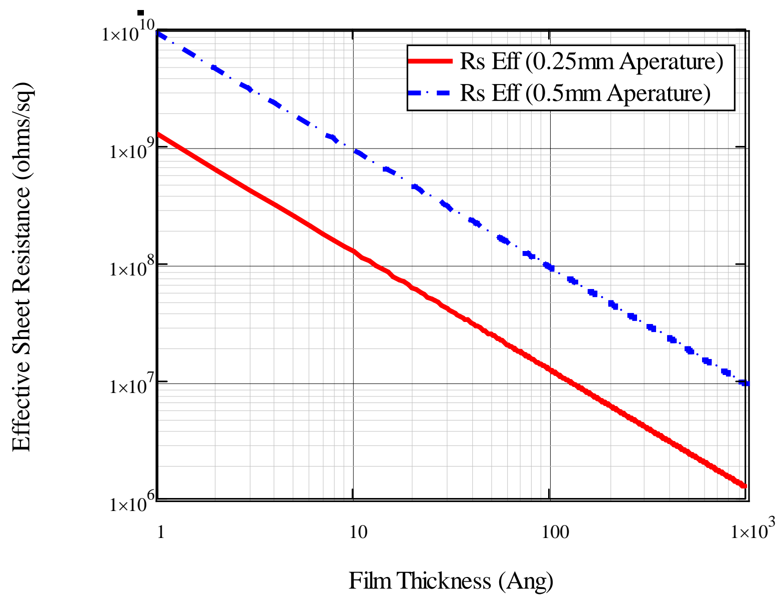

Figure 6-7. A plot of the effective sheet resistance of non-uniform SnO_2 films as a function of thickness and deposition aperture.

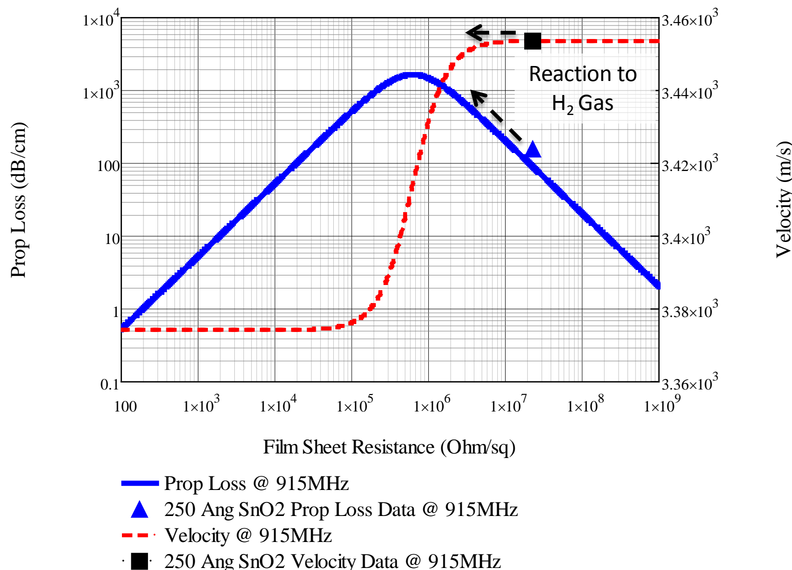

Figure 6-8. Plot of the 915MHz propagation loss and velocity of a 250Å non-uniform SnO_2 film on YZ-$LiNbO_3$. When the film is exposed to H_2 gas there is an increase in propagation loss and a decrease in velocity.

6.4 Hydrogen Gas Sensitivity

From the propagation loss versus film thickness predictions of Figure 6-6, films thicker than 500Å are prohibited due to high propagation loss. SnO_2 films were evaluated using thin film resistors, 2-point and 4-point probes and differential delay 915MHz OFC-SAW devices. The 2 and 4-point probes were used to evaluate the sheet resistance of the uniform films. The SAW is the only device that can determine the resistivity of the non-uniform film and evaluate the sensor response simultaneously. The SAWs were measured using the procedure in section 4.2.1. The SAW propagation loss was measured as the difference between the differential amplitudes of the reflector pulses before and after film deposition. The films were exposed to a 2% H_2 98% N_2 gas mixture, to evaluate their response. The temperature coefficient of resistance (TCR) was also measured because it must be known in order to account of the temperature anomalies and reduce false readings.

The experimentation began with uniform a 500Å SnO_2 film with no Pd that was annealed for 20 minutes in order to serve as a reference; this device barely measured H_2 gas sensitivity at room temperature. A 10Å Pd film was added to the 500Å SnO_2 in the next experiment and H_2 gas sensitivity increased to 3% with relatively slow response times of 30 seconds to turn on and 3mintues to return. The Pd film thickness and anneal times was doubled and increased to 50min, respectively; this device showed no H_2 gas sensitivity at room temperature. The first working device was a uniform 500Å SnO_2 with 20Å of Pd and a 20min anneal time (Figure 6-9); this device showed a 25% change in resistance when exposed to H_2 gas with a response time of 20 seconds to turn on and 2mintues to return. The group delay increased because the wave velocity slows due to the decrease in sheet resistance toward the short circuit case. From Figure 5-5, 20Å Pd may be the ideal thickness selection because it is the transition area (percolation point) between the ultra-thin (i.e. discontinuous) and continuity, and this is the area where H_2 gas sensitivity is the greatest. Next, the SnO_2 film thickness was halved (250Å) which decreased sensitivity to 20% but decreased response times to 20 seconds for turn-on and 2 minutes to return (Figure 6-10). The films were made non-uniform by depositing them through a shadow mask. The 500Å SnO_2 film (Figure 6-11) showed 3 orders of magnitude higher sheet resistance and the sensitivity to H_2 gas also increased to 35% with on-off times decreased to 25 and 75 seconds, respectively. The SnO_2 film thickness was halved once more (250Å) and the sensitivity decreased to 10% the on-off times also decreased to 20 seconds. The anneal time on the 250Å non-uniform films was decreased from 20 to 12 and finally 5minutes and the sensitivity increased to 50% and 80%, respectively, and the on-off time decrease to around 1 second (Figure 6-12 and Figure 6-13). A non-uniform 250Å SnO_2 film with 20Å Pd and 5 minute anneal time

(using the anneal process shown in Figure 6-2) produced the fastest responding and most stable sensors. A summary of the experimentation is presented in Table 6-3.

It is remarkable that these non-uniform SnO_2-Pd films posses such a high H_2 gas sensitivity at room-temperature considering that they are not doped with In_2O_3 (or another acceptor impurity) as was necessary with the work of Shukla [51, 52]. There may interesting physics at play here which warrant further investigation. The CAAT research group has recently began a collaborative effort with Oakridge National Labs' (ORNL) Center for Nanophase Material Science (CNMS) facility in order to fully characterize the nano-structure of the SnO_2 films on YZ-$LiNbO_3$ substrate.

Table 6-3. A summary of the key process parameters: SnO_2 and Pd thickness, anneal time and film profile and their effect on film parameters: sheet resistance, H_2 gas sensitivity, aging rate and temperature coefficient of resistance (TCR).

Measurement Method	SnO_2 (Å)	Pd (Å)	Anneal Time (min)	Film Thickness Profile	Rs (Ω/□)	H_2 Gas Sensitivity at 25°C	On Time (sec)	Off Time (sec)	TCR
2 point probe	500	0	20	Uniform	3×10^{5}	0	----	----	-0.05
2 point probe	500	10	20	Uniform	8×10^{4}	3%	30	180	-0.12
2 point probe	500	20	50	Uniform	10^{5}	0	----	----	-0.06
SAW	500	20	20	Uniform	5.5×10^{4}	25%	30	120	-0.1
SAW	250	20	20	Uniform	1×10^{5}	20%	20	120	-0.12
SAW	500	20	20	non-uniform	7.7×10^{6} *	35%	25	75	-0.02
SAW	250	20	20	non-uniform	7×10^{7} *	10%	20	20	----
SAW	250	20	12	non-uniform	1.3×10^{7} *	50%	6	13	-0.1
SAW	**250**	**20**	**5**	**non-uniform**	**3×10^{7} ***	**80%**	1	1	-0.05

*** These are effective sheet resistance because the film is non-uniform and sheet resistance varies across the film.**

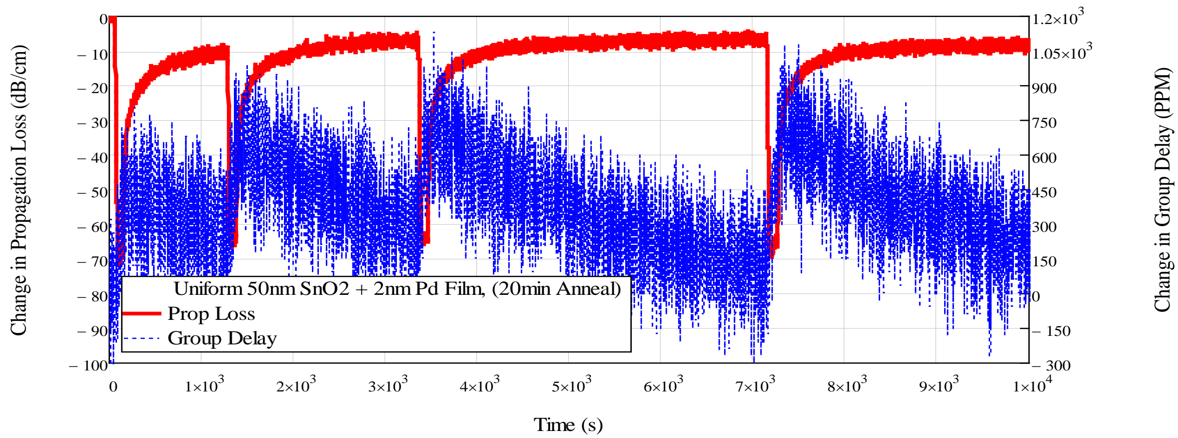

Figure 6-9. The propagation loss and group delay change when a uniform 500Å SnO_2 +20Å Pd film is exposed to H_2 gas. The group delay increase during H_2 exposure because the wave velocity slows due to the decrease in sheet resistance toward the short circuit case.

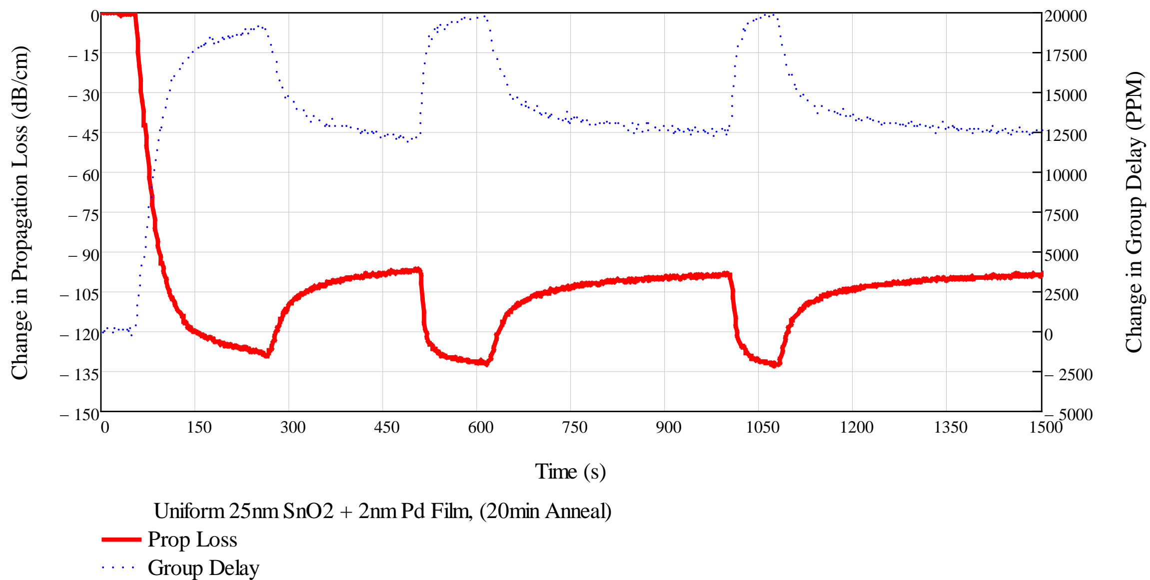

Figure 6-10. The propagation loss and group delay change when a uniform 250Å SnO_2 +20Å Pd film is exposed to H_2 gas. The group delay increase during H_2 exposure because the wave velocity slows due to the decrease in sheet resistance toward the short circuit case.

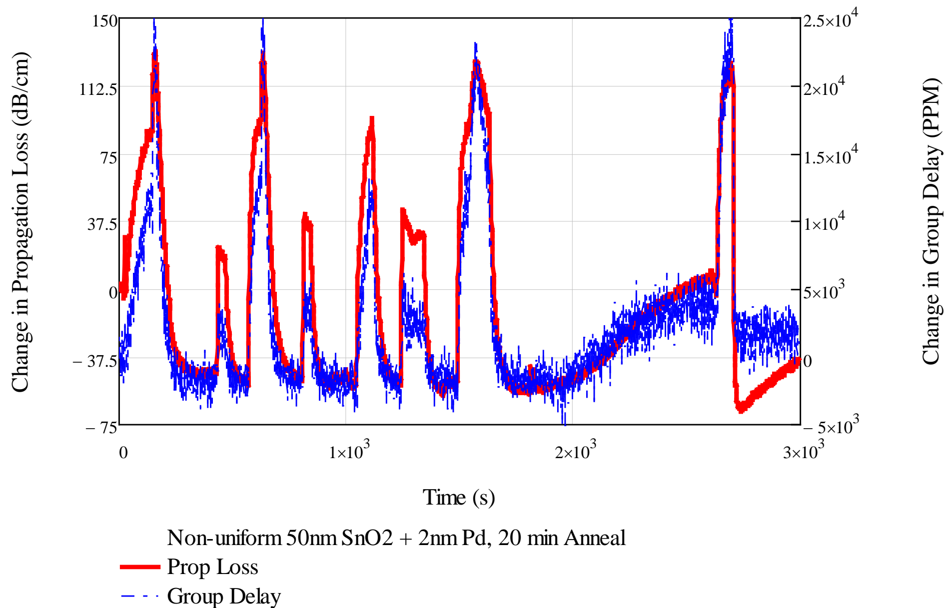

Figure 6-11. The propagation loss and group delay change when a non-uniform 500Å SnO_2 +20Å Pd film is exposed to H_2 gas. The film is annealed for 20 minutes. The group delay increase during H_2 exposure because the wave velocity slows due to the decrease in sheet resistance toward the short circuit case. After each large cycle the gas lines were purged of any remaining H_2 which resulted in the small changes in propagation loss every other cycle.

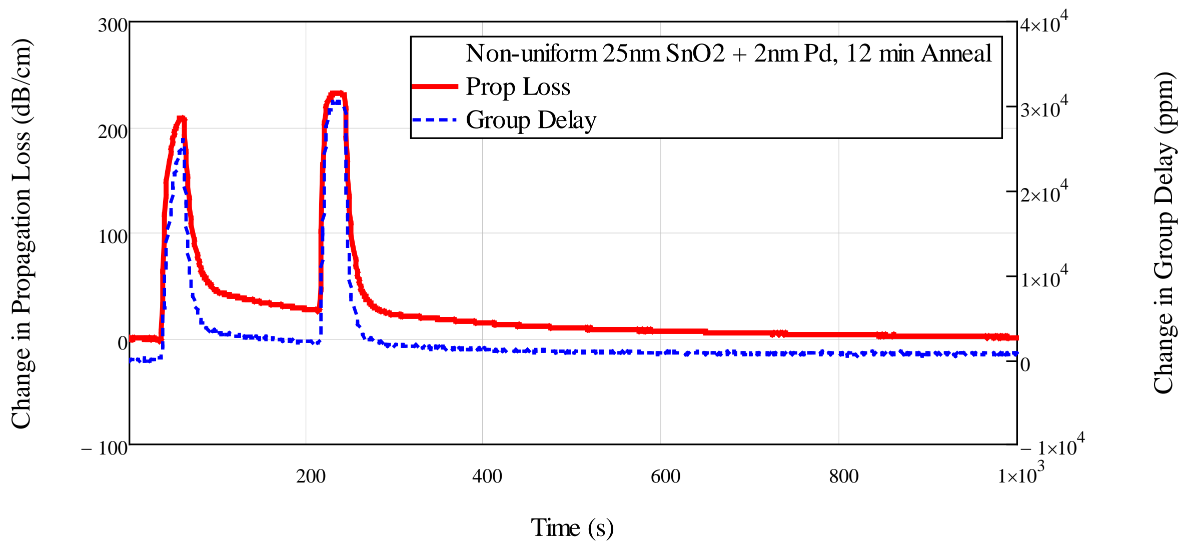

Figure 6-12. The propagation loss and group delay change when a non-uniform 250Å SnO_2 +20Å Pd film is exposed to H_2 gas. The film is annealed for 12 minutes. The group delay increase during H_2 exposure because the wave velocity slows due to the decrease in sheet resistance toward the short circuit case.

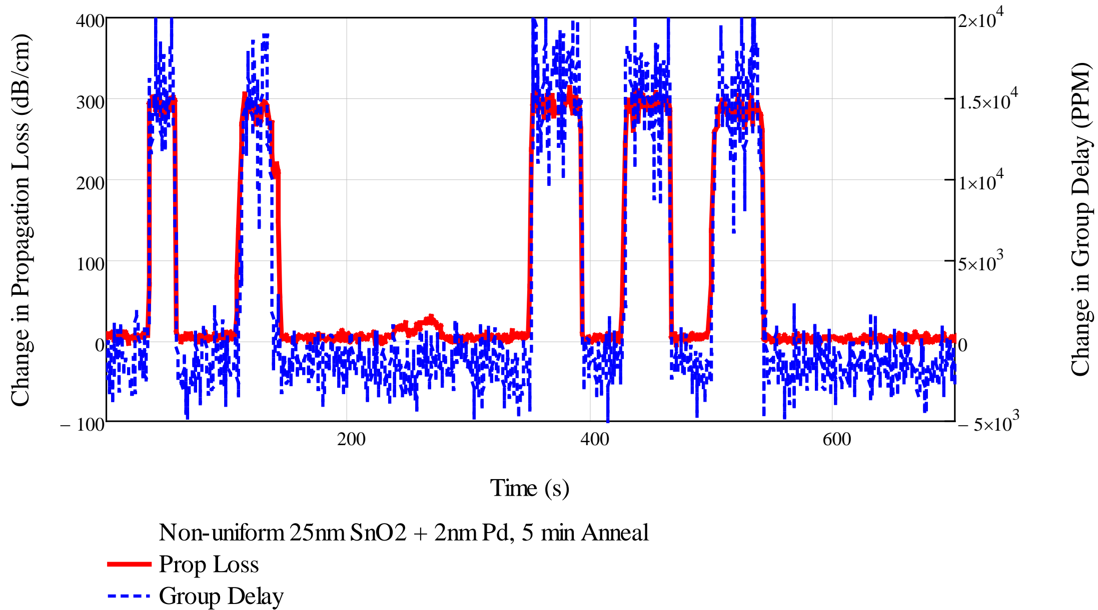

Figure 6-13. The propagation loss and group delay change when a non-uniform 250Å SnO_2 +20Å Pd film is exposed to H_2 gas. The film is annealed for 5 minutes. The group delay increase during H_2 exposure because the wave velocity slows due to the decrease in sheet resistance toward the short circuit case.

6.5 Film Aging

The biggest threat to the long-term H_2 gas sensitivity of the Pd-SnO_2 film is exposure to large concentrations of hydrogen. Hydrization (PdH_x) robs the catalytic ability of Pd when H_2 consumes all the available bonding sites on the Pd atom. Pd is called alpha phase (α-phase) and PdH_x is called Pd's beta phase (β-phase)[48]. This is observed as a gradual decrease in sensitivity with each cycle. This effect is seen in the 250Å uniform SnO_2 films (Figure 6-10) but is not evident in the non-uniform 250Å-5minute annealed films (Figure 6-13).

The resistance may also increase over time due to the annihilation of conducting Sn ions by absorbed O_2 molecules. A 3 hr observation of the non-uniform 250Å 20-minute annealed film did not show this effect (Figure 6-14). This resulted is promising but more conclusive long term observation must be made.

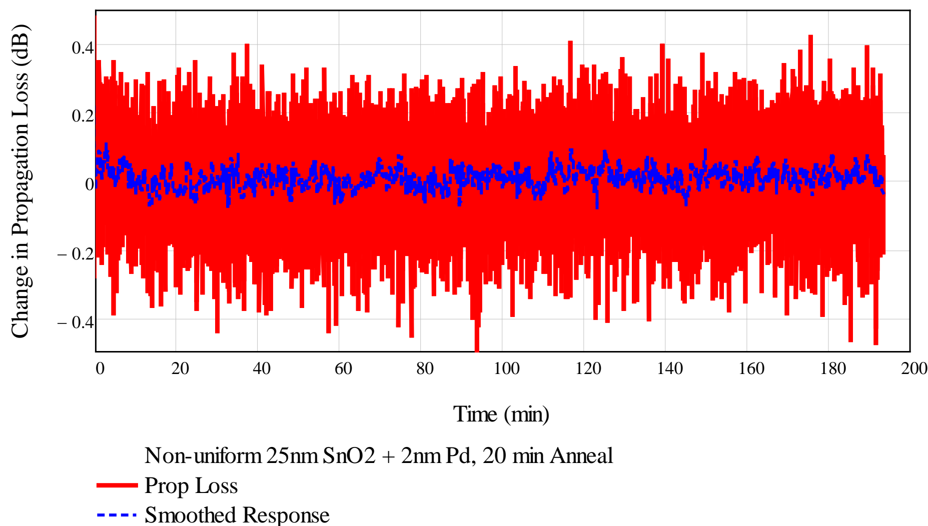

Figure 6-14. Plot of the change in propagation loss for a over a 3hr period. There is no observed change for this time period.

6.6 CHAPTER 6 Summary

The most important points from chapter 6 is presented below:

1. Tin dioxide (SnO_2) films have been used for the detection of hydrocarbon gases since the 1970s . The addition of a thin-film activation layer of palladium (Pd) or platinum (Pt)

makes the film more sensitive and selective to H_2 gas and lowers the activation energy (and thereby the operating temperature).

2. The response kinetics of the H_2-Pt-SnO_2 interaction are discussed in section 6.2.
3. The reproducible growth of thin semiconducting films requires the identification and precise control of critical process parameters using an experimental decision analysis. From Table 6-1 the most important parameter is the film thickness profile, followed by tie between the annealing time and Pd film thickness then SnO_2 film thickness .
4. SnO_2 Film depositions were performed using an electronic beam evaporator using 99.9% pure pellets were purchased from Kurt J Lesker Company. It was evaporated from and Al_2O_3 crucible liner and evaporated using 10kV and 28 to 32mA of current.
5. Successful integration of SnO_2 with a the YZ-$LiNbO_3$ substrate requires that the annealing temperature be kept below 400°C to protect the piezoelectric properties of the substrate the Al electrodes from oxidizing. To err on the side of caution, 350° was chosen as the anneal temperature for all devices.
6. SnO_2 films need to be grown precisely in the propagation path of the SAW which was accomplished in two methods: (1) the films were patterned using standard photolithographic techniques (which created a uniform thickness profile) or (2) it is evaporated through a shadow mask onto a packaged and bonded device (which created a non-uniform thickness profile).
7. A SAW propagation loss prediction model for non-uniform films was developed using the acoustoelectric equation and Mayadas-Shatzkes approximation for the resistivity of a

polycrystalline films. It predicts the film insertion loss as a function of deposition aperture and film thickness.

8. A non-uniform 250Å SnO_2 film with 20Å Pd and 5 minute anneal time (using the anneal process shown in Figure 6-2) produced the fastest responding and most stable sensor.

CHAPTER 7 OFC-SAW H2 GAS SENSORS

7.1 Chapter Overview

This chapter discusses the embodiment for the OFC-SAW H_2 gas sensors in section 7.2, the requirements for the integration of the sensors in a system in section 7.3, sensor fabrication in section 7.4, measurement (section 7.5) and H_2 gas sensitivity of a network of 3 sensors in section 7.6, future work is discussed in section 7.7, and a summary of the major points of the chapter in section 7.8.

7.2 Embodiment of OFC RFID Tag Sensor

The tags that were used for the H_2 sensors were 5 chip, dual delay OFC-SAW tags, which are centered at 915MHz with a 9.1% factional null bandwidth (NBW). Four different OFC codes (BHF401 to BHF404) were designed; the OFC codes on each device was spaced such that all the reflector banks are contiguous in time and fit in a *1.2* to *5μs* window (Figure 7-2). The SnO_2 film is grown between the first and second reflector bank. The chip time length is given by

$$\tau_c = \frac{N_c + 1}{NBW} \qquad (7\text{-}1)$$

where N_c is the number of chips. The chip frequencies are given by

$$f_{c_i} = f_0 - \frac{NBW}{2} + \frac{i}{\tau_c} \qquad i = 1 \ldots N_c \qquad (7\text{-}2)$$

The number of wavelengths per chip is given by

$$\lambda_{c_i} = f_{c_i} \tau_c \tag{7-3}$$

and must be equal to an integer number of wavelengths or half wavelength in order to maintain the conditions of orthogonality. λ_{ci} is also equal to the number of electrodes in each reflector chip, N_{Pi}. Assuming that there is minimal energy storage in the reflectors, the OFC reflector bank may be modeled as a sum of *sinc* functions given by

$$H_{OFC}(f) = \sum_{i=1}^{N_c} \left[\operatorname{sinc}\left(\frac{\pi (f_{c_i} - f) N_{pi}}{f_{c_i}} \right) \exp\left(- j2\pi \cdot f \cdot \left(\tau_c i + \tau_d\right)\right) \right] \tag{7-4}$$

where τ_d is the initial delay of the first chip in the reflector bank. The properties of the IDT are $f_s = 2 \cdot fo$, $N_P = 10$, $W_B = 45\lambda$; two IDTs were connected in parallel to create two tracks and match the impedance of the dipole antenna (Figure 2-11). The specifications for the 4 tags are shown in Table 7-1; a schematic of the 4 devices and a plot of the measured S_{11} time domain response of the four codes is shown in Figure 7-1 and Figure 7-2. The insertion loss in a matched tag is a combination of the *6dB* bi-directional loss from the IDT, substrate free-space propagation loss and the reflector losses. From (2-25) the free space propagation loss of YZ-$LiNbO_3$ is *0.911dB/µs* at 915MHz. The net reflectivity of each chip is a function of the electrode thickness and a/p ratio given by (2-19), the reflector loss for a each chip is around *2dB*. The total insertion loss for the reference reflectors (Ref1) tag is 9 to 10.25dB (9 dB for BHF401 and 10.25dB for BHF404) and the insertion loss for the sensing reflectors (Ref2) is 11.15 to 12.25dB. The 250Å non-uniform SnO_2 films adds about 8dB of loss to the sensing reflectors, so 20dB insertion loss is expected− assuming that there are no fabrication defects.

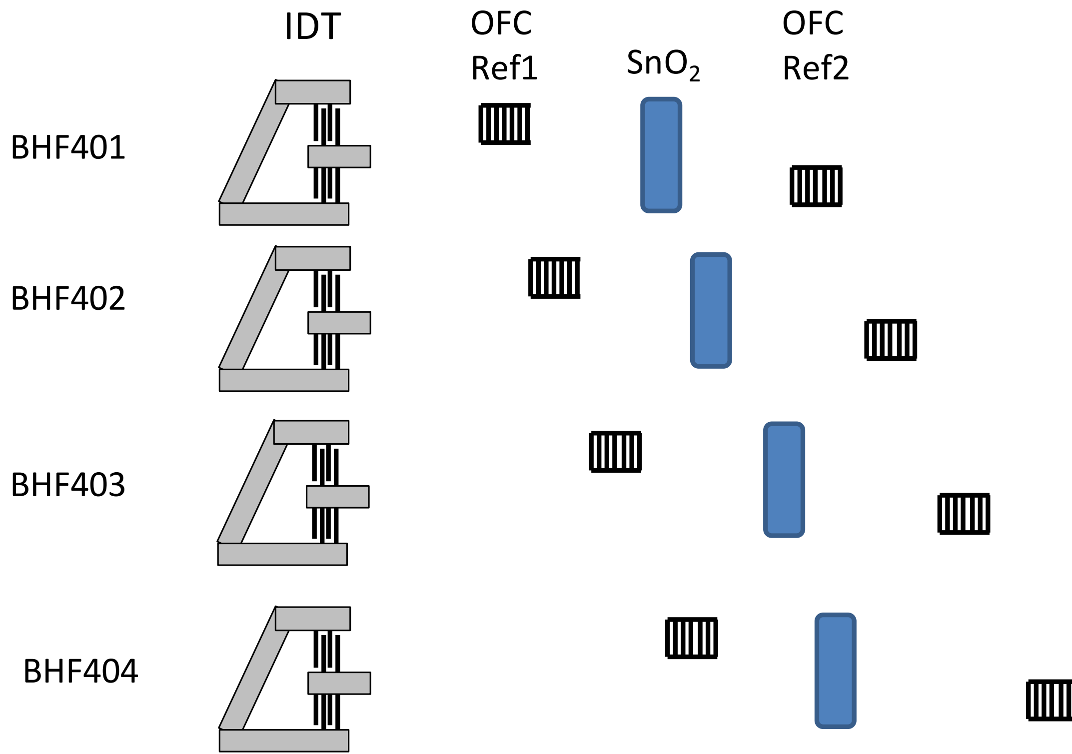

Figure 7-1. A schematic of the 4 OFC-SAW codes that were created

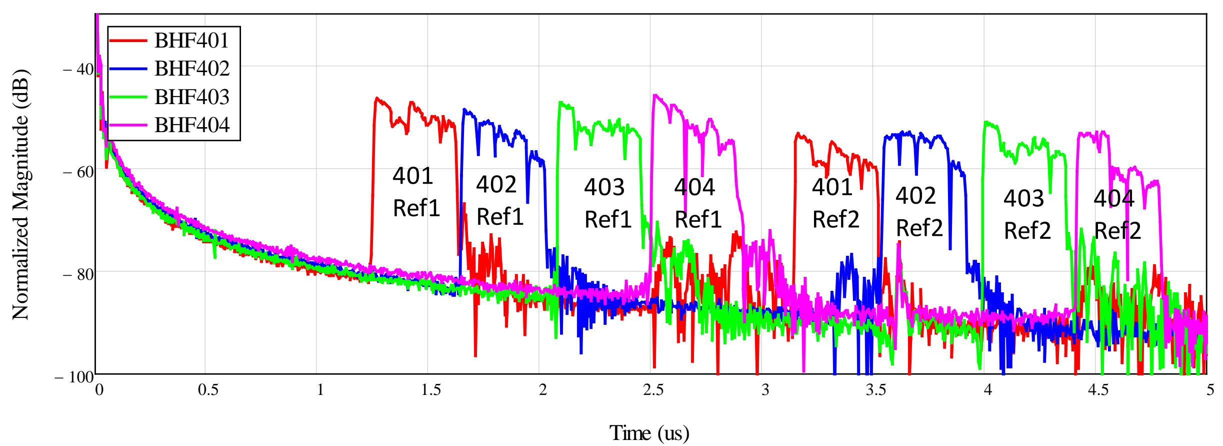

Figure 7-2. A plot of the measured S_{11} response of OFC-SAW tags BHF401 to 404.

Table 7-1. A summary of the specifications of OFC-SAW H_2 gas sensors

Device	Code	Ref1 (µs)	Ref2(µs)	Chip Length (µs)
BHF401	21435	1.2387	3.1526	74.865ns
BHF402	54231	1.6405	3.5544	74.865ns
BHF403	41253	2.059	4.0063	74.865ns
BHF404	45132	2.4942	4.4248	74.865ns
	Freq (MHz)	**Np**	**h (Å)**	**a/p**
f1	888.282	66	950	0.5
f2	901.641	67	950	0.5
f3	915	68	950	0.5
f4	928.359	69	950	0.5
f5	941.718	70	950	0.5

7.3 Tag Insertion Loss and Delay Change Predictions

From Figure 6-6 films that are deposited through a 0.25mm aperture possess 5dB less propagation loss than films deposited through a 0.5mm aperture and 250Å films have a much faster H_2 gas response time as compared to the 500Å films. These results indicate that the 250Å SnO_2 + 20Å Pd film that is annealed for 5mins is the best film candidate from passive wireless H_2 gas detection using OFC-SAW devices. To use this film in a wireless sensor system the following conditions must be met:

1. Total insertion loss (*IL*) must be less than maximum allowable *IL* for the system to detect the tag and changes in amplitude and delay in a sensing event.

2. The change in IL due to H_2 exposure must be greater than the random fluctuations (noise) in the system.

The effective sheet resistance (R_{S_eff}) as a function of the deposition aperture and film thickness plot in Figure 6-7 is used to predict the change in IL and group delay as a function of the fractional change in the film's resistance when exposed to H_2 gas. The equations for the change in IL (in dB) and the fractional change in group delay are given by

$$\Delta IL_{dB} = -8.686 \cdot [\alpha\left(R_{s_eff}(1-\Delta)\right) - \alpha\left(R_{s_eff}\right)] \tag{7-5}$$

$$\Delta GD = \frac{\dfrac{1}{v_{AE}(R_{s_eff})} - \dfrac{1}{v_{AE}(R_{s_eff}(1-\Delta))}}{\dfrac{1}{v_{AE}(R_{s_eff})} - \dfrac{1}{v_{oc}}} \tag{7-6}$$

where Δ is the fractional decrease in %, α is given by acoustoelectric portion of equation (3-50) and V_{AE} is the acoustoelectric velocity (3-55). Figure 7-3 and Figure 7-4 shows plot of the predicted change in IL for a 500 and 250Å film deposited through and 0.5 and 0.25mm aperture, respectively; the predicted change in group delay for both films is shown in Figure 7-7. The predicted IL plots show the H_2 gas detection range for a system that can accept *50dB* of insertion loss and has +/- *0.2dB* of amplitude noise on the signal. The H_2 detections begins when the ΔIL is greater the noise and stops when the total IL, $(IL_0 + \Delta IL)$, is greater than or equal to the maximum acceptable IL of the system; the 250Å film has a larger detection range than the 500Å film for this hypothetical system.

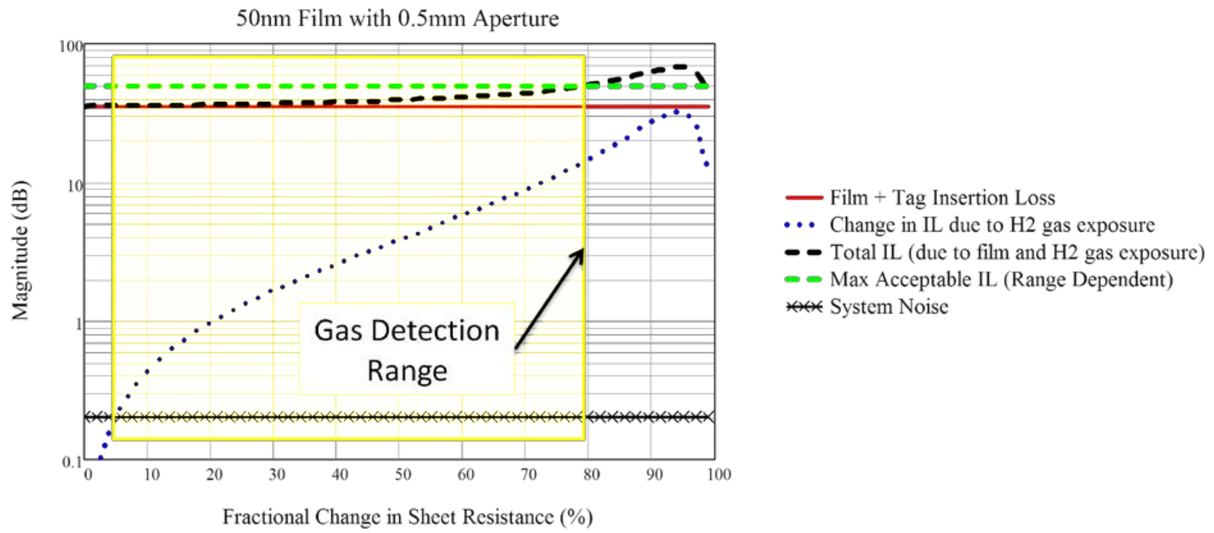

Figure 7-3. A plot of the change in insertion as a function of the change in sheet resistance when a 500Å non-uniform SnO_2 film exposed to H_2 gas.

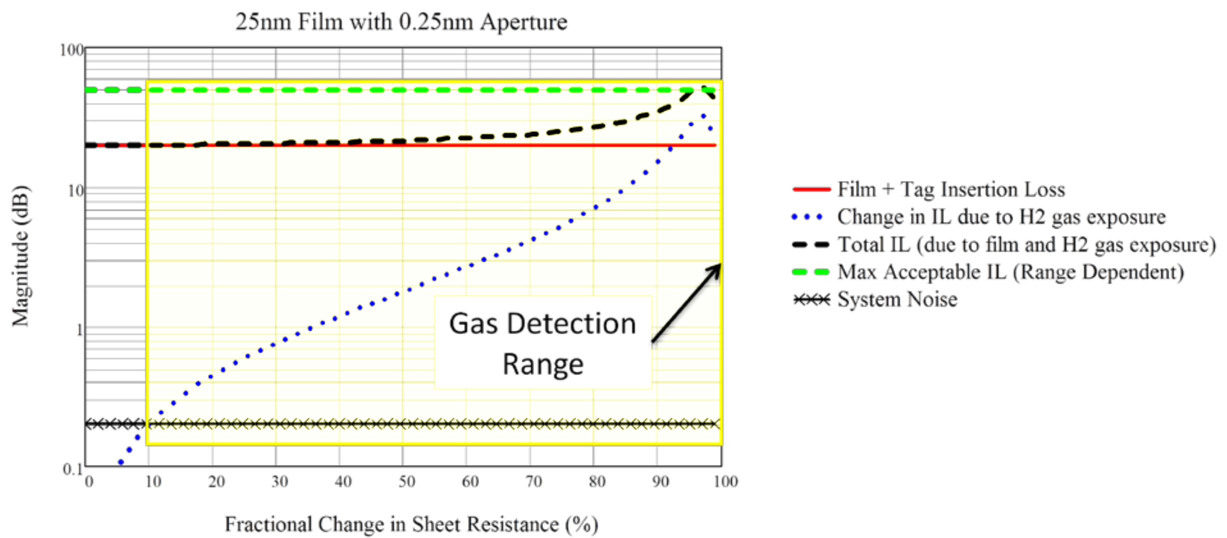

Figure 7-4. A plot of the change in insertion as a function of the change in sheet resistance when a 250Å non-uniform SnO_2 film exposed to H_2 gas.

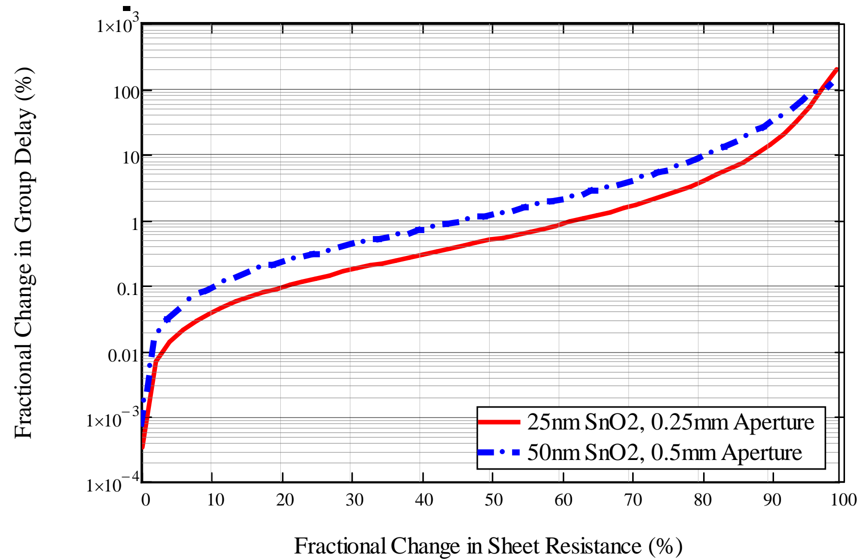

Figure 7-5. A predictive plot of the change in group delay as a function of the change in sheet resistance.

7.4 Fabrication

The experimental details of growth and processing of SnO_2 films was presented in chapter 6. A new fixture was designed to allow the fabrication of up to four devices simultaneously. This fixture saved fabrication time and reduced experimental variability. The fixture was made from a Teflon and FR4 base and lid, with 150µm copper foil for the aperture (Figure 7-6). The copper foil was masked with PCB transfer paper and etched in sodium per sulfate in order to create the apertures and ensure that their widths were equal. After film deposition the packaged devices were placed in a glass Petri dish and annealed. After annealing each device was tested to ensure that it was operational and sensitive to hydrogen. A protective copper lid with small perforations above the film was soldered to each package and finally the package was soldered to a planar antenna (Figure 7-7).

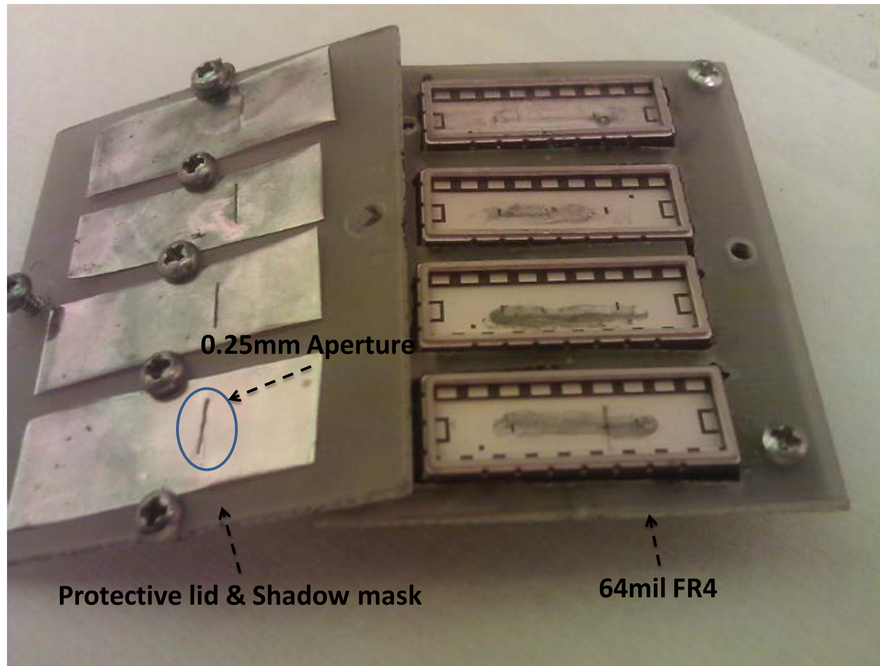

Figure 7-6. A picture of the shadow mask fixture for the film growth on 4 OFC-SAW tags simultaneously.

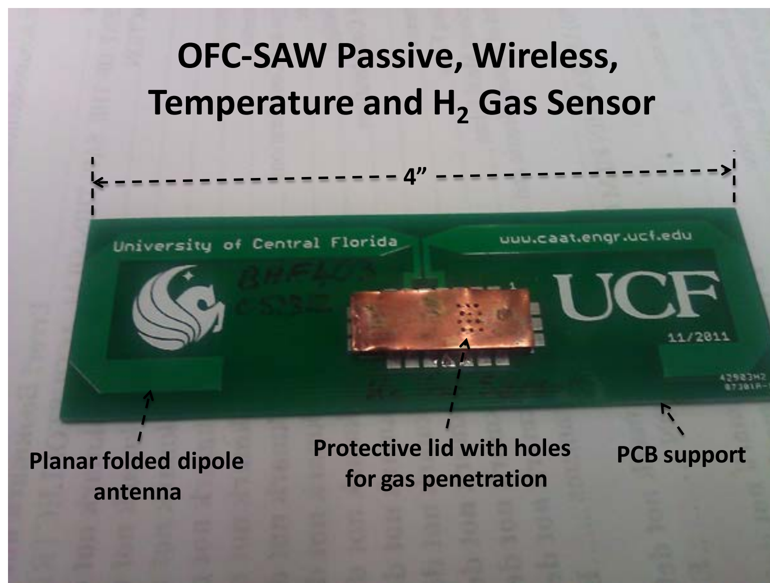

Figure 7-7. A picture of the packaged OFC-SAW temperature and H_2 gas sensor with antenna.

7.5 Measurements

Three devices (BHF402 to 404) where simultaneously interrogated from a distance of 1.5 feet while they were exposed to various flow rates of 2% H_2, 98% N_2 gas. A foam board was used to hold the antenna and sensors in place during experimentation (Figure 7-8) and provided excellent mechanical stability. The sensors were placed directly above the gas flow tubes in order to benefit from the buoyancy of H_2 gas and increases the chances of exposure at low flow rates; the transmitting/receiving (Tx/Rx) antenna was placed above sensors (Figure 7-9). Tx/Rx and tag antennas are a planar folded-dipole design at 915 MHz [113]. The mixed H_2-N_2 was flowed into a flow rate controller with a capacity of 0 to 6 cubic centimeters per minute (ccm). The output of the flow rate controller was divided into three tubes of equal length (Figure 7-10) and flowed directly onto the OFC-SAW H_2 sensors (Figure 7-11). The division of the flow into 3 equal length lines means that the maximum H_2 flow that each sensor can receive is 0 to 2 ccm. The interrogation was performed using an Agilent network analyzer that was controlled using the software that was developed for real-time, *in-situ* monitoring and grabbed data at a rate of 1.2 seconds per sample (Figure 7-12). The VNA was set to a center frequency of 915 MHz with a span of 150 MHz, collected 1601 points per sweep with 10 dBm output power. The data were grabbed in the time domain, the OFC reflector banks of each device was time gated then correlated against the gated a reference reflector (upper left of Figure 7-13). This produced two compressed pulses (upper right of Figure 7-13), the first an autocorrelation of the reference reflector (Ref1) and the second a cross-correlation of the sentencing (Ref2) and reference reflectors. The group delay of the two pulses was calculated using a center-of-amplitude function given by

$$C_A = \frac{\sum_{n=0}^{N-1}(|x_n| \cdot n)}{\sum_{n=0}^{N-1}|x_n|} \quad (7\text{-}7)$$

where N is the number of data points and x_n is each data point. This function calculates the time location of the average energy, and as the pulse amplitude changes so does C_A. The fractional change in C_A is plotted in the lower half of Figure 7-13. The amplitude of the second pulse decreases when the SnO_2 is exposed to 2% H_2 gas, which shifts the C_A toward to first pulse and decreases C_A. All 3 sensors respond instantaneously with 1second turn on and off times. Device BHF404 is the most sensitive; it is attenuated into noise at flow rates greater or equal to 1ccm. BHF403 is attenuated into noise for flow rates greater than or equal to 1.17ccm. The amplitude changes of BHF402 appears to be directly proportional to the H_2 gas flow rate. None of the devices responded to a gas flow lower than 0.667ccm.

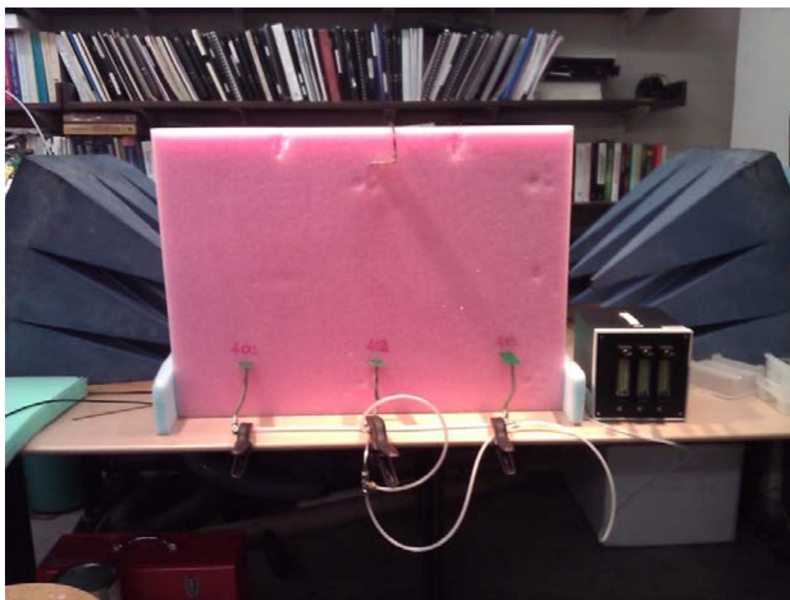

Figure 7-8. A picture of the wireless test setup for the passive, wireless, OFC-SAW H_2 gas sensors.

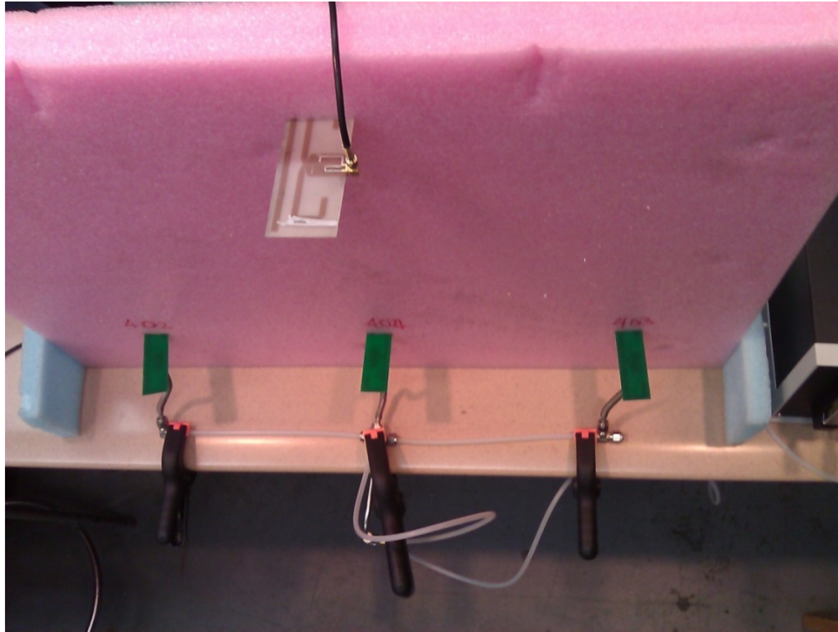

Figure 7-9. A picture of the placement of the Tx/Rx antenna and OFC-SAW tags.

Figure 7-10. This is a picture of the 3-way splitter and the gas flow to the three sensors.

Figure 7-11. A picture of the gas flow tube filling gas precisely onto the SnO_2 film.

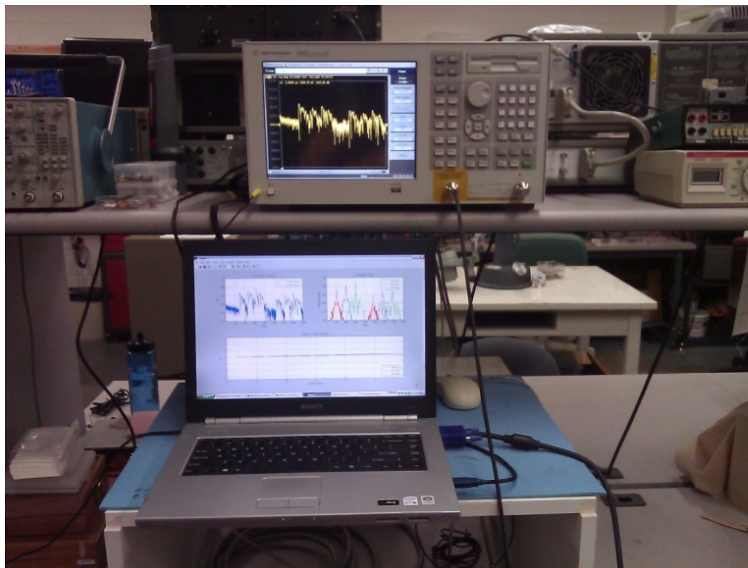

Figure 7-12. A picture of the VNA and decor data acquisition computer.

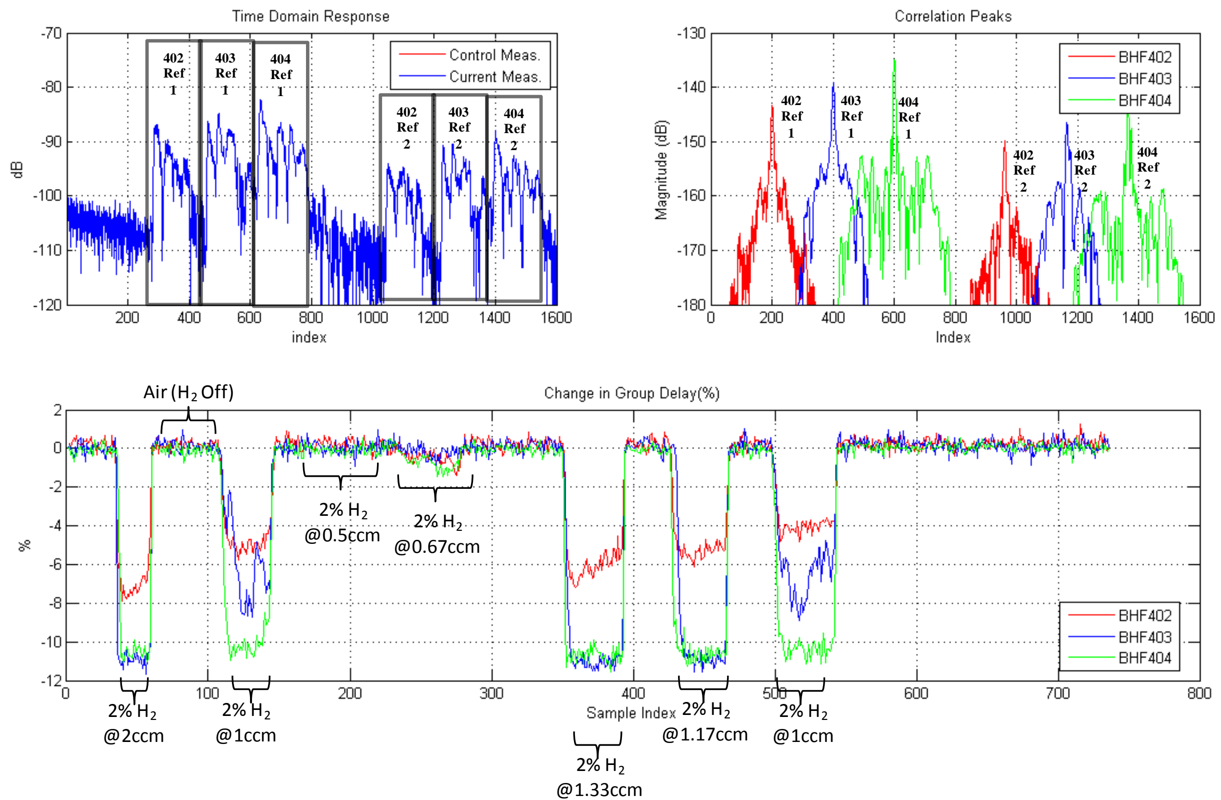

Figure 7-13. A plot of the MATLAB data acquisition software, which grabs data from the network analyzer, in real time and process 3 devices in ~ 1 second.

7.6 H_2 Sensitivity

In the absence of a gas mixing equipment the sensors were exposed to various flow rates of H_2 gas. This is equivalent to exposing the film to various concentrations of hydrogen gas because the number of H_2 molecules that react with SnO_2 changes with flow rate and gas concentration. The change in propagation loss and the fractional change in group delay of the sensors is plotted in Figure 7-14 and Figure 7-15. BHF402 is used to determine the amplitude and delay sensitivity because BHF403 and BHF404 becomes saturated at relatively low flow

rates. Figure 7-14B and Figure 7-15B shows a linear relationship the change in propagation loss and group delay as a function of gas flow rate for BHF402. This suggests that the sensors may have a linear response to various concentrations of H_2 gas. Given the high fractional change at relatively low flow rates, the sensors are may be best utilized for low concentrations (in hundreds of ppm range) of H_2 in order to prevent saturation and observe a linear response.

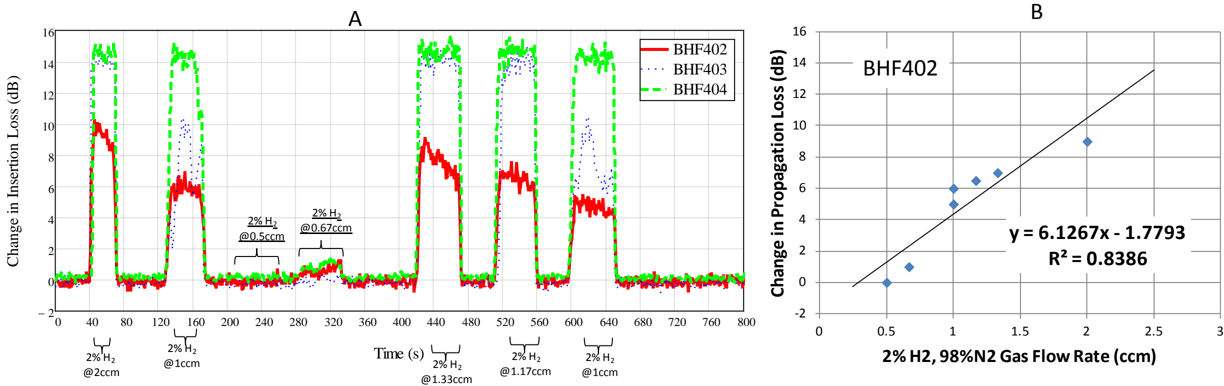

Figure 7-14 A: Plot of the change in propagation loss as a function of time for 3 passive wireless OFC-SAW devices. B: a plot of the change in propagation loss vs. the flow rate of 2% H_2 gas for device BHF402.

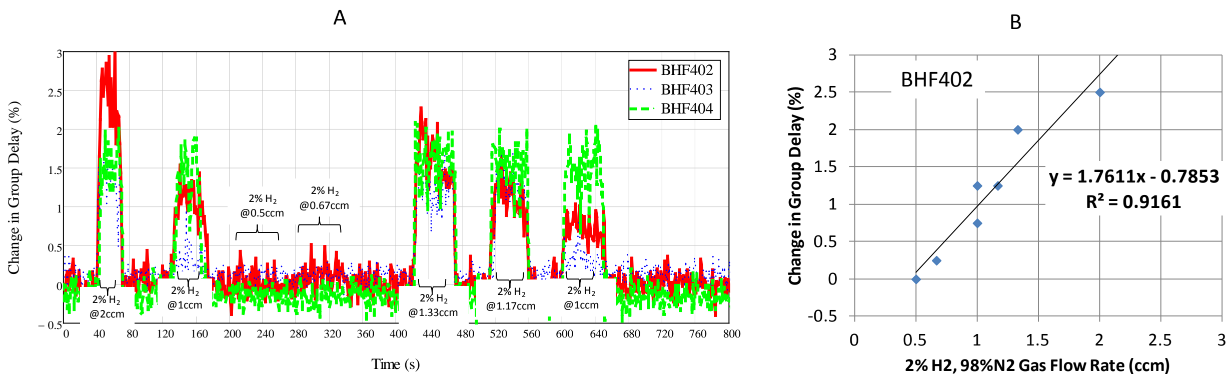

Figure 7-15 A: Plot of the change in group delay as a function of time for 3 passive wireless OFC-SAW devices. B: is a plot of the change in group delay vs. the flow rate of 2% H_2 gas for device BHF402.

7.7 Future Work

The YZ-$LiNbO_3$ substrate has been shown to operate up to 450°C [109]; however, the operation of the OFC-SAW tag-sensor is limited to 120°C due the temperature limitations of solder and the printed circuit board (PCB) antenna (Figure 7-7). An integrated, single-wafer OFC-SAW tag and antenna on YZ-$LiNbO_3$ (called the SAWtenna) was recently demonstrated (Figure 7-16)[114]. This modification extends the temperature of operation of the tag to 450°C by eliminating the temperature restrictions of the PCB and solder. Future work will include the integration of the SnO_2 film with the SAWtenna and yield a high temperature H_2 gas sensor. The integration of the SnO_2 films with the OFC-SAWtenna device requires significant process development and characterization of the SnO_2 films for high temperature operation on YZ-$LiNbO_3$.

A thorough analysis of the adsorption and desorption physics of the non-uniforms films is necessary. Films of this may prove useful for other types of gas and physical sensors.

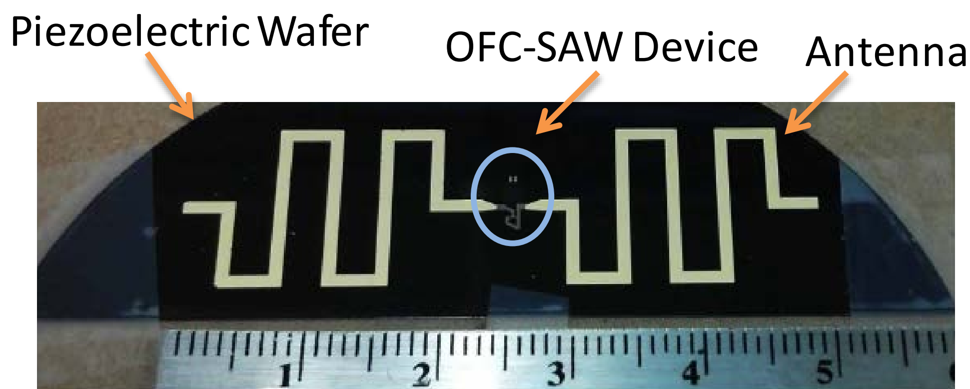

Figure 7-16. Picture of the SAWtenna on black YZ-$LiNbO_3$ substrate. SAW sensor is integrated with the piezoelectric wafer, which eliminates the needs for chip packing, bond wires, solder and PCB. The maximum temperature of operation for this integrated sensor is around 450°C.

7.8 CHAPTER 7 Summary

1. The tags that were used for the H_2 sensors were 5 chip, dual delay OFC-SAW tags which are centered at 915MHz with a 7.1% factional bandwidth (NBW).
2. The total insertion loss for the reference reflectors (Ref1) tag is 9 to 10.25dB (9 dB for BHF401 and 10.25dB for BHF404) and the insertion loss for the sensing reflectors (Ref2) is 11.15 to 12.15dB. The 250Å non-uniform SnO_2 films adds about 8dB of loss to the sensing reflectors, so 20dB insertion loss is expected− assuming that there are no fabrication defects.
3. To use this film in a wireless sensor system the following conditions must be met:
    a. Total insertion loss (*IL*) must be less than maximum allowable *IL* for the system to detect the tag and changes in amplitude and delay due in sensing event.
    b. Change in *IL* due to H_2 exposure must be greater than the random fluctuations (noise) in the system.
4. A new fixture was designed to allow the fabrication of up to four devices simultaneously. This fixture saved fabrication time and reduced experimental variability.
5. Three devices (BHF402 to 404) where simultaneously interrogated from a distance of 1.5 feet while they were exposed to various flow rates of 2%H_2, 98%N_2 gas.
6. Figure 7-14B and Figure 7-15B shows a linear relationship the change in propagation loss and group delay as a function of gas flow rate for BHF402. This suggests that the sensors may have a linear response to various concentrations of H_2 gas. Given the high

fractional change at relatively low flow rates the sensors are may be best utilized for low concentrations (in hundreds of ppm range) of H_2 in order to prevent saturation and observe a linear response.

CHAPTER 8 CRYOGENIC LIQUID LEVEL SENSING

8.1 Chapter Overview

It is documented that acoustic and shear wave devices operate well at cryogenic temperatures [4, 115, 116]. In concept SAW devices maybe ideal for cryogenic liquid level applications because the wave energy is damped by the liquid and returns to normal operation once the liquid is removed, a simple switch. The robustness of a SAW cryogenic sensor is contingent upon the ability of the crystal substrate and metal electrodes to repeatedly withstand thermal shock resulting from large temperature gradients. These concepts are addressed by first examining the behavior of commercial SAW lithium niobate ($LiNbO_3$) and quartz filters, initially hermetically sealed and then with the lids removed (section 8.2). Commercial devices were first examined because they would provide verification that a standard, commercial and manufacturable process could be used in the ultimate fabrication of devices for operation at cryogenic temperatures. The issue of thermal shock (section 8.4) is investigated by the rapid temperature cycling of bare die of varying sizes, as well as packaged commercial and coded devices.

Lastly, experimentation was performed on Orthogonal Frequency Coded (OFC) devices fabricated at UCF (section 8.5). In a cryogenic liquid tank, this device serves as a switch, a temperature sensor and a unique RFID tag. This ability is ideal in a cryogenic tank environment as the level of the liquid may be quickly discerned passively and wirelessly (Figure 8-1).

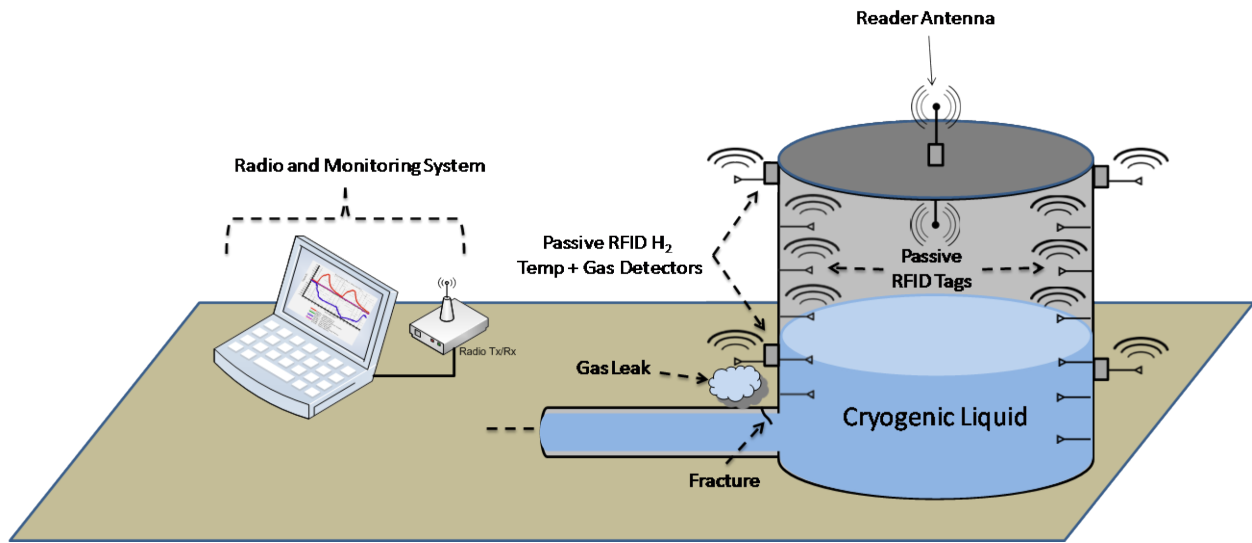

Figure 8-1. Schematic of cryogenic liquid tank with a passive wireless liquid level and gas leak detection system.

8.2 Commercial SAW Device Performance

8.2.1 Hermetical Sealed Surface Mount Packages

Initial tests were performed on commercially available SAW parts provided by Triquint Semiconductor Inc., (formerly SAWTEK). These devices were lithium niobate ($LiNbO_3$) and quartz filters that are in surface mount packages.

Figure 8-2. Dual-sided OFC SAW Device on $LiNbO_3$

The following device information is provided:

Part # 523750 Quartz SAW Filter
Die size ≈ Length: 10.5mm; Width: 2mm
Substrate: ST Quartz
Package Dimensions: 1.8cm x 0.6cm
Center Frequency: 140MHz
Bandwidth: 0.73MHz

Part # 856070 Lithium Niobate Filter
Die size: ≈ Length: 10.5mm; Width: 2.5mm
Substrate: YZ $LiNbO_3$
Package Dimension: 1.3cm x 0.6cm
Center Frequency: 140MHz
Bandwidth: 14.2MHz

One of each device was solder mounted to a printed circuit board (PCB) to which two subminiature version-A (SMA) female connectors were attached. Semi-rigid 50-ohm coaxial cables were used to connect the SMA connectors to a vector network analyzer (VNA), which extracted the RF signal. The device under test (DUT) passband, S_{21}, was measured before, during and after immersion in liquid nitrogen (Figure 8-3 & Figure 8-4). Multiple immersions in liquid nitrogen were measured and observed to test survivability and operating changes. The measured S_{21} performance of both devices looked nearly identical after repeated temperature cycling. They exhibited lower device loss primarily due to the decrease in the aluminum thin film resistance, which is expected**.** The center frequency of the $LiNbO_3$ filter shifted upward by approximately 3MHz during immersion; the 3dB bandwidth also increased by approximately 0.14MHz. This frequency shift is to be expected based on the temperature coefficient of frequency (TCF) being positive[117]. Also evident is an increased passband ripple during submersion, this is an unexpected result. It is believed that the acoustic absorber used to damp

the unwanted wave energy becomes rigid at low temperatures and no longer acts as an acoustic absorber. The quartz filter's center frequency shifted downward by approximately 0.1 MHz and the 3dB bandwidth increased by approximately 0.03MHz. The frequency shift downward is expected because the TCF is negative at low temperatures[118]. The flattened passband at low temperature is also consistent with a time echo due to the loss of acoustic damping at the crystal edges.

Equally as important as the device performance over repeated cycles was that of the test fixture; the solder, PCB and SMA connectors all survived without any evident electrical or mechanical damage. This allowed the design of a test fixture that could facilitate quick measurement of a large number of samples without soldering. It is necessary to cycle large number of devices in order to verify the previously observed behavior.

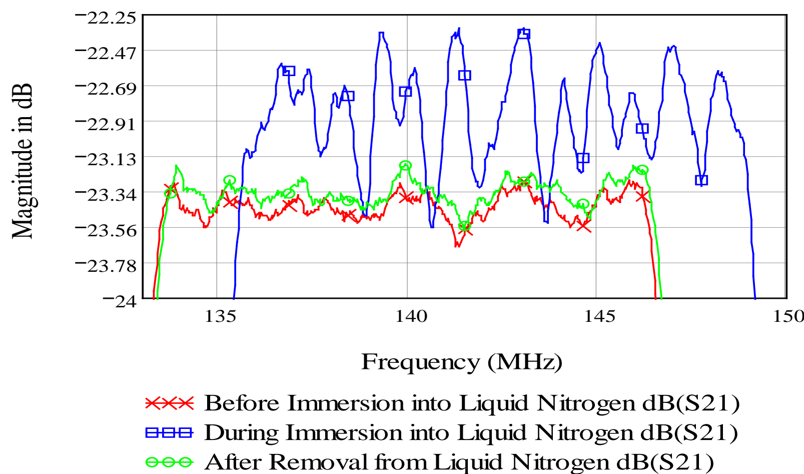

Figure 8-3. Hermetically sealed lithium niobate filter passband comparisons, before during and after submersion in liquid nitrogen

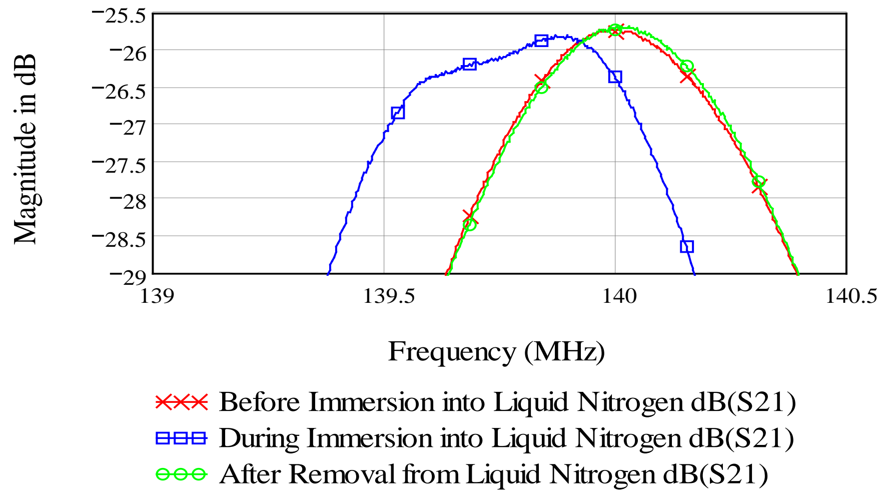

Figure 8-4. Hermetically sealed quartz filter passband comparisons, before during and after submersion in liquid nitrogen.

This fixture consisted of a PCB to which two SMA female connectors were soldered (Figure 8-5); a powerful clip was used to enforce a firm contact between the devices and the PCB. Ten samples of each filter were temperature cycled twenty times and measured before the first cycle and after the last. A comparison of the first and last cycle confirmed the previous observation: there is no degradation in the passband response as a result repeated of thermal cycling.

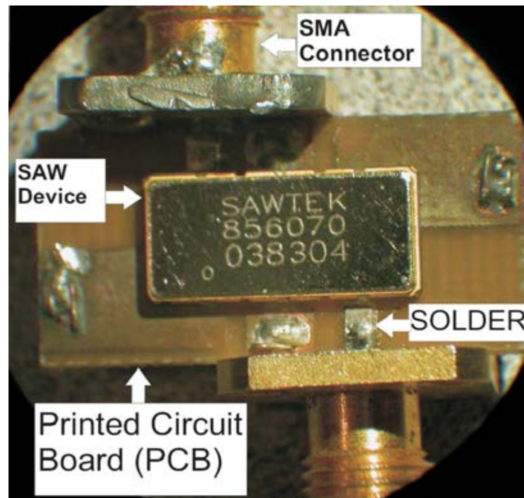

Figure 8-5. A picture of the test fixture that was used to measure the SAW devices when they were submerged in liquid nitrogen.

8.2.2 Opened Lid Surface Mount Devices

This phase of experiments focused on examining the device behavior after the die has direct contact with cryogenic liquid. To accomplish this, a variety of apertures were cut in the lids of the hermetically sealed packages. Initially three 0.454mm holes were drilled in each of the cases. One hole was drilled at either end of the case and one in the middle. Using this method of hole placement in combination with lowering the chip length-wise into liquid nitrogen allows air to escape the case's cavity thereby allowing cryogenic fluid to flow over the substrate. Once the liquid is in contact with the crystal surface, the SAW couples into the liquid and 40-50 dB of attenuation occurs, which is its "off state," once removed it returned to its peak. The wave energy became damped as the die warmed and humidity condensed. After approximately 35 minutes normal operation was restored. Larger apertures were placed in the lids in order to study device operation. The devices were tested with 1mm x 6mm slits at either end of the package (Fig. 4). These slit lid devices were cycled from room to cryogenic temperature six times, a plot of the passband after each cycle is shown in figures 5 and 6. The random attenuation of the

passband with each successive cycle indicates that particulates and contamination are increasingly growing on the active area of the die after the condensation evaporates. The randomization here is possibly due to particulates of metal on the transducers, as a result of drilling and cutting the package lid. These issues would not occur in practice because contamination due to lid removal would not occur and condensation will also be eliminated in a cryogenic tank environment. The important result from this phase of testing is that the devices never ceased working, an indication that thermal shock is not an issue under these testing conditions.

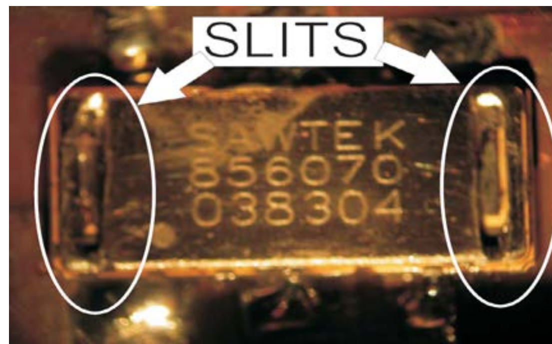

Figure 8-6. $LiNbO_3$ packaged device soldered to PCB with 1mm x 6mm silts in both ends of the package.

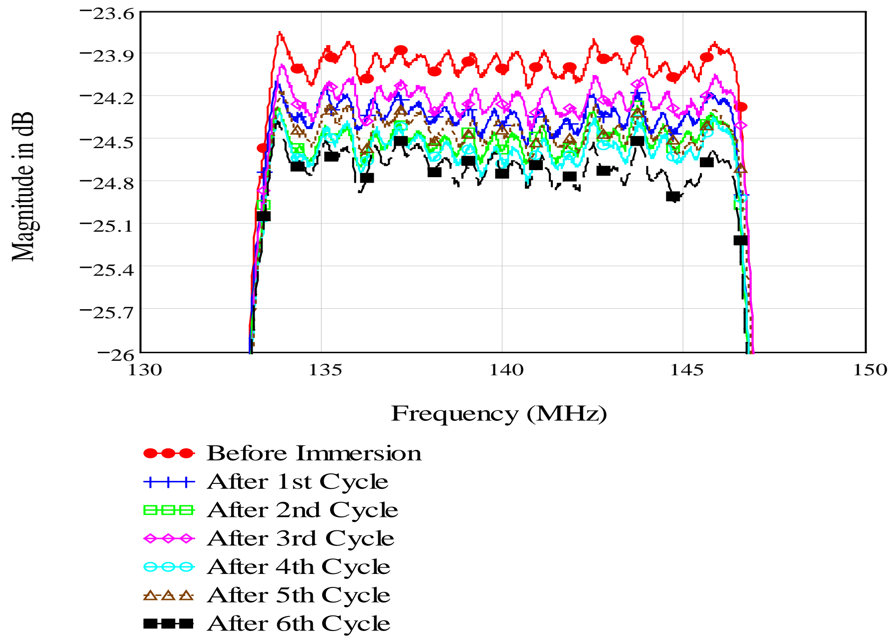

Figure 8-7. Passband response of repeated cycling of $LiNbO_3$ device with 1mm x 6mm slits in the package lid.

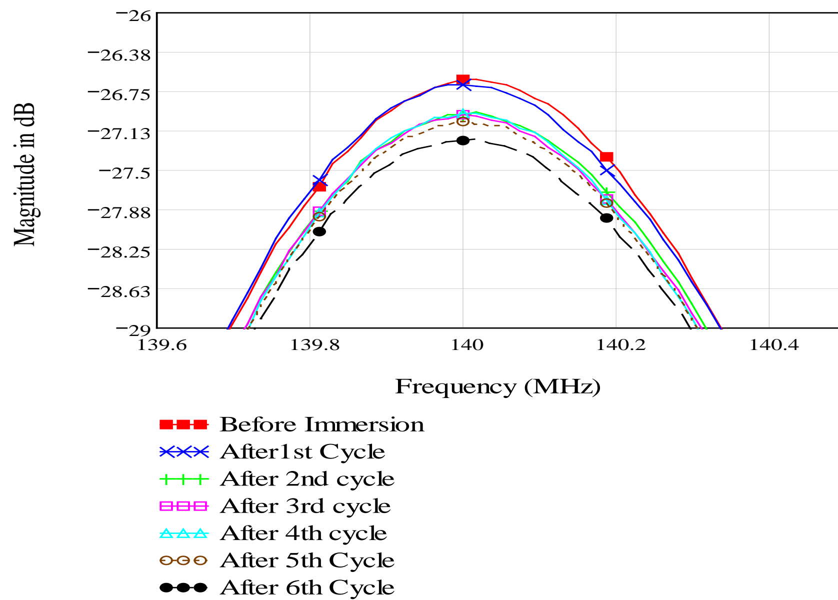

Figure 8-8 Passband response of repeated cycling of quartz device with 1mm x 6mm slits in the package lid.

8.3 Cryogenic Head Space Temperature Cycling

To simulate the environment of a cryogenic tank; a glass Dewar environment was modified such that the liquid nitrogen was contained, and a lid with feedthroughs allowed the devices under test to be lowered and raised in the flask. The lid kept the gas volume in the head space at a near cryogenic temperature, similar to what is expected in a real tank. The head space is much cooler than room temperature and is a water free environment, which will prevent condensation of the devices. The lid for the test flask was constructed using Styrofoam. This material was chosen for its good insulation properties and ease of handling. Two semi-rigid transmission lines pierced this lid in order to connect the device under test to the VNA. The lid was sealed for minimal openings left by the transmission lines piercing the lid. In addition to measuring the passband with the VNA, the real time behavior of the passband was captured using digital video. The time-code from digital video is very accurate and serves as an excellent means of extracting the switching speeds of the filters. The turn-off switching cycle was designated as the time from submersion until the passband was obscured in noise; and the turn-on cycle was designated as the time from removal from cryogenic fluid until the passband returned to normal, or near normal, room temperature operation. The human error in these times is approximately ±0.2s. The testing fixture was the same as previously reported—a PCB with SMA connectors and the surface mount SAW filters which were all solder mounted. The devices were oriented vertically with respect to the surface of the cryogenic fluid so that the cryogenic liquid will invade through the lower slits and force air out of the cavity during the submersion process, and the converse process occurs during removal. The cycling procedure as

before was: measure S_{21} response of device prior to submersion, submerge in cryogenic fluid for a period of time, then measure S_{21} response once the device is removed.

8.3.1 Temperature Head Space Cycling of Devices with Slit lids

Devices were immersed in the liquid nitrogen and the resulting S_{21} response was observed on the VNA. The lithium niobate devices turned-off in 0.32 seconds on average and the quartz devices turned-off in 0.55 seconds on average. It was hypothesized that the turn off times are not instantaneous because liquid nitrogen boils and evaporates when it makes initial contact with the room temperature chip surface, forming a vapor barrier until equilibrium is reached. The turn-on times however, were fairly long because it is most likely a function of the actual device temperature, the area of the slits, and the liquid adhesion properties on the active die surface. After removal from the liquid, the lithium niobate devices turned-on in 40.1 seconds (average) and the quartz devices turned-on in 20 seconds (average). The difference in turn-on times is most likely due to the size of the device packages, the topology of the active device areas and the difference in the package slit openings. The quartz is a simple in-line SAW filter with an unapodized input transducer and an apodized output transducer. The fractional bandwidth is small and the impulse response is longer than that for the $LiNbO_3$ filter. The niobate device however, has both apodized input and output transducers with a multi-strip coupler between the transducers and damping material between the transducer and the couplers (Figs. 7 & 8). The active area of the two filters are dramatically different, as well as topography and acoustic absorber areas. The S_{21} responses produced a practically constant passband

response, with only a few tenths of a dB in amplitude variation, after repeated cycling for both Quartz and Lithium Niobate (Figs. 9 & 10).

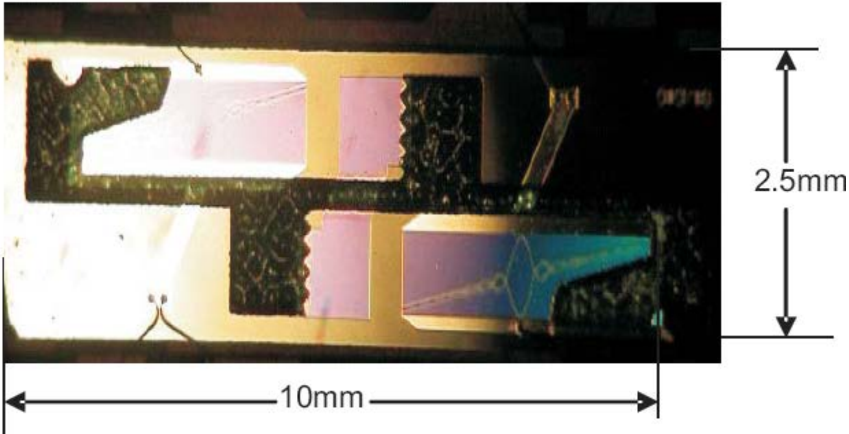

Figure 8-9. Photo of $LiNbO_3$ device topology

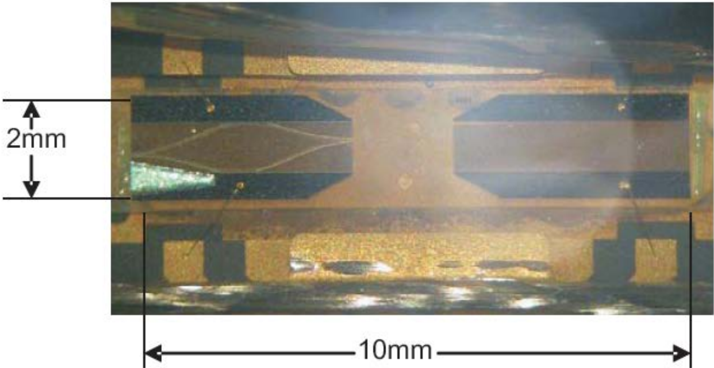

Figure 8-10. Photo of Quartz device topology

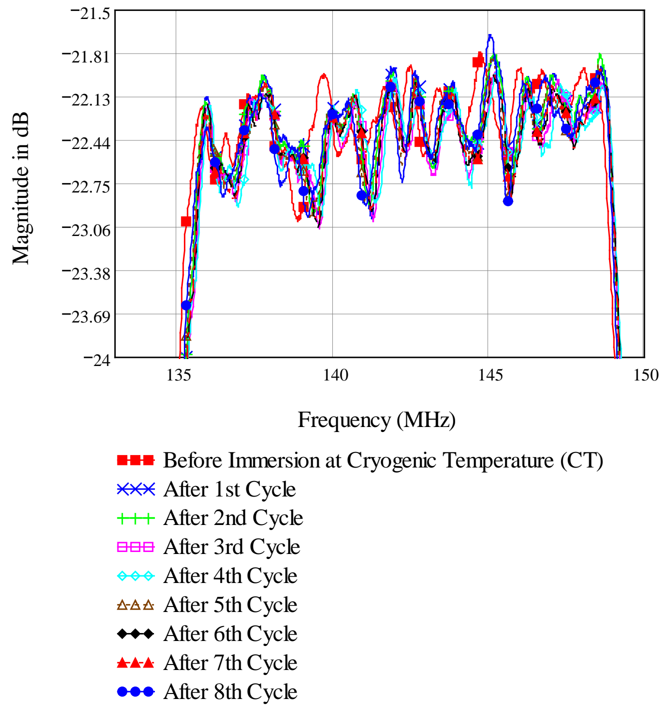

Figure 8-11. $LiNbO_3$ cryogenic head-space temperature cycling, after lid removal.

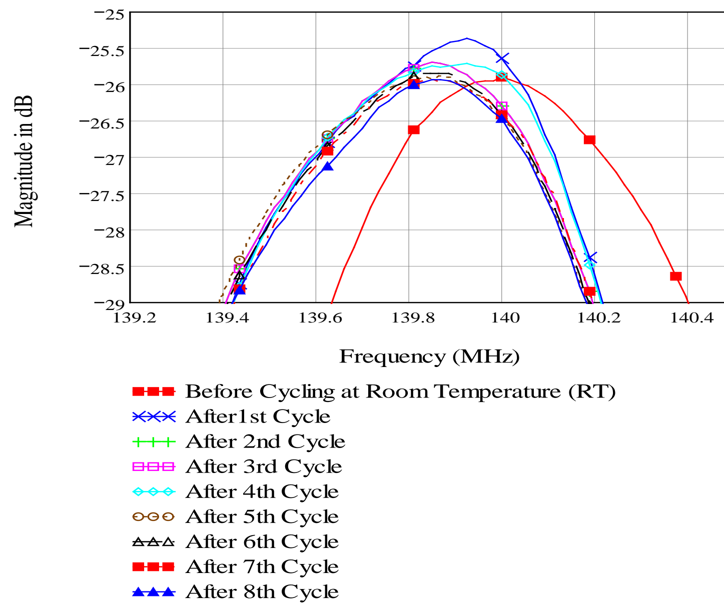

Figure 8-12. Quartz cryogenic head-space temperature cycling, after lid removal.

8.3.2 Package Lid Removal and Inspection

The package lids were removed with the use of a Dremel® tool and grinding wheel. In order to prevent the lid from falling onto the delicate die, only three sides of the package was opened then the lid was bent and broken off. Upon inspection with a microscope, the transducers were littered with microscopic pieces of metal on the die surface and throughout the package cavity due to the lid removal process. Cleaning failed to remove many of these pieces of metal but the devices still worked well and it is was determined that the experiments could move forward.

8.3.3 Temperature Head Space Cycling of Opened Devices

The testing of the devices without the lid was performed in the manner as with the slit experiments as previously discussed. The lithium niobate devices turned-off in 0.33 seconds on average and the Quartz devices turned-off in 0.59 seconds on average, very similar to results of the slit-open devices. The lithium niobate and quarts devices turned-on in 6.38 and 4.22 seconds on average, respectively. The device turn-on times were much faster than reported in the previous section, most likely due to the difference in the opening area. The difference in turn-on time between the quartz and niobate devices is most like due to the size of the device die and packages. The S_{21} responses revealed a near constant passband after repeated cycling for lithium niobate. The S_{21} response of the quartz device, however, showed a gradual increase in insertion loss with each successive cycle. Once the device was removed from the test fixture, allowed to return to room temperature and measured, the insertion loss returned to a value closer to the value before the temperature cycling began. A second cycle revealed a similar result, and a

second device was tested with similar outcome. However, depending on the device and the immersion cycle, the insertion loss would show tendencies of both increasing and decreasing slightly. It is possible that the contamination of the die surface due to the Dremel tool lid removal is having an effect on the performance of the quartz devices. Interestingly, similar contamination is present on the niobate device yet their performance is as expected. The device designs on the quartz and niobate are very different due to their difference in bandwidth. The die of both devices were inspected with a microscope and in both cases the cryogenic liquid cycling had actually reduced the quantity of the metal pieces on the die area. Another possible culprit of the slow degradation of the quartz passband may be micro-cracks in the substrate. There is currently no evidence to confirm or deny this speculation. The quartz loss issue will be addressed in the thermal shock of experiments.

8.3.4 Parallel Oriented Devices

This experiment is intended to discover if the device's orientation when lowered into liquid nitrogen has an effect on its operation. The test fixture was redesigned to orient the longer length of the die parallel to the surface of the liquid nitrogen; this means that the transducer's fingers are normal to the liquid. The devices response was measured using the technique as previously discussed.

When compared to previous measurements with a 90° rotation compared to the current test device orientations, the turn-off times were approximately the same as with prior experiments, when the margin of error is considered. The quartz device's turn-on times were slightly longer than before (approximately a half a second on average). The lithium niobate

devices, however, showed a 3.6 fold increase in turn-on time. It is conjectured that the primary method for device turn-on is the removal of liquid from the transducers by means of gravity; therefore, the switching speeds for both devices should be approximately the same. However, there are large differences in the device layout topography and it is presumed that switching speed differences are mainly due to the physical layout of the devices (as previously discussed).

8.4 Thermal Shock

Quartz and $LiNbO_3$ die are vulnerable to fracture attributable to thermal shock due to: poor thermal conductivity, large temperature change (~213°C) and the dicing process. Quartz and lithium niobate wafers were diced by both Vectron Int. and UCF. The die from Vectron were larger (~ 12mm x 18mm x 0.5mm) than the die diced from UCF (~ 9.5mm x 4.5mm x 0.36mm). This was done purposefully to see if the effect of size in the shock tests. Tests would investigate the relative effects between die size, dicing method and thermal shock. It should be remembered that none of the packaged devices failed during the numerous temperature cycling. The die edges were inspected using a metallurgical microscope on various magnifications and a polarizing lens prior to any submersion into the liquid nitrogen. The die edges are stressed and chipped during normal dicing operations; consequently, cracks from thermal stress are likely to propagate from these areas. Based on our inspection and our qualitative analysis, both the Vectron and UCF samples had very similar edges after dicing. The dies were temperature cycled from room to cryogenic temperature and then inspected again. Five lithium niobate die (larger samples) were cycled, four fractured violently upon submersion into the liquid nitrogen. All the smaller samples survived. Upon inspection with a microscope, it was not clear exactly where the

cracks in the lithium niobate originated. The sample that survived looked just as it did before cycling, i.e. no excessive cracks or chipping (other than the edges) were evident. All the quartz samples survived and after microscopic inspection appeared unchanged by the temperature cycling. In order to perform automated die cycling, a temperature cycling apparatus was constructed; this machine kept the die in the head space for ten minutes then submerged the die for ten minutes. The temperature difference was from the cryogenic Dewar head space temperature to the liquid nitrogen submersion (~104°C). Two samples each of lithium niobate and quartz from UCF and Vectron were examined by microscope then cycled for four hours, using the temperature cycling machine. None of the die were damaged or destroyed from the cycling process.

The results of these tests confirm what was expected. First, quartz is known to be a fairly robust material, is weakly piezoelectric, non-pyroelectric to any degree, and has a relatively small expansion coefficient. Manufacturing SAW quartz devices over the past 30 years has been fairly easy and thermal shock has typically been no problem. On the other hand, lithium niobate has higher piezoelectric constants than quartz, is pyroelectric, and has larger expansion coefficients than quartz. Manufacturing SAW niobate devices over the past 30 years has resulted in more controlled manufacturing processes than quartz, especially in regards to thermal shock.

8.5 OFC Device Performance

The last phase of experimentation involved an examination of OFC devices in response to temperature cycling. UCF fabricated OFC device using a common method: contact

lithography, ebeam metallization and lift-off. The devices were fabricated on $LiNbO_3$, the die sizes were (~14mm x 4mm x 0.36mm). This is a one port device and reflections are easily visible in the time domain, thus, the S_{11} time domain response was examined and recorded in order to asses device behavior and switching speed. The device was head space cycled in order to determine its switching speeds. It turned-off in an average time of 0.6seconds and turned-on in an average of 3.7seconds. Because the OFC device uses reflectors, the signal has to traverse the die surface twice, thus the signal loss is more sensitive to surface damage than the commercial filters and yet there was no degradation of the passband as compared to the commercial filters (Fig. 11). This suggests that the previous behavior was in fact due to metal remnants from cutting the package lid. A close-up of the second reflector bank shows the delay of the reflection decreased when submerged in liquid nitrogen (Fig. 11); the first reflector bank exhibited an equivalent response. This makes sense because the material TCF of $LiNbO_3$ is positive, and TCD is negative. The OFC device was also cycled from room to cryogenic temperature five times in order to assess its response to thermal shock. A comparison of the first and last cycled revealed no serious degradation (Fig. 12). The aluminum electrodes were inspected before and after cycling to determine if they were damaged by the cycling process, they looked practically the same, cleaner in some cases. A performance summary of the OFC and commercial devices is presented in Table 8-1.

Table 8-1. Performance summary, Off-submersion until the device's signal is lost in noise; On-time after removal from liquid for device to recover to its nominal insertion loss in dry air.

$LiNbO_3$	Off (sec)	On (sec)	Quartz	Off (sec)	On (sec)
Slits	0.3	40.4	Slits	0.6	20.0
Filter with Open Lid (Vertical Orientation)	0.3	6.4	Filter with Open Lid (Vertical Orientation)	0.6	4.2
Filter with Open Lid (Horizontal Orientation)	0.4	23.0	Filter with Open Lid (Horizontal Orientation)	0.6	5.2
OFC Device (Vertical Orientation)	0.6	3.7			

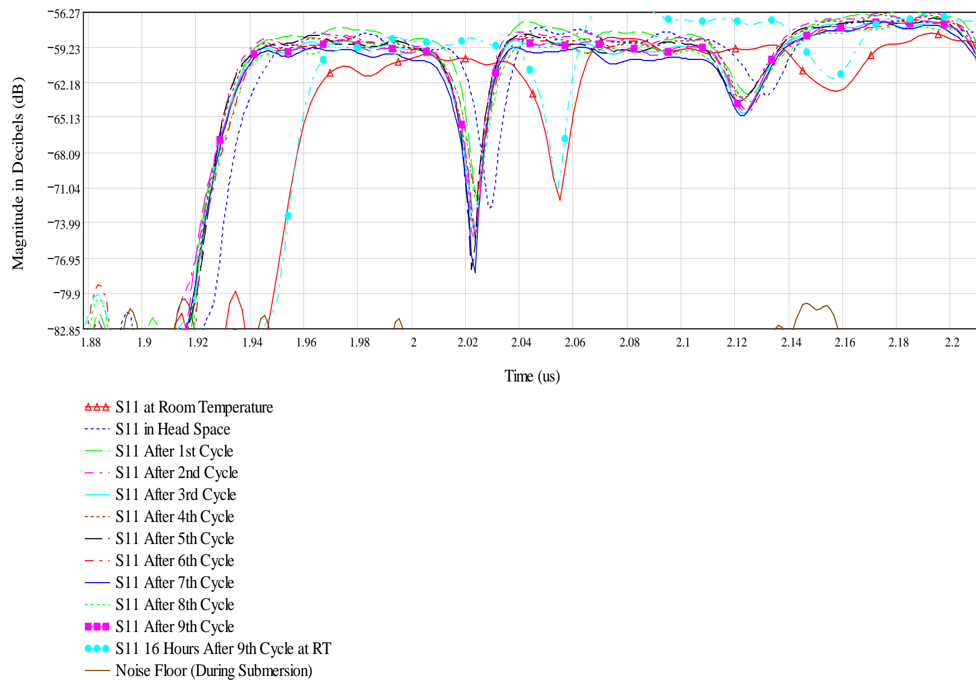

Figure 8-13. Close-up of second reflector bank of OFC device. This shows the response to repeated temperature cycling from headspace to liquid. The first reflector bank exhibited an equivalent response.

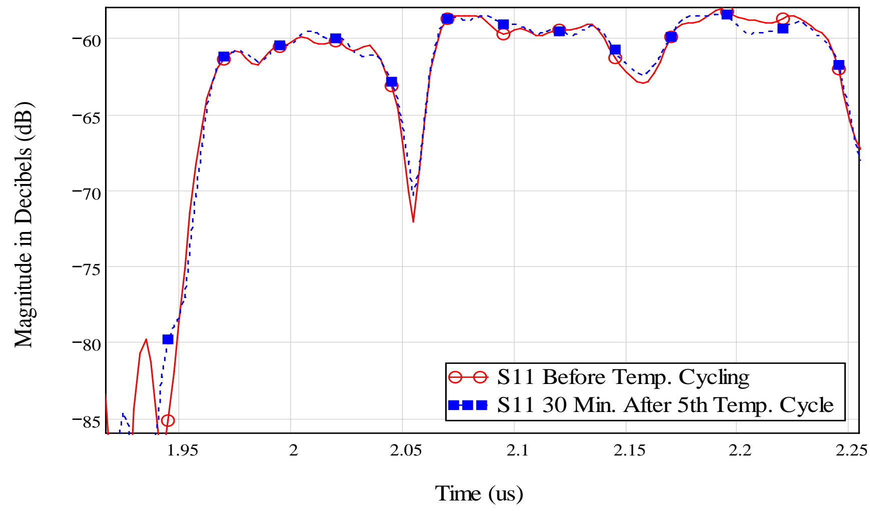

Figure 8-14. Close-up of the response of the second reflector bank of OFC device after five temperature cycles from room to cryogenic temperature. The first reflector bank exhibited an equivalent response.

8.6 CHAPTER 8 Summary

The most enlightening aspect of the temperature cycling tests is the fact that by mounting the devices into a commercial package using standard mounting techniques, the thermal shock at cryogenic temperatures seems to be controllable. Hundreds of cycles of commercial devices at cryogenic liquid to gas, or even room temperature, have resulted in no device failures. This is a clear indication that producing a SAW liquid sensor that operates at cryogenic temperatures is feasible on either quartz or lithium niobate.

CHAPTER 9 DISCUSSION AND CONCLUSIONS

The OFC-SAW was shown to be mechanically resistant to failure due to thermal shock from repeated cycles between room to liquid nitrogen temperature. Hundreds of cycles of over 30 devices produced no electrical or mechanical failures, suggesting that these tags are ideal for integration into cryogenic Dewar environments for the purposes of cryogenic liquid level detection.

The first ever integrated, passive, wireless, H_2 gas and temperature sensing OFC-SAW RFID tag was also demonstrated. This was accomplished by first performing a derivation of the acoustoelectric and acoustoelastic dispersion mechanisms for the SAW-thin-film interaction. A simple and intuitive SAW velocity dispersion approximation was developed which compared well to the established, rigorously-derived theory of Tiersten and the empirical approximation of Morgan. These equations, coupled with the design of a real-time data acquisition system and *in-situ* test fixture, allowed the SAW device to be used for the characterization of ultra-thin and semiconducting thin films.

A new technique to extract the electrical and mechanical parameters of a thin-film using SAW amplitude and velocity dispersion measurements were presented. The electrical and mechanical losses of a 10Å thick discontinuous Pd film, 500Å SnO_2 film and a 1000Å SiO were extracted. The deposition of thin films through a shadow mask produced non-uniform profiles, which are ideal for gas sensing purposes. This advancement is previously unreported in literature and needs to be studied further. There is a relationship between the film-thickness profile, the distance between the substrate and the aperture, and the width and thickness of the

aperture, which needs to be characterized and reported. These films may be used to study a variety of physical phenomena such as gas adsorption, desorption and diffusion rates or the sensitivity of these non-uniform films to magnetic or other forces.

A procedure that allowed the reproducible deposition of ultrathin films of Pd and collaborative work with Dr. Donald Malocha resulted in a derivation of a resistivity approximation for discontinuous ultrathin films to continuous thin films and thick films. Pd-UTFs are incredibly sensitive to H_2 gas at room temperature, but is also attractive for oxygen adsorption in air, which causes a dramatic increase in resistance and reduces the film's H_2 gas sensitivity. Oxygen adsorption on the surface of an ultrathin noble metal such as Pd is previously unreported; there may also be some interesting physics that warrant further inquiry. Tin dioxide films proved to be the most stable hydrogen gas sensors. The sensitivity of SnO_2 is highly dependent upon its processing. An experimental design procedure was used to tune the process parameters and produce a highly sensitive and stable H_2 gas detecting film. Three OFC-SAW H_2 gas detectors were simultaneously and wirelessly interrogated while they were being exposed to various flow rates of H_2 gas. Rapid H_2 detection was achieved for flow rates as low as 1ccm of a 2% H_2, 98% N_2 mixture.

This dissertation summarizes many years of cumulative research dedicated to developing acoustoelectric and acoustoelastic equations, derived from previously-cited research and rigorous experimentation, that provides researchers with a simplified, yet comprehensive direction to approximate the SAW thin-film interaction. These equations, not only provides additional empirical clarity, but saves researchers in this domain hours of calculations and experimentation.

The equations are not the only strength noted in this research. The development of a network of integrated, passive, wireless, H_2 gas, RFID-tag sensors, has yet to be demonstrated in this capacity in literature to date. The research that advanced this technology required innovative thought, numerous experiments, and theoretical validation. Though remarkable in theory, this technology responds to the well-defined need declared by various organizations, most notably, NASA. Properly implemented, these sensors can prevent catastrophic accidents and save millions of dollars in cost.

LIST OF REFERENCES

[1] "Mission Achives," www.nasa.gov/mission_pages/shuttle/shuttlemissions/archives/sts-1.html: NASA, 2011.

[2] N. Berg and J. Speulstra, "The Operation of Acoustic Surface Wave Delay Lines in a Nuclear Environment," *Nuclear Science, IEEE Transactions on,* vol. 20, pp. 137-143, 1973.

[3] J. A. Thiele and M. P. da Cunha, "High temperature SAW gas sensor on langasite," 2003, pp. 769-772 Vol.2.

[4] Y. Aoki, Y. Wada, Y. Sekimoto, W. Yamaguchi, A. Ogino, M. Saitoh, R. Nomura, and Y. Okuda, "Application of Surface Acoustic Wave Sensors for Liquid Helium-4 and Helium-3," *Journal of Low Temperature Physics,* vol. 134, pp. 945-958, 2004.

[5] B. H. Fisher and D. C. Malocha, "Cryogenic Liquid Sensing Using SAW Devices," in *Frequency Control Symposium, 2007 Joint with the 21st European Frequency and Time Forum. IEEE International*, 2007, pp. 505-510.

[6] N. Y. Kozlovski and D. C. Malocha, "SAW passive wireless multi sensor system," in *Ultrasonics Symposium (IUS), 2009 IEEE International*, 2009, pp. 1541-1544.

[7] N. Kozlovski, D. Malocha, and A. Weeks, "A 915 MHz SAW Sensor Correlator System," *Sensors Journal, IEEE,* vol. PP, pp. 1-1, 2011.

[8] A. Bryant, D. L. Lee, and J. F. Vetelino, "A Surface Acoustic Wave Gas Detector," in *1981 Ultrasonics Symposium*, 1981, pp. 171-174.

[9] A. Pohl, G. Ostermayer, L. Reindl, and F. Seifert, "Spread spectrum techniques for wirelessly interrogable passive SAW sensors," in *IEEE 4th International Symposium on Spread Spectrum Techniques and Applications Proceedings*, 1996, pp. 730-734.

[10] D. M. Dobkin, *The RF in RFID: Passive UHF RFID in Practice*. Boston: Elsevier, 2008.

[11] D. Morgan, *Surface Acoustic Wave Filters: With Application to Electronic Communiations and Signal Processing*, 2nd ed. Boston: Elsevier, 2007.

[12] S. Datta, *Surface Acoustic Wave Devices*. New Jersey: Prentice-Hall, 1986.

[13] D. S. Ballantine, R. M. White, S. J. Martin, A. J. Ricco, E. T. Zellers, G. C. Frye, and H. Wohltjen, *Acoustic Wave Sensors: Theory, Design and Physico-Chemical Applications*. New York: Academic Press, 1997.

[14] C. K. Campbell, *Surface Acoustic Wave Devices for Mobile and Wireless Applications*. San Diego: Academic Press, 1998.

[15] C. S. Hartmann, Jr., D. T. Bell, and R. C. Rosenfeld, "Impulse Model Design of Acoustic Surface-Wave Filters," *Microwave Theory and Techniques, IEEE Transactions on,* vol. 21, pp. 162-175, 1973.

[16] D. C. Malocha and C. D. Bishop, "The Classical Truncated Cosine Series Functions with Applications to SAW Filters," *Ultrasonics, Ferroelectrics and Frequency Control, IEEE Transactions on,* vol. 34, pp. 75-85, 1987.

[17] H. Engan, "Surface Acoustic Wave Multielectrode Transducers," *Sonics and Ultrasonics, IEEE Transactions on,* vol. 22, pp. 395-401, 1975.

[18] D. R. Gallagher and D. C. Malocha, "Orthogonal Frequency Coding for Use in Ultra Wide Band Communications and Correlators," in *International Frequency Control Symposium and Exposition, 2006 IEEE*, 2006, pp. 494-499.

[19] C. K. Campbell and P. J. Edmonson, "An empirical method for obtaining the harmonic response coefficients of a SAW interdigital transducer," in *Ultrasonics Symposium, 2002. Proceedings. 2002 IEEE*, 2002, pp. 283-287 vol.1.

[20] N. Saldanha, "Coupling of Modes Model and Analysis of One-Port SAW Resonators on Langasite and Langatate," M.S.E.E., Electrical Engineering, Central Florida, Orlando, 2003.

[21] N. Y. Kozlovski and D. C. Malocha, "Multi-track low-loss SAW tags with flexible impedance matching for passive wireless sensor applications," in *Frequency Control Symposium (FCS), 2010 IEEE International*, 2010, pp. 279-286.

[22] D. Puccio, "Design, Analysis and Implementation of Orthogonal Frequency Coding in SAW Devices Used for Spread Spectrum Tags and Sensors," Ph.D, Electrical Engineering and Computer Science, University of Central Florida, Orlando, FL, 2006.

[23] N. Saldanha and D. C. Malocha, "Improved reflectivity and velocity model for aluminum gratings on YZ $LiNbO_3$," *Ultrasonics, Ferroelectrics and Frequency Control, IEEE Transactions on,* vol. 58, pp. 798-807, 2010.

[24] T. Hubert, L. Boon-Brett, G. Black, and U. Banach, "Hydrogen sensors - A review," *Sensors and Actuators B: Chemical,* vol. 157, pp. 329-352, 2011.

[25] G. Ostermayer, A. Pohl, C. Hausleitner, L. Reindl, and F. Seifert, "CDMA for wireless SAW sensor applications," in *Spread Spectrum Techniques and Applications Proceedings, 1996., IEEE 4th International Symposium on*, 1996, pp. 795-799 vol.2.

[26] R. E. Ziemer and W. H. Tranter, *Principles of Communications: Systems Modulation and Noise*, 5th ed. Hoboken: John Wiley & Sons, Inc., 2002.

[27] "Wireless TEC Room Temperature Sensor (Mesh)," Siemens Building Techologies Inc., Buffalo Grove, IL2007.

[28] B. Dietz and H. Seifried, "Harris Semiconductor Introduces the World's First Radiation Hardened Dual MOSFET Driver," Harris Semiconductor, Melbourne, FL1999.

[29] T. M. Flynn, *Cryogenic Engineering*, 2nd ed. New York: Marcel Dekker, 2005.

[30] J. G. Weisend, *Handbook of Cryogenic Engineering*. Philadelphia: Taylor & Francis, 1998.

[31] R. Stuart, "Cryogenics and nuclear power," *Advances in cryogenic engineering,* vol. 20, pp. 61-69, 1975.

[32] T. R. Wilson, R. Cherney, S. Rickman, R. Kichak, and E. Ungar, "STS-114 Engine Cut-off Sensor Anomaly: Technical Consultation Report," NASA Engineering and Safety Center Technical Consultation Report2005.

[33] T. Malik. (2006, September, 09, 2011). Mission Atlantis: Errant Fuel Sensor Scrubs Shuttle Launch. *Space.Com*.

[34] "Code of Practice: Safe Use of Liquid Nitrogen," Royal Free Hampstead NHS Trust & Royal Free & University College Medical School, London2004.

[35] "Hydrogen Embrittlement: An Overview from a Mechanical Fastenings Aspect," The Fastener Engineering and Research Association2006.

[36] B. Somerday and A. Burns, "Hydrogen embrittlement mechanisms in metals," Sandia National Laboratories, New Mexico2007.

[37] S. Hawkswort and L. d. Broisi, "Hydrogen Ignition," HSL and INERIS2007.

[38] I. L. Drell and F. E. Belles, "Report 1383: Survey of Hydrogen Combustion Properties," Lewis Flight Propulsion Laboratory, National Advisory Committee for Aeronautics, Cleveland1957.

[39] T. B. Jones, "Nomograms for assessment of ignition risk associated with capacitive discharges," Department of Electrical Engineering, University of Rochester, Rochester1998.

[40] "Hydrogen Properties," US Department of Energy: Energy Efficiency and Renewable Energy, CA2001.

[41] J. Jun, B. Chou, J. Lin, A. Phipps, X. Shengwen, K. Ngo, D. Johnson, A. Kasyap, T. Nishida, H. T. Wang, B. S. Kang, F. Ren, L. C. Tien, P. W. Sadik, D. P. Norton, L. F. Voss, and S. J. Pearton, "A hydrogen leakage detection system using self-powered wireless hydrogen sensor nodes," *Solid-State Electronics,* vol. 51, pp. 1018-1022, 2007.

[42] Y.-S. Huang, Y.-Y. Chen, and T.-T. Wu, "A passive wireless hydrogen surface acoustic wave sensor based on Pt-coated ZnO nanorods," *Nanotechnology,* vol. 21, 2010.

[43] J. Chou, *Hazardous Gas Monitors*. New York: McGraw-Hill, 2000.

[44] J. Smallwood, "Are air temperature and humidity important to static electricity?," in *Static Consultants Notebook*, ed, 2005.

[45] A. J. Dessler, D. E. Overs, and W. H. Appleby, "The Hindenburg Fire: Hydrogen or Incendiary Paint?," *Buoyant Flight,* vol. 52, pp. 1-11, January 12, 2005 2005.

[46] M. Meyyappan and M. K. Sunkara, *Inorganic Nanowires- Applications, Properties and Characterization*. Boca Raton: CRC Press, 2010.

[47] F. Ren and S. J. Pearton, *Semiconductor device-based sensors for gas, chemical, and biomedical applications*. Boca Raton: CRC Press, 2011.

[48] F. A. Lewis, *The Palladium Hydrogen System*. New Tork: Academic Press, 1967.

[49] J. E. Morris, A. Kiesow, M. Hong, and F. Wu, "Effects of Hydrogen Absorption on the Electrical Conduction of Discontinuous Palladium Thin Films," *International Journal of Electronics,* vol. 81, pp. 441-447, 1996.

[50] T. Xu, M. P. Zach, Z. L. Xiao, D. Rosenmann, U. Welp, W. K. Kwok, and G. W. Crabtree, "Self-assembled monolayer-enhanced hydrogen sensing with ultrathin palladium films," *Applied Physics Letters,* vol. 86, p. 203104, 2005.

[51] S. Shukla, S. Seal, L. Ludwig, and C. Parish, "Nanocrystalline indium oxide-doped tin oxide thin film as low temperature hydrogen sensor," *Sensors and Actuators B: Chemical,* vol. 97, pp. 256-265, 2004.

[52] S. Shukla, P. Zhang, H. J. Cho, S. Seal, and L. Ludwig, "Room temperature hydrogen response kinetics of nano–micro-integrated doped tin oxide sensor," *Sensors and Actuators B: Chemical,* vol. 120, pp. 573-583, 2007.

[53] K. Kyun Tae, S. Jun, and C. Sung Min, "Hydrogen gas sensor using Pd nanowires electro-deposited into anodized alumina template," *Sensors Journal, IEEE,* vol. 6, pp. 509-513, 2006.

[54] A. D'Amico, A. Palma, and E. Verona, "Palladium-surface acoustic wave interaction for hydrogen detection," *Applied Physics Letters,* vol. 41, pp. 300-301, August 1, 1982 1982.

[55] A. D'Amico, A. Palma, and E. Verona, "Hydrogen Sensor Using a Palladium Coated Surface Acoustic Wave Delay-Line," *IEEE Ultrasonics Symposium,* pp. 308-311, 1982.

[56] A. D'Amico, A. Palma, and E. Verona, "Surface Acoustic Wave Hydrogen Sensor," *Sensors and Actuators,* vol. 3, p. 31, 39 1982.

[57] W. P. Jakubik, M. W. Urbanczyk, S. Kochowski, and J. Bodzenta, "Bilayer Structure for Hydrogen Detection in a Surface Acoustic Wave Sensor," *Sensors and Actuators B,* vol. 82, pp. 265-271, 2002.

[58] K. Yamanaka, S. Ishikawa, N. Nakaso, N. Takeda, T. Mihara, and Y. Tsukahara, "Ball SAW Device For Hydrogen Gas Sensor," presented at the IEEE Ultrasonics Symposium, 2003.

[59] W. P. Jakubik and M. W. Urbanczyk, "SAW hydrogen sensor with a bilayer structure based on interaction speed," *Sensors and Actuators B: Chemical,* vol. 106, pp. 602-608, 2005.

[60] W. P. Jakubik, M. W. Urbanczyk, and E. Maciak, "Palladium and Metal-Free Phthalocyanine Bilayer Structures for Hydrogen Detection in the SAW Sensor System Based on Interaction Speed," *Sensors Journal, IEEE,* vol. 6, pp. 1178-1185, 2006.

[61] B. Fisher and D. C. Malocha, "Room Temperature Hydrogen Gas Sensing Using SAW Devices," presented at the Proceedings of the Joint Japan-USA International Meeting on Acoustic Wave Devices, Orlando, FL, 2008.

[62] D. C. Malocha and B. H. Fisher, "Acoustoelectric Effect Study for SAW Sensors," in *IEEE International Frequency Control Symposium*, Besançon, France, 2009, pp. 254-259.

[63] B. Fisher and D. Malocha, "Study of the Acoustoelectric Effect for SAW Sensors," *IEEE Transactions on Ultrasonics, Ferroelectrics and Frequency Control,* vol. 57, pp. 698-706, 2010.

[64] B. H. Fisher and D. C. Malocha, "SAW-Thin-Film Acoustoelectric In-Situ Observation and Measurement " in *Joint Conference of the IEEE International Frequency Control and the European Frequency and Time Forum (IFCS)*, 2011, pp. 1-6.

[65] H. E. Bommel, "Ultrasonic Attenuation in Superconducting Lead," *Physical Review,* vol. 96, p. 220, 1954.

[66] W. P. Mason, "Ultrasonic Attenuation Due to Lattice-Electron Interaction in Normal Conducting Metals," *Physical Review,* vol. 97, p. 557, 1955.

[67] W. P. Mason, "Phonon Viscosity and Its Effect on Acoustic Wave Attenuation and Dislocation Motion," *The Journal of the Acoustical Society of America,* vol. 32, pp. 458-472, 1960.

[68] E. G. Spencer and P. V. Lenzo, "Temperature Dependence of Microwave Elastic Losses in LiNbO3 and LiTaO3," *Journal of Applied Physics,* vol. 38, pp. 423-424, 1966.

[69] M. J. Rice, "Acoustic attenuation in crystalline solids " *Proceedings of the Physical Society,* vol. 89, pp. 373-378, 1966.

[70] K. A. Ingebrigtsen, "Surface Waves in Piezoelectrics," *Journal of Applied Physics,* vol. 40, pp. 2681-2686, 1969.

[71] A. R. Hutson and L. W. Donald, "Elastic Wave Propagation in Piezoelectric Semiconductors," *Journal of Applied Physics,* vol. 33, pp. 40-47, 1962.

[72] M. N. O. Sadiku, *Elements of Electromagnetics*, 3 ed. New York: Oxford University Press, 2001.

[73] K. A. Ingebrigtsen, "Linear and Nonlinear Attenuation of Acoustic Surface Waves in a Piezoelectric Coated with a Semiconducting Film," *Journal of Applied Physics,* vol. 41, pp. 454-459, 1970.

[74] R. Adler, "Simple Theory of Acoustic Amplification," *IEEE Transactions on Sonics and Ultrasonics,* vol. 18, pp. 115-117, 1971.

[75] I. L. Bajak, A. McNab, J. Richter, and C. D. W. Wilkinson, "Attenuation of acoustic waves in lithium niobate," *The Journal of the Acoustical Society of America,* vol. 69, pp. 689-695, 1981.

[76] P. J. King and F. W. Sheard, "Viscosity Tensor Approach to the Damping of Rayleigh Waves," *Journal of Applied Physics,* vol. 40, pp. 5189-5190, 1969.

[77] A. J. Slobodnik, Jr., "Attenuation of Microwave Acoustic Surface Waves Due to Gas Loading," *Journal of Applied Physics,* vol. 43, pp. 2565-2568, 1972.

[78] Z. Hadjoub, I. Beldi, M. Bouloudnine, A. Gacem, and A. Doghmane, "Thin film loading effects on SAW velocity dispersion curves," *Electronics Letters,* vol. 34, pp. 313-315, 1998.

[79] J. D. N. Cheeke, *Fundamentals and Applications of Ultrasonic Waves*. Boca Raton: CRC Press, 2002.

[80] H. F. Tiersten and B. K. Sinha, "A perturbation analysis of the attenuation and dispersion of surface waves," *Journal of Applied Physics,* vol. 49, pp. 87-95, 1978.

[81] D. Penunuri and K. M. Lakin, "Surface Acoustic Wave Velocities of Isotropic Metal Films on Selected Cuts of $Bi_{12}GeO_{20}$, Quartz, Al_2O_3, and $LiNbO_3$," *Sonics and Ultrasonics, IEEE Transactions on,* vol. 21, pp. 293-295, 1974.

[82] D. F. Morgan and D. Graig, Eds., *SAWs in LiNbO3: Properties of Common Orientations* (Properties of Lithium Niobate. London: INSPEC, 2001, p.^pp. Pages.

[83] T. A. Anastasio, "Dielectric Properties of Reactively Evaporated Silicon Monoxid," *The Journal of Vacuum Science and Technology,* vol. 6, p. 5, 1968.

[84] K. L. Davis and J. F. Weller, "SAW Attenuation in Metal Film-Coated Delay Lines," presented at the 1979 Ultrasonics Symposium, 1979.

[85] E. H. Sondheimer, "The Mean Free Path of Electrons in Metals," *Advances in Physics,* vol. 1, pp. 1-42, 1952.

[86] T. B. Flanagan and W. A. Oates, "The Palladium Hydrogen System," *Annual Review of Material Science,* vol. 21, pp. 269-304, 1991.

[87] E. A. Owen and J. I. Jones, "The Palladium-Hydrogen System," *Proceedings of the Physical Society,* vol. 49, pp. 603-610, 1937.

[88] L. L. Jewell and B. H. Davis, "Review of Absorption and Adsorption in the Hydrogen-Palladium System," *Applied Catalysis A: General,* vol. 310, pp. 1-15, 2006.

[89] C. Chrostofides and A. Mandels, "Solid-state Sensors for Trace Hydrogen Gas Detection," *Journal of Applied Physics,* vol. 68, pp. R1-R30, September 15, 1990 1990.

[90] R. C. Hughes and W. K. Schubert, "Thin Films of Pd/Ni Alloys for Detection of High Hydrogen Concentrations," *Journal of Applied Physics,* vol. 71, pp. 542-544, 1991.

[91] Y. Sakamoto, K. Takai, I. Takashima, and M. Imada, "Electrical Resistance Measurements as a Function of Composition of Palladium-Hydrogen (Deuterium) Systems by a Gas Phase Method," *Journal of Physics: Condensed Matter,* vol. 8, pp. 3399-3411, 1996.

[92] D. B. Wolfe, J. C. Love, K. E. Paul, M. L. Chabinyc, and G. M. Whitesides, "Fabrication of palladium-based microelectronic devices by microcontact printing," *Applied Physics Letters,* vol. 80, pp. 2222-2224, 2002.

[93] S. Dongyoun, A. Mizukami, S. Akao, I. Satoh, M. Bryan, N. Takeda, T. Ohgi, N. Nakaso, T. Miyagishi, H. Tanaka, K. Fukiura, H. Kazato, H. Watanabe, T. Mihara, and K. Yamanaka, "Spherical 1 mm SAW device based on Ball Semiconductor/MEMS technology," presented at the IEEE Ultrasonics Symposium, 2004.

[94] J. RaviPrakash, A. H. McDaniel, M. Horn, L. Pilione, P. Sunal, R. Messier, R. T. McGrath, and F. K. Schweighardt, "Hydrogen sensors: Role of palladium thin film morphology," *Sensors and Actuators B: Chemical,* vol. 120, pp. 439-446, 2007.

[95] M. Wang and Y. Feng, "Palladium-silver thin film for hydrogen sensing," *Sensors and Actuators B: Chemical,* vol. 123, pp. 101-106, 2007.

[96] K. L. Chopra, L. C. Bobb, and M. H. Francombe, "Electrical Resistivity of Thin Single-Crystal Gold Films," *Journal of Applied Physics,* vol. 34, pp. 1669-1702, 14 November 1962 1963.

[97] S. Harsha, *Principles of Physical Vapor Deposition of Thin Films*. San Diego: Elsevier, 2006.

[98] C. A. Neugebuer and M. B. Webb, "Electron Conduction Mechanism in Ultrathin, Evaporated Metal Films," *Journal of Applied Physics,* vol. 33, pp. 74-82, January 1962 1962.

[99] O. Dankert and A. Pundt, "Hydrogen-induced percolation in discontinuous films," *Applied Physics Letters,* vol. 81, pp. 1618-1920, 2002.

[100] J. v. Lith, A. Lassesson, S. A. Brown, M. Schulze, J. G. Partridge, and A. Ayesh, "Hydrogen Sensor Based on Tunneling Between Palladium Clusters," *Applied Physics Letters,* vol. 91, 2007.

[101] R. M. Hill, "Electrical Conduction in Discontinous Metal Films," *Contemporary Physics,* vol. 10, pp. 221-240, 1969.

[102] M. Ohring, *The Material Science on Thin Films*. Boston: Academic Press Inc., 1992.

[103] J. C. Yen, "An Investigation of the Electrical properties of Zinc Oxide Thin Films Influenced by Oxygen Adsorption," *Journal of Vacuum Science,* vol. 10, pp. 47-51, 1974.

[104] R. Pitts, P. Liu, S.-H. Lee, E. Tracy, R. D. Smith, and C. Salter, "Interfacial Stability of Thin Film Hydrogen Sensors," presented at the Proceedings of the DOE Hydrogen Program Review, 2001.

[105] R. D. Smith, P. Liu, S.-H. Lee, E. Tracy, and R. Pitts, "Interfacial Stability of Thin Film Fiber-Optic Hydrogen Sensors," presented at the Proceedings of the 2002 U.S. DOE Hydrogen Review., 2002.

[106] R. W. Berry, P. M. Hall, and M. T. Harris, *Thin Film Technology*. New York: Van Nostrand Reinhold Company, 1968.

[107] B. H. Fisher and D. C. Malocha, "A Study on the Aging of Ultra-Thin Palladium Films on SAW Hydrogen Gas Sensors," in *IEEE International Frequency Control Symposium (FCS)* 2010, pp. 242-247.

[108] J. Chou, *Hazardous gas monitors: a practical guide to selection, operation and applications*. Columbus, OH, USA: McGraw-Hill, 2000.

[109] R. Hauser, L. Reindl, and J. Biniasch, "High-temperature stability of $LiNbO_3$ based SAW devices," in *IEEE Symposium on Ultrasonics*, 2003, pp. 192-195 Vol.1.

[110] A. F. Khan, "Effects of annealing on the structrual, optical and electrical properties of SnO_2, TiO_2, Ge and multi--layer TiO_2-Ge thin films prepared by physical vapor deposition techniques," Ph.D, Department of Chemical and Materials Engineering, Pakistan Institute of Engineering and Applied Sciences, Islamabad, Pakistan, 2010.

[111] D. H. Piehl, "Oxidation of aluminum foil under simulated high temperature annealing using thermogravimetry," *Journal of Thermal Analysis,* vol. 6, p. 9, 1974.

[112] A. F. Mayadas and M. Shatzkes, "Electrical-Resistivity Model for Polycrystalline Films: the Case of Arbitrary Reflection at External Surfaces," *Physical Review B,* vol. 1, pp. 1382-1389, 1970.

[113] B. M. C. Santos, "SAW Reflective Transducers and Antennas for Orthogonal Frequency Coded SAW Sensors," M.S., Electrical Engineering and Computer Science, University of Central Florida, Orlando, FL, 2009.

[114] M. W. Gallagher, B. C. Santos, and D. C. Malocha, "Wireless wideband SAW sensor - antenna design," in *IEEE International Frequency Control Symposium (IFCS)*, 2010, pp. 291-296.

[115] B. R. McAvoy and H. L. Salvo, Jr., "Cryogenic Experiments with Microwave Acoustic Resonators," *IEEE Ultrasonics Symposium,* pp. 343-348, 1986.

[116] K. Yamanouchi, H. Nakagawa, and H. Odagawa, "GHz-range surface acoustic wave low loss filter at super low temperature," *Joint Meeting of the European Frequency and Time Forum and the IEEE International Frequency Control Symposium,* vol. 2, pp. 911-914 vol.2, 1999.

[117] J. Hornsteiner, E. Born, G. Fischerauer, and E. Riha, "Surface acoustic wave sensors for high-temperature applications," *IEEE International Frequency Control Symposium,* pp. 615-620, 1998.

[118] T. E. Parker and G. K. Montress, "Precision surface-acoustic-wave (SAW) oscillators," *IEEE Transactions on Ultrasonics, Ferroelectrics and Frequency Control,* vol. 35, pp. 342-364, 1988.